

Physico-mechanical design of conducting polymers for neural interface applications

Author:

Baek, Sungchul

Publication Date:

2012

DOI:

<https://doi.org/10.26190/unsworks/15921>

License:

<https://creativecommons.org/licenses/by-nc-nd/3.0/au/>

Link to license to see what you are allowed to do with this resource.

Downloaded from <http://hdl.handle.net/1959.4/52371> in <https://unsworks.unsw.edu.au> on 2024-04-18

Physico-mechanical design of conducting polymers for neural interface applications

Sungchul Baek

A Thesis Submitted for the Degree of Doctor of Philosophy
At the University of New South Wales,
Faculty of Engineering, Graduate School of Biomedical Engineering

August 31, 2012

Acknowledgments

First and foremost, I am deeply grateful to my advisor, Prof. Laura Poole-Warren, for her incredible patience, inspiration, encouragement and guidance. Her perspicacious advice helped me in many ways throughout the four years that I have been at UNSW. I also have a deep sense of gratitude to Dr. Rylie Green for her honest but generous mentoring. I am in debt to several people who helped me along the way.

I want to thank Dr. Kobayashi Hisatoshi and Dr. Chiaki Yoshikawa of the National Institute of Material Science (NIMS) in Japan, for the opportunity to visit the group in 2010 and for providing excellent training on SI-ATRP. I thank Dr. Anthony Granville of UNSW's Centre for Advanced Macromolecular Design (CAMD) for his advice and help during my time in their lab. I would also like to thank Dr. Mark Hoffman, Dr. Ruiping Hoo and Dr. Philip Boughton of UNSW Material Science Department for their assistance in performing the nanoindentation tests, Dr. Henner Kampwerth and Dr. Patrick Campbell of UNSW Photovoltaic Engineering for lending their ellipsometers, and Scientia Prof. Nigel Lovell and Mr. Phil Preston of Bionic Vision Australia (BVA) for their technical help and collaboration in research.

I am appreciative of all the members of the conducting polymer and hydrogel group. I would like to thank Dr. Penny Martens, Johnson Chung, Jenny Cheng, Eman Nafea, Josef Goding, Khoon Lim and Rachelle Hassarati for our great discussions and meetings as well as for their excellent work and assistance.

Abstract

A key limitation associated with conducting polymers (CP) for implantable electrode applications is their inferior physico-mechanical properties and the effect of this on biological performance. This research investigates the physico-mechanical cues of conventional conducting polymer coatings and aims to understand their effects on neural adhesion and neurite extension. The underlying hypothesis was that the biological performance of CPs can be effectively controlled by physical cues such as surface topography and mechanical softness.

Poly(3,4-ethylenedioxythiophene) (PEDOT) doped with perchlorate, benzenesulfonate, tosylate (pTS), dodecylbenzenesulfonate and polystyrenesulfonate were compared across a range of baseline material properties. Additionally, the deposition charge used to produce PEDOT was varied from 0.05 to 1 C/cm² to determine an optimal thickness for electrode coatings. To address the need for electroactive biomaterials with improved neural interfacing, nanobrush-CP hybrids were fabricated. Dense poly(2-hydroxyethyl methacrylate) (PHEMA) brushes were grafted via surface-initiated atom transfer radical polymerisation (SI-ATRP). PEDOT/pTS was electrochemically deposited through this nanobrush substrate. The formation of the hybrid was confirmed and characterised across implant performance metrics.

The physical, mechanical, electrical and biological performance of PEDOT coatings was used to assess ideal fabrication parameters, optimised for neural cell interactions. Nanoindentation techniques were used to yield the first quantitative values for stiffness moduli of electrodeposited CP coatings on metal substrates. It was found that the nodularity of the CP surface increased with increasing coating thickness and decreasing dopant size. A major finding of this study was that high roughness of conventionally doped PEDOT produced on the micron scale, prevented attachment of neural cells. Consequently, thin PEDOT films doped with the low toxicity anion, pTS, supported the greatest cell attachment and neurite outgrowth. Electrochemical performance was analyzed and supported the finding that thin PEDOT/pTS provides significant biological and electrochemical advantages over platinum electrodes. The nanobrush/CP hybrid further improved the electrochemical properties of conventional CPs and offers a new approach for selective cell attachment via the CP coated region of the brush substrate.

This thesis demonstrates that the biological performance of CPs is strongly influenced by the physico-mechanical properties with optimal coatings produced in the sub-micron range using conventional doping ions. A new hybrid nanobrush/CP is presented with fabrication parameters which can be tailored for target material properties. Future work will focus on delineating the interfacial structure of the hybrid to optimise the cushioning effect of the brushes for neural interface applications.

Contents

List of Figures	xi
List of Tables.....	xv
List of Abbreviations.....	xvii
List of Publications Arising From This Thesis.....	xix
CHAPTER 1. INTRODUCTION	1
1.1. Research Motive.....	3
1.2. Aims and Hypotheses	8
1.3. Thesis Structure.....	9
CHAPTER 2. An Introduction to the Fabrication of CPs for Biomedical Applications.....	11
2.1. Introduction.....	13
2.2. PEDOT – Monomer of choice	15
2.3. Non-nucleophilic dopants	20
2.4. Electrochemical fabrication.....	21
2.5. Biomedical performance of PEDOT in neural applications	23
2.5.1. Electrochemical characterisation.....	24
2.5.2. Biological performance	25
2.5.3. Physico-mechanical Performance	26

CHAPTER 3. Indentation of Polymers	29
3.1. Introduction.....	31
3.2. General testing procedure and theories	32
3.3. Indentation of Polymers.....	40
3.3.1. Tip Selections	41
3.3.2. Loading Profile.....	42
3.3.3. Pile-up	43
3.3.4. Adhesion.....	44
CHAPTER 4. The Effect of Doping Species on the Properties of Electrodeposited CP	47
4.1. Introduction.....	49
4.2. Materials and methods	53
4.2.1. Electrochemical synthesis of PEDOT	53
4.2.2. Scanning electron microscopy (SEM).....	55
4.2.3. Indentation.....	55
4.2.4. Cyclic Voltammetry (CV).....	56
4.2.5. Electrochemical Impedance Spectroscopy (EIS)	58
4.2.6. Neuronal PC12 outgrowth assay.....	60
4.2.7. Cytotoxicity Assay - L929 cell growth inhibition	62
4.3. Results	64
4.3.1. The effect of dopants on the microstructures of PEDOT films	64
4.3.2. Indentation modulus.....	66
4.3.3. Charge storage capacity (CSC) and electrochemical stability	68
4.3.4. Electrochemical impedance	71
4.3.5. Neuronal attachment and outgrowth.....	73
4.3.6. Intrinsic Toxicity of Dopants - L929 Cell Growth Inhibition Assay	75

4.4. Discussion	77
4.5. Conclusion	85
CHAPTER 5. The effect of film thickness on the properties of electrodeposited CP.....	87
5.1. Introduction.....	89
5.2. Materials and Methods.....	91
5.3. Results	94
5.3.1. Physical Changes Associated with the Deposition Charge Density	94
5.3.2. Charge Storage Capacity (CSC) and Electrochemical Stability	100
5.3.3. Electrochemical Impedance	102
5.3.4. PC12 Cell Attachment and Neurite Outgrowth.....	105
5.4. Discussion	109
5.5. Conclusion	114
CHAPTER 6. Fabrication of PHEMA nanobrush – CP hybrids.....	115
6.1. Introduction.....	117
6.2. Materials and Methods.....	121
6.3. Results	129
6.3.1. Synthesis and characterisation of the surface initiator monolayer.....	129
6.3.2. Fabrication and characterisation of PHEMA brushes via ATRP	130
6.3.3. Electrodeposition of PEDOT/pTS through PHEMA brush modified gold substrate.....	134
6.4. Discussion	135
6.5. Conclusion	140
CHAPTER 7. PHEMA nanobrush – CP hybrids as neural interfaces	143
7.1. Introduction.....	145
7.2. Materials and Methods.....	148
7.3. Results	152

7.3.1. Mechanical modulus - AFM.....	152
7.3.2. Electrochemical stability - CV.....	153
7.3.3. Electrochemical Impedance spectroscopy (EIS).....	154
7.3.4. Biphasic stimulation	155
7.3.5. PC 12 adhesion and neurite Outgrowth.....	157
7.4. Discussion	159
7.5. Conclusion	163
CHAPTER 8. Final Conclusion and Recommendations	165
8.1. Conclusion	167
8.2. Future Work and Recommendations	170
Appendices.....	177
APPENDIX A. Mechanical and Electrical properties of PEDOT and PPy	179
APPENDIX B. Determination of the water window for CV	181
APPENDIX C. Statistical analysis of Indentation data.....	183
APPENDIX D. Stoichiometric calculation of the amount and thickness of CP formed	184
References	187

List of Figures

Figure 1.1: The typical design components and fabrication of conducting polymers.....	4
Figure 1.2: A schematic representing the interplay of biological properties with other properties.	5
Figure 2.1: Schematic representation of π delocalisation along the conjugated backbone.	15
Figure 2.2: The structural resemblance between a) cis-polyacetylene and b) five membered heterocyclic aromatics.	16
Figure 2.3: Three possible couplings of Pyrrole.	17
Figure 2.4: Structures of conducting polymers used in biomedical applications.	18
Figure 2.5: Structures of hydrophilic EDOT variants. a) sulfonatoalkoxy 3,4-ethylenedioxythiophene (S-EDOT), b) hydroxymethylated 3,4-ethylenedioxythiophene (EDOT-MeOH).	20
Figure 2.6: Dopants of conducting polymers – non-nucleophilic anions. a. benzenesulfonate (BS), b. para-toluenesulfonate (pTS), c. polystyrene sulfonate (PSS), d. Perchlorate (ClO_4).	21
Figure 2.7: Schematic of three-electrode cell used for electrodeposition.	22
Figure 3.1: A typical load versus displacement graph.	33
Figure 3.2: Schematic diagram of the unloading process.....	35
Figure 4.1: Silicone well system used in electrochemical fabrication	54
Figure 4.2: A typical trapezoidal load function for indentation experiments.	56
Figure 4.3: An example of a cyclic voltammogram.....	57
Figure 4.4: The INPHAZE 3-Terminal Sample Chamber	58
Figure 4.5: Schematic of INPHAZE impedance analyser..	59
Figure 4.6: Schematic illustration of procedures of L929 cell inhibition assay.	62
Figure 4.7: SEM of PEDOT films doped with LiClO_4 , BS, pTS, SDS, DBS and PSS at a) 30,000 \times , b) 1,500 \times , and c) 300 \times magnification.....	65
Figure 4.8: SEM of PEDOT films doped with NaCl at a) 30,000 \times and b) 1,500 \times magnification.	66
Figure 4.9: An optical micrograph of an indentation left on a PEDOT/BS film.	67

Figure 4.10: Box plots of Indentation elastic modulus (E) of PEDOT films doped with LiClO_4 , BS, pTS, DBS or PSS, and a platinum foil. ($n=9$).	68
Figure 4.11: Cyclicvoltammogram of PEDOT/ (a) ClO_4 , (b) BS, (c) pTS, (d) DBS and (e) PSS over ± 700 mV vs. 3 M AgCl in 0.9 % saline at 1 st , 50 th , 100 th , 200 th , 400 th , 600 th and 800 th cycles.....	69
Figure 4.12: (a) The electrical impedance and (b) the phase angle of platinum and PEDOT samples in 0.9 % saline at the frequency range between 0.1 Hz and 10 kHz ($n=3$).	71
Figure 4.13: (a) The capacitance and (b) the resistance of PEDOT sample and Pt in 0.9 % saline at the frequency range between 0.1 Hz and 10 kHz. Graphs comparing the capacitance and the resistance of CP samples at the frequency range of 10 ~ 1000 Hz are shown in (c) and (d), respectively.	73
Figure 4.14: Fluorescent micrographs of PC12 cells after 96 h culture on laminin coated substrates, (a) PEDOT/PSS (b) PEDOT/ LiClO_4 (c) TCP (d) BS (e) pTS and (f) DBS.....	74
Figure 4.15: Box plots of PC12 proliferation data. (a) Average PC12 cell density on the substrates at 96h post-plating (b) Average number of neurites per cm^2 (c) neurite length.....	75
Figure 4.16: Optical micrographs of L929 cell growth inhibition of (a) dopants including ClO_4 , BS, PTS, DBS, and PSS and (b) controls including null (TCP) and 4, 5, and 7.5 % EtOH.....	76
Figure 4.17: Percentage cell growth inhibition of each dopant at concentrations of 1 and 10 mg/ml.	76
Figure 5.1: The colour and transparency of the PEDOT/pTS films changed with the amount of charge.....	95
Figure 5.2: Scanning electron micrograms of PEDOT/ LiClO_4 deposited with charges of (a) 0.05, (b) 0.1, (c) 0.5 and (d) 1 C/cm^2	97
Figure 5.3: Scanning electron micrograms of PEDOT/pTS deposited with charges of (a) 0.05, (b) 0.1, (c) 0.5 and (d) 1 C/cm^2	98
Figure 5.4: Scanning electron micrograms of PEDOT/PSS deposited with charges of (a) 0.05, (b) 0.1, (c) 0.5 and (d) 1 C/cm^2	99
Figure 5.5: Cyclicvoltammograms of (a) PEDOT/ ClO_4 , (b) PEDOT/pTS, and (c) PEDOT/PSS.	100
Figure 5.6: Changes in charge storage capacity over 800 cycles.....	101
Figure 5.7: (a) Electrical impedance and (b) corresponding phase angle of films having different thicknesses.	103
Figure 5.8: Graphs of (a) electrical impedance, (b) resistance, and (C) capacitance versus deposition charge.	104
Figure 5.9: Neurite growth in PC12 cells on PEDOT substrates.	106

Figure 5.10: Results of 96 h pc12 adhesion and neurite outgrowth assay. (a) Number of cells adhered on each sample, (b) Number of neurites found on each sample, and (c) length of neurites outgrown from PC12 cells..	107
Figure 5.11: Graph of (1) number of neurite per attached PC12 cell (shown in green), (2) neurite length per attached PC12 cell (shown in blue).....	108
Figure 6.1: Schematic of the fabrication of the CP/brush hybrid. Step 1. Self-assembly of the surface initiator. Step 2. SI-ATRP of PHEMA. Step 3. Electrodeposition of PEDOT/pTS on PHEMA/Au.....	121
Figure 6.2: Synthesis of the surface initiator.	122
Figure 6.3: SI-ATRP of PHEMA on gold.	124
Figure 6.4: The GPC results of SI-ATRP of PHEMA. Data obtained from four samples from different batches. (a) low polydispersity index (PDI <1.2) and (b) the molecular weight.....	131
Figure 6.5: The graph of elliptical length versus molecular weight. The grafting density (σ) is estimated at 0.35 chains/nm ² , calculated from the gradient of the black line. Red dots represent each sample.....	132
Figure 6.6: XPS analysis of C 1s on PHEMA brushes.	133
Figure 6.7: A picture of the 0,05C PEDOT/pTS film deposited on the gold substrate bearing PHEMA brushes..	134
Figure 6.8: High resolution XPS spectrum of 0.03C PEDOT formed on the PHEMA brushed modified gold at (a) O 1s range (b) C 1s range.	134
Figure 6.9: The typical “pinhole” defects found on thiol SAMs formed on Au. Reprinted from [260].....	137
Figure 6.10: Schematic illustration of the electrodeposition of CP through brushes.....	138
Figure 6.11: Schematic illustration of the interface between the brush and CP.....	140
Figure 7.1: The AFM stiffness map of (a) the Hybrid, (b) PEDOT and (c) the Brush.....	152
Figure 7.2: (a) The Cyclic voltammogram at cycle 1 and (b) the change in CSC during 800 cycles of Au, PEDOT/pTS, BRUSH and HYBRID in 0.9 % saline (n=3, error bar = standard deviation, scan rate = 120 mv/s)..	153
Figure 7.3: (a) the electrical impedance, (b) phase angle, (c) capacitance and (d) conductance of the samples. (n =3, error bar = SE).	154
Figure 7.4: (a) Oscilloscopic diagrams of the voltage responses of the gold, PEDOT/pTS, and hybrid samples to the galvanostatic biphasic stimulation with the current amplitude and phase of 0.1 A and 0.4 ms (3013.6 μA/mm ² , 1205.4 nC/mm ² /phase). (b) the change in the maximum negative and positive potentials of the gold and HYBRID samples over the stimulation period of 20 days.	156

Figure 7.5: Fluorescence micrographs of (a) Au, (b) BRUSH, (c) PEDOT/pTS and (d) Hybrid.	157
Figure 7.6: The box plots of (a) the PC12 cell density (b) the number of neurites and (c) the neurite length (N=4).	158
Figure 7.7: (a) The optical and (b) the fluorescence micrograms of the border between the hybrid and the brush/Au. It can be seen that the brush prevents adhesion of PC12 cells.	158
Figure 8.1: Concept-Knowledge (C-K) diagram of this dissertation.	172
Figure 8.2: Schematics of the formation of the hybrid with dopant anions (or other functional)	176
Figure A.1: Pourbaix diagram of water at 25 °C, 1 atm.	181
Figure A.2: Cyclicvoltammograms of PEDOT/DBS with scan ranges of ± 0.6 , ± 0.7 , and ± 0.8 V. The graphs represent the 200 th cycle measured versus 3M AgCl. Scan rate was 120 mV/s and Pt counter was used.	182
Figure A.3: Histogram of indentation data.	183
Figure A.4: S(2p) XPS signals from (a) PEDOT/CIO ₄ , (b) PEDOT/pTS and (c) PEDOT/PSS formed with the deposition charge of 0.05, 0.1, 0.5 and 1 C/cm ²	185

List of Tables

<i>Table 3.1: Different types of indentation instrumentations [148, 152]</i>	<i>32</i>
<i>Table 3.2: Common indenter geometries [154]</i>	<i>34</i>
<i>Table 3.3: Contact area functions $A = f(hc)$ for common indenter geometries</i>	<i>36</i>
<i>Table 3.4: Poisson's ratio and elastic modulus of indenter materials.....</i>	<i>37</i>
<i>Table 3.5: Poisson's ratio of common polymers, conducting polymer and metal electrodes.....</i>	<i>37</i>
<i>Table 3.6: Hertz and Sneddon contact mechanics models.....</i>	<i>38</i>
<i>Table 3.7: Values of correction factors β</i>	<i>39</i>
<i>Table 3.8: Common surface contact models for indentation.....</i>	<i>45</i>
<i>Table 4.1: The chemical structure, molecular weight and toxicity (LD_{50}) of dopants compared in this chapter ..</i>	<i>51</i>
<i>Table 4.2: Amount of chemicals used to make 2 ml of a monomer solution.....</i>	<i>54</i>
<i>Table 4.3: Indentation modulus of PEDOT films doped with ClO_4, BS, pTS, DBS, and PSS ($n = 9$)</i>	<i>68</i>
<i>Table 4.4: Comparison of charge storage capacity at 1st and 800th cycles and corresponding electroactivity loss ($n=3$).....</i>	<i>70</i>
<i>Table 4.5: Summary of the PC12 adhesion and neurite outgrowth, dopant cytotoxicity and qualitative surface roughness studies</i>	<i>82</i>
<i>Table 5.1: Amount of chemicals used to make 2 ml of a monomer/dopant solution.....</i>	<i>91</i>
<i>Table 5.2: Amount of charge used to fabricate samples with four different thicknesses.....</i>	<i>92</i>
<i>Table 5.3: Film thickness of PEDOT/LiClO₄, pTS and PSS deposited with charges of 0.1, 0.5, and 1 C/cm²</i>	<i>95</i>
<i>Table 5.4: The initial and the final charge storage capacity (CPC) of films and corresponding loss in CSC during 800 cycles.....</i>	<i>101</i>
<i>Table 5.5: Changes in theoretical and measured thickness, and qualitative surface roughness with deposition charge. SE is shown in the bracket.....</i>	<i>111</i>
<i>Table 6.1: Amount of chemicals used to make 2 ml of a monomer solution.....</i>	<i>127</i>
<i>Table 6.2: Theoretical and empirical atomic composition of the surface initiator monolayer</i>	<i>130</i>
<i>Table 6.3: The elliptical length of dry PHEMA brushes</i>	<i>132</i>
<i>Table 6.4: The change in static contact angle upon the grafting of PHEMA brushes.....</i>	<i>132</i>

<i>Table 6.5: Theoretical and empirical atomic composition of the PHEMA brushes</i>	<i>133</i>
<i>Table 6.6: The theoretical and experimental C 1S peak ratio of PHEMA.....</i>	<i>133</i>
<i>Table 7.1: The maximum positive and negative voltages recorded after 3h of stimulation.....</i>	<i>156</i>
<i>Table A.1: Mechanical properties of PEDOT and PPy</i>	<i>179</i>
<i>Table A.2: Electrical properties of PEDOT and PPy</i>	<i>180</i>
<i>Table A.3: The result of Shapiro-Wilk normality test</i>	<i>183</i>
<i>Table A.4: The doping ratio, equivalent molecular weight EW, theoretical total amount W_{cp}, and theoretical thickness of PEDOT/ClO_4, pTS and PSS prepared with the deposition charge of 0.05, 0.1, 0.5 and 1 C/cm²</i>	<i>186</i>

List of Abbreviations

AFM	: Atomic force microscopy
ANOVA	: Analysis of variance
ATRP	: Atom transfer radical polymerisation
Au	: Gold
BS	: Benzenesulfonate
ClO ₄	: Perchlorate
CP	: Conducting polymer
CRO	: Cathode-ray oscilloscope
CSC	: Charge storage capacity
CV	: Cyclic voltammetry
DBS	: Dodecylbenzenesulfonate
DI	: Deionised
DMA	: Dynamic mechanical analysis
DMEM	: Dulbecco's modified Eagles medium
DPBS	: Dulbecco's phosphate buffered saline
EDOT	: 3,4-ethylenedioxythiophene
EDOT-MeOH	: hydroxymethylated EDOT
EHS	: Engelbreth-Holm-Swarm
EIS	: Electrochemical impedance spectroscopy
EtOH	: Ethanol
FBS	: Fetal bovine serum
GFP-PC12	: Green fluorescent protein transfected PC12
GPC	: Gel permeation chromatography
GSBmE	: Graduate School of Biomedical Engineering, UNSW
HS	: Horse serum
ITO	: Indium tin oxide
LD50	: Lethal dose, 50 %
M	: Molar concentration (mol/L)
M _n	: Number average molecular weight
M _w	: Weight average molecular weight
NIMS	: National Institute for Materials Science, Tsukuba, Japan
NGF	: Nerve growth factor
NSD	: No significant difference
OLED	: Organic light-emitting diode
PAC	: Polyacetylene
PANI	: Polyaniline
PBS	: Phosphate buffered saline
PC	: Propylene carbonate
PC12	: Cloned pheochromocytoma cell line from the rat adrenal medulla
PDI	: Polydispersity index
PEDOT	: Poly(3,4-ethylenedioxythiophene)
PEG	: Polyethylene glycol
PPy	: Polypyrrole

PSS	: Poly(styrenesulfonate)
Pt	: Platinum
pTS	: Para-toluenesulfonate or tosylate
Q	: Electrical charge
Redox	: Reduction and oxidation
RPMI	: Roswell Park Memorial Institute medium
SAM	: Self-assembled monolayer
SCE	: Saturated calomel electrode
SDS	: Sodium dodecyl sulfate
SE	: Standard error of the mean
S-EDOT	: Sulfonatoalkoxy-substituted EDOT
SEM	: Scanning electron microscopy
SS	: Stainless steel
TCP	: Tissue culture plastic
TEABF ₄	: Tetraethylammonium tetrafluoroborate
TEAPF ₆	: Tetraethylammonium hexafluorophosphate
TV	: Trypsin-versene
UNSW	: University of New South Wales, Sydney, Australia
UV	: Ultraviolet light
w/v	: Weight per volume
XPS	: X-ray photoelectron spectroscopy

List of Publications Arising From This Thesis

Journals

- Green, R.A.; Hassarati, R.T.; Goding, J. A.; Baek, S.; Lovell, N.H.; Martens, P.J.; Poole-Warren, L.A. Conductive hydrogels: Mechanically robust hybrids for use as biomaterials *Macromolecular Bioscience*, 2012, 12, 494-501 doi: 10.1002/macp.201100490
- Green, R.A.; Baek, S.; Poole-Warren, L.A.; Martens, P.J. Conducting polymer-hydrogels for medical electrode applications, *Science and Technology of Advanced Materials*, 2010, 11, 014107 doi:10.1088/1468-6996/11/1/014107.
- Poole-Warren, L.A.; Lovell, N.H.; Baek, S.; Green, R.A. Development of bioactive conducting polymers for neural interfaces, *Expert Review of Medical Devices*, 2010, 7, 35-49 doi:10.1586/erd.09.58.

Book Chapter

- Green, R.A.; Baek, S.; Lovell, N.H.; Poole-Warren, L.A. "Nanostructured Conductive Polymers as Biomaterials", in *Nanostructured Conductive Polymers* (editor: A. Eftekhari), 2010, John Wiley & Sons, Ltd, Chichester, UK.

doi: 10.1002/9780470661338.ch18

Patent

- Poole-Warren, L.A.; Green, R.A.; Martens, P.J.; Baek, S. - "bioactive hybrid conducting polymer hydrogels", provisional patent (NewSouth Innovations (NSi) Ref: 10_2487)

CHAPTER 1. INTRODUCTION

1.1. Research Motive

From sensory and cognitive prostheses to artificial limbs, the advent of neuroprosthetic technology opens the era of neural interfaces, the interface that connects electrodes to neurons. This offers hope for millions of patients suffering chronic neural injuries such as vision loss [1-3], deafness [4-6], Alzheimer's disease [7], epilepsy [8, 9], Parkinson's disease [10, 11], paralysis [12], amputations [13, 14], and spinal cord injuries [15-18]. Conventional metal electrodes suffer from low charge injection limit [19], mechanical mismatch between electrode and neural tissue [20, 21], absence of biological cues and ultimately fibrous or glial encapsulation [22]. A key challenge in developing robust, stable neural interfaces is in the design and realisation of new electroactive biomaterials that can facilitate integration between neurons and electrodes. Conducting polymers (CPs) hold great potential in such neural interface applications [19, 22], and there is great motivation to understand, analyse, and improve their performance as an interface technology.

Figure 1.1 illustrates the types of CP systems that have been used for biomedical applications. Properties of CPs are influenced by the choices of the two constituents, the conjugated backbone and dopant, as well as the fabrication process. Electrochemically synthesised CPs doped with conventional molecules such as sulfonates [23-33] and perchlorates [34-36] yield excellent electrode coatings. These coatings provide high electrochemical conductivity and present a good combination of stability, compatibility and performance in neural electrode applications [26-36].

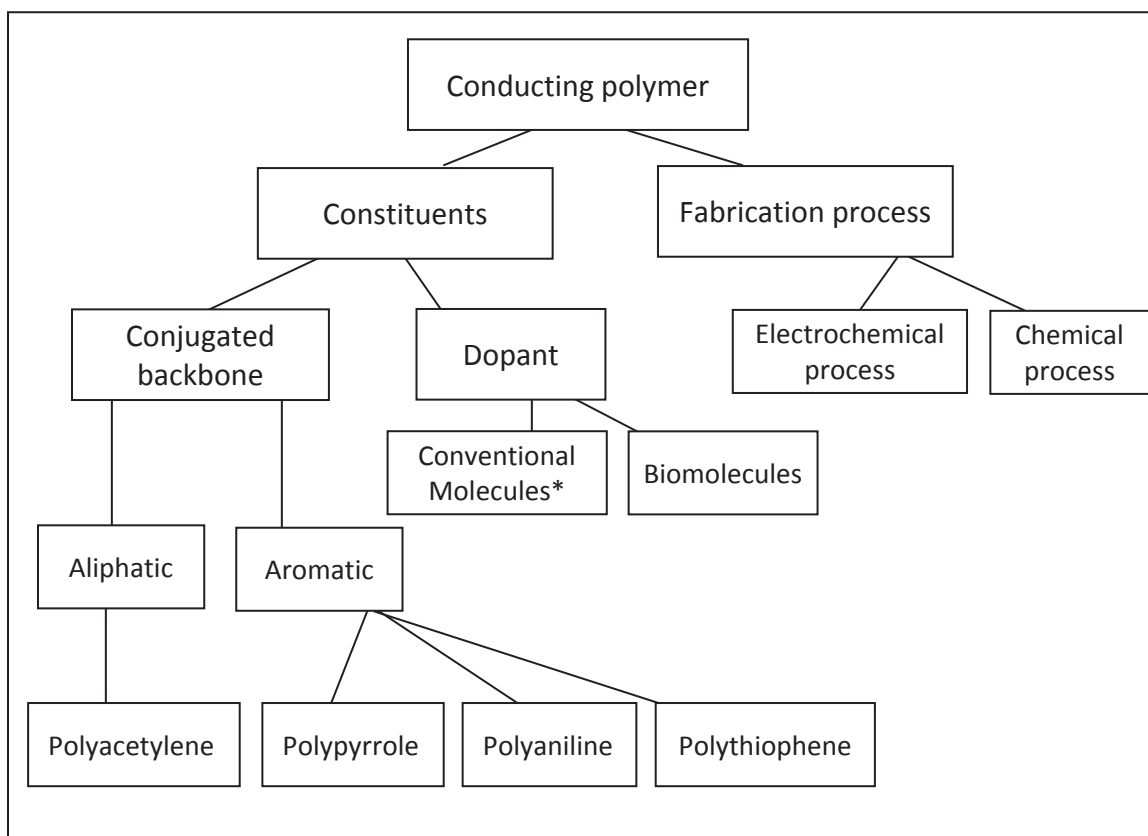


Figure 1.1: The typical design components and fabrication of conducting polymers.

*Conventional molecules refer to non-nucleophilic anions such as sulfonates and perchlorates.

However, despite a decade of research CPs have not found application as implantable electrodes due to limitations relating to their biological performance [36, 37]. The biological performance of electrode materials is driven by the interplay between specific physico-chemical and electrical properties. Figure 1.2 shows a schematic that outlines the key properties of importance to neural electrode applications as they relate to biological performance.

While it is widely known that neural tissues are sensitive to physical/mechanical cues conveyed by the topography [38, 39], surface roughness [40] and mechanical rigidity [41-43] of substrates, the influence of physical/mechanical properties of CPs on biological performance has been overlooked. This is mainly due to the fact that most CP research

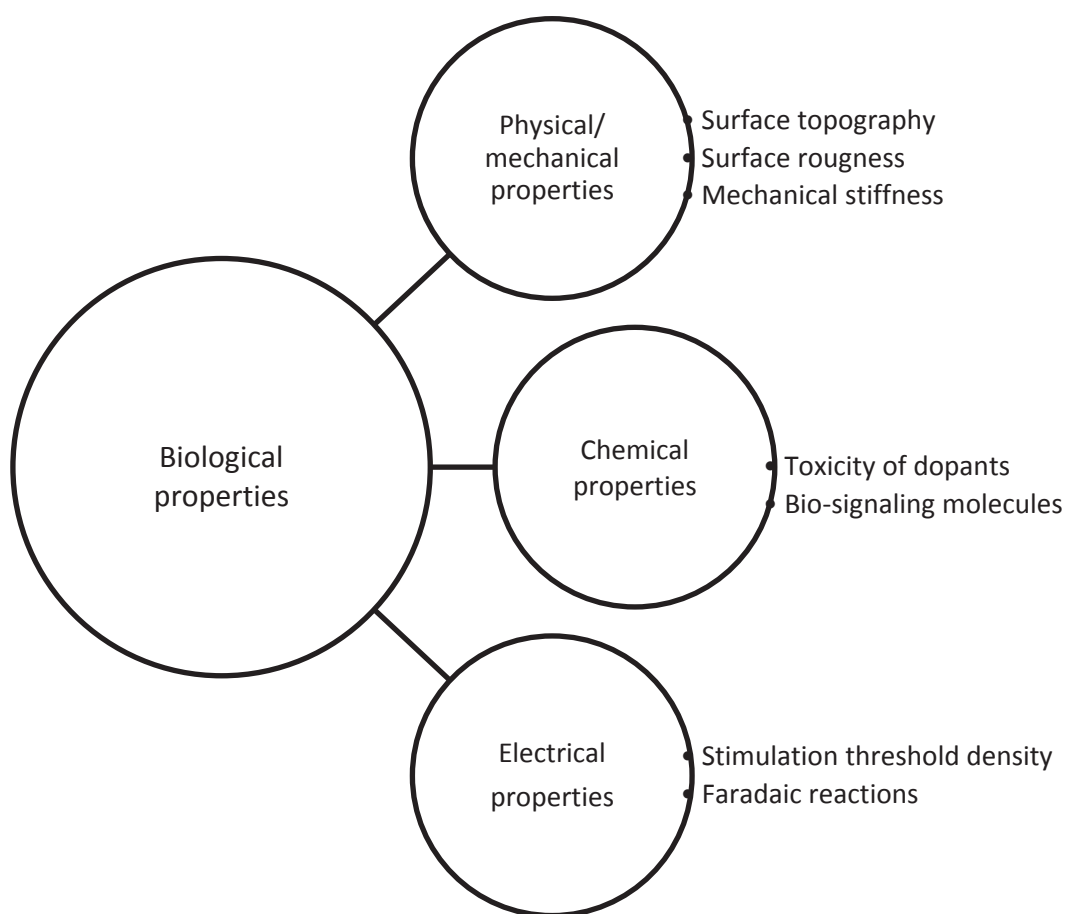


Figure 1.2: A schematic representing the interplay of biological properties with other properties.

has been focused on increasing the electrical conductivity rather than on improving the interaction between electrodes and tissues [25, 26, 35]. The electrical properties of CPs improve with increasing surface area and polymer thickness. In efforts to increase CP surface area coatings have been fabricated by varying the CP monomer chemistry, the dopant type [44] and the applied charge during polymerisation [26, 35, 45], all of which also determine the film thickness [46]. However, in the current literature there is a clear absence of systematic comparison of biological performance with regard to these variables which are dominant in influencing surface topography and hence cell guidance cues.

The other missing link in the literature is the mechanical properties of electrodeposited CPs on metal substrates. CPs are thought to reduce the mechanical mismatch between the rigid platinum electrodes ($E = 10^{11}$ Pa) and the soft neural tissue ($E = 10^{2\sim 4}$ Pa). However, the mechanical rigidities of CPs are ill-defined due to technical difficulties of testing the “thin-film-on-substrate” structures. In this thesis, mechanical analysis protocols are developed and properties are quantified in an effort to fill these gaps in the literature. Additionally, with the advent of composite materials aimed at further reducing the stiffness of electrode materials, these methods for quantifying mechanical performance are expected to be integral to assessing the efficacy of hybrid fabrication processes.

Chemical characteristics of an electrode material, such as whether it is a metal, polymer or ceramic, or whether it is reactive or stable in air and water, undoubtedly influence the biological outcome of the electrode implants. Developing a new conjugated backbone (i.e. a new type of monomer) is a difficult task requiring both time and money. Hence, the chemical properties such as cell signalling and toxicity of CPs are mostly controlled by the chemical nature of dopants. Cell signalling is essentially a chemical reaction between receptors and ligands, but conventional CP chemistries and dopants lack the ligands to attract neural tissues. In an effort to support improved cellular interactions, various biomolecules have been introduced to CP systems either by physical adsorption through the surface or by electrostatic incorporation during the electrodeposition. The latter method may prolong the effect of biomolecules but also reduces the mechanical stability, which in turn impacts on the chronic biocompatibility of these materials. It is proposed that conventional dopants can provide the best combination of performance and stability,

and neural interaction of CPs can be improved by modifying the aforementioned physical properties while maintaining the conventional chemistry.

Electrical properties of a material are especially important in neural stimulation applications where electrical charge above the stimulation threshold density must be delivered to induce neural signals. The threshold density is known to be affected by the geometry such as size and shape and material of the electrodes as well as the stimulation waveform. More importantly, the distance between the electrode and tissue has been identified as a single most important factor affecting the threshold magnitude. Irrespective of the electrically conductivity of a material, the device will fail at neural interface if it does not provide a conducive environment for neural cell adhesion. Accordingly, this study will optimise conventional CP coatings for neural attachment and outgrowth rather than for electrical properties.

Thus the approach in this thesis relied first, on understanding the biophysical cues associated with CPs produced using conventional chemistry. Second, optimisation of these cues via systematic variation of components and fabrication parameters was studied. Finally, since neural engineering applications demand soft, deformable substrates that allow preferential attachment and differentiation of neurons while suppressing astroglial scar formation [47, 48], a novel approach to the design of softer CP based electrode coatings was pursued. A common strategy used in the latter field has been to make CP composites with hydrogels. However, CP/hydrogel composites suffer from the electrical percolation [49], which results in a tradeoff between the electrical and mechanical properties. Nanostructured hybrid materials, composites that contain one or

more nanostructures, are proposed in this thesis to provide properties that are not achievable in bulk materials. Therefore in addition to optimising conventional CP chemistries for neural interfacing, a new hybrid system was explored to take advantage of the mechanical softness of hydrophilic polymer brushes and the electrical conductivity of CPs.

1.2. Aims and Hypotheses

This thesis focuses on the understanding and optimisation of the effect of physical/mechanical cues of conventional CP coatings on the adhesion and outgrowth of neural cells. The underlying hypothesis was that the interaction between CP based coatings and neurons are improved by modulation of their physical and mechanical properties via either manipulation of conventional chemical compositions through producing hybrid CPs based on nanobrush structures.

The specific aims of this thesis were to:

1. Understand the effect of dopant size on implant related characteristics of the conventional CP poly(3,4-ethylenedioxythiophene) (PEDOT) and to identify the ideal dopant size to achieve long-term function and stability.
2. Understand the effects of deposition charge on physical, electrochemical and biological properties of CPs, and to determine the optimal film parameters which support neural cell adhesion and outgrowth

3. Explore the feasibility of fabricating a novel nanobrush-CP hybrid via grafting of nanobrushes on metal substrate using SI-ATRP and subsequent electrochemical deposition of CP on the substrate bearing nanobrushes.
4. Characterise the nanobrush-CP hybrid electrode coatings for neural interface applications,

1.3. Thesis Structure

CPs in neural interface applications serve not only as electrical conductors, signalling to and from neurons, but also as platforms supporting the survival, attachment, integration, and differentiation of surrounding neurons. Accordingly, this research focused on studying electrochemically synthesised CP films doped with conventional dopants such as sulfonate and perchlorate moieties and extending this into design and characterisation of a hybrid nanobrush-CP. The rationale behind the choice of materials and fabrication methods is discussed in Chapter 2. Chapter 3 explores the theories and strategies of nanoindentation techniques, which were explored to investigate the mechanical properties of CP films having the film-on-substrate structure. The remainder of the thesis is divided into four experimental chapters and a conclusions and recommendations chapter and a brief outline of each is given below.

Chapter 4 presents the effect of the choice of the dopant on the physico-mechanical properties of electrodeposited PEDOT films. The mechanical properties of substrate-bound PEDOT films were analysed using the indentation technique described in Chapter

2. The interplay between the physico-mechanical properties and other biomedically relevant properties such as electrical and biological properties was discussed.

Chapter 5 examines the changes in biophysical cues associated with the charge applied to form a film. PEDOT films doped with ClO_4^- , pTS and PSS were fabricated by applying a range of total charge metrics. These films were characterised to determine the optimal parameters with reference to critical neural interface application requirements.

Chapter 6 describes the fabrication steps of a novel hybrid conducting polymer. The initiator monolayer is formed on gold substrates through thiol self-assembly. ATRP of PHEMA is carried out on the initiator modified gold substrates. PEDOT/pTS films were electrochemically deposited on the gold substrates carrying PHEMA brushes. The length and grafting density of PHEMA brushes were characterised using Ellipsometry and gel permeation chromatography (GPC). The formation of the hybrid was confirmed by X-ray photoelectron spectroscopy (XPS).

Chapter 7 characterises the electrochemical and biological performance of the hybrid for neural electrode applications. The hybrid, comparable PEDOT/pTS, and bare gold samples are directly compared in terms of charge storage capacity, electrochemical impedance, biphasic stimulation, and PC-12 attachment and neurite outgrowth.

Chapter 8 presents the conclusion and future studies of this research. Using the knowledge gained through this research, a number of new design concepts was generated.

CHAPTER 2. **An Introduction to the Fabrication of CPs for Biomedical Applications**

Portions of this chapter, which were written by the candidate, have been published in [R.A. Green, S. Baek, N.H. Lovell and L.A. Poole-Warren, *Ch 18. Nanostructured Conductive Polymers as Biomaterials* in the book, *Nanostructured Conductive Polymers*, edited by Ali Eftekhari; DOI: 10.1002/ 9780470661338.ch18.Copyright 2010 John Wiley & Sons] and [R.A. Green, S. Baek, L.A. Poole-Warren and P.J. Martens, *Conducting polymer-hydrogels for medical electrode applications, Science and Technology of Advanced Materials 11 (1) 014107*. Accepted 1 Feb; Copyright 2010 IOP Publishing] with permission from the publishers

2.1. Introduction

This thesis hypothesises that the interactions between neurons and CPs can be improved by optimising their biophysical cues such as topography and mechanical rigidity. The properties of CPs are mostly determined by two fundamental choices, which are selection of the chemical components, comprised of the conjugated backbone and dopant, and the selection of the method of polymerisation. It is important to understand the trade-offs inherent in each of these choices, and how the properties of the resulting CP can be controlled by the interplay of the components.

The choice of the backbone structure involves a tradeoff between the stability and the conductivity. CPs are characterised by a π conjugated backbone. The electroactivity and stability of CPs can, respectively, be estimated by the diene and aromatic character of the backbone. Polyacetylene (PAC), a pure diene polymer, exhibits the highest electrical conductivity but has limited stability in air [50]. Aromatic conjugated backbones, such as poly(3,4-ethylenedioxythiophene) (PEDOT), polypyrrole (PPy), and polyaniline (PANI), greatly improve the stability but are not as electrically conductive as PAC [50].

Dopants are usually anions that introduce positive charge carriers in the oxidised conjugated backbone. Upon the oxidation and reduction (Faradaic) reactions, CPs undergo consequent doping and dedoping processes. This behaviour is known as pseudo-capacitance. Since dopants are the main charge carrier in pseudo-capacitive transfer, the electrochemical stability and biocompatibility are important. Conventionally, highly stable anions such as sulfonate and perchlorate have been widely used in both

electronics and biomedical applications. Biomolecules have been used as dopants to improve the biofunctionality but lacked electrochemical stability [51].

Two broad forms of polymerisation have been used to produce CPs in the past. These are chemical polymerisation approaches and electropolymerisation. Each of these methods has advantages and disadvantages. Chemical polymerisation provides better options for controlling chain length and conformation and is applicable for wider variety of monomers. Electrochemical polymerisation, on the other hand, while not as controllable or versatile as the counterpart, allows direct deposition of highly conductive CP films on electroactive surfaces.

For neural stimulation, an application that demands both electrical performance and biochemical stability, the logical choices of CPs are electrodeposited PEDOT films doped with conventional dopants. Such films offer significant electrical and biological advantages over conventional platinum electrodes and have the added benefit of a high charge storage capacity and low impedance at mid-frequencies (~ 1 kHz) as well as in-vitro and in-vivo stability [26].

The following provides an overview of the structure and the properties of electrodeposited PEDOT films. The rationale for the selection of PEDOT and the details of electrochemical synthesis are described in Sections 2.2 and 2.3 respectively. The interdependency of electrochemical, biological and physico-mechanical properties is discussed in Section 2.4.

2.2. PEDOT – Monomer of choice

The electrical conductivity of a material can be described in terms of the availability of mobile charge carriers. In good conductors, such as metals, valence electrons are readily delocalised from individual atoms to conduct electricity whereas in insulators including glass and wood, valence electrons are held up within atomic domains by strong sigma (σ) bonds (i.e. single covalent bond). Figure 2.1 demonstrates the delocalisation occurring in a simplest conducting polymer, polyacetylene (PAC). The conjugated backbone of conducting polymers contains alternating single (σ) and double (σ and π) bonds that, upon doping, facilitate the delocalisation of π electrons along the sigma (σ) bonded chain. When π electrons are fully delocalised, the backbone, which theoretically has equidistant bonds and one unpaired electron per atom, becomes a quasi-one-dimensional metal.

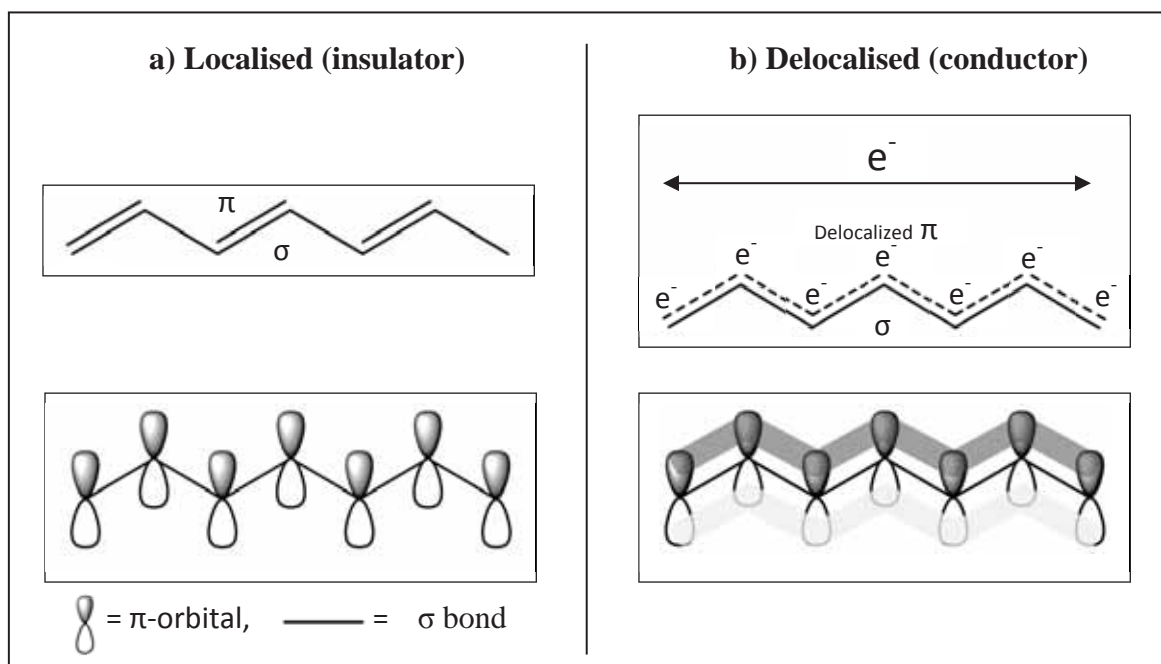


Figure 2.1: Schematic representation of π delocalisation along the conjugated backbone.

The first conducting polymer reported, polyacetylene, has no practical biomedical application due to the lack of stability in air [52]. As depicted in Figure 2.2, this problem was successfully overcome by polymers of five membered heterocyclic aromatics (see Figure 2.2-b) that have the electronic structure similar to *cis*-polyacetylene (see Figure 2.2-a) but the heteroatoms (i.e. sulphur, nitrogen) in the aromatic ring stabilises the conjugated backbone. Consequently, heterocyclic aromatics such as thiophene, pyrrole and aniline having good stability in air and high conductivity upon doping have been widely used for biomedical applications [53-58]

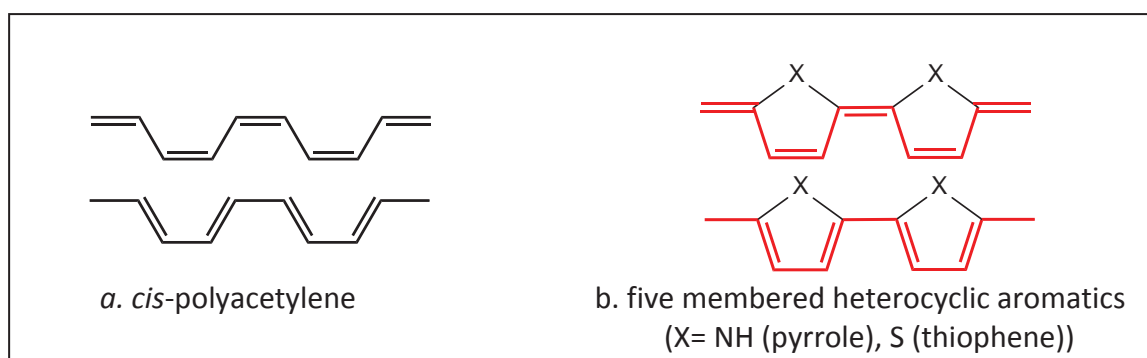


Figure 2.2: The structural resemblance between a) *cis*-polyacetylene and b) five membered heterocyclic aromatics.

PPy was the first heterocyclic CP to be electrochemically synthesised [59] and is a better p-type conductor than unsubstituted polythiophene [60]. Figure 2.3 (a) shows the chemical structure of pyrrole monomer. One major drawback of PPy is its susceptibility to α - β and β - β couplings, which reduce the electrical conductivity and stability of the backbone. Examples of defective couplings are illustrated in Figure 2.3 (c) and (d). In order to minimise these undesirable couplings as well as to impart new functionalities to the chain, the β sites of the heteroaromatics (see Figure 2.3-a) have been substituted

with different functional chains. The synthesis and properties of these derivatives have been extensively reviewed in the literature [61-64].

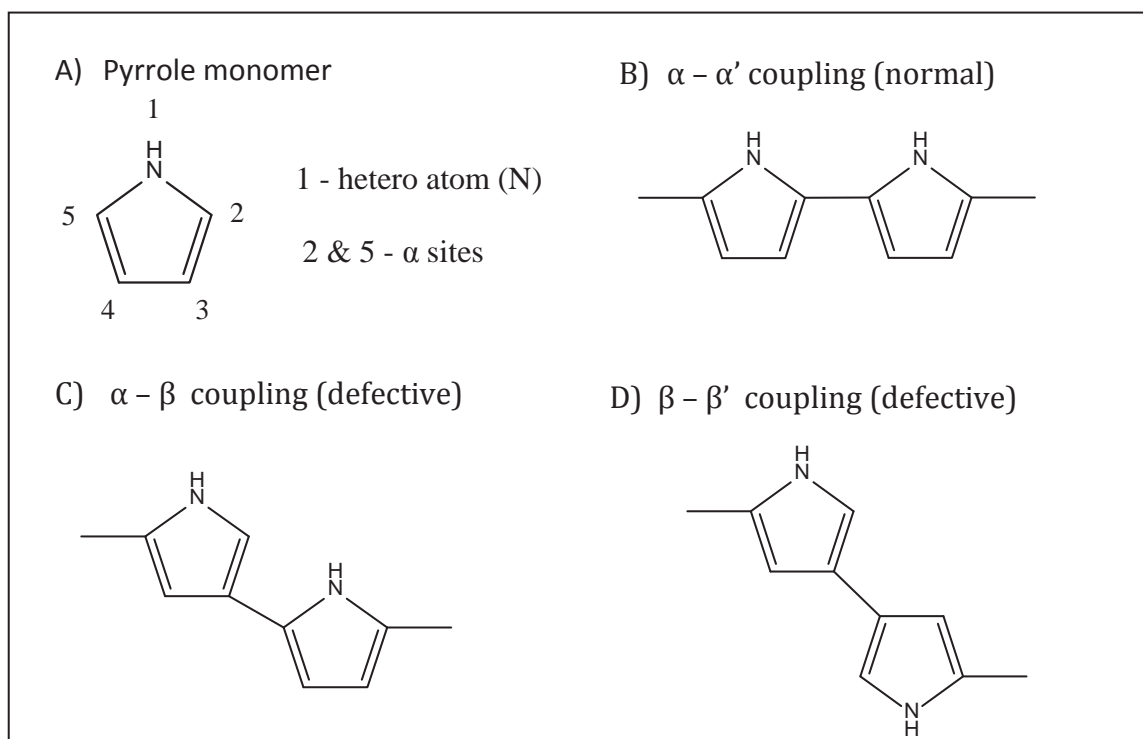


Figure 2.3: Three possible couplings of Pyrrole. A) Pyrrole monomer has five possible coupling sites, B) normal (α - α) coupling, C) $\alpha - \beta$ coupling (defective), D) $\beta - \beta'$ coupling (defective).

Among many derivatives, poly(3,4-ethylenedioxythiophene) (PEDOT), a polythiophene (PTh) derivative that has a heterocyclic ring fused along the β sites, has shown high electrical conductivity (200 S/cm) [65] as well as high stability in the doped state. These desirable material properties have made PEDOT the conducting polymer of choice for a broad range of biomedical applications from drug delivery [66] and biosensing [58] to neural tissue engineering [26, 32, 33, 36, 67]. The structures of PEDOT as well as other biomedically significant conducting polymers such as PPy and PANI can be found in Figure 2.4.

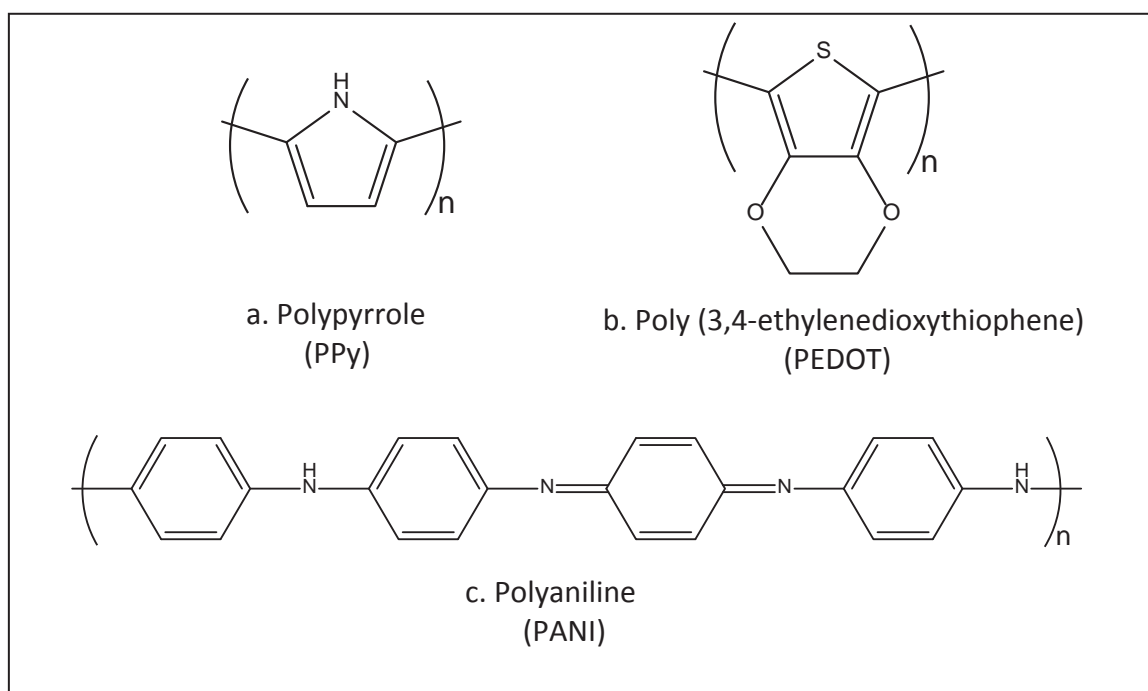


Figure 2.4: Structures of conducting polymers used in biomedical applications.

Due to its solubility and cost effective processing, PANI has gained much attention for use in commercial electronic applications. However, its biomedical application has been impeded by concerns about possible carcinogenic degradation products [68-70]. While the issue of the toxic degradation products remain unclear, proliferation and growth of cardiac myoblasts have been reported on electrically conductive PANI [71] and PANI/gelatin nanofibers [72].

Unlike PANI, electrodeposited PEDOT is insoluble and hence cannot be reformed into a different shape once polymerised. Baytron P[®], a dispersion of PEDOT-PSS in water, is commercially available product that provides a solution to this demanding problem. The chemical constituents of Baytron P[®], PEDOT and PSS, are identical to those of the electrodeposited films but this chemically prepared product has different chemical composition to the electrochemically prepared counterpart. In Baytron P[®], the typical

monomer to dopant ratio is 1:2.5 whereas that of the counterpart is 3:1 [73]. Having only a small amount of conductive component, Baytron P is generally not as conductive as electrodeposited films. While this water dispersible PEDOT-PSS system is not typically desirable for bio-applications, it forms a transparent film and has been widely used as a replacement for indium-tin oxide (ITO) in electronic devices such as OLEDs [74] and solar cells [75]. With the ease of film preparation by spin-coating, dip-coating, or casting, mechanical properties of Baytron P[®] are well characterised by tensile testing [76-78]. This provides an indirect reference to the mechanical properties of the electrodeposited films and also exemplifies the importance of delineating the interplay of polymerisation methods and constituents.

In one-dimensional conductors like CPs, their electrical properties are largely determined by the chain orientation that includes isotropy, crystallinity and chain packing density. The inter-chain distance, which provides a good indication of the electrical conductivity of the conjugated system, is reported to be affected by the method of polymerisation and the choices of constituents. Electrochemically prepared films have shorter inter-chain distance than chemically synthesised ones and hence have higher electrical conductivities [79]. The use of nucleophilic dopants, such as hydroxides, alkoxides, and carboxylates, and/or bulky biomolecules disrupts chain orientation and hence decreases electrical properties while providing additional functions.

The addition of a functional group on the EDOT structure has been shown to have a similar decrement to electrical conductivity. A major shortcoming of EDOT was its poor water solubility. With the addition of hydrophilic side groups, sulfonatoalkoxy EDOT (S-

EDOT) [80] and hydroxymethylated-EDOT (EDOT-MeOH) [81, 82] have been synthesised as shown in Figure 2.5. The water solubility was greatly improved from 0.01 M of EDOT to 0.1 M of EDOT-MeOH and S-EDOT. The amount of biologic agents able to be incorporated into the CP was also increased. However, these benefits came at the cost of losing conjugation, conductivity, and stability [83]. For this reason PEDOT is still commonly used for neural applications requiring high electrical environmental stability, high charge transfer capacity and long-term functionality.

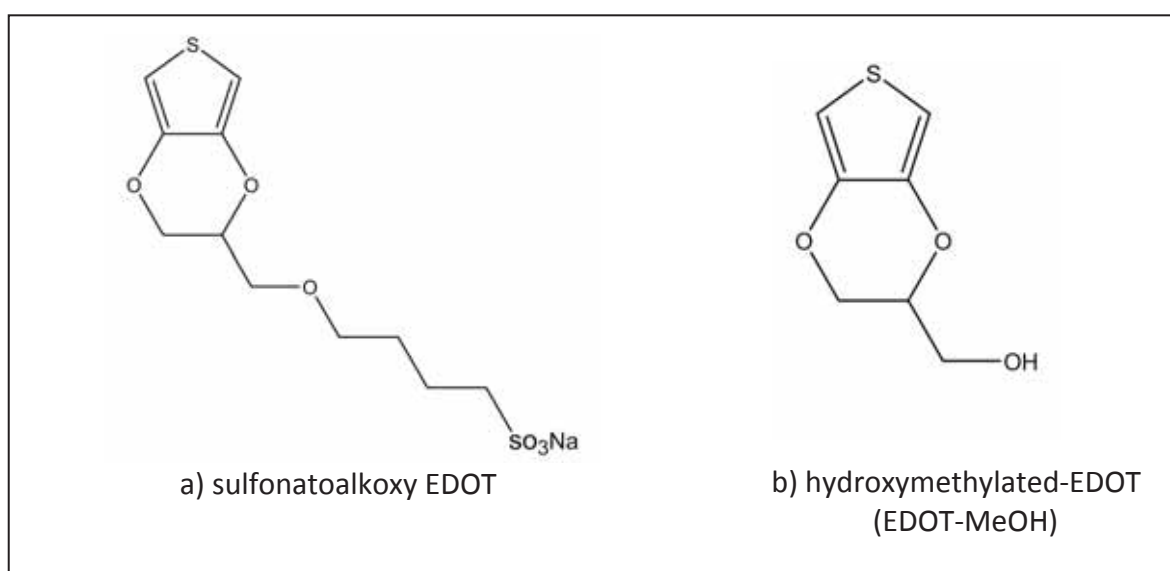


Figure 2.5: Structures of hydrophilic EDOT variants. a) sulfonatoalkoxy 3,4-ethylenedioxythiophene (S-EDOT), b) hydroxymethylated 3,4-ethylenedioxythiophene (EDOT-MeOH).

2.3. Non-nucleophilic dopants

Highly conductive polymers are usually obtained with the doping of non-nucleophilic and hydrotropic anions such as variants of benzenesulfonate and perchlorate [44, 84, 85]. When nucleophilic anions, such as halides, hydroxides, alkoxides, carboxylates and thiolates, are used, the monomers and their radicals undergo nucleophilic attack and

turn into soluble products that tint the solution, instead of forming polymers [86]. The structures of common dopants, including BS, pTS, PSS and ClO_4^- , can be found in Figure 2.6. When dissolved in water, sodium sulfonate electrolytes have a pH range (pH 7 ~ 9) close to the body pH level and this helps minimise pH induced cytotoxicity when implanted in the body. Temperature can affect the solubility of dopant and even the viscosity of electrolyte. Generally, low temperature [87, 88] helps to produce smoother, more conductive films, but the reduced dopant solubility and the increased viscosity can be problematic [89].

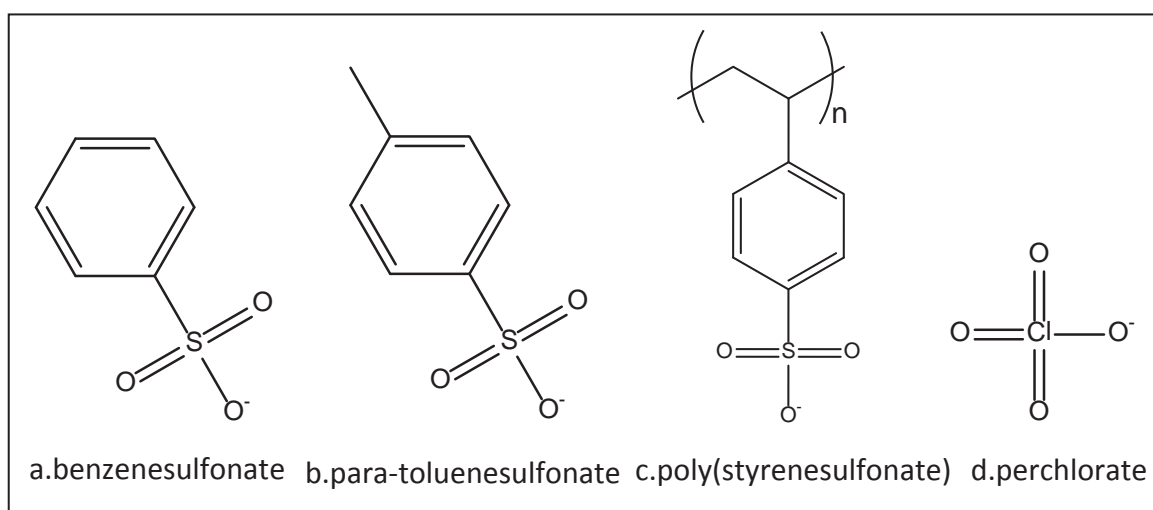


Figure 2.6: Dopants of conducting polymers – non-nucleophilic anions. a. benzenesulfonate (BS), b. para-toluenesulfonate (pTS), c. polystyrene sulfonate (PSS), d. Perchlorate (ClO_4^-).

2.4. Electrochemical fabrication

Electrochemical deposition of a CP is generally carried out in a single compartment, three-electrode (working, counter, and reference electrodes) cell with a solution of a monomer and an electrolyte (dopant) dissolved in an appropriate solvent. A schematic of a typical electrochemical deposition rig is shown in Figure 2.7. Upon galvanostatic

(constant current), potentiostatic (constant potential) or potentiodynamic (pulsed current or pulsed potential) oxidation of the monomer, homogeneous polymer thin film is directly deposited on the working electrode (cathode) surface.

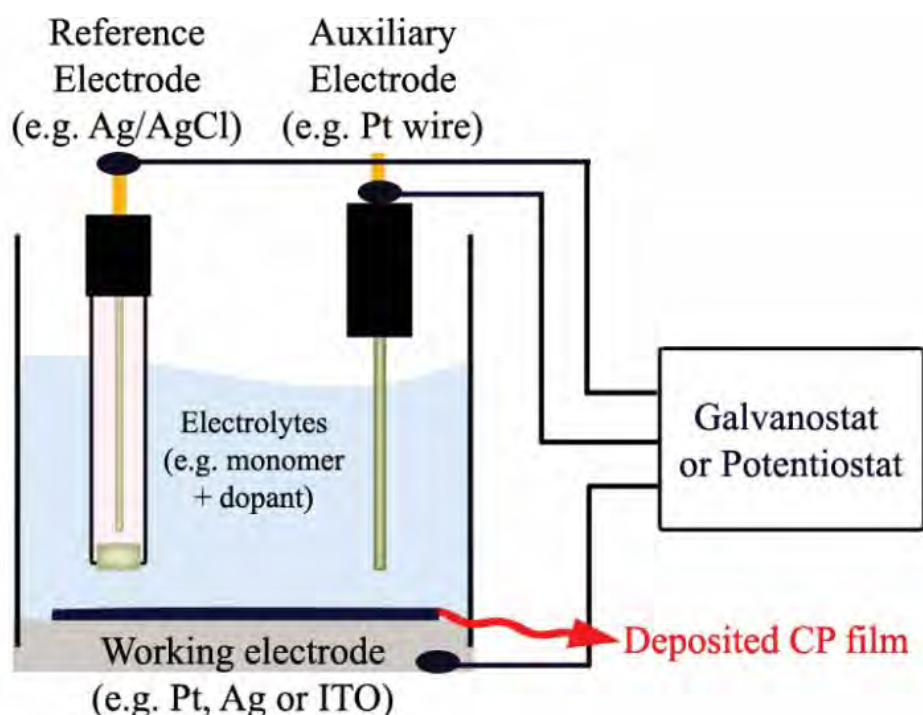


Figure 2.7: Schematic of three-electrode cell used for electrodeposition [90].

In typical electrochemical polymerisation of EDOT, the monomer is oxidised to its radical cation and the coupling of two radicals form a dimer. The oxidation potential (E_p) of the dimer ($E_{p,bis} = 0.51$ V) is lower than that of the monomer ($E_p = 1.11$ V) [91] and therefore, consequent reoxidation of the dimer induces a further coupling with a monomeric radical until an insoluble oligomer is formed and nucleates onto the cathode [92]. The nucleation process and following three dimensional growth processes are largely influenced by the nature of electrodes [93]. With a high density of initial nucleation sites, platinum electrodes produce highly dense CPs with high conductivities [94, 95]. When fully

polymerised, PEDOT forms a translucent to opaque blue coloured film on the anode and shows static oxidation potential of -0.2 V [91].

The quality of electrodeposited films is largely determined by synthesis conditions including solvent, dopant, electrolyte concentration, pH level and applied electrical signals [96]. Conducting polymers can be synthesised in both aqueous [97, 98] and organic solvents [99, 100]. The most commonly used solvent in biomedical applications, water, is an oxygen nucleophile. While beneficial in a biological system, it is not an ideal solvent for polymer formation. When water is reduced, the oxygen forms hydroxide which reacts with radical intermediates and disrupts chain growth [101].

A good solvent for electrodeposition should have a high dielectric constant to dissolve ions involved in the polymerisation process and needs to be aprotic and non-nucleophilic to minimise undesirable side reactions. Among several organic solvents, acetonitrile matches all the criteria and hence has been most commonly used [100]. Some of the most conductive CPs have been synthesised in a water and acetonitrile mixture. Kanazawa et al. [53] reported that films grown from the water and acetonitrile mixture are more conductive and are better adhered to the electrode surface than the ones grown from dry acetonitrile.

2.5. Biomedical performance of PEDOT in neural applications

The effect of the physico-mechanical characteristics of PEDOT films on other associated properties including electrochemical and biological properties are reviewed in this

section. The electrical performance of PEDOT films in neural applications is summarised in 2.5.1. The biological performance is reviewed in 2.5.2. Physico-mechanical properties in 2.5.3 include surface properties and mechanical characteristics, which will provide background information leading to the next chapter.

2.5.1. Electrochemical characterisation

The charge injection limit of an electrode material indicates the amount of charge which can be safely injected without deteriorating the surrounding tissue or the electrode itself. The charge injection limit of PEDOT/PSS, which Cui et al. [27] reported as 2.3 ± 0.6 mC/cm², is roughly seven times higher than that of platinum (i.e. $0.1 \sim 0.35$ mC/cm² [102] or $0.03 \sim 0.1$ mC/cm² [103] depending on the surface roughness).

The electrochemical stability, which can be measured by cyclic voltammetry, is another important parameter for chronic bioimplant applications. In a typical cyclic voltammogram, the charge storage capacity is measured by the total amount of charge transferred within a potential cycle. By comparing this capacity before and after several cycles, the electrochemical stability of an electrode can be estimated. This technique also provides useful reduction/oxidation related information such as potentials and reversibility.

The electrochemical stability of PEDOT is generally considered to be good or at least better than PPy. Yamato et al. [58] compared the charge capacity loss of PPy/PSS film to

that of PEDOT/PSS film after polarisation at 400 mV for 16 h, a condition which is of significant importance for enzymatic sensor applications, and found PPy film lost 95 % of activities while PEDOT counterpart lost only 11 %. PEDOT films reported to have from ten to twenty times higher charge storage than platinum depending on the film thickness [27].

2.5.2. Biological performance

The incorporation of appropriate functional biomolecules within conducting polymers leads to the formation of bioactive electrode coatings that can proactively prevent tissue encapsulation by preserving and attracting more neurons towards to the stimulation surface. A number of different biomolecules that have been incorporated in conducting polymers include cell adhesion proteins [31, 104-106], growth factors [107-110] and anti-inflammatory drugs [111, 112]. With the addition of biomolecules lowering the ionic conductivity in the electrolyte solution, the high electrical potential during electrodeposition results in reduction of conjugation and thereby degradation of electrical conductivity and stability [31, 110, 113]

The development, differentiation and proliferation of cells are affected not only by classical biochemical signals but also by physico-mechanical cues such as the surface morphology, surface energy, hydrophilicity and stiffness of implanted biomaterials [43, 114, 115].

The surface morphology of a biomaterial influences cell adhesion by providing different types of geometric constraints to the cell. Khan et al. [40] tested the adhesion and

viability of primary cortical neural cells on silicon wafers with different surface roughness ranging from 10 to 250 nm. It was reported that the surface roughness between 20 ~ 100 nm best promotes cell adhesion and longevity. The surface roughness of electrodeposited conducting polymer correlates directly with the film thickness [27, 116, 117]. Thin films are smooth and featureless but become rough, porous, globular and nodular as thickness is increased.

In a study by Fonner et al. [96], the influence of surface morphology on cell viability has been tested by culturing PC12 and Schwann cells on thin (50 nm) and thick (650 nm) PPy produced with three different dopants, pTS, PSS and Cl. For pTS and PSS doped samples, more cells attached to the thin film than the thick film regardless of cell type. While this result may indicate cells' affinity to a smooth surface, a follow-up leaching study indicated that leached dopant molecules may contribute to this decrease. It is noticeable that the thick (650 nm) film in this study is significantly thinner than the typical PEDOT films, which are usually 1.7 ~ 10.2 μm thick, used in neural electrode applications [26, 27, 35]. Since several studies reported the adhesion and neurite proliferation of PC12 cells on the thick PEDOT films [104, 118], a study is required to provide the missing link between the film thickness, surface morphology, leached dopant and cell viability.

2.5.3. Physico-mechanical Performance

An important finding from the study by Cui et al. [27] is that stability of PEDOT films is largely influenced by the film thickness. While all thin films tested remained electrically

and physically stable during two weeks of biphasic stimulation, proving their suitability to chronic applications, cracks developed on intermediate and thick films after 5.4 and 9.1 days respectively and most of the films delaminated from the electrodes. This physical instability of thick films, along with the twofold difference in charge storage capacity between thin and thick films, creates the dilemma of ideal film thickness. Since the neural application demands the high electrical performance of thick films, a notion of improving physical stability while maintaining the high conductivity of thick films has developed but has not yet been realised.

The elastic modulus, E , of a material, a mechanical parameter that implicates the strain mismatch at the tissue interface, is usually measured by tensile testing. This is a technique that requires free standing samples with typical dumbbell geometries. Electrodeposited PEDOT films are physically bound to platinum substrates through the chemisorption of the sulfur moieties on PEDOT and sulfonates into the substrate. Additionally, it has been known that CPs electrodeposited from aqueous solutions are more adherent to the substrate [53]. In order to prepare a free standing sample, electrodeposited CP is mechanically scraped from the substrate using either an adhesive tape or a razor blade.

Previously, tensile tests were performed on the free standing samples of Baytron P [76-78], a water dispersion that was dry-casted into a film, and electrodeposited PPy [119-122], of which were mechanically detached from substrates using a razor blade. The tensile testing of Baytron P exhibited an ultimate tensile strength of 1 – 2.7 GPa and yield strength of 25 – 55 MPa [78]. In the study by Diaz and Hall [119], a number of different

PPy films were synthesised from various dopant and solvent combinations and showed ultimate tensile strengths in range between 8.27 - 59.23 MPa and elastic moduli between 0.34~2.41 kPa [119]. The thicknesses of the tested films were 15 - 35 μm , which were at least 1.5 times thicker than those of typical films used in the neural applications, 0.05 ~ 10.2 μm [35, 96]. It was expected that the difference in thickness would result in different morphology, geometry and hence mechanical properties. Satoh et al. [120] reported that the tensile moduli of 2 ~ 3 μm thick PPy films were 0.2- 1.5 GPa depending on the polymerisation potential. Gandhi et al. [122] showed that the tensile moduli of 20 μm thick PPy films were affected by the choice of a substrate. The E of PPy deposited on stainless steel (SS), carbon coated SS, and Pt coated SS were 2.4 ± 0.4 , 3.0 ± 0.4 and 3.2 ± 0.2 GPa, respectively. It is important to note that there is scant cohesive data and a comprehensive study of thin film mechanics is required.

Recent advances in indentation techniques have enabled direct contact mechanical measurements of a film on a substrate system with experimental simplicity and flexibility. Previously, Yang et al. [35] examined the mechanical properties of the electrodeposited PEDOT/LiClO₄ using indentation technique and reported that the mechanically softest film, which also showed the lowest electrical impedance, was fabricated with the polymerisation charge of 0.88 C/cm². However, this data was not quantified as an absolute mechanical stiffness. Modeling and interpretation of indentation data have been key challenges to the widespread use and understanding of nanoindentation techniques. The next chapter describes the detailed background and procedure of indentation techniques to understand the local mechanical behaviour of conducting polymer films on platinum electrode.

CHAPTER 3.

Indentation of Polymers

3.1. Introduction

Due to the difficulties experienced in making measurements on materials which inherently require supporting substratum, there is a lack of available data on thin film mechanics. Approaches to mechanical characterisation of such structures include substrate curvature testing, bulge testing, buckling testing, impulsive stimulated thermal scattering (ISTS) and indentation testing. As reviewed previously by Jansen et al. [123] and Stafford et al. [124], the first four techniques are light-scattering based analysis, which necessitates a smooth and reflective surface. Unlike these techniques or conventional mechanical tests requiring free standing samples with specific geometries, the use of micro to nano sized indenters allows the local mechanical profiling of intricate micro/nano structures within bulk samples as well as the characterisation of smaller samples that cannot be tested by conventional bulk testing methods.

Atomic force microscopy (AFM) and nanoindentation techniques provide a range of force resolutions as detailed in Table 3.1 and thereby, permit testing of both nano and (sub)micro structures. These techniques have widely been performed on structurally complex biomaterials such as tissues [125-129], cells [130-134], gels [134-138], foams [139-141], and polymers [142-147]. In addition they have found application in characterising multilayer samples having a film-on-substrate structure [147-151], such as that presented by electrodeposited CPs. Taking guidance from the literature on techniques used to examine other film-on-substrate materials, indentation techniques were applied throughout this thesis to address the previously unmet need for characterising CP mechanical properties. Throughout this process a number of important

considerations were made apparent which will influence the application of indentation to CPs and ultimately the resulting calculation for film stiffness. This chapter aims to analyse the theory and approaches used for indentation testing of polymeric materials with an emphasis on CPs. The general testing procedure and the experimental variables involved, such as indenter geometry and load profile, are described in Section 3.2 and 3.3 respectively.

Table 3.1: Different types of indentation instrumentations [148, 152]

Instrumentation	Transducer	Force Resolution	Testing Resolution
Nanoindentation/ Instrumented indentation	Springs	1 nN ~ 1 Mn	(sub)micro-scale
Atomic force microscope (AFM)	Single cantilever	30 pN ~ 1 nN	Nano-scale

3.2. General testing procedure and theories

Indentation is a process where a nano or micro sized tip is introduced to and then removed from a sample surface. The resulting force-displacement curve is used to model the plasto-elastic behaviour of the material under test. This process forms the basis of both nanoindentation and AFM techniques used in this thesis. Indentation testing requires a rigid indenter, having a specific axisymmetric geometry, which is loaded onto a specimen to induce plasto-elastic deformation. During the process, the load–displacement, P - h , behaviour of the local surface undergoing the deformation is recorded

continuously and plotted into a graph as shown in Figure 3.1 (a). The surface deformations are presented in a schematic manner in Figure 3.1 (b). The graph represents sequential loading (from 1 to 2 in Figure 3.1) and unloading (from 2 to 3 in Figure 3.1) phases of indentation.

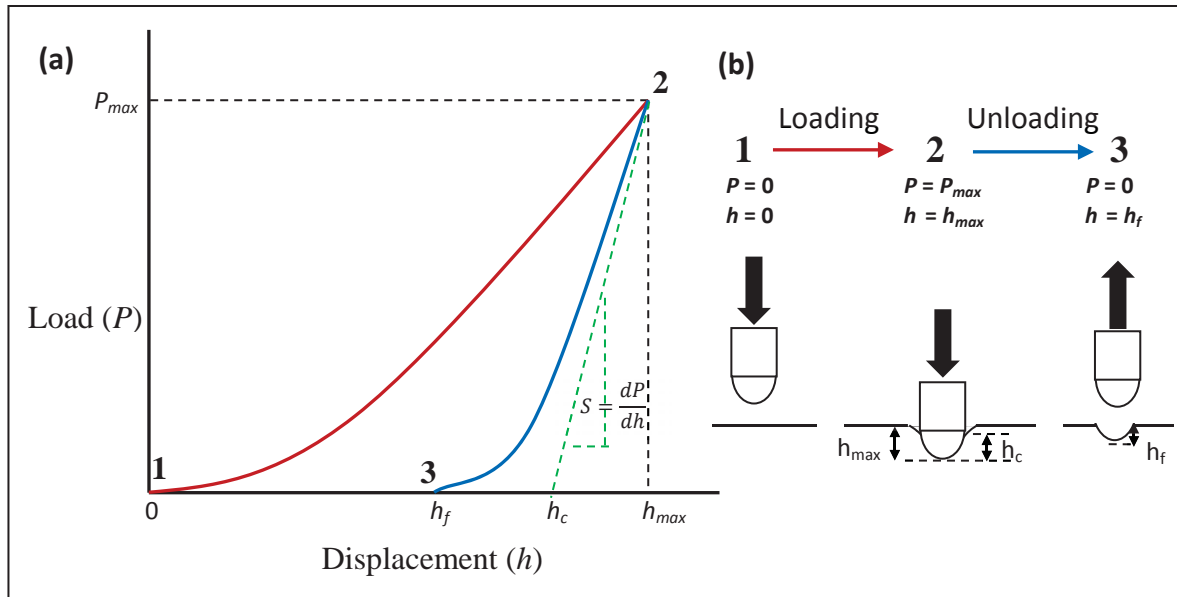
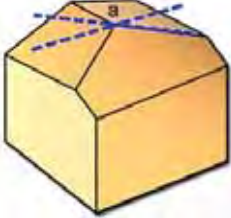
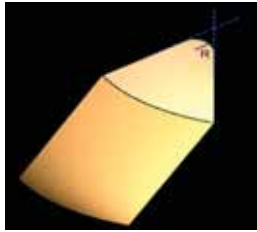
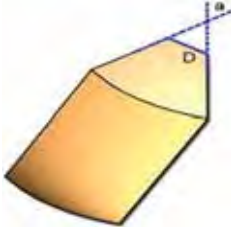


Figure 3.1: A typical load versus displacement graph represents the loading (1→2) and unloading (2→3) processes of indentation where P_{max} is the maximum force applied, h_{max} is the maximum displacement of the indenter, h_c is the contact displacement, h_f is the final displacement and S is the contact stiffness, a gradient tangential to the start of the unloading curve.

The elastic properties of the sample are typically extracted from the unloading curve, which is assumed purely elastic. The maximum displacement h_{max} , after loading phase (step 2 in Figure 3.1), contains both plastic and elastic deformations. During the unloading process, the elastic component of h_{max} is recovered and the remaining plastic counterpart is defined as the final displacement h_f . The unloading curve provides values of h_{max} , h_f , and the contact stiffness $S = \frac{dP}{dh} \big|_{h_{max}}$, which is used to analyse the contact displacement h_c that determines the contact area A .

A major challenge in indentation analysis is the determination of the contact area between the sample and the indenter. The unloading graph of a flat-punch indenter, providing constant contact area, is linear [153], whereas those of other geometries, such as Berkovich and cono-spherical, are typically curved as shown in Figure 3.1 (a), indicating that the contact area is not constant. Common indenter geometries are shown in Table 3.2.

Table 3.2: Common indenter geometries [154]

Geometry		Radius size	Applications
Berkovich (Three-sided pyramidal)		40~150 nm (AFM – 5 ~ 60 nm)	Thin films, Micro/nano structured materials, Hard polymers, bulk materials
Conospherical		<1 μm – 100 μm	Soft Polymers, Biomaterials, Microelectromechanical systems (MEMS)
Flat punch		<1 μm – 100 μm	extremely soft samples (gels, tissues)

The compliance method, described by Oliver and Pharr [155], is the *de facto* standard for indentation unloading curve analysis. The method estimates the contact area A based on the elastic contact model at maximum loading conditions (h_{max} , P_{max}). Schematic diagram illustrating the unloading process of a conical indenter is shown in Figure 3.2. At maximum load P_{max} , the projected contact area A , between the indenter and the sample,

is defined in terms of the contact radius a : $A = \pi a^2$. Through geometric calculations, this equation is then expressed as a function of the contact displacement h_c : $A = f(h_c)$. Detailed calculations can be found in [156]. The contact area functions for different indenter geometries are summarised in Table 3.3.

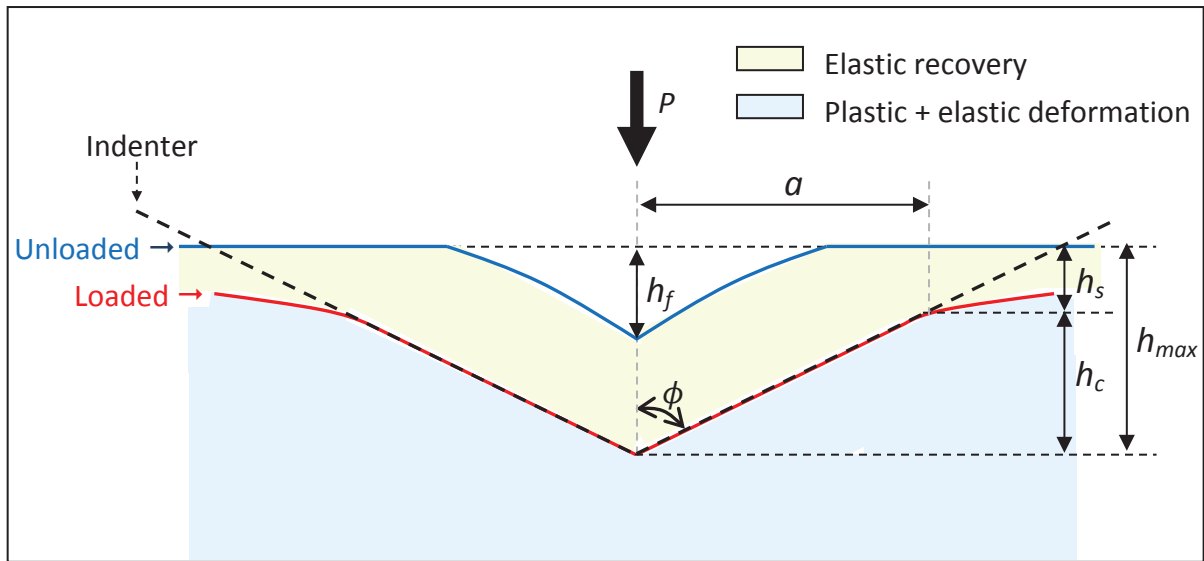


Figure 3.2: Schematic diagram of the unloading process. The blue region indicates the plastic and elastic deformations at maximum loading and the green region represents elastic recovery during the unloading process.

The contact displacement h_c , and the sink-in displacement h_s indicate displacements that occurred in the contact region and its vicinity, respectively. As illustrated in Figure 3.2, the sum of these two is equal to the maximum displacement h_{max} ; $h_{max} = h_c + h_s$. Assuming no pile-up, see 3.3.3 for more details, of material occurs, the sink-in displacement h_s is geometrically calculated as:

$$h_s = \epsilon \frac{P_{max}}{S} \quad \text{hence} \quad h_c = h_{max} - \epsilon \frac{P_{max}}{S}, \quad (\text{Equation 3.1}),$$

where ϵ is a constant depending on indenter geometry. The values of ϵ for different indenter geometries are summarised in Table 3.3. h_{max} , P_{max} , and S can be obtained from

the unloading curve. Therefore, the projected contact area A is obtained by substituting the calculated h_c value, from equation (1), into the contact area equation, shown in Table 3.3.

Table 3.3: Contact area functions $A = f(h_c)$ for common indenter geometries

Indenter geometry	Contact area $A = f(h_c)$ at P_{max}	Geometric constant ε
Berkovich indenter ($\theta = 65.27^\circ$)	$A = (3\sqrt{3} \tan^2 \theta) h_c^2$ $= 24.49 h_c^2$	0.72
Spherical indenter	$A = \pi(2Rh_c - h_c^2)$ $\approx 2\pi R h_c$	0.75
Cylindrical punch	$A = \pi(R^2)$ (constant)	1

Extracting elastic properties from the load-displacement curve involves an assumption that the indenter and the sample are continuous elastic media. The reduced modulus E_r , a combined modulus of the indenter and the sample, is then defined by

$$\frac{1}{E_r} = \frac{1-\nu_s^2}{E_s} + \frac{1-\nu_i^2}{E_i}, \quad (\text{Equation 3.2}),$$

where ν_s and E_s , and ν_i and E_i are the Poisson's ratio and elastic modulus of the sample and the indenter, respectively. The Poisson's ratio of common polymer samples ν_s and indenter materials ν_i as well as the elastic moduli of indenters E_i are summarised in Table 3.4 and 3.5. With these ν_s , ν_i , and E_i values known, the elastic modulus of the sample E_s can be calculated by evaluating the reduced modulus E_r .

Table 3.4: Poisson's ratio and elastic modulus of indenter materials

Indenter material	Poisson's ratio ν_i	Elastic modulus E_s (GPa)	References
Diamond	0.07	1,140 ~ 1,141	[154, 157]
Silicon	0.26 ~ 0.28	130 ~ 185	[158]
Silicon nitride	0.2 ~ 0.27	160 ~ 290	[159]

Table 3.5: Poisson's ratio of common polymers, conducting polymer and metal electrodes

Material	Poisson's ratio ν_s (at 25°C)	References
Elastomer (i.e. rubbers)	≈ 0.5	[160, 161]
Polyvinyl alcohol (PVA) hydrogel	≈ 0.5	[162]
high density polyethylene (HDPE)	0.43 ~ 0.47	[163, 164]
polystyrene (PS)	0.33 (at 30°C)	[165]
Polypyrrole	0.38 ~ 0.40 (estimate)	[166, 167]
PEDOT (Baytron P)	0.34	[77]
Gold	0.42	[168]
Platinum	0.39	[168]
Silver	0.367	[168]
Iridium	0.26	[168]

The reduced modulus E_r can be calculated by fitting an elastic contact model to the unloading curve. The contact mechanical models developed by Hertz [169], and Sneddon [160, 170] predict the load-displacement behaviour of a flat elastic surface with respect to common indenter geometries such as spherical, conical, Berkovich, and flat indenters. The load-displacement equations of these models are shown in Table 3.6.

Table 3.6: Hertz and Sneddon contact mechanics models

Contact model	Indenter geometry	Load (P) – displacement (h) equations*
Hertz	Spherical	$P = \left[\frac{4}{3} E_r R^{1/2} \right] h^{3/2}$
Sneddon	Conical (or Berkovich)	$P = \left[\frac{2}{\pi} E_r \tan \phi \right] h^2$
	Flat(cylindrical)-punch	$P = [2RE_r]h$

*where P = load, E_r = reduced modulus, R = radius of indenter, h = displacement, and ϕ = half-angle of conical indenter.

The equations in Table 3.6 can be generalised into the following “power-law” equation:

$$P = \alpha(h - h_f)^m, \quad (\text{Equation 3.3}),$$

where α is a geometric constant, described by the bracketed terms in Table 3.6; the expression $(h - h_f)$, which is used in place of h , distinguishes the elastic component of the displacement; and m is a geometric power-law exponent. From the equations in Table 3.6, for a flat punch, $m = 1.0$, for a sphere or other paraboloids, $m = 1.5$, and for a cone or an equivalent Berkovich, $m = 2.0$.

By considering the maximum loading (h_{max} , P_{max}) condition, Equation (3) can be rewritten in terms of the reduced modulus E_r :

$$E_r = \frac{S}{2(\beta) \sqrt{A}} \sqrt{\pi}, \quad (\text{Equation 3.4}),$$

where $S = \frac{dP}{dh} |_{h_{max}}$ is the contact stiffness, β is a correction factor that is applicable to instrumented indentation techniques; and $A = f(h_c)$ is the projected contact area, see Table 3.3. The empirical correction factor β in Equation 3.4 is applied to reduce the error caused by imperfect geometries, which is a common problem with sharp tips such as the Berkovich or conical tip. While several values have been suggested as shown in Table 3.7, there is no strong theory suggesting an optimal value. Fischer-Cripps [171] indicated that the factor is usually greater than 1.034 and Oliver and Pharr [172] suggested a value of 1.05.

Table 3.7: Values of correction factors β

Indenter geometry	Poisson's ratio of the sample ν_s	Correction factor β	Reference
Flat punch		1.001~ 1.034	[173]
Berkovich $\phi = 70.32^\circ$	0.17	1.063	[174]
	0.3	1.096	[175]
conical indenter $\phi = 68^\circ$	0.3	1.085	[176]
conical indenter $\phi = 70.32^\circ$	0.3	1.0595	[175]
	0.3	1.067	[177]
Geometry independent	$(0.2 \leq \nu \leq 0.35)$	$1.018 < \beta < 1.051$	[178]

The evaluation of contact stiffness S is usually carried out by fitting a power law equation such as Equation 3 to the unloading curve and differentiating that equation with respect to displacement h to calculate the slope, shown in Equation 5:

$$S = \frac{dP}{dh} = \alpha m (h - h_f)^{m-1}, \quad (\text{Equation 3.5}).$$

The fitting procedure is started by fitting a second order polynomial function into the unloading data and then carried out iteratively using a least squares approach until at least 80 % of the data is fitted to the power law function [171].

3.3. Indentation of Polymers

Most polymers are viscoelastic materials that exhibit time- and temperature- dependent phenomena such as creep, and damping, and are also often ionic entities that may adhere to a surface upon contact. The presence of these behaviours contradicts the several assumptions which made in the Oliver-Pharr method, such as entirely elastic unloading and negligible adhesion. It has been previously reported that the compliance method (i.e. Oliver-Pharr method) overestimates the elastic modulus of a polymer by up to 70 % [161, 179]. Kranenburg et al [165] listed a set of factors that contribute to the error associated with the indentation of a polymer including viscoelasticity, unloading rate, material pile up, and shallow indentation depth. By considering experimental settings, such as tip selection, specimen preparation, and loading profile, as well as polymer characteristics, including viscoelasticity, and adhesion, the following section examines the best available practices for indentation of polymers.

3.3.1. Tip Selections

Indenter geometries can be categorized into sharp and blunt tips. The former, which include three-sided pyramidal tips such as Berkovich and cube-corner as well as conical tips, are typically used with the samples where the indent needs to be confined in nanoscale such as nanoparticles and thin films. These geometries usually provide a radius of curvature below 200 nm. The Berkovich indenter is the most widely used geometry for AFM and nanoindentation tests on hard substrates such as metals, ceramics, bones, teeth and glassy polymers.

For indentation of soft materials, blunt tips such as the spherical and flat-punch geometries are used to minimise sample damage. The small stress concentration of the spherical tip helps to minimise plastic deformation. The flat-punch imparts considerably high stress concentrations and is very sensitive to axial misalignment [180] but provides a constant contact area attributing no plasticity at initial contact. Additionally, Ebenstein and Pruitt [136] provided this guideline for tip choice: if the testing specimen is a tissue, a large spherical tip ($R > 25 \mu\text{m}$) should be used to avoid testing an individual cell ($\sim 8 \mu\text{m}$) or fiber. One of the assumptions made in the contact mechanical model is that sample surface is flat and smooth. To minimise the effect of sample roughness on the measured mechanical properties, large indenters could be used to make the effect of surface roughness negligible.

Electrodeposited PEDOT is an aromatic polymer with up to 40 % crystallinity [181]. This structural attribute indicates that the CP would behave like an amorphous polycarbonate,

which contains benzene rings and has crystallinity up to 25 % [182]. Testing of such glassy polymers is generally carried out by using a sharp tip such as a Berkovich tip with a radius between 100 ~ 200 nm. Considering its application to neuronal tissues, indentation of CP using a large blunt tip would be biomedically significant as this would reveal the mechanical properties at the microscale relevant to tissue. Additionally, this also helps to resolve surface roughness issues associated with nodular morphology of conducting polymer.

3.3.2. Loading Profile

Maximum load should be selected to yield a fully developed plastic zone in the specimen. For sharp tips, the contact displacement h_c needs to be greater than the one-third of the indenter radius. For spherical tips, shallow indentation is usually used following the assumption of the Hertz model, contact radius $a \ll$ indenter radius R . However, when indentation is very shallow, confinement effects, which produce localised response at the surface, could take place and could produce results that are different from those obtained from the bulk material.

To minimise the viscoelastic effects of polymers such as thermal drift and creep, the indenter and the sample as well as the fluid cell, which is required for testing hydrated samples, need to be thermal tuned prior to the test. This is usually done by leaving the indenter tip on hold at initial contact ($h = 0, P = 0$) until thermal equilibrium is reached. In AFM analyses used in Chapter 7, it was found that 20 min was sufficient to reach thermal

equilibrium in a fluid cell with CP and hybrid CP samples. Holding at maximum load (h_{max} , P_{max}) for ~ 120 s is also known to help to remove creep effects, but this technique is only applicable to static mode nanoindentation. The amount of creep is also dependant on the unloading rate. Cheng and Cheng [183] recommended quick unloading for viscoelastic materials to minimise creep.

3.3.3. Pile-up

When material piles up around the indent parameter, load is distributed through more of the material bulk than estimated by the compliance method and hence hardness and elastic modulus can be overestimated by up to 50 % [161, 171]. The only viable resolution to the problem is imaging the indent by AFM or SEM. Fischer-Cripps [171] noted that “ignoring the effect and treat the resulting values of E and H as comparative values” could be an option. This judgment was based on the fact that ISO standard [157] refer these quantities specifically as the “indentation modulus” and the “indentation hardness”, rather than the absolute elastic modulus.

Brittle CPs were found to exhibit pile-up in both nanoindentation and AFM. In nanoindentation visualisation of the pile-up was noted when using sharp tips, this was minimised through selection of a flat punch tip as specified above. When pile-up occurred during AFM scanning which uses a Berkovich tip, the measurements became erratic with less deformation and higher adhesion recorded on each indent. Both had significant effect on the stiffness modulus which exhibited time-course drift under these

conditions. Reducing the scanning frequency from 1 Hz down to 0.3 Hz was found to minimise this effect. In addition maintaining the indentation force close to 1 nN prevented brittle fracture of nodules which were likely to cause pile-up.

3.3.4. Adhesion

Polymers, especially biomolecules, are often ionic and can have adhesive interactions with a contacting surface. This could clearly bias the result obtained by the compliance method, where the Hertz model, neglecting interactions between contacting bodies, is used in the analysis. To compensate for the adhesion occurring during the testing, modified Hertz models such as Johnson-Kendall-Roberts (JKR) [184] and Derjaguin-Muller-Toporov (DMT) [185-187] models have been developed as shown in Table 3.8. These models, respectively, describe the adhesion, between the two contact bodies, that are limited to the inside or outside of the contact area. While commonly applied to the AFM techniques, these adhesion contact models are seldom applied to nanoindentation due to the limited spatial resolution.

In this thesis the Derjaguin-Muller-Toporov (DMT) was applied to AFM peak-force quantitative nanomechanical mapping (PF-QNM). This allowed compensation for interactive adhesion forces, which are particularly important when scanning hydrogel hybrid CPs.

Table 3.8: Common surface contact models for indentation [159]

Contact model	Hertz	Johnson-Kendall-Roberts (JKR) [184]	Derjaguin-Muller-Toporov (DMT) [185-187]
Contact radius (a)	$\sqrt[3]{\frac{RF}{E_r}}$	$\sqrt[3]{\frac{R(F + 2\pi RW)}{E_r}}$	$\sqrt[3]{\frac{R(F + 3\pi RW + \sqrt{6\pi RW F + (3\pi RW)^2})}{E_r}}$
Displacement (h)	$\frac{a^2}{R} = \left(\frac{F^2}{RE_r^2}\right)^{1/3}$	$\frac{a^2}{R} = \frac{(F + 2\pi RW)^{2/3}}{\sqrt[3]{RE_r^2}}$	$\frac{a^2}{R} = \frac{2}{3} \sqrt{\frac{6\pi W a}{E_r}}$
Adhesion force (F_{ad})	0	$2\pi RW$	$\frac{3\pi RW}{2}$

CHAPTER 4.

The Effect of Doping Species on the Properties of Electrodeposited CP

4.1. Introduction

CPs are of great interest in neural tissue engineering, where the significant strain mismatch between the tissue and metallic electrodes has been identified as a prevalent cause of the failure of implants [22]. Along with the implicit mechanical benefits, the nodular morphology of electrodeposited CPs brings significant electrical benefits by raising the surface area to volume ratio, hence improving the impedance. The size and shape of nodules, which primarily regulate the physico-mechanical properties, are thought to be influenced by various factors including fabrication parameters such as solvent, temperature, pH and deposition scheme as well as, by the chemistry of the monomer and choice of dopant. This study aimed to examine systematically the effect of dopant size and chemistry on physical and electrical properties and biological performance of a PEDOT CP.

Dopant anions, ranging from small inorganic halogens such as chloride and perchlorate to a large aromatic sulfonate such as PSS, play a significant role in determining the structural and orientational orders of CP chains. Warren et al. [44] showed that the doping with an aromatic sulfonate anion leads to enhanced order and crystallinity of PPy. This, in turn, improves the electrical conductivity, which is essentially a measure of charge transport along and in between the CP chains. This implies that there is a direct relationship between doping species and the resulting physical characteristics, such as morphology and density of the CP system.

Several studies have been conducted to investigate the effect of a particular dopant on the surface properties of the CP film, but the results obtained from these studies are

often incomparable due to far-ranging variations in deposition and testing conditions. These have been summarised in detail in Appendix A.

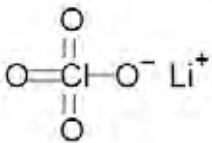
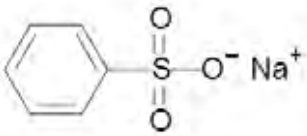
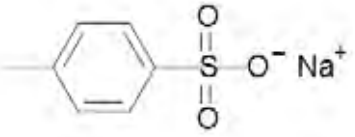
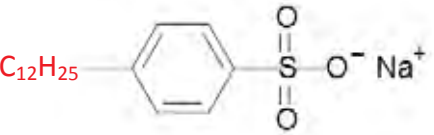
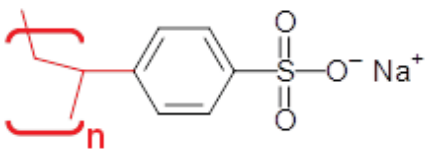
While studies into the effect of dopants and the biocompatibility of CP systems tend to be undertaken separately in much of the literature, Fonner et al. [96] brought these two lines of research together to compare the biomedical efficacy of PPy films doped with three different dopants: pTS, PSS, and Cl. All PPy films tested were able to support cultured Schwann cells and PC-12 cells for the testing period of 24 hr. The electrical conductivity of PPy/pTS (~53 S/cm [96]) was noticeably higher than that of the PPy/Cl and PPy/PSS (3 and 6 S/cm respectively). The other noticeable result was superior chemical stability of PSS films in two different media, water and phosphate buffered saline (PBS).

It is important to consider that both pTS and PSS are benzene sulfonate anions with different molecular sizes. This leads to a question of optimal dopant size for chronic function of CPs. The collective result of previous studies indicates that smaller dopants result in rougher, more nodular surfaces, which make the film more conductive, but less stable. To gain a broad picture of the impact of dopant size on the biomedical performance and stability of CPs, this study seeks to compare the physical, mechanical, electrochemical and biological properties of PEDOT films electrodeposited with different sized dopants under identical fabrication conditions.

The chemical structure, molecular weight and cytotoxicity of five dopants compared in this chapter are shown in Table 4.1. Commonly known as the leaving group, perchlorate

and sulfonate moieties are highly stabilised anions that help produce highly conductive and stable forms of CPs. Perchlorate is a small inorganic molecule with a central chlorine atom surrounded by four oxygen atoms, whereas sulfonate is an organic molecule having a central sulfur atom covalently bound to three oxygen atoms and a carbon chain that varies in size and structure. The chemical structure of benzenesulfonate (BS), the smallest sulfonate in the test, consists of a sulfonate group connected to a benzene ring. pTS, DBS, and PSS have extra methyl, dodecyl and polymeric groups in addition to the structure of BS. The comparison of the PEDOT films doped with these dopants is likely to provide important insights into how physical aspects of dopant may affect the biological performance of CPs.

Table 4.1: The chemical structure, molecular weight and toxicity (LD₅₀) of dopants compared in this chapter

Dopant	Chemical structure	MW (g/mol)	Toxicity (LD ₅₀ , mg/kg)
Lithium perchlorate (LiClO ₄)		106.39	2,100 (rat, oral) [188]
Sodium benzenesulfonate (BS)		180.16	9,378 (mouse, oral) [189]
Sodium p-toluenesulfonate (pTS)		194.18	1,700 (mouse, Intravenous) [190]
Sodium dodecylbenzene sulfonate (DBS)		348.48	438 (rat, oral) [191]
Poly(sodium 4-styrenesulfonate) (PSS)		~70000 (monomer = 206.19)	8,000 (rat, oral) [192]

It is difficult to directly compare the toxicity of dopants as they are conducted in different species with variable exposure routes, however in general, the lower the LD₅₀, the more toxic the chemical. In addition, the range of reported LD₅₀ values across the dopants is within the lower range of toxicity as defined by ratings scales such as those developed by Hodge and Sterner [193].

The difficulty in characterising electrodeposited CPs is often complicated further by their inherent “film-on-substrate” structure. In preparing free standing samples for common characterisation techniques such as four-point probe electrical conductivity test and tensile test, films are peeled from the substrates using either a tape or a razor blade. The damage arising during this process can result in microcracks and fractures that may not be visible to eyes, leading to inaccurate results. For neuronal applications where PEDOT films should remain intact with both the underlying metallic electrodes and the interfacial neural tissues, a direct characterisation of films on substrates is of interest. Yang et al. [35] previously studied the nanoindentation of PEDOT/LiClO₄ films to correlate the mechanical and electrical properties to the film thickness. While these results demonstrated qualitative behaviours, they were not quantified to yield the stiffness moduli.

In this study, PEDOT films doped with BS, pTS, DBS, PSS, or ClO₄ were electrodeposited on platinum (Pt) substrates under identical fabrication conditions. The physical, mechanical, chemical and biological characteristics of these films were investigated using non-destructive surface characterisation techniques including scanning electron microscopy (SEM), nanoindentation, cyclic voltammetry (CV), electrochemical impedance

spectroscopy (EIS), and PC-12 neurite outgrowth assays. The main aim of this research was to understand the effect of dopant sizes on implant related characteristics of PEDOT and to identify the ideal dopant size to achieve long-term function and stability.

4.2. Materials and methods

4.2.1. Electrochemical synthesis of PEDOT

The monomer, EDOT (97 %, cat#: 483028), and the dopants, LiClO_4 (≥ 95 %, cat#: 205281), NaBS (97 %, cat#: 147281), NapTS (95 %, cat#: 152536), NaDBS (technical grade, cat#: 289957), and NaPSS (average $M_w \sim 70,000$ Da, cat#: 243051), were purchased from Sigma-Aldrich Co. and were used as received without further purification.

Reaction solutions were prepared by dissolving 0.1 M of EDOT and 0.05 M of a dopant in a solvent mixture of 50 % acetonitrile (ACN) (anhydrous, 99.8 %, Sigma-Aldrich, cat#: 271004) and 50 % deionised water (Millipore, Milli-Q, resistivity $\geq 18 \text{ M}\Omega\cdot\text{cm}$). Table 4.2 below shows the amount of each constituent needed to make 2 ml reaction solutions. For the molarity of PSS, the molecular weight of a single styrene sulfonate ($MW = 206.19$ Da) was considered rather than that of the polymer ($M_w \sim 70,000$ Da).

Electrodeposition was implemented in an in-house manufactured silicone well system. FlexiPERM[®] micro12A (Greiner Bio-One GmbH, cat#: 90011436), a self-adherent silicone gasket having 12 circular wells each with a diameter of 6.5 mm^{*}, was attached to a

^{*}The specified diameter was 5.0 mm. However, the diameter measured from the deposited film was 6.5 mm.

platinum foil, which served as the working electrode. The assembled structure was placed in between two computer-numerical-control (CNC) machined polycarbonate (PC) sheets and clamped together as shown in Figure 4.1. In each well, having the surface area of 0.3318 cm^2 , 150 μL of monomer solution was placed. An array of platinum wire loops was subsequently placed in the well gasket and used as the counter electrode.

Table 4.2: Amount of chemicals used to make 2 ml of a monomer solution

Solutions	ACN (mL)	H ₂ O (mL)	EDOT (μL)	LiClO ₄ (mg)	NaBS (mg)	NapTS (mg)	NaDBS (mg)	NaPSS (mg)
EDOT/ClO ₄	0.871	0.871	21.4	10.639				
EDOT/BS	0.813	0.813			18.016			
EDOT/pTS	0.806	0.806				19.418		
EDOT/DBS	0.729	0.729					34.848	
EDOT/PSS	0.764	0.764						20.619

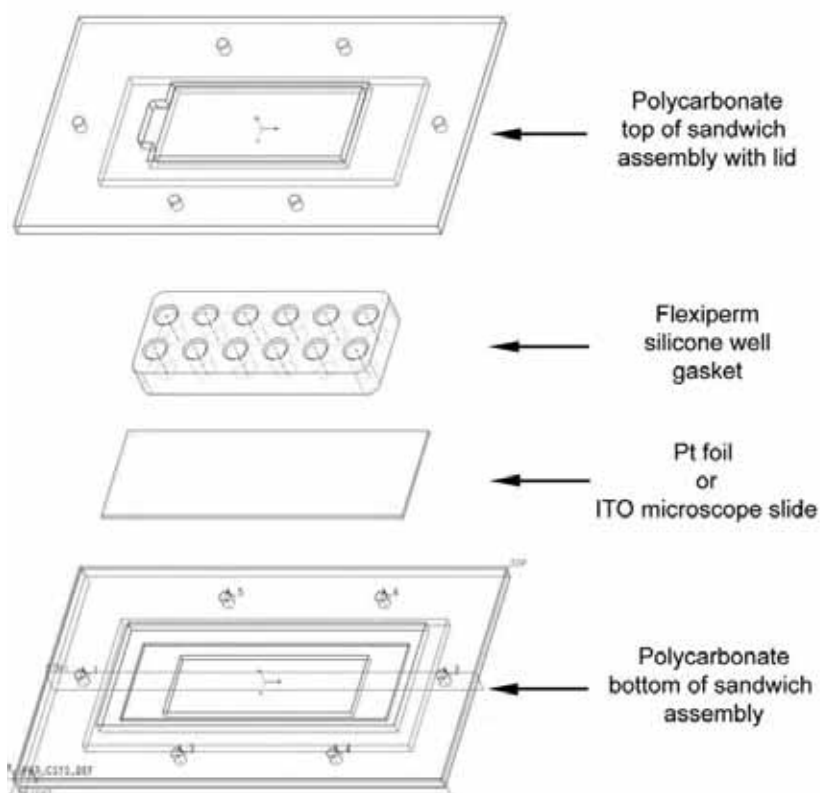


Figure 4.1: Silicone well system used in electrochemical fabrication [194].

Polymerisation was carried out galvanostatically at room temperature using a custom-made 12 channel galvanostat. A constant current of 0.5 mA/cm^2 was applied through each well for 33 min 20 sec. The total charge applied was equivalent to 1 C/cm^2 . When the deposition was completed, all films were soaked in DI water for 24 hours to remove excess electrolyte and dried in an isolated condition at room temperature for another 24 hours.

4.2.2. Scanning electron microscopy (SEM)

A platinum foil supporting CP films was directly mounted on an aluminium stub with double sided carbon tape. Samples were sufficiently conductive for imaging without further metallic coating. Electron micrographs were taken with an acceleration potential of 5 kV at magnifications of 30,000x, 1,500x, and 300x using a Hitachi S3400 scanning electron microscope (Hitachi High-Technologies Co., Japan).

Only for SEM studies, additional samples doped with either sodium dodecyl sulfate (SDS) (99 %, Sigma-Aldrich, cat#: 71726) or sodium chloride (Ajax Finechem Pty. Ltd., Cat #:465) were prepared in the same manner described above.

4.2.3. Indentation

The mechanical properties of CP films and a platinum foil were characterised by depth-sensing indentation using the Hysitron TI-900 TriboIndenter (Hysitron Inc., Minneapolis, MN, USA) with a $100 \text{ }\mu\text{m}$ spherical indenter or a standard Berkovich indenter. Samples

were mounted on a ferromagnetic stub using super glue at least 24 hours prior to the test. All indentations were performed using a trapezoidal loading function, consisting of 10 s loading to the maximum load of 1.5 mN, 5 s holding and 10 s unloading, as presented in Figure 4.2. Thermal drift was compensated to less than <0.05 nm/s. To minimise the substrate effect, the penetration depth was monitored to be less than 10 % of the film thickness and was typically around 500 – 800 nm. A square array of 9 indentations with an average spacing of 500 μm between the adjacent points was examined in each sample and three samples of each type were tested. Before and after each indentation, the surface of the sample was monitored using a built-in optical microscope to ensure full contact between the sample and the tip. The indentation data was analysed as discussed in Chapter 3 to determine the elastic moduli of the samples.

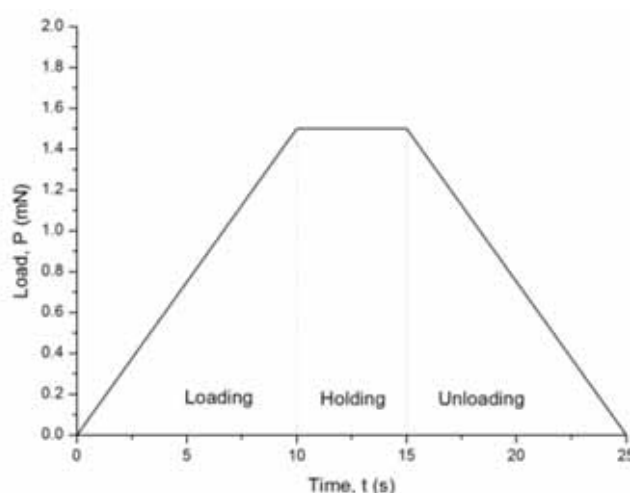


Figure 4.2: A typical trapezoidal load function for indentation experiments.

4.2.4. Cyclic Voltammetry (CV)

Cyclic voltammetry was carried out in a standard three electrode setup connected to an eDAQ EA163, ER466 integrated potentiostat system (eDAQ, Australia). The supporting electrolyte solution was Baxter's sterile saline (0.9 % sodium chloride solution, Baxter

Healthcare Corp., Australia, ref code: AH7124) with a nominal pH of 5.5 [195]. An isolated silver/silver chloride electrode (Ag/AgCl/3 M KCl solution) and a platinum wire were used as the reference and counter electrodes, respectively. Following the empirical process in Appendix B, the potential sweep range was determined to ± 0.7 V.

Cyclic voltammograms, graphs of current versus applied voltage, were recorded for 800 potential cycles between - 700 mV and +700 mV at the scan rate $\frac{dV}{dt}$ of 120 mV/s. As shown in Figure 4.3, each cycle of the CV represents a reduction-oxidation (redox) reaction pair involving the activation (oxidation) and deactivation (reduction) of PEDOT as well as the movement of ions in and out of the electrode. The charge storage capacity (CSC), the total amount of charge (q) transferred during a voltage cycle, is measured by the area enclosed by a voltammogram and is represented by the following equation:

$$I = \frac{dq}{dt}; \quad dt = 0.12 \, dV; \quad q = \int_0^{11.67} I dt = \int_{-0.7}^{0.7} |I| dV, \quad (\text{Equation 4.1}).$$

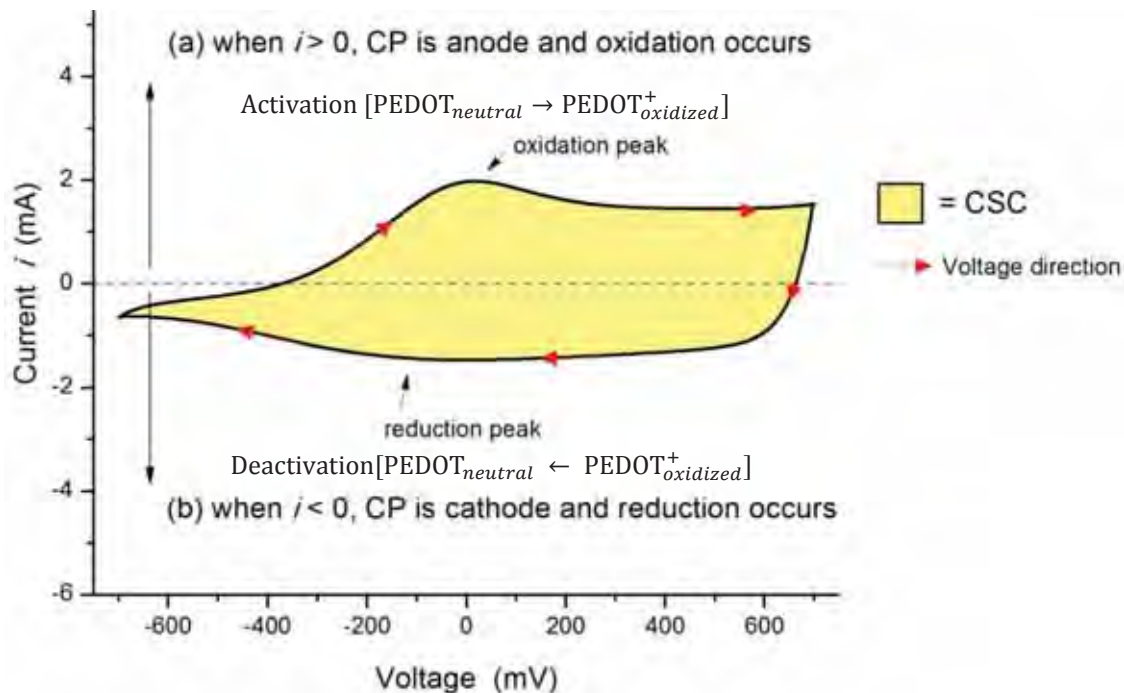


Figure 4.3: An example of a cyclic voltammogram. When the current is positive, the working electrode, CP, acts as anode and is subject to oxidation. If the current is negative, CP is cathode and reduction occurs. Charge storage capacity (CSC) of a cycle is given by the area enclosed within the curve.

4.2.5. Electrochemical Impedance Spectroscopy (EIS)

EIS measurements were performed using an INPHAZE HiRes-EIS System (eDAQ, Australia) and an INPHAZE 3-Terminal Sample Chamber (eDAQ, Australia). The schematic of the chamber is shown in Figure 4.4. This apparatus provided a typical one-compartment three-electrode configuration where the PEDOT sample was the working electrode, a gold wire formed the counter electrode, and a Ag/AgCl (3.5 M KCl) electrode served as the reference electrode. The chamber was filled with 11.8 ml of 0.9 % saline (Baxter Healthcare Corp., Australia), which was purged with N₂ for 10 mins prior to the test.

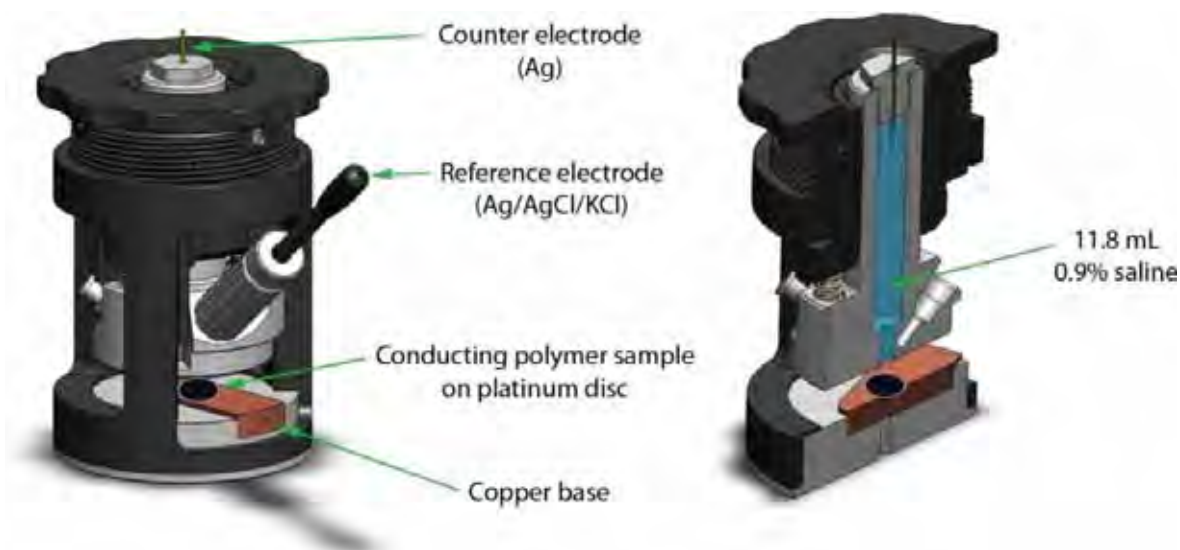


Figure 4.4: The INPHAZE 3-Terminal Sample Chamber[196].

The sample chamber and a reference circuit, a Randles circuit that composed of two resistors ($R_{\text{electrolyte}}$ and R_{sample}) and one capacitor (C_{sample}), were connected in parallel to a sine wave signal generator as shown in Figure 4.5. The resistance of the electrolyte ($R_{\text{electrolyte}}$), the capacitance of the sample (C_{sample}), and the resistance of the sample (R_{sample}) were measured from the chamber at the current frequency of 100 kHz, 0.01 and

1000 Hz, respectively. The reference circuit was built using electronic components compatible with the measured $R_{\text{electrolyte}}$, R_{sample} and C_{sample} . Building a reference circuit was an iterative process for each sample. The accuracy of the reference circuit was, however, limited by the magnitude of resistors and capacitors, which were available in the power of 10. Hence, a typical reference circuit built from a CP sample was composed of 100 Ohm, 1k Ohm, 1 μF for $R_{\text{electrolyte}}$, R_{sample} and C_{sample} . When the reference circuit was formulated, a single-frequency current, generating voltage amplitude of 30 mV, was applied simultaneously to the reservoir and the reference circuit. The impedance of the Pt/PEDOT/saline interface was then evaluated by comparing the current amplitude and the voltage phase angle of these two circuits as illustrated in Figure 4.5. The impedance spectra were measured at room temperature (25 °C) over the frequency range from 10^{-1} Hz to 10 MHz. Three samples of each type were tested.

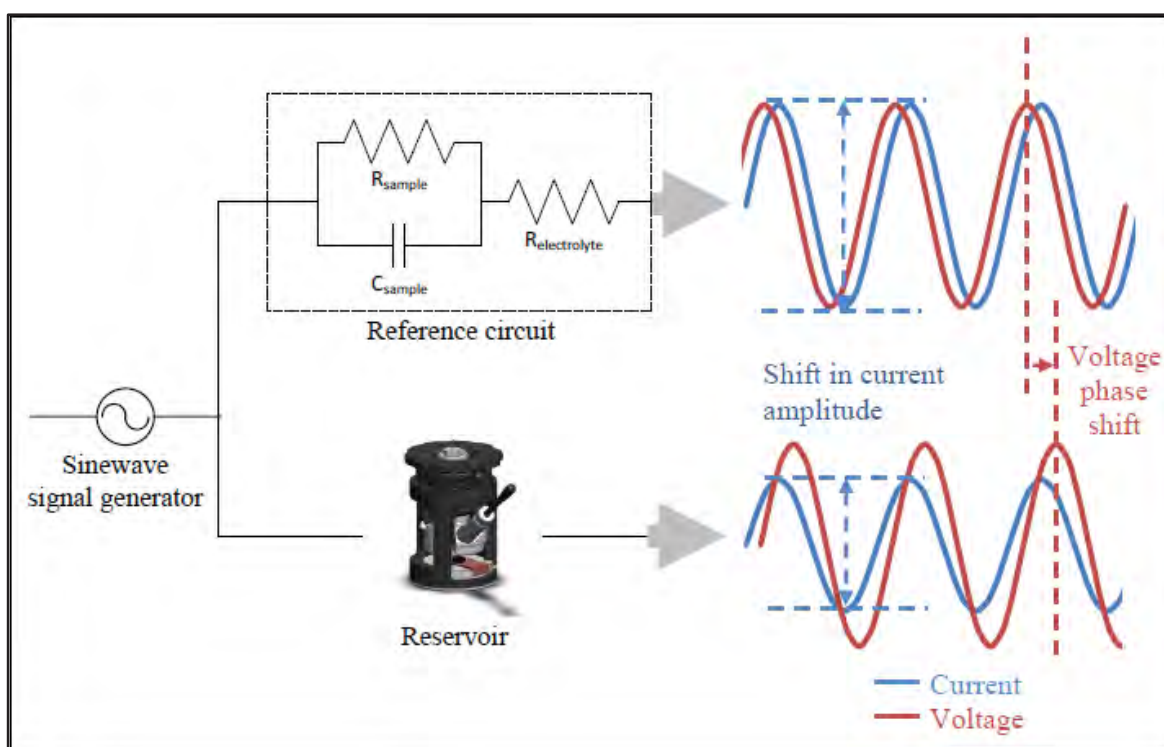


Figure 4.5: Schematic of INPHAZE impedance analyser. A single frequency current is applied simultaneously to the reservoir and reference circuit. This produces equivalent output voltage of 30 mV in each circuit. The impedance of the reservoir is calculated from the shift in current amplitude and the voltage phase shift.

4.2.6. Neuronal PC12 outgrowth assay

PEDOT samples were disinfected under germicidal ultraviolet (UV) light ($\lambda = 253.7$ nm, Philips TUV 30W/G30 T8) in a laminar flow hood for 30 minutes on each side. Silicone gaskets (FlexiPERM[®] micro12A, Greiner Bio-One) and stainless steel nuts and bolts were placed in separate 250 ml polycarbonate containers (Gamma sterilised, Techno-Plas Pty. Ltd., Australia) and disinfected by soaking in 200 ml of 65 vol% ethanol (EtOH) for 30 minutes. This was followed by drying in a laminar flow hood for 1 hour. With these disinfected components, the silicone well system, shown previously in Figure 4.1, was assembled under sterile laminar air flow.

Green fluorescent PC12 cells, transfected with a plasmid vector coding for pTurboGFP-N (excitation/ emission max = 482/ 502 nm, Evrogen, Moscow, Russia), were purchased from Marinpharm GmbH (Luckenwalde, Germany). Unlike normal PC12 cells, the NGF induced differentiation to neuronal phenotype is irreversible in these cells [197]. It is important to note that several other differences in properties, which have not yet been reported, may have arisen from the transfection. In the context of the neurite outgrowth study, however, these cells behaved like the original line, such that the extent and amount of neurite outgrowth were dependent on the concentration of NGF.

Prior to the seeding, CP surfaces were modified with 5 μ g/ml laminin (derived from Engelbreth-Holm-Swarm (EHS) sarcoma, Sigma Aldrich, cat#: L2020) in PBS (Sigma-Aldrich, cat#: D5652) which was free of divalent cations such as magnesium and calcium ions. Amino acid sequences in laminin such as RGD, YIGSR and IKVAV help to attach

otherwise non-adherent PC12 cells to a test substrate. After the incubation at 37 °C for 12 hours, laminin was immobilised on polymer films and white film was observed on top of the CP layer. The resulting surface was washed three times with PBS.

Fluorescent PC12 cells were grown in suspension culture in Roswell Park Memorial Institute (RPMI)-1640 medium (Sigma-Aldrich, cat#: R4130) supplemented with 10 % horse serum (HS) and 5 % fetal bovine serum (FBS). Passage number was kept to less than fifteen. To prepare a single cell suspension for passaging and plating, 10 ml of cell solution kept in a 25 cm² cell culture flask (CELLSTAR brand, Greiner Bio-One GmbH, cat#: 690175) was transferred to a 15 ml tube (CELLSTAR brand, Greiner Bio-One GmbH, cat#: 188 271) in a laminar flow hood. The tube was then allowed to stand for 10 mins until the cell clumps settled to the bottom of the tube. 1 ml of the solution, containing the cell clumps as well as the supernatant, was pipetted to a 5 ml polypropylene (PP) tube (Gamma sterilised, Techno-Plas Pty. Ltd., Australia). 1 ml of RPMI media was added to the tube. The clumps were then triturated with a plastic pipette into a single cell suspension. For the neurite outgrowth assay, the cell solution was diluted to a concentration of 6.6×10^4 cell/ml with low serum RPMI1640 containing 1 % horse serum and 100 ng/ml NGF. 150 µl of cell suspension was plated in each well (surface area = 0.3318 cm²) to provide a seeding density of 2.5×10^4 cells /cm². The neurite outgrowth was assessed using fluorescence microscopy after 96 hours of incubation at 37 °C with 5 % CO₂. During the culture, two thirds of culture medium was replaced at 48 h with fresh low serum medium containing 100 ng/ml NGF.

4.2.7. Cytotoxicity Assay - L929 cell growth inhibition

The overview of the procedure is schematically illustrated in Figure 4.6. A confluent monolayer of the murine fibroblastic cell line, L929, was harvested from a 75 cm² tissue culture flask (CELLSTAR brand, Greiner Bio-One GmbH, cat#: 658 175) by pouring off the initial media, washing twice with DPBS, and incubating for 5 minutes at 37 °C in 3ml of Trypsin-EDTA solution(Sigma-Aldrich, cat#: 59430C). The trypsinisation process was then halted by adding 6 ml of Eagle's minimal essential medium (EMEM) (Sigma-Aldrich, cat#: D5523) containing 10 % fetal bovine serum (FBS). Cell clumps were aspirated with 10 ml pipette and transferred to a 15 ml sterile centrifuge tube for centrifugation for 3 minutes at 1000 rpm. The cell pellet was formed at the bottom of the tube. After pouring off the medium, the pellet was suspended in 8 ml of fresh medium, EMEM + 10 % FBS, to obtain single-cell suspension. The cell density of the suspension was determined using a haemocytometer.

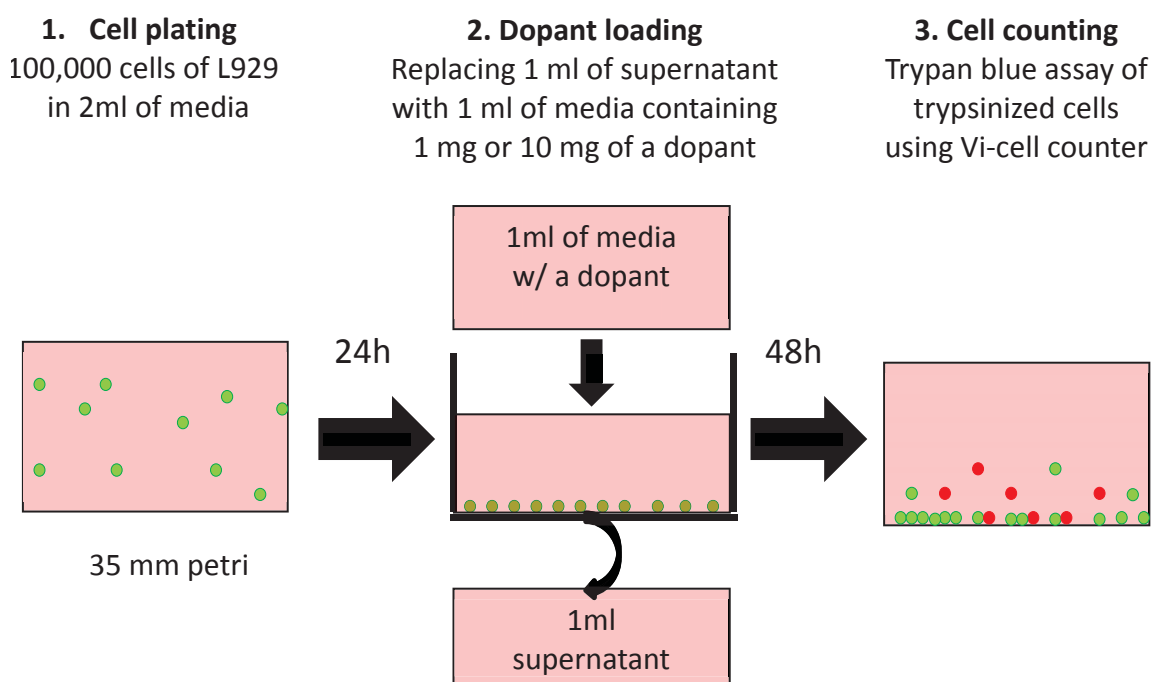


Figure 4.6: Schematic illustration of procedures of L929 cell inhibition assay.

The cell seeding solution, having the cell density of 50,000 cells/ml, was prepared by diluting the suspension. 2 ml of the seeding solution was added into each of 35mm tissue culture plates (Iwaki brand, Asahi glass Co., Japan, cat#: 3000-035). Plates were then incubated for 24 hours at 37 °C in a humidified atmosphere.

Test solutions containing 1mg/ml and 10 mg/ml of pure dopant were prepared by dissolving 50 mg of each dopant in 5 ml of EMEM containing 10 % FBS. The cell plates were checked for infection and the media was aspirated and replaced with 1 ml of the test solution. After 48 hours, the medium was poured off and the plates were washed with 2 ml of DPBS. The cells were trypsinised with 1ml of TV and the viable cell numbers in each plate were determined by trypan blue staining using a Vi-cell cell counter (Beckman Coulter Inc.).

4.3. Results

4.3.1. The effect of dopants on the microstructures of PEDOT films

Scanning electron micrographs of ClO_4 , BS, pTS, SDS, DBS and PSS doped PEDOT films taken at 30,000x, 1,500x and 300x magnifications are shown in Figure 4.7. The nodular microstructure of each sample can be observed at the lowest magnification, 300x, and the shape of the individual nodule was depicted at the highest magnification, 30,000x. The morphology that a biological tissue would perceive was illustrated at 1500x magnification where the scale bar represents 20 μm , a typical diameter of a biological cell body.

Micrographs were arranged in an ascending order of molecular weight from ClO_4 to PSS. It can be seen in Figure 4.7 that the surface roughness generally decreased with the increasing size of the dopant. Doping using the largest dopant, PSS, produced films that were smooth at the micron level. PEDOT doped with DBS, the second largest dopant, showed small nodules about 15 μm in diameter. SDS, an aliphatic dopant that has a molecular weight in between DBS and pTS, produced a microstructure similar to DBS. Smaller sulfonates, pTS and BS, resulted in significantly rougher films. The nodules of these films were arranged into a fibrillar secondary structure, which is illustrated in Figure 4.7 c).

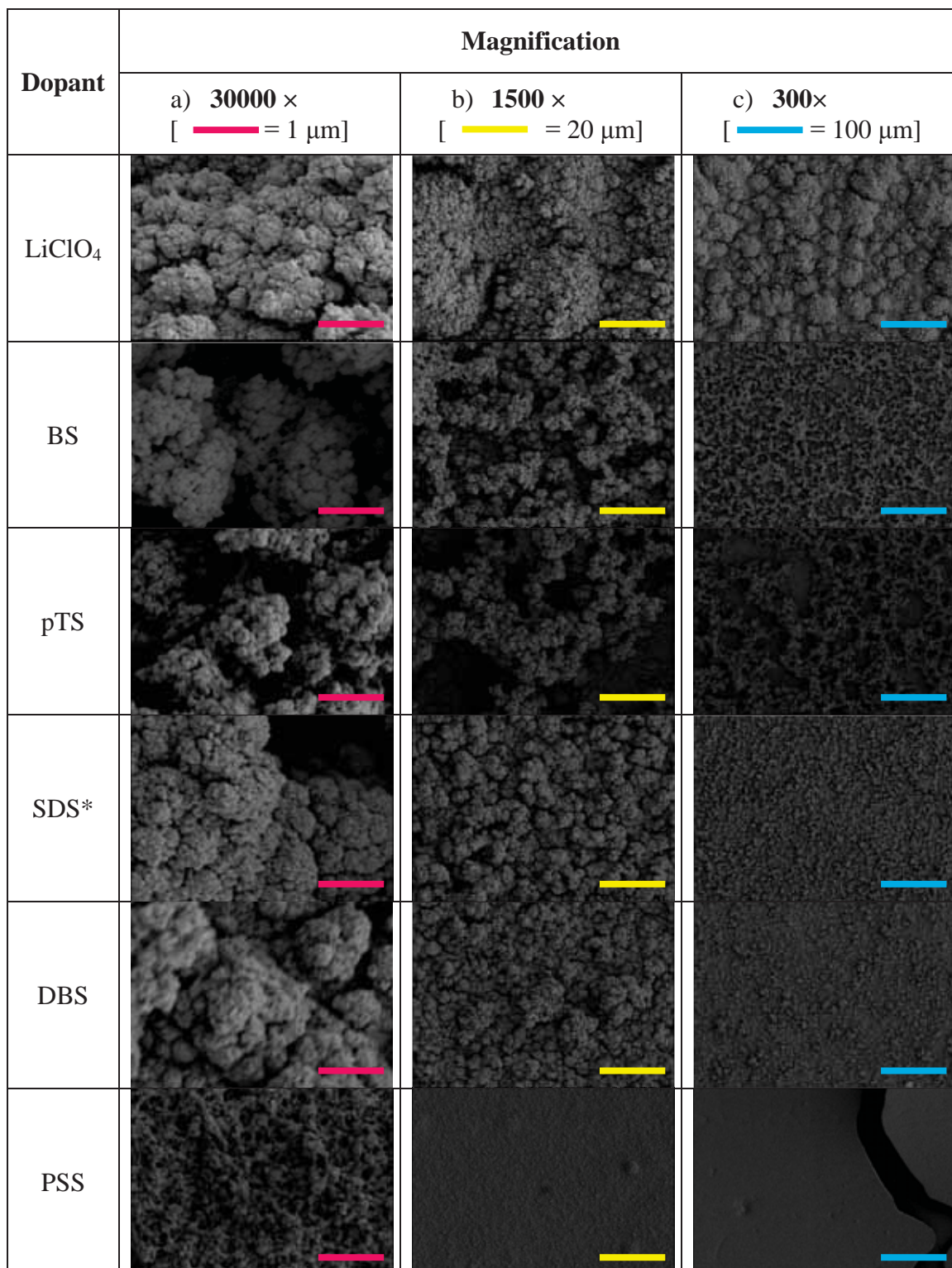


Figure 4.7: SEM of PEDOT films doped with LiClO₄, BS, pTS, SDS, DBS and PSS at a) 30,000×, b) 1,500×, and c) 300× magnification.

* The MW of SDS is 288.37 g/mol. The molecular structure consists of a sulfate (SO₄) ion attached to a lauryl chain, which is also found on DBS.

The morphology of PEDOT films was greatly influenced by the type of anions. PEDOT/ ClO_4 exhibited a unique rough morphology that was distinct from sulfonate doped films. The size of the surface features ranged from 10 to 100 μm in diameter. To discern the cause of this unique morphology, a control film doped with NaCl was also produced. CP films are often doped with chloride ions [96, 198] because of their biocompatibility and relatively low nucleophilicity. Chlorine and sodium ions are, respectively, the main anion and cation species in extracellular fluid (ECF). The microstructure of the NaCl doped film was rather flat and fibrillar as shown in Figure 4.8. This indicated that the high nodularity of perchlorate film was not a direct result of the small dopant size. Rather, it resulted from a combination of both the small molecular size and the stable, non-nucleophilic, nature of ClO_4 anion.

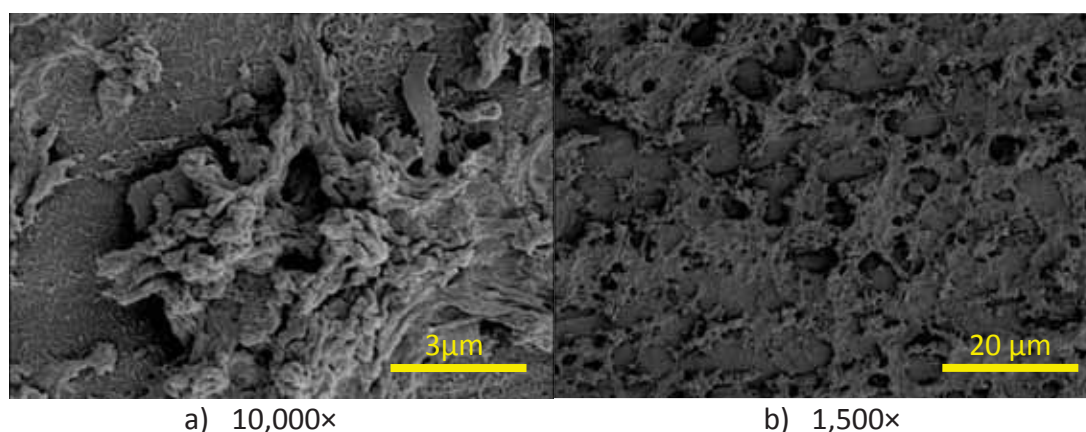


Figure 4.8: SEM of PEDOT films doped with NaCl at a) 30,000 \times and b) 1,500 \times magnification.

4.3.2. Indentation modulus

Instrumented depth sensing indentation (DSI) was performed to investigate the effect of dopant on the mechanical compliance of PEDOT films. Indentation with the Berkovich tip, which was strongly influenced by the surface nodularity, yielded statistically insignificant

results (data not shown). To reduce the errors arising from the rough surface of CPs, indentations were performed with a large spherical tip which compensates for surface irregularities such as pores and nodules. The direct mechanical contact between the tip and the sample was confirmed through optical microscopy. Figure 4.9 shows a micrograph of an indent made by a spherical indenter on PEDOT/BS film. The circular shape of the indented area, the bright region in the middle of the image, indicates that the nodules were flattened during the indentation and hence that the indenter surface was in full contact with the sample surface.

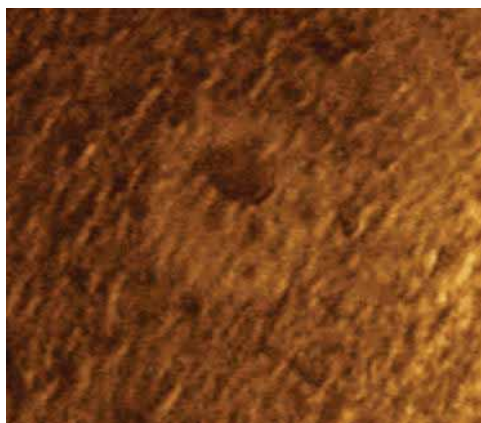


Figure 4.9: An optical micrograph of an indentation left on a PEDOT/BS film. The bright circle in the middle indicates the area indented.

Figure 4.10 illustrates the box plots of indentation moduli, E , of platinum and CP samples calculated from indentation using a conospherical tip with a radius of curvature of 100 μm . Indentation data was comprised of 81 indentation points, 9 indentations on each of three samples from three separate tests (9 indentations \times 3 samples \times 3 tests). Shapiro-Wilk test indicated that the distribution of the indentation was Gaussian, i.e. normal distribution. The histogram and statistical details are shown in the Appendix C. The average indentation moduli of PEDOT films doped with ClO_4 , BS, pTS, DBS, and PSS is

summarised in Table 4.3. The indentation modulus increased with the size of the dopant.

The modulus of PEDOT, in general, was two orders magnitude lower than that of platinum, $E_{Pt} = 108.91 \pm 22.74$ GPa.

Table 4.3: Indentation modulus of PEDOT films doped with ClO_4 , BS, pTS, DBS, and PSS (n = 9)

Sample	Indentation modulus (GPa)
PEDOT/ ClO_4	1.29 ± 0.72
PEDOT/BS	1.55 ± 0.74
PEDOT/pTS	2.44 ± 0.88
PEDOT/ DBS	2.94 ± 0.87
PEDOT/ PSS	3.23 ± 1.00

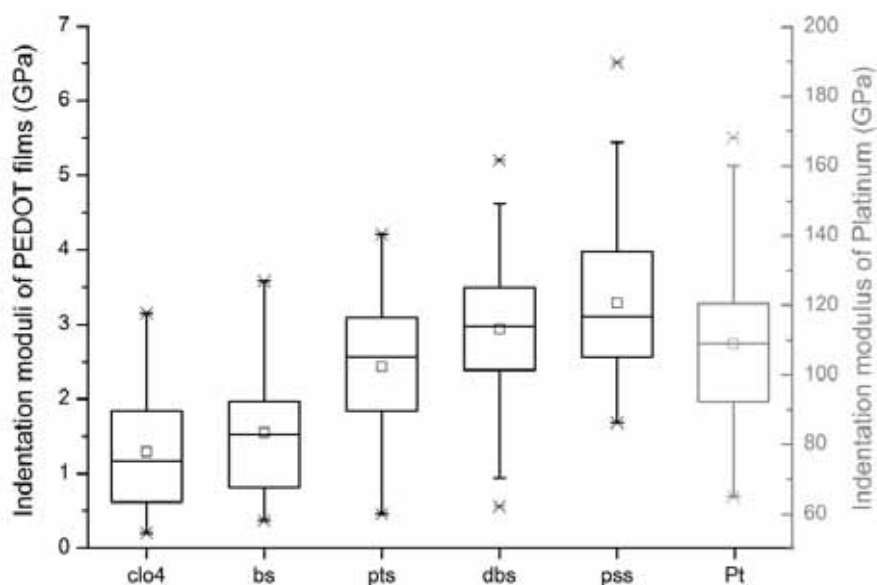


Figure 4.10: Box plots of Indentation elastic modulus (E) of PEDOT films doped with LiClO_4 , BS, pTS, DBS or PSS, and a platinum foil. (n=9). Note that the scale for Pt is 2 orders of magnitude higher than for the CP films.

4.3.3. Charge storage capacity (CSC) and electrochemical stability

The cyclic voltammograms of ClO_4 , BS, pTS, DBS and PSS doped films are shown in Figure 4.11 (a) - (e), respectively. Each figure contains voltammograms at 1st, 50th, 100th, 200th,

400th, 600th and 800th cycles to illustrate the electroactivity loss associated with the redox reactions. The percentage of electroactivity loss in CP, after 800 continuous activation and deactivation cycles, was calculated by the Equation 4.2.

$$\text{Electroactivity loss}_{800 \text{ cycles}}(\%) = 1 - \frac{CSC_{final}}{CSC_{initial}}, \quad (\text{Equation 4.2}).$$

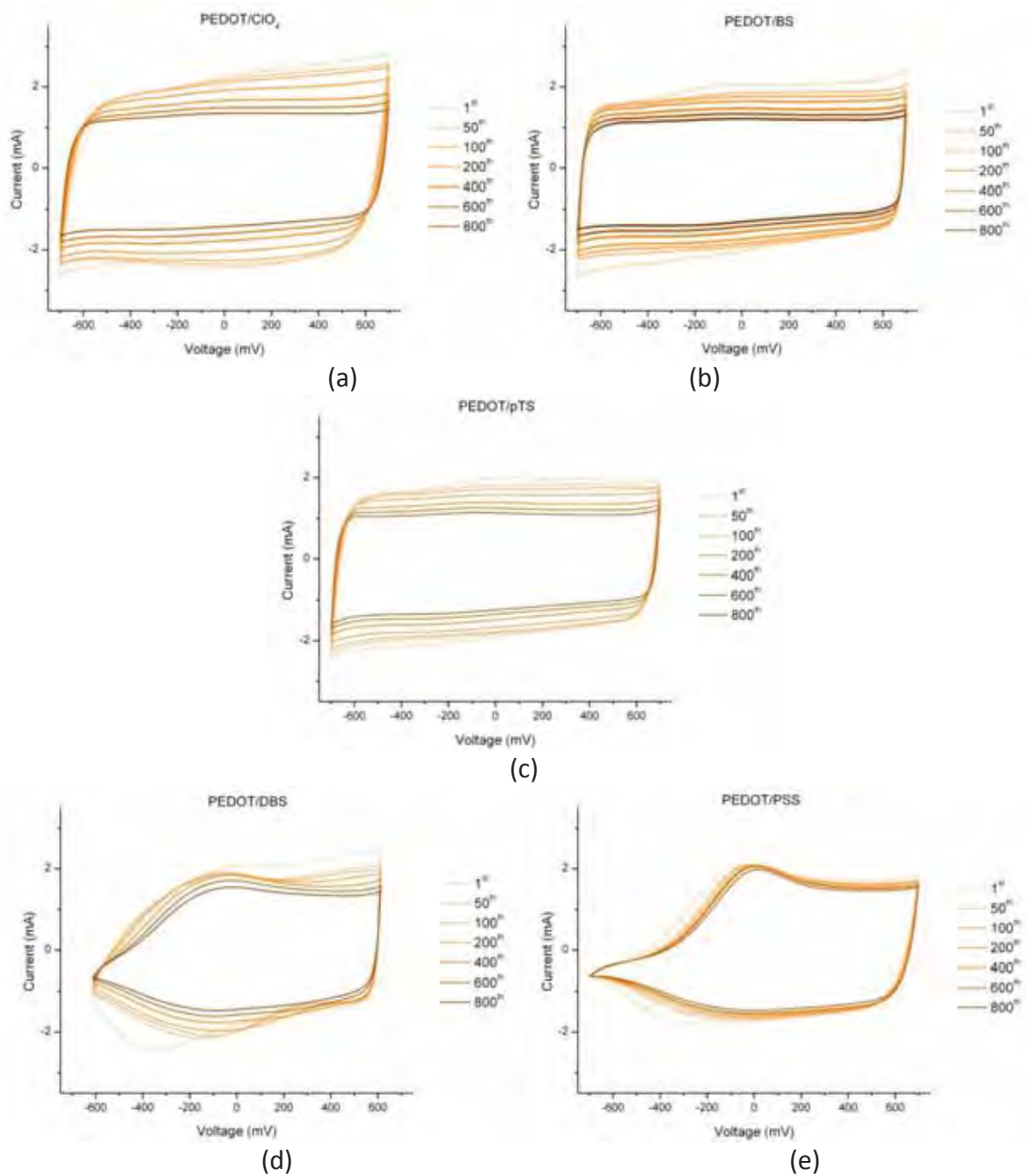


Figure 4.11: Cyclic voltammogram of PEDOT/ (a) CIO₄, (b) BS, (c) pTS, (d) DBS and (e) PSS over ± 700 mV vs. 3 M AgCl in 0.9 % saline at 1st, 50th, 100th, 200th, 400th, 600th and 800th cycles.

The initial and final charge storage capacity (CSC) and the electroactivity loss of PEDOT films are summarised in Table 4.4. It can be seen that all three measurements in Table 4.4 decreased with increasing dopant size from ClO_4 to PSS. Films doped with the smallest dopant, ClO_4 , showed the highest initial and final CSCs, 150.5 ± 6.3 and $91.9 \pm 5.1 \text{ mC/cm}^2$ respectively, as well as the most significant electroactivity loss of $38.9 \pm 5.2 \%$ after 800 cycles. Films synthesised with the largest dopant, PSS, had the lowest initial and final CSCs of 100.0 ± 4.3 and $68.2 \pm 4.3 \text{ mC/cm}^2$, respectively. PSS films, however, lost the least amount of electroactivity after 800 cycles, $31.7 \pm 4.5 \%$.

It can be seen in Figure 4.11 that the shape of the voltammogram was dependent on the size of the dopant. Films doped with small dopants such as ClO_4 , BS, and pTS exhibited trapezoidal voltammograms whereas those doped with the larger dopants such as DBS and PSS exhibited concave curves in the negative voltage range. These concave curves reduce the area enclosed by the voltammogram and result in the low CSCs of DBS and PSS doped films. The shape of voltammograms will be discussed further in the discussion section

Table 4.4: Comparison of charge storage capacity at 1st and 800th cycles and corresponding electroactivity loss (n=3)

Dopant	Initial CSC (1st cycle) (mC/cm ²)	Final CSC (800th cycle) (mC/cm ²)	Loss of electroactivity (% of original activity)
ClO_4	150.5 ± 6.3	91.9 ± 5.1	38.9 ± 5.2
BS	139.2 ± 4.7	87.9 ± 4.0	36.8 ± 3.9
pTS	135.4 ± 7.2	86.7 ± 3.9	36.0 ± 4.4
DBS	116.9 ± 4.6	79.0 ± 4.5	32.4 ± 3.4
PSS	100.0 ± 4.3	68.2 ± 4.3	31.7 ± 4.5

4.3.4. Electrochemical impedance

The electrochemical impedances of solid-liquid interfaces between 0.9 % saline and PEDOT samples were compared to determine the effect of the dopant on the electrochemical characteristics of PEDOT films. The impedance magnitude $|Z(\omega)|$ and the phase angle ϑ were plotted against frequency f , $f = 2\pi\omega$, as shown in Figure 4.12(a) and (b), respectively. As shown in Figure 4.12 (a), PEDOT coatings significantly reduced the electrical impedance at the conventional metal-fluid interface over four decades of frequencies ranging from 100 mHz to 1 kHz. At 100 mHz, the lowest frequency tested, the impedance of PEDOT was two orders magnitude lower than that of bare platinum.

The impedance of CP was not greatly affected by the choice of the dopant. In the frequency range relevant to neural communications, 100 Hz \sim 1 kHz, all CP samples exhibited the impedance of 100 Ohm, which is identical to the resistance of the electrolyte, 0.9% saline. At frequencies below 3 Hz, ClO_4 film exhibited the lowest impedance and the impedance increased in order from pTS, BS, DBS to PSS films.

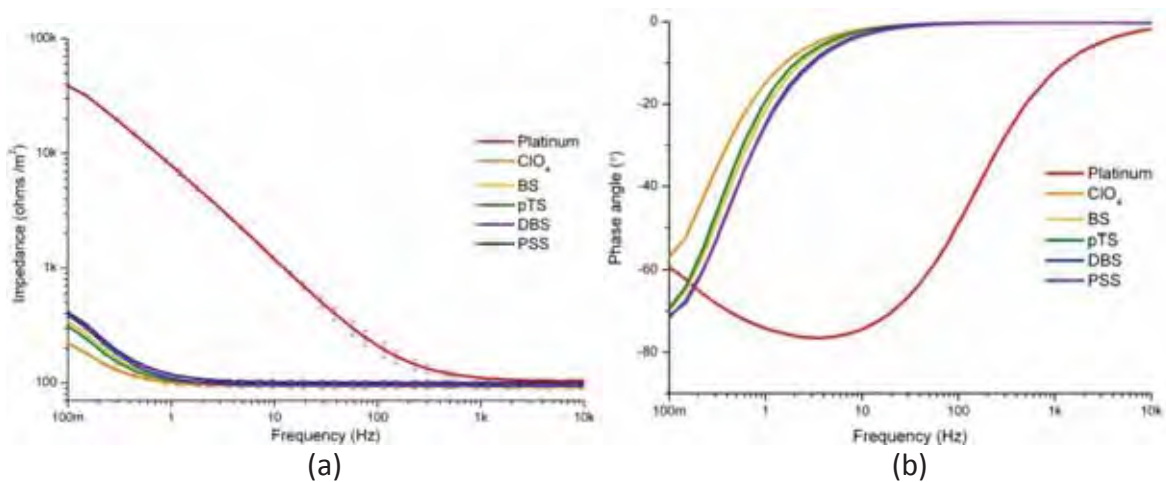


Figure 4.12: (a) The electrical impedance and (b) the phase angle of platinum and PEDOT samples in 0.9 % saline at the frequency range between 0.1 Hz and 10 kHz (n=3).

Negative phase angle, exhibited in Figure 4.12 (b), indicated that the impedance of CPs carried capacitive components at frequencies below 10 Hz but became purely resistive, giving zero phase angle, at frequencies above 30 Hz. On the other hand, the impedance of platinum is predominantly capacitive, through the double layer, at all frequencies below 10 kHz.

The impedance spectra can be split into capacitive and resistive (Faradaic) components shown in Figure 4.13 (a) - (d). Capacitance and frequency is inversely proportional to the imaginary part of impedance whereas resistance is directly proportional to impedance. Figure 4.13 (b) shows that the resistance of platinum is higher than CPs at frequencies below 1000 Hz and that CPs provide the same low resistance, ~ 100 ohm, at all testing frequencies. Hence, the higher impedance of CP at frequencies below 3 Hz was resulted from the capacitive reactance which decreases with increasing capacitance and frequencies. Figure 4.13 (a) indicates that the capacitance of the electroactive coating was gradually decreased with increasing frequencies. The amount of the capacitive reactance of CPs seemed to be negligible at frequencies above 3 Hz. This is clearly depicted by the constant impedance magnitude at higher frequencies in Figure 4.12 (a).

Figure 4.12 (c) and (d) present the capacitance and resistance of CPs in the frequency range significant for neural communications, 100 Hz \sim 1 kHz. As mentioned above, the capacitive reactance at this frequency range was negligible towards the overall impedance. The resistance, which is shown in Figure 4.13 (d), determined the overall impedance and was shown to be increased with increasing dopant size. One exception was PEDOT/BS. The resistance of PEDOT/BS was slightly higher than that of PEDOT/pTS.

This could be related to the size of the hydrophobic group that provides the hydrotropic or surfactant nature to the dopants. This will be further detailed in the Discussion.

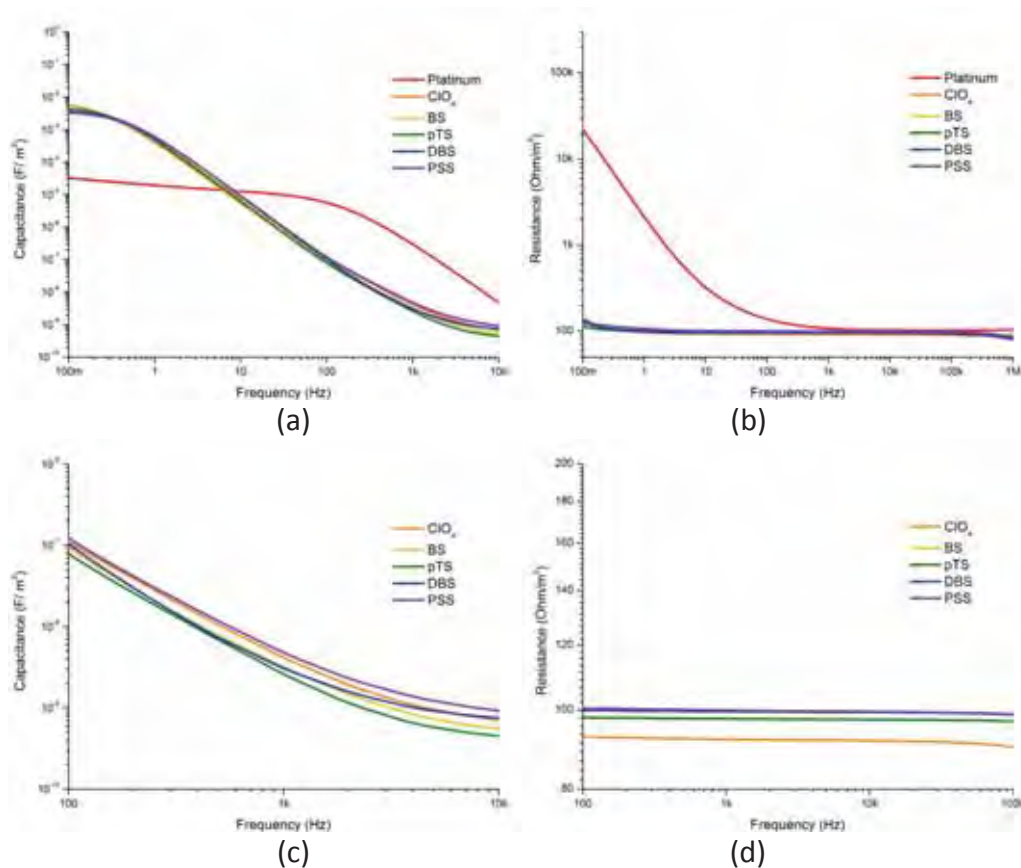


Figure 4.13: (a) The capacitance and (b) the resistance of PEDOT sample and Pt in 0.9 % saline at the frequency range between 0.1 Hz and 10 kHz. Graphs comparing the capacitance and the resistance of CP samples at the frequency range of 10 ~ 1000 Hz are shown in (c) and (d), respectively.

4.3.5. Neuronal attachment and outgrowth

Fluorescent micrographs of PC12s after 96 h culture on PEDOT films and tissue culture plastic (TCP) controls are shown in Figure 4.14. PC12 cells on PEDOT/PSS, PEDOT/ ClO_4^- , and TCP were clumped into small clusters and displayed significant neurite outgrowth as

shown in Figures 4.14 (a-c). On the other hand, micrographs of BS, pTS and DBS films, shown in Figure 4.14 (d-f), contained images of mostly cell debris without neurite extension. The relative cell adhesion and neurite outgrowth performance of each PEDOT sample was measured and the comparison shown in a series of box plots. Figure 4.15 (a), (b), and (c) present the average cell density, number of neurites and neurite length.

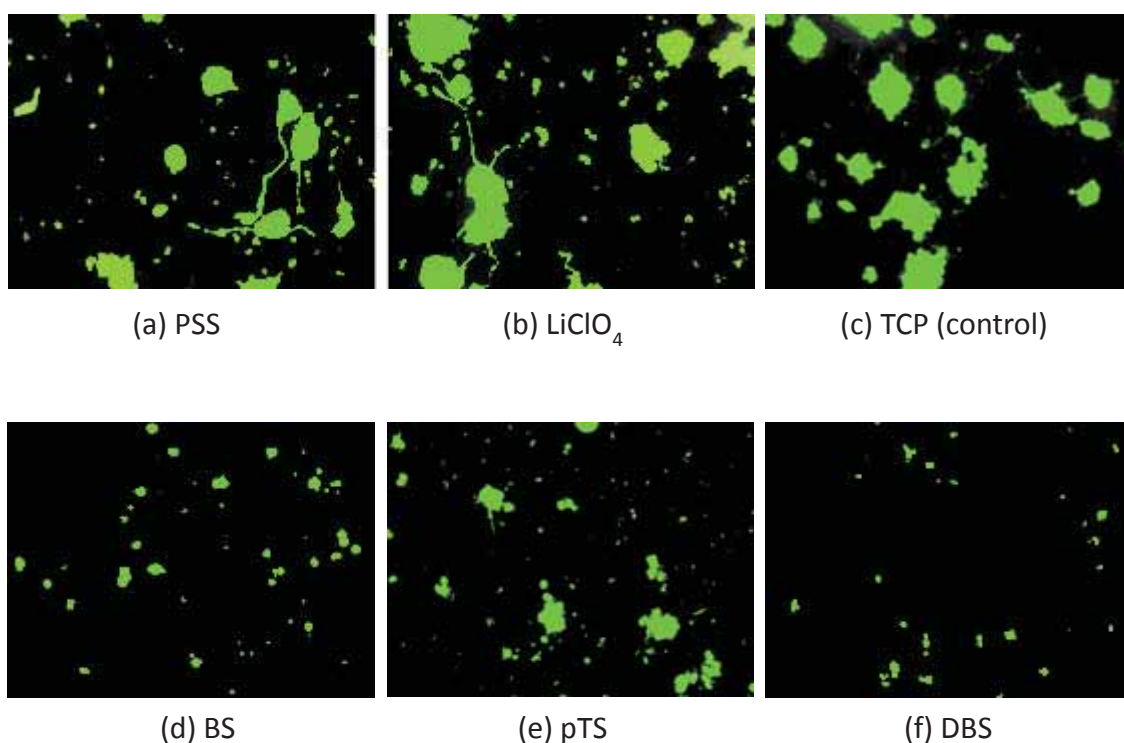


Figure 4.14: Fluorescent micrographs of PC12 cells after 96 h culture on laminin coated substrates, (a) PEDOT/PSS (b) PEDOT/LiClO₄ (c) TCP (d) BS (e) pTS and (f) DBS.

It can be seen in Figure 4.15 that, unlike electrical and mechanical properties, the result of PC12 assay was not directly affected by the size of the dopant. Both the cell density and the number of neurites were decreased with doping in the following order: ClO₄, PSS, pTS, BS and DBS. Other than DBS samples on which no neurite outgrowth was observed, neurite length was not greatly influenced by the choice of dopant.

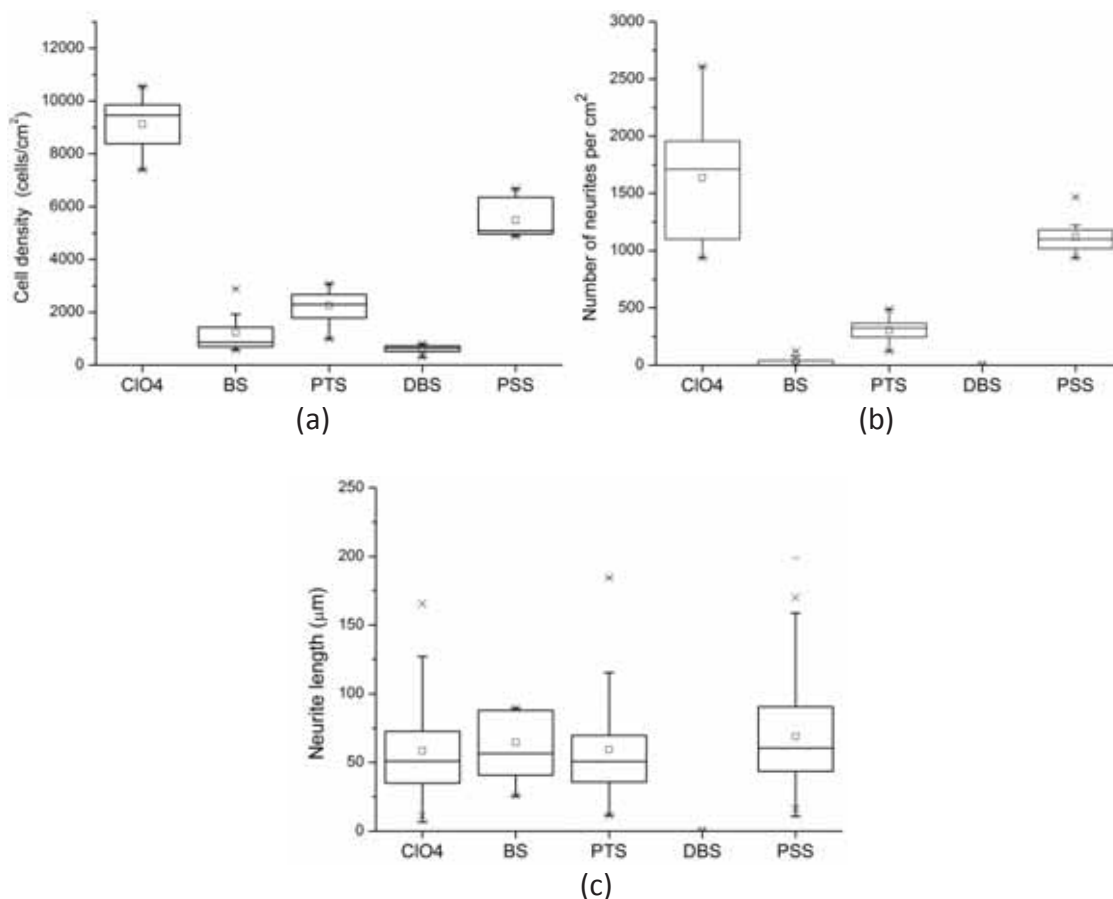


Figure 4.15: Box plots of PC12 proliferation data. (a) Average PC12 cell density on the substrates at 96h post-plating (b) Average number of neurites per cm² (c) neurite length.

4.3.6. Intrinsic Toxicity of Dopants - L929 Cell Growth Inhibition Assay

The growth of L929 cells was affected by both type and concentration of dopants as shown in Figure 4.16. The percentage cell growth inhibition, outlined in Figure 4.17, indicated that all dopants induced significant cytotoxic effects at 10 mg/ml concentration. At the lower concentration, 1 mg/ml, non-aliphatic sulfonates such as BS and pTS exhibited significantly less inhibition than other dopants in the test. The half maximal inhibitory concentrations, IC₅₀, of BS and pTS were in between 1 and 10 mg/ml. IC₅₀ of ClO₄ was close to 1 mg/ml and those of the bulky sulfonates, DBS and PSS, was significantly lower than 1 mg indicating the higher cytotoxicity of these dopants.

(a) Dopant	Concentration = 1 mg/ml	Concentration = 10 mg/ml	(b) Control	
ClO_4			TCP	
BS			4 % ETOH	
PTS			5 % ETOH	
DBS			7.5 % ETOH	
PSS				

Figure 4.16: Optical micrographs of L929 cell growth inhibition of (a) dopants including ClO_4 , BS, PTS, DBS, and PSS and (b) controls including null (TCP) and 4, 5, and 7.5 % EtOH.

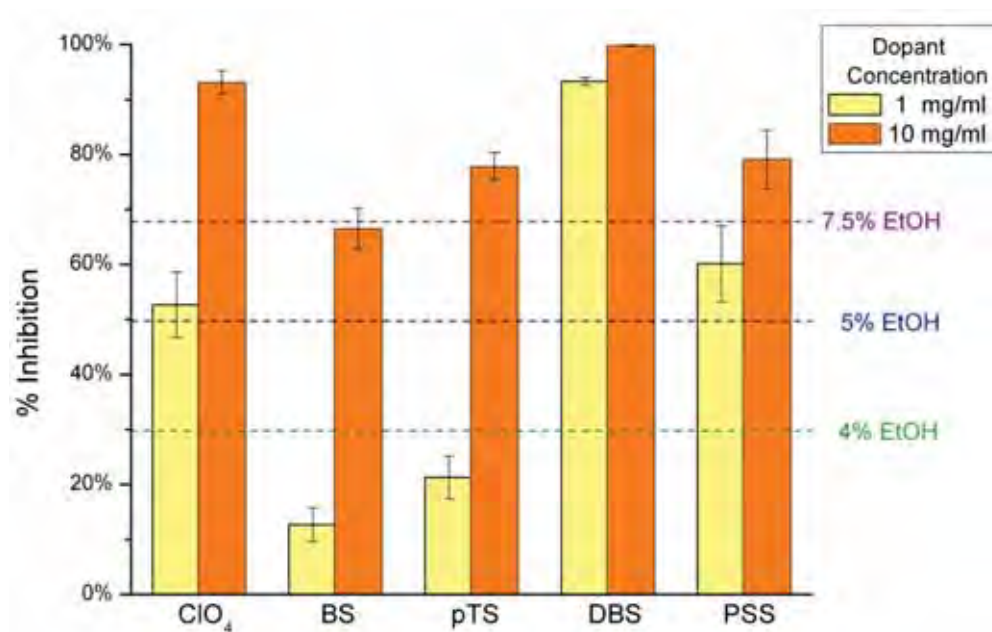


Figure 4.17: Percentage cell growth inhibition of each dopant at concentrations of 1 and 10 mg/ml.

4.4. Discussion

Dopant dependent behaviour was established across all PEDOT performance metrics, with most results indicating a size dependant relationship. The exception was the biological result which indicated additional mechanisms are involved in determining cell interactions. Scanning electron micrograms and indentation results, which are shown in Figure 4.7 and 4.10 respectively, illustrated that the physico-mechanical properties of PEDOT films are significantly affected by the choice of the dopant. The surface roughness generally decreased with the increasing size of the dopant while the indentation modulus was increased with the size of the dopant.

Considering that both mechanical and electrical properties of CPs are highly dependent on the structural properties such as composition, microstructure, and crystallinity, it was notable that the mechanical modulus of PEDOT did not vary with dopant size as dramatically as the electrical conductivity. Zotti et al. [199] reported a two-fold difference in the conductivity (σ) of PEDOT films doped with ClO_4 , pTS and PSS ($\sigma = 650, 400$ and 1 S/cm , respectively). X-ray photoelectron spectroscopy (XPS) revealed that the low conductivity of PEDOT/PSS was related to the increased spacing between CP chains, which makes it difficult for electrons to hop from one chain to another. This was believed to be due to the polymeric nature of PSS. Having one doping group per repeating unit, PSS was present in excess of the amount required by PEDOT films. Polymeric dopants, hence, consume more space than other monomeric dopants of which only the required amounts, one dopant per 4~5 CP repeating unit, are incorporated into the films.

Intuitively, the larger interstitial spacing between PSS doped films, which presumably have less defined crystallinity, would result in mechanically softer films. In contrast to this general speculation, the elastic moduli of PEDOT films increased with the size of the dopant. It is likely that the high stiffness of PEDOT/PSS is derived from that of the dopant which bears structural resemblance to polystyrene which forms a relatively stiff polymer. Similarly, films made with sulfonate dopants containing a hard benzene ring were marginally stiffer than perchlorate doped films. This result indicates that the mechanical stiffness of CPs is likely to be more dependent on the mechanical characteristic of the dopant itself rather than on induced structural changes. This is also consistent with the findings of a published x-ray scattering study [200] where PEDOT/pTS was described as a highly anisotropic material with a very low degree of crystallinity. With the limited degree of structural order at the microscale, CPs may behave as a particle composite of which its modulus is given by the fractional sum of the elastic modulus of each component. As a rule of thumb, the elastic modulus of such composites having two phases with similar elastic modulus can be predicted by the rule of mixtures where the upper and the lower bounds are defined by the following equations[201, 202]:

$$\textbf{\textit{The upper bound:}} E_{c,upper} = E_f V_f + E_m (1 - V_f), \quad (\text{Equation 4.3}),$$

$$\textbf{\textit{The lower bound:}} E_{c,lower} = \left[\frac{V_f}{E_f} + \frac{(1-V_f)}{E_m} \right]^{-1}, \quad (\text{Equation 4.4}),$$

where E_c , E_f , and E_m are the elastic modulus of the composite, filler, and matrix, and V_f and V_m are the volume fraction of the filler and matrix, respectively. This mechanical modelling of CPs as a composite is considered a direction for future work.

The moduli of PEDOT films, $1.3 \pm 0.7 \sim 3.2 \pm 1.0$ GPa, are two orders of magnitude lower than that of platinum, $E_{Pt} = 109.0 \pm 23.0$ GPa, but are significantly higher than that of neural tissue, $G' = \sim 5$ kPa [203]. Several studies have shown that soft substrates such as hydrogels are beneficial for neurite adhesion, growth, branching and differentiation [41, 204, 205]. More importantly, softer substrates prevent the proliferation of glial cells [48]. The formation of glial tissue, which physically and electrochemically isolates the electrode from neurons, is a leading cause of the device failure in chronic neural implants [22]. Consequently, a hybrid of conducting polymer and soft polymer brushes, which is of particular interest for neural applications, is considered later in Chapter 6.

Electrical properties such as charge storage capacity (CSC) and electrical impedance were shown to benefit from the high surface area and the facile charge transport provided by the doping of small dopants. Films doped with the smallest dopant, ClO_4 , showed the highest initial and final CSCs as well as the lowest impedance. On the other hand, doping using PSS, a polymeric dopant, resulted in the films with the lowest CSCs and the highest impedance.

The high CSC of PEDOT films results from fast, reversible doping/dedoping reactions which allow charging through the volume of material. It is known that CPs are pseudo-capacitors that utilize continuous redox reactions, but suffer from instability due to the imperfect reaction reversibility during cycling. The redox reversibility is likely to be influenced by the size of the dopants that are transferred during the redox cycles. The dopant size dependent redox behaviour is well depicted in the shape of the cyclic voltammograms shown in Figure 4.11. The curves of small dopants such as ClO_4 , BS,

and pTS were trapezoidal in shape where as those of large dopants such as DBS and PSS were concave in the negative potential range, where PEDOT was reduced and hence was electrically inactive. The Y-axis of the voltammogram indicates the amount of current passing through the sample. Current is determined by the amount of charge passed through the sample in a given amount of time. Hence, the shape of voltammogram can be explained in term of the mobility of a dopant, which affects the charge (ion) flux across the CP films.

When cationic PEDOT is reduced to the neutral state, relatively small anions such as ClO_4 , BS, and pTS are shown to be driven out from the CP system to balance the net charge [206, 207]. The trapezoidal voltammograms with broad redox peaks imply a stable charge transport which is achieved by the facile anionic charge transfer (i.e. dopants fluxed out from the CP films to create the current) when PEDOT is electrically inactive. It is well known that large anions such as PSS and DBS are structurally immobilised within the CP domain. Hence, when PEDOT is reduced, rather than the anionic transfer exhibited by small dopants, cations such as sodium ions in saline solution are moving into the CP domain to counter balance the immobilised anions. This cationic ion flux is, however, severely limited by the steric and structural constraints imposed by the CP domain. It is likely that this limited ion flux lead to the concave voltammograms and the limited CSC of PSS and DBS doped films. Since the anions are immobilised with the CP domain, the electroactivity loss of PSS and DBS were typically less those of small dopants.

As discussed previously, large dopants increase the interchain spacing between adjacent conjugated backbones and, thereby, increase the resistance of the resulting films.

Accordingly, the smallest dopant, ClO_4 , produces the film with the lowest resistance and, hence, the lowest impedance. However, the impedance of PEDOT/pTS was lower than that of films doped with BS, which is smaller than pTS by a methyl group. While specific cause is unclear, similar results have been previously reported [44].

The capacitance spectra of PEDOT films are almost identical regardless of dopants. Similarly, all PEDOT films provide the same low impedance at a frequency range between 100 Hz and 10 kHz, a range significant for neural communications. It can be seen that the PEDOT films have significantly higher capacitance than platinum in a low frequency range where capacitive impedance dominates. At high frequencies, the low resistance of the PEDOT have been directly translated into high neural recording sensitivity and selectivity as well as into high signal to noise ratio. Ludwig et al. [36] compared the quality of neural signals recorded from PEDOT and iridium electrodes in rat motor cortex over 6 weeks, and showed that PEDOT outperformed the counterpart in terms of signal-to-noise ratio and number of viable unit potentials. These electrochemical advantages make PEDOT a promising alternative for platinum electrodes at neuronal interface.

The results of PC12 attachment/neurite outgrowth, summarised in Table 4.5, indicate that films doped with ClO_4 and PSS support greater cell adhesion and neurite outgrowth. However, ClO_4 and PSS anions present higher intrinsic cytotoxicity than BS and pTS ions (see Table 4.5). This result does not agree with the PC12 and Schwann cell adhesion study performed by Fonner et al. [96] where more cells were attached on PPy/Cl Films than on PPy/pTS or PPy/PSS. It was claimed that the cytotoxicity of the leached dopant influenced the cell results. Degradation and subsequent dedoping of PPy films in aqueous conditions

have been widely reported [58, 208-211]. Yamato et al. [58] and Kros et al. [211] showed that PEDOT films provide superior stability over PPy films in biological redox conditions. The β positions of the pyrrole rings are susceptible to nucleophilic attacks [212] as well as defective α - β coupling [213]. The dioxy substituted structure of EDOT prevents the formation of β defects, and is less likely to degrade and release dopants.

Table 4.5: Summary of the PC12 adhesion and neurite outgrowth (see Figure 4.14 and 4.15), dopant cytotoxicity (see Figure 4.16 and 4.17) and qualitative surface roughness (observed from SEM images shown in Figure 4.7) studies

Sample	PC 12 adhesion (cells/cm ²)	Neurite outgrowth (Neurites/cm ²)	Dopant cytotoxicity (% inhibition @ 1mg/ml)	Qualitative roughness (+)
PEDOT/ClO ₄	9130 \pm 1045	1635 \pm 574	52.7 \pm 5.9	+++
PEDOT/BS	1228 \pm 767	36 \pm 43	12.7 \pm 3.1	+++
PEDOT/pTS	2250 \pm 648	303 \pm 115	21.3 \pm 3.9	+++
PEDOT/DBS	594 \pm 180	0	93.3 \pm 0.7	++
PEDOT/PSS	5490 \pm 751	1123 \pm 159	60.2 \pm 6.9	+

The amount of pTS and BS contained in a film is unlikely to be toxic to cells. The amount contained within a PEDOT film can be calculated from the total charge consumed in a similar manner described by Tallman et al. [214] where the film thickness is calculated from the charge applied. Assuming all charge applied is used in faradaic reactions (i.e. no ohmic loss), the weight of the film formed is estimated by the equation:

$$W_{CP} = \frac{q}{F} \times EW \quad \text{Equation 4.5,}$$

where q is the total charge applied across the surface area ($1\text{C}/\text{cm}^2 \times 0.332\text{ cm}^2 = 0.332\text{ C}$), F is the Faraday constant (96485.3365 C/mol) and EW is the amount of CP formed per mole of electrons. The detailed calculation of W_{CP} is shown in Appendix D. The amount of PEDOT/pTS formed is calculated at 0.29 mg . The corresponding amount of pTS in the film as determined from the XPS is 0.07 mg . Hence, the maximum concentration of pTS which can be released in PC12 culture is 0.46 mg/ml , assuming all pTS is released from the film. At twice the concentration in the L929 cytotoxicity study, pTS inhibited only $21.3 \pm 3.9\%$ of cell growth. Additional studies on the eluents using inductively coupled plasma mass spectrometry (ICP-MS) and ultraviolet–visible spectroscopy (UV-vis) (data not shown) indicated there was no significant difference in the amount of eluents from each film. Hence, the cytotoxicity of the dopant is not a major factor contributing to the poor PC12 performance of PEDOT/pTS.

It was thus anticipated that the nodular surface topography as well as the intrinsic toxicity of the dopant were the likely causes of the poor biological performance of pTS, BS and DBS. The microstructure of PEDOT films significantly changed with the choice of the dopant as shown in Figure 4.7. The qualitative surface roughness evaluated from SEM micrograms is summarised in Table 4.5. The surface roughness decreases with increasing dopant size. Similar trends have been reported for PPy films doped with different sized anions [96]. Films doped with ClO_4^- , BS, pTS are significantly rougher than films doped with bigger dopants such as DBS and PSS. Specifically, PEDOT/PSS films are almost as flat as TCP. Since the adhesion and outgrowth of PC12 cells are commonly tested on flat substrates, the topographical effect of PEDOT/PSS is not as significant as other films.

Perchlorate is almost as cytotoxic as PSS, and is significantly more cytotoxic than BS and pTS. Although the nanostructure of PEDOT/CIO₄ is as rough as films doped with BS or pTS (see 30000x micrographs in Figure 4.7), PC12 cells are adhered and differentiated well on the PEDOT/CIO₄. One possible explanation is the difference in microstructure patterns. At 1500x and 300x magnifications, PEDOT/CIO₄ presents a more uniform, "bubble-wrap" like, morphology with the bubbles sized between 10 ~ 100 μm. Surface morphologies of PEDOT/pTS and PEDOT/BS are less uniform, fuzzier, and more nodular. Since PEDOT films used in the PC12 assay are coated with laminin, an ECM protein that assists in the neuronal adhesion and outgrowth, the interaction between PC12 and PEDOT films can be affected by the focal adhesion. Chen et al. [39, 214] previously showed that the cell apoptosis can be geometrically promoted by using the focal adhesion islands 20 μm in diameter. The disperse nodular morphology of pTS and BS films may present similar apoptotic cues to the PC12 cells.

One of the main assumptions made in this chapter was that the chemical and physical structure of laminin coatings formed on PEDOT films are not affected by the nature of dopant. Although the formation of laminin layers were visually confirmed on each sample, further studies on the effects of doping anions on the geometry, chemistry, biofunctionality and biostability of the laminin coating are required to further understand the biological implications for the CP films. Other future studies will include quantification of surface roughness and features relative to cell attachment and growth properties.

4.5. Conclusion

It is clear that finding an optimal dopant type is strongly dependent on the critical performance required for a given electrode. While mechanical and electrical properties are determined primarily by the size of the doping anion, the biological performance appears to be related to a combination of surface morphology and material chemistry. While an increase in electrical performance and decrease in rigidity by choice of a small dopant might be desirable, it will clearly have a significant impact on the biological properties. This trade-off between ideal properties is an important consideration when selecting an optimal dopant. It is shown that some of the ions studied, BS and DBS perform at the extremes of examined properties, and are not considered potential dopants for neural applications. The remaining dopants pTS, PSS and ClO_4^- , have some benefits across electrical, mechanical and biological properties. As such the next chapter will redress this aim to delineate the effect of surface topography through varying film thickness across these film chemistries.

CHAPTER 5.

The effect of film thickness on the properties of electrodeposited CP

5.1. Introduction

It has been shown that neural cell survival and differentiation on PEDOT films is dependent on dopant type. However, cell growth variability on PEDOT doped with ions of similar chemistry indicates that dopant chemistry is not the sole factor contributing to biological properties. Despite the low cytotoxicity of pTS, films doped with this anion in Chapter 4 caused a greater inhibition of PC12 attachment and neurite outgrowth than those doped with more cytotoxic dopants such as ClO_4 and PSS. It was hypothesised that the nodular topography of PEDOT/pTS interrupted the adhesion of PC12 cells. This result signifies the importance of physical guidance cues in neural interaction. In order to improve the performance of CPs in neural applications, the studies conducted in this chapter aimed to control the physical properties of CPs by the passage of charge.

The physical properties of electrochemically synthesised CPs are greatly affected by the amount of charge applied during electropolymerisation. As more electrical energy is used to create a film, conservation of energy means that physical parameters such as surface area and film thickness also increase. A conventional approach for designing CPs for neural electrode applications is to increase the surface area to improve the electrical performance. Following this approach, a number of studies have been conducted to optimise the electrical properties of CPs through the passage of charge. Thick CP films have demonstrated significant electrical advantage as described below. However, the biological consequences associated with increasing film thickness have commonly been overlooked or have only been examined across a narrow charge range.

Yang et al. [35] compared the physical and electrochemical properties of PEDOT/CIO₄ films synthesised across varied deposition charge ranging from 1.8 μC (0.14 C/cm^2) to 43 μC (3.4 C/cm^2). The surface area generally increased when more charge was delivered, but plateaued at 11 μC (0.88 C/cm^2). This charge corresponded to a 4 μm thick film with the roughest surface and the lowest electrical impedance. While the biological performance of these films was not reported, adhesion of SY5H cells on surfactant-template ordered PEDOT/CIO₄ films was previously demonstrated by the same author [34].

Fonner et al. [96] showed that rat pheochromocytoma (PC12) and neurolemmocytes (Schwann cells) had higher viability on thin (0.0107 C/cm^2) PPy/PSS and PPy/pTS films than on thick (0.084 C/cm^2) films after 24 hour in culture. This result was interpreted in terms of the toxicity of the eluate. This is roughly one-tenth of the charge required to make the low impedance film by Yang et al [35]. A comparison across the broader range of charge is required to encompass the thick CPs commonly used in neural stimulation applications.

The main aim of this study was to understand the effects of deposition charge on physical, electrochemical and biological properties of CPs, and to determine the optimal film parameters which support neural cell adhesion and outgrowth. The main hypothesis of this study is that thin films having low surface roughness can improve the adhesion and outgrowth of neural cells. To test this hypothesis, PEDOT films were fabricated with four different thicknesses using a total charge of 1, 0.5, 0.1, and 0.05 C/cm^2 . Dopants used in this chapter were pTS, CIO₄, and PSS. In Chapter 4, films produced from 1 C/cm^2 of

PEDOT/pTS inhibited the PC12 adhesion whereas the same charge used to produce PEDOT/CIO₄ and PEDOT/PSS supported cell attachment and differentiation. In this chapter, a total of 12 sample variants were directly compared in terms of morphology, charge storage capacity, electrical impedance, and PC12 adhesion and neurite outgrowth.

5.2. Materials and Methods

5.2.1. Electrochemical synthesis of PEDOT

Three types of PEDOT films were prepared using the dopants, LiClO₄, pTS and PSS. Monomer solutions containing 0.05 M EDOT and 0.1 M dopant were prepared in 50/50 volume percent mixture of acetonitrile and water. The amount of each chemical used to make 2 ml solutions are shown in Table 5.1.

Table 5.1: Amount of chemicals used to make 2 ml of a monomer/dopant solution

Solutions	ACN (mL)	H ₂ O (mL)	EDOT (μL)	LiClO ₄ (mg)	NapTS (mg)	NaPSS (mg)
EDOT/CIO ₄	0.871	0.871	21.4	10.639		
EDOT/pTS	0.806	0.806			19.418	
EDOT/PSS	0.764	0.764				20.619

Electrodeposition was carried out in a silicone well system as described in Section 4.2.1. A platinum foil and a platinum probe array were used as the working and counter electrodes, respectively. A constant current of 0.166 mA, provided a current density of

0.5 mA/cm² and was applied through each well. Films with four different thicknesses were fabricated by varying the deposition time, as shown in Table 5.2. When the deposition was completed, each film was flushed with 150 µl DI water three times and then soaked in 300 µl DI water for 24 hours to remove excess electrolyte. Films were dried in a sealed chamber at room temperature for another 24 hours.

Table 5.2: Amount of charge used to fabricate samples with four different thicknesses

Current	0.5 mA/cm ²			
Deposition Time (s)	100	200	1000	2000
Total charge (C/cm ²)	0.05	0.1	0.5	1

5.2.2. Physical Changes Associated with the Deposition Charge Density

a) Macroscopic images

The optical changes (i.e. colour and transparency) associated with the film thickness were observed from stereoscopic images. PEDOT/pTS samples deposited with 0.05, 0.1, 0.5 and 1 C/cm² were imaged at 7.5x magnification using the Modular Routine Stereo Microscope (Leica M80, Germany).

b) SEM

All electron micrographs were taken with an acceleration potential of 5 kV using a Hitachi S3400 scanning electron microscope (Hitachi High-Technologies Co., Japan). To measure

the thickness of films, a platinum foil supporting CP films was mounted vertically on an L – shape metal bar on an aluminium stub with double sided carbon tape. The cross-sectional SEM of 0.1, 0.5 and 1 C/cm² films were taken at magnifications of 15,000x, 6,500x and 3000x. The thickness of 0.05 C/cm² films could not be measured with SEM. Morphological SEM of each film was taken at magnifications of 5000x and 1000x. Additionally, the macroscopic structure of 1 C/cm² films was examined at 100x magnification.

5.2.3. Charge Storage Capacity (CSC) and Electrochemical Stability

CV was performed according to methods described in Section 4.2.4. CV was recorded for 800 potential cycles between - 700 mV and +700 mV at the scan rate $\frac{dV}{dt}$ of 120 mV/s. The CSC was evaluated from the area enclosed by the voltammogram. Three samples of each dopant and thickness were tested. The CSC value was given by the average and standard deviation of three samples. The percentage CSC loss was evaluated by comparing the CSC of 1st and 800th cycles. It was generally considered that the smaller the CSC loss, the higher the electrochemical stability.

5.2.4. Electrochemical Impedance

EIS was performed according to methods described in Section 4.2.5. A single-frequency current, generating voltage amplitude of 30 mV, was applied simultaneously to the reservoir and the reference circuit. The impedance of the PEDOT/saline interface was

then evaluated by comparing the current amplitude and the voltage phase angle of these two circuits as illustrated in Figure 4.5. The impedance spectra were measured at room temperature (25 °C) over the frequency range from 1 Hz to 10 kHz. Three samples of each type were tested. The results were presented as the average and standard deviation of three samples.

5.2.5. PC12 Cell Attachment and Neurite Outgrowth

PC12 assays were also performed according to methods described in Section 4.2.6. Samples deposited with 0.05, 0.1 and 0.5 C/cm² were tested. The data for 1 C/cm² films were established in Chapter 4 are represented in this chapter for comparative purposes. The number of cells, neurites and the length of neurites were compared.

5.3. Results

5.3.1. Physical Changes Associated with the Deposition Charge Density

Regardless of the choice of a dopant, general appearance of electrodeposited films such as thickness and colour were largely determined by the amount of charge applied to form a film. Figure 5.1 shows the photo images of PEDOT/pTS films at various deposition charge. The colour of PEDOT films varied with the charge density and hence with the film thickness. As films grow thicker, they become more opaque and darker in colour. The colour of thin PEDOT films, synthesised with 0.05 or 0.1 C/cm², was translucent blue

whereas that of thick films, formed with 0.5 or 1 C/cm², was opaque dark blue. Similar colour changes were observed for all film chemistries.

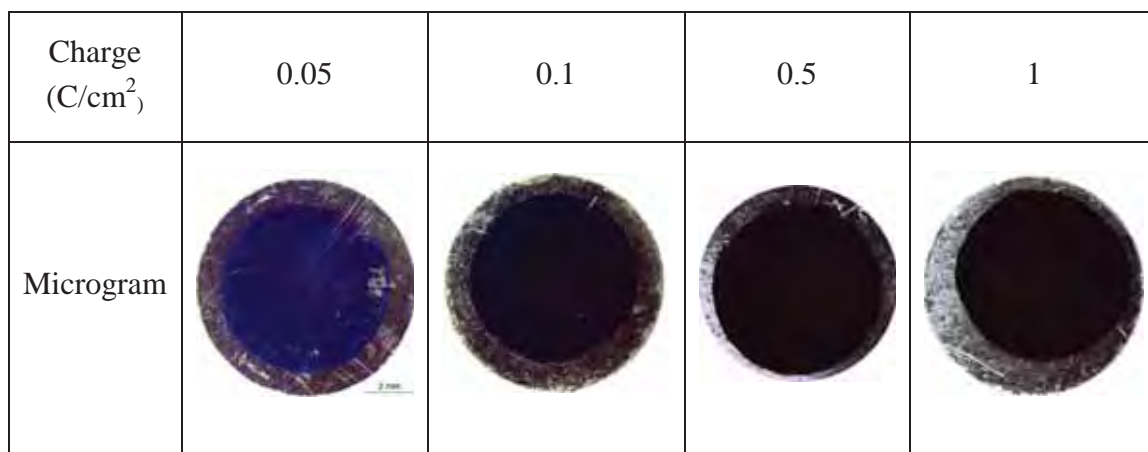


Figure 5.1: The colour and transparency of the PEDOT/pTS films changed with the amount of charge.

The thickness of PEDOT films measured from cross-sectional SEM was increased with increasing charge density as summarised in Table 5.3. Although there was some variability between dopant types it was observed that the charge used to deposit the film produced films of similar thickness, with the same order of magnitude, across all dopant variants.

Table 5.3: Film thickness of PEDOT/LiClO₄, pTS and PSS deposited with charges of 0.1, 0.5, and 1 C/cm²

	0.1 C/cm ² (μm)	0.5 C/cm ² (μm)	1 C/cm ² (μm)
PEDOT/ClO ₄	0.10 ± 0.02	2.11 ± 0.28	6.52 ± 0.62
PEDOT/pTS	0.12 ± 0.02	2.23 ± 0.39	6.27 ± 0.87
PEDOT/PSS	0.10 ± 0.02	2.89 ± 0.17	5.90 ± 0.31

This transition in translucency between thin and thick films is not only represented in the stereoscopic images, but is also evident in the scanning electron micrographs shown in Figures 5.2, 5.3 and 5.4. The SEM images of 0.05 and 0.1 C/cm² films, shown in Figure 5.2 ~ 5.4 (a) and (b), exhibit striations which are indicative of the platinum substrate, clearly visible through the overlying CP layer. As the films get thicker, striations are covered with the typical nodular morphology of CPs. Above the applied charge of 0.5 C/cm², only the nodular structures were present on the films indicating the transition from transparent to opaque film.

The size of nodules and, therefore, the surface roughness of PEDOT films were influenced both by the charge density, a fabrication parameter, and by the doping ion, a constituent. While there was a general observation that higher charge density resulted in bigger nodules, the overall morphology of films, especially 1 C/cm² films, was largely influenced by the choice of dopant. At all thicknesses, PEDOT/PSS films were flatter than films doped with ClO₄ or pTS. Thick PEDOT/ClO₄ films exhibited 'bubble-wrap' like morphology with an average bubble diameter of 40 µm. This unique morphology is well illustrated in Figure 5.2 (e). The 1 C PEDOT/pTS film was comprised of nodules, with an average diameter of 15 µm, that are randomly stacked together to form a gorge like structure shown in Figure 5.3 (d).



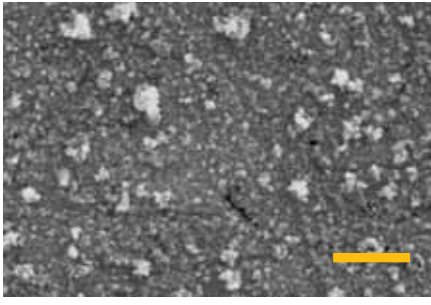
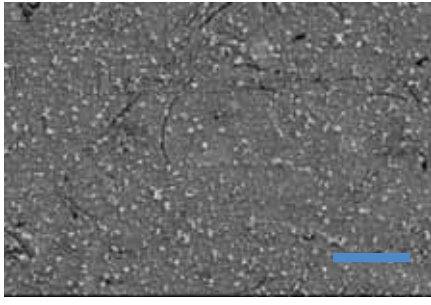
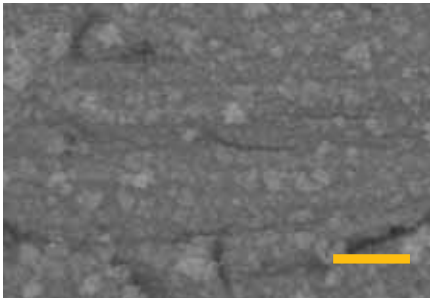
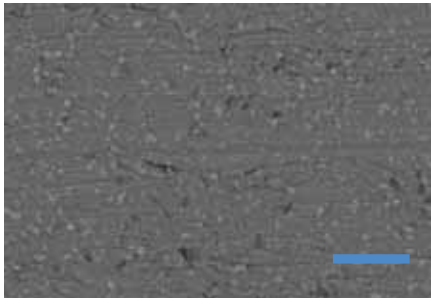
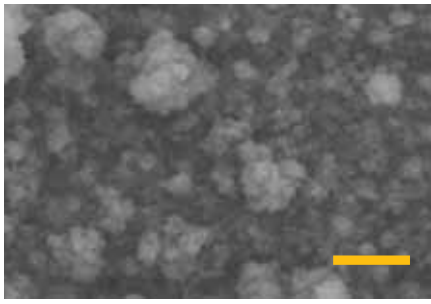
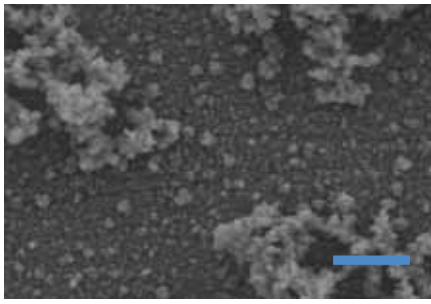
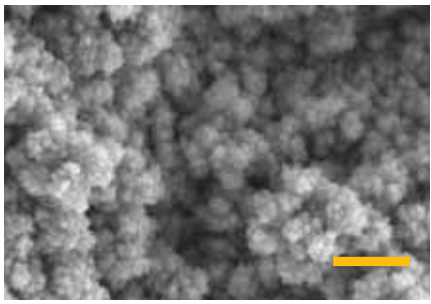
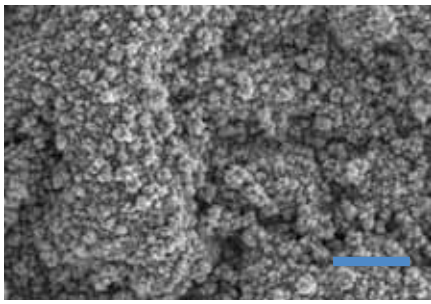
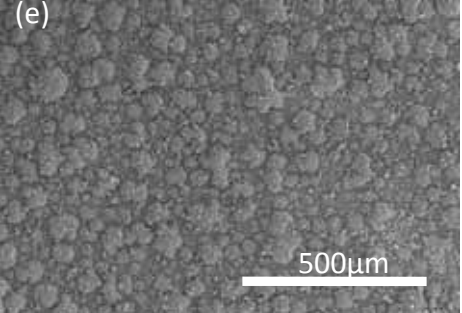
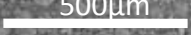
		5000x ( = 5 μm)	1000x ( = 25 μm)
LiClO₄	(a) 0.05 C/cm^2		
	(b) 0.1 C/cm^2		
	(c) 0.5 C/cm^2		
	(d),(e) 1 C/cm^2		 <div>  <div> (e) SEM of 1 C/cm^2 PEDOT/LiClO₄ at 100x magnification  </div> </div>

Figure 5.2: Scanning electron micrograms of PEDOT/LiClO₄ deposited with charges of (a) 0.05, (b) 0.1, (c) 0.5 and (d) 1 C/cm^2 . Pictures were taken at 5000x and 1000x magnifications. Picture (e) is taken on 1 C/cm^2 film at 100x.


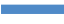
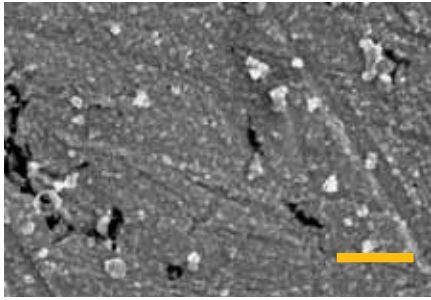
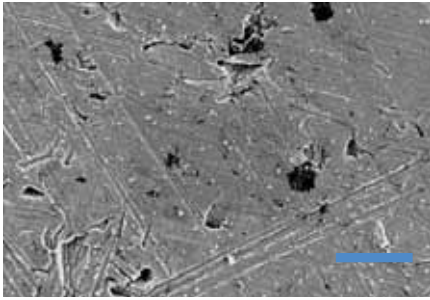
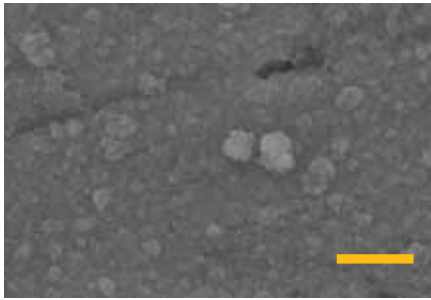
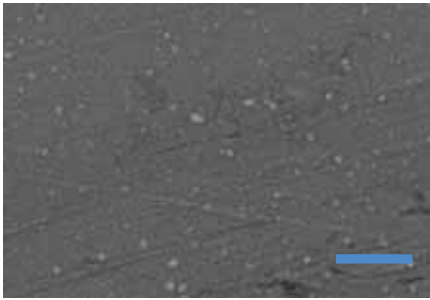
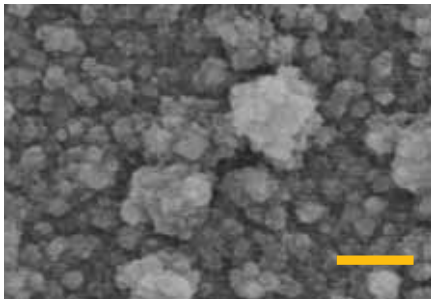
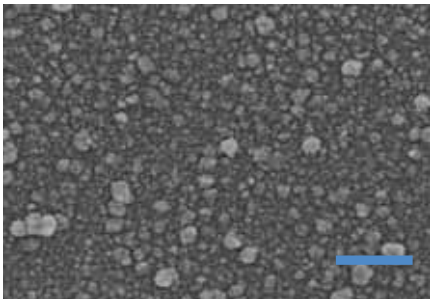
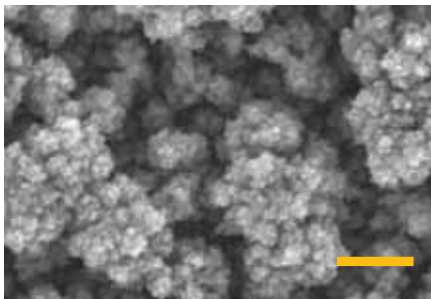
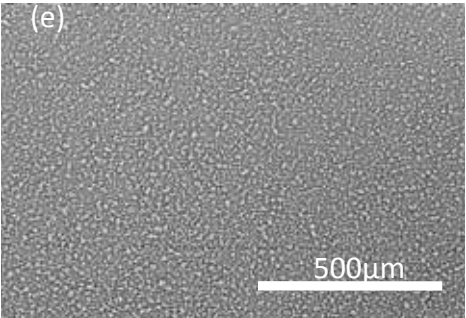
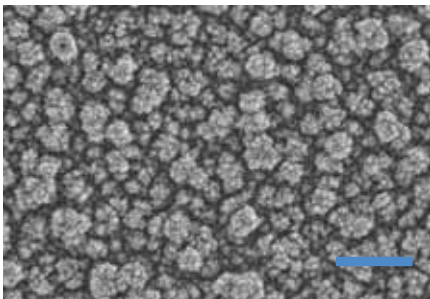
		5000x ( = 5 μm)	1000x ( = 25 μm)
pTS	(a) 0.05 C/cm^2		
	(b) 0.1 C/cm^2		
	(c) 0.5 C/cm^2		
	(d),(e) 1 C/cm^2	 <div> <p>(e) Macroscopic SEM of 1 C/cm^2 PEDOT/pTS at 100x magnification</p>  </div>	

Figure 5.3: Scanning electron micrograms of PEDOT/pTS deposited with charges of (a) 0.05, (b) 0.1, (c) 0.5 and (d) 1 C/cm^2 . Pictures were taken at 5000x and 1000x magnifications. Picture (e) is taken on 1 C/cm^2 film at 100x.



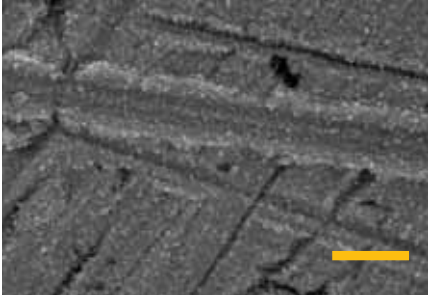
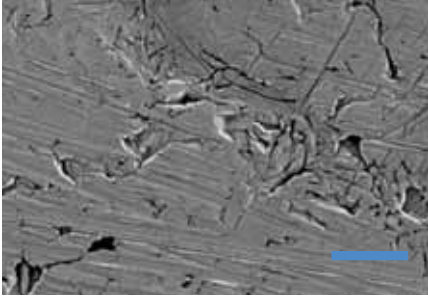
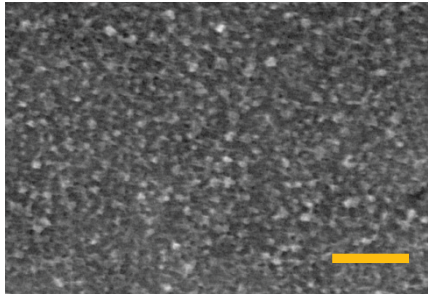
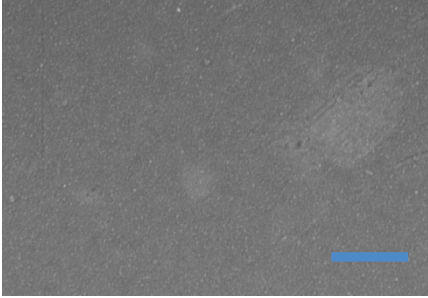
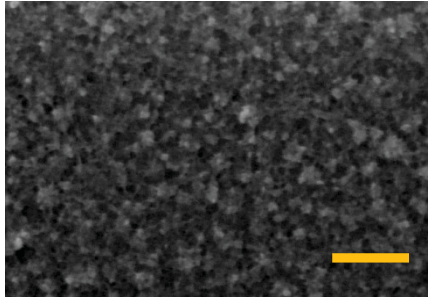
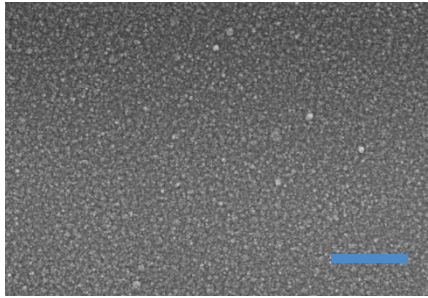
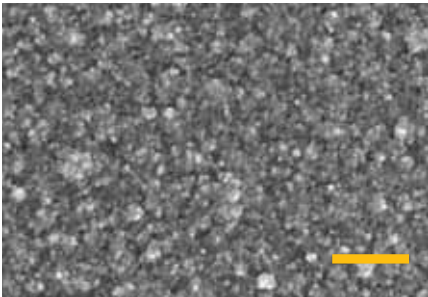
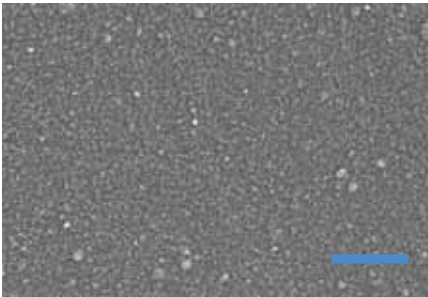
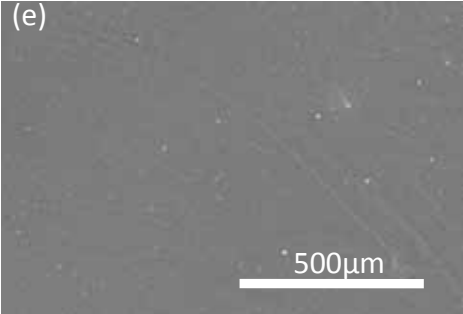
		5000x ( = 5 μm)	1000x ( = 25 μm)
PSS	(a) 0.05 C/cm^2		
	(b) 0.1 C/cm^2		
	(c) 0.5 C/cm^2		
	(d),(e) 1 C/cm^2		 <div>  <p>(e) Macroscopic SEM of 1 C/cm^2 PEDOT/PSS at 100x magnification</p> <p>500μm</p> </div>

Figure 5.4: Scanning electron micrograms of PEDOT/PSS deposited with charges of (a) 0.05, (b) 0.1, (c) 0.5 and (d) 1 C/cm^2 . Pictures were taken at 5000x and 1000x magnifications. Picture (e) is taken on 1 C/cm^2 film at 100x.

5.3.2. Charge Storage Capacity (CSC) and Electrochemical Stability

Conducting polymers are pseudo-capacitors that allow concurrent resistive and capacitive charge transfer. In cyclic voltammetry, purely capacitive and resistive charge transfers are respectively indicated by square and linear curves. The cyclic voltammograms of PEDOT films, shown in Figure 5.5, were generally trapezoids, representing the combined geometry of a linear and a square. One exception was PEDOT/PSS films deposited with 1 C/cm^2 of charge. Instead of trapezoids exhibited in other samples, thick PEDOT/PSS films showed concave curves in a negative voltage range and a distinctive oxidation peak at -50 mV and a reduction pair at -151 mV .

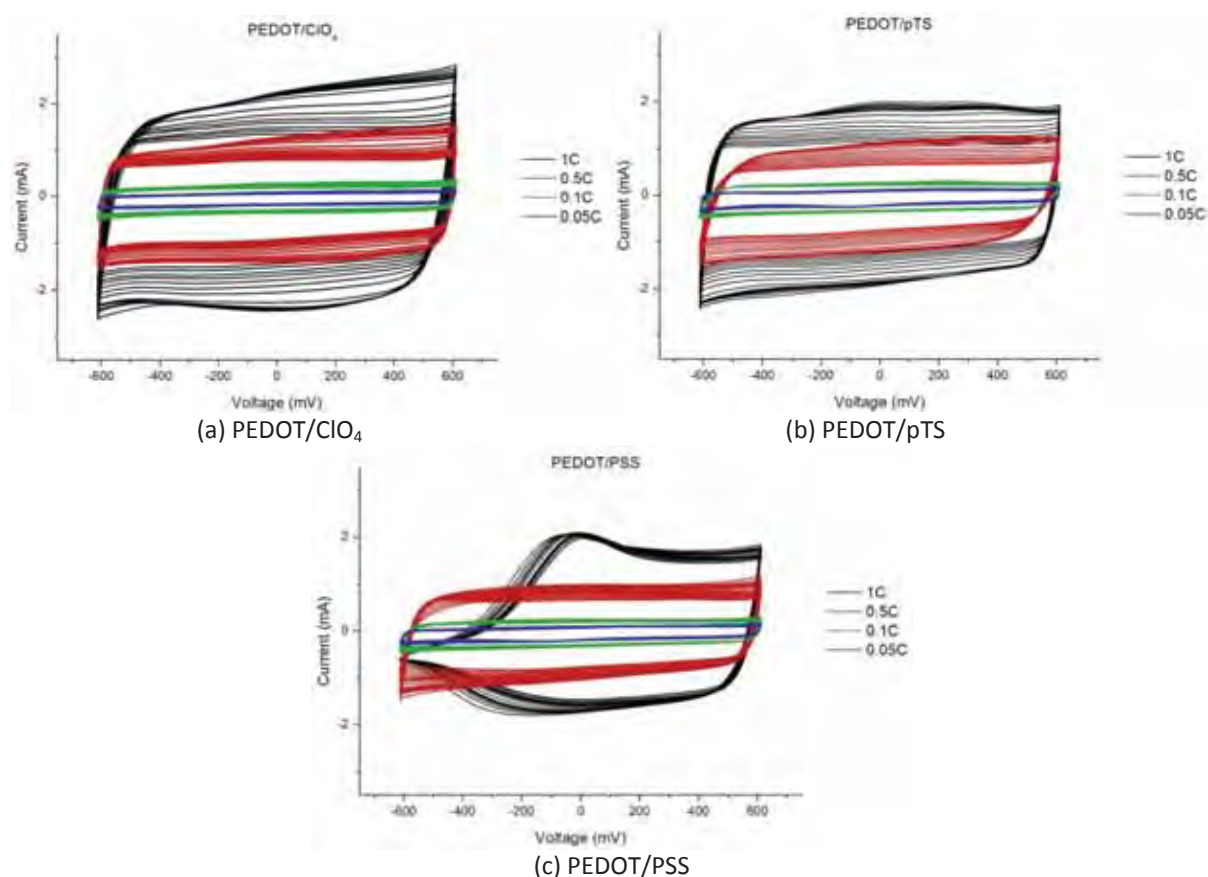


Figure 5.5: Cyclicvoltammograms of (a) PEDOT/CIO₄, (b) PEDOT/pTS, and (c) PEDOT/PSS. Colour indicates the charge applied to form a film. black: 1 C/cm^2 , red: 0.5 C/cm^2 , green: 0.1 C/cm^2 and blue: 0.05 C/cm^2 . Each curve having the same colour indicates the cycle number. As moving inward from the outermost curve, each curve indicates 1st, 10th, 20th, 30th, 40th, 50th, 100th, 200th, 300th, 400th, 500th, 600th, 700th, and 800th cycle.

The amount of charge transferred during each cycle is typically analysed by the charge storage capacity (CSC), which is measured by the area enclosed within a single cyclic voltammogram. The size and percentage loss of CSC, which respectively indicates the electrochemical performance and stability, is depicted and tabulated in Figure 5.6 and Table 5.4

Table 5.4: The initial and the final charge storage capacity (CPC) of films and corresponding loss in CSC during 800 cycles

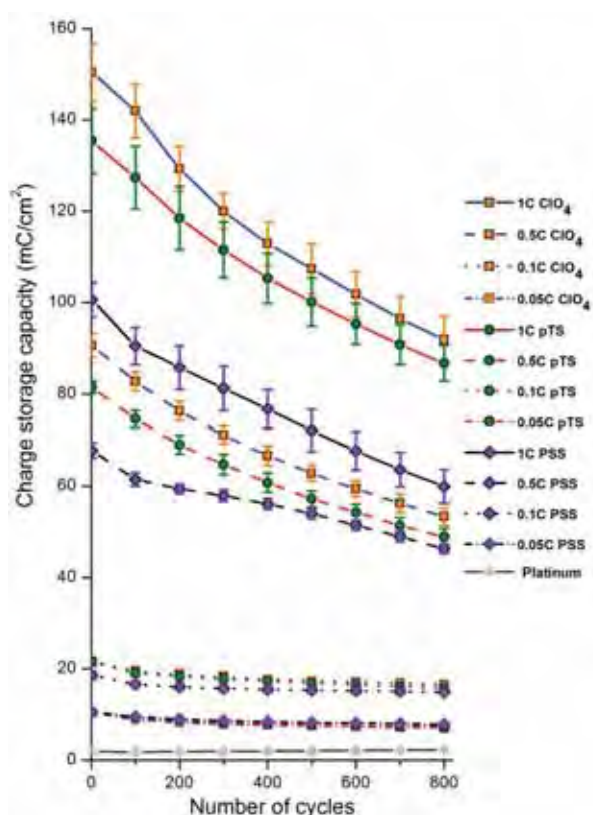


Figure 5.6: Changes in charge storage capacity over 800 cycles.

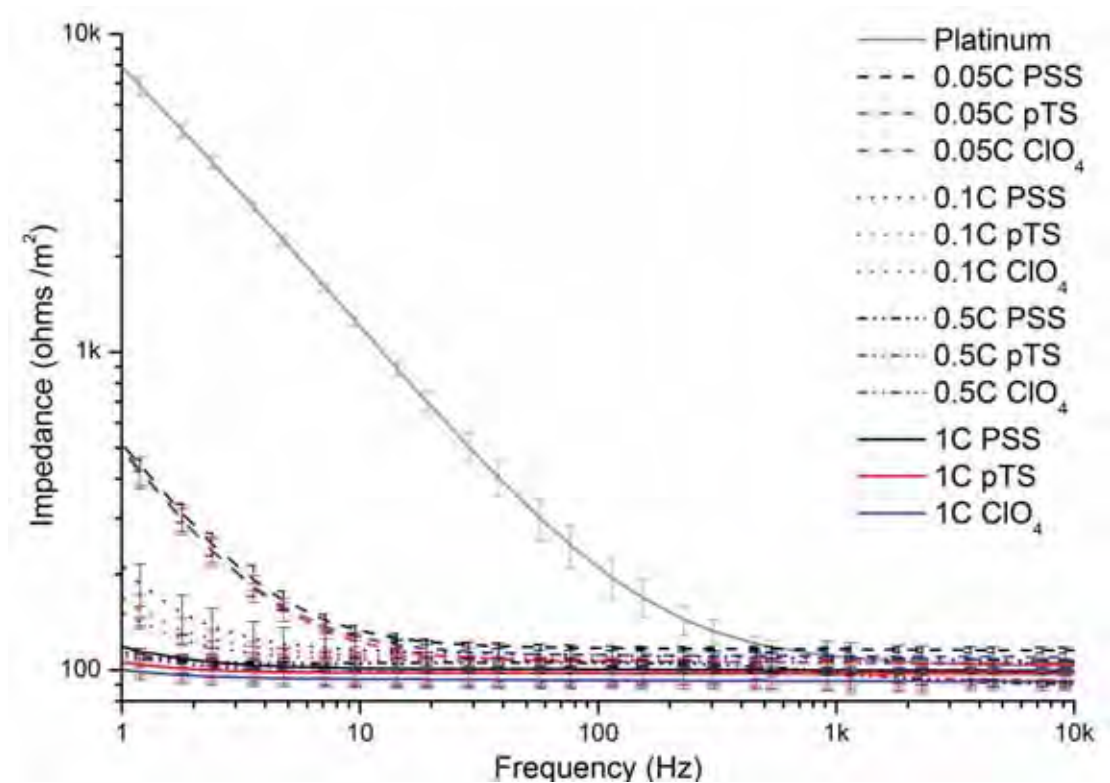
Charge [C/cm ²]	Film	Initial CSC [mc/cm ²]	Final CSC [mc/cm ²]	CSC Loss [%]
1	ClO ₄	150.47 (± 6.29)	91.88 (± 5.08)	38.9 ± 4.2
	pTS	135.43 (± 7.16)	86.71 (± 3.90)	36.0 ± 4.4
	PSS	100.04 (± 4.30)	68.23 (± 4.33)	31.7 ± 4.5
0.5	ClO ₄	90.66 (± 2.54)	53.34 (± 1.92)	41.2 ± 2.7
	pTS	81.49 (± 1.37)	48.91 (± 1.78)	40.0 ± 2.41
	PSS	67.78 (± 1.59)	46.35 (± 1.03)	31.6 ± 2.21
0.1	ClO ₄	21.71 (± 0.39)	16.59 (± 0.49)	23.6 ± 2.7
	pTS	21.37 (± 0.71)	15.83 (± 0.38)	25.9 ± 3.0
	PSS	18.62 (± 1.01)	14.93 (± 0.6)	19.8 ± 5.4
0.05	ClO ₄	10.50 (± 0.70)	7.34 (± 0.45)	30.1 ± 6.3
	pTS	10.43 (± 0.76)	7.1 (± 0.88)	31.9 ± 9.8
	PSS	10.52 (± 0.63)	7.84 (± 0.37)	25.5 ± 5.7
-	Pt	1.89 (± 0.43)	2.28 (± 0.15)	-

There were two general trends observed regarding the electrochemical performance of PEDOT films. Firstly, films formed with higher charge density had higher CSC. Secondly, with an exception of the 0.05 C/cm² films having similar CSC values regardless of dopants,

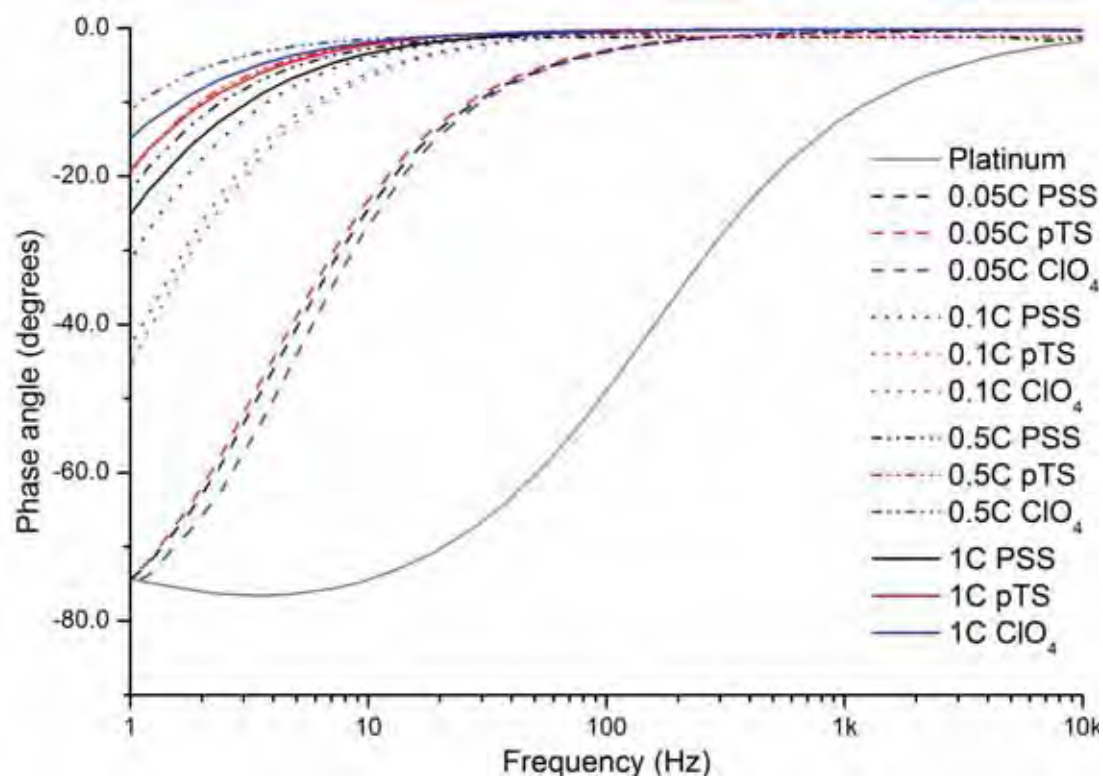
the CSC of a film increased in an order of decreasing dopant size from PSS, pTS to ClO_4 . The initial CSC of 1 C/cm^2 ClO_4 film, $150.47 \pm 6.29 \text{ mC/cm}^2$, was roughly fifteen times higher than that of a 0.05 C/cm^2 film, $\sim 10.5 \text{ mC/cm}^2$, and more than seventy five times higher than that of platinum, $1.89 \pm 0.43 \text{ mC/cm}^2$. It can be seen in Figure 5.5 that the CSC of the 1 C/cm^2 PSS film is significantly less than the CSC of the other 1 C/cm^2 films. This was the direct result of the non-trapezoidal cyclovoltammogram, which significantly reduced the CSC in the negative voltage range.

5.3.3. Electrochemical Impedance

Figure 5.7 (a) and (b), show the electrical impedance and corresponding phase angle measured at frequencies ranging from 1 Hz to 10 kHz. The electrical impedance was shown to decrease with increasing thickness. All CPs presented significant electrochemical advantage over platinum electrodes. This advantage was more apparent at low frequencies where the capacitive reactance is more prominent. The capacitive reactance is inversely proportional to the frequency and capacitance. At 1 Hz, The impedance of 0.05 C/cm^2 films were an order of a magnitude lower than that of platinum. The magnitude was further reduced by increasing the PEDOT thickness from the 0.05 to 0.5 C/cm^2 films. No significant difference was observed between the films produced from 0.5 and 1 C/cm^2 of deposition charge. Among the films deposited with the same amount of charge, ClO_4 films, shown as blue lines, exhibited lowest impedance followed by pTS (red lines) and PSS (black lines). The smaller phase angles plotted in Figure 7.5 (b) indicate that the reduced impedance was the result of high capacitance.



(a)



(b)

Figure 5.7: (a) Electrical impedance and (b) corresponding phase angle of films having different thicknesses.

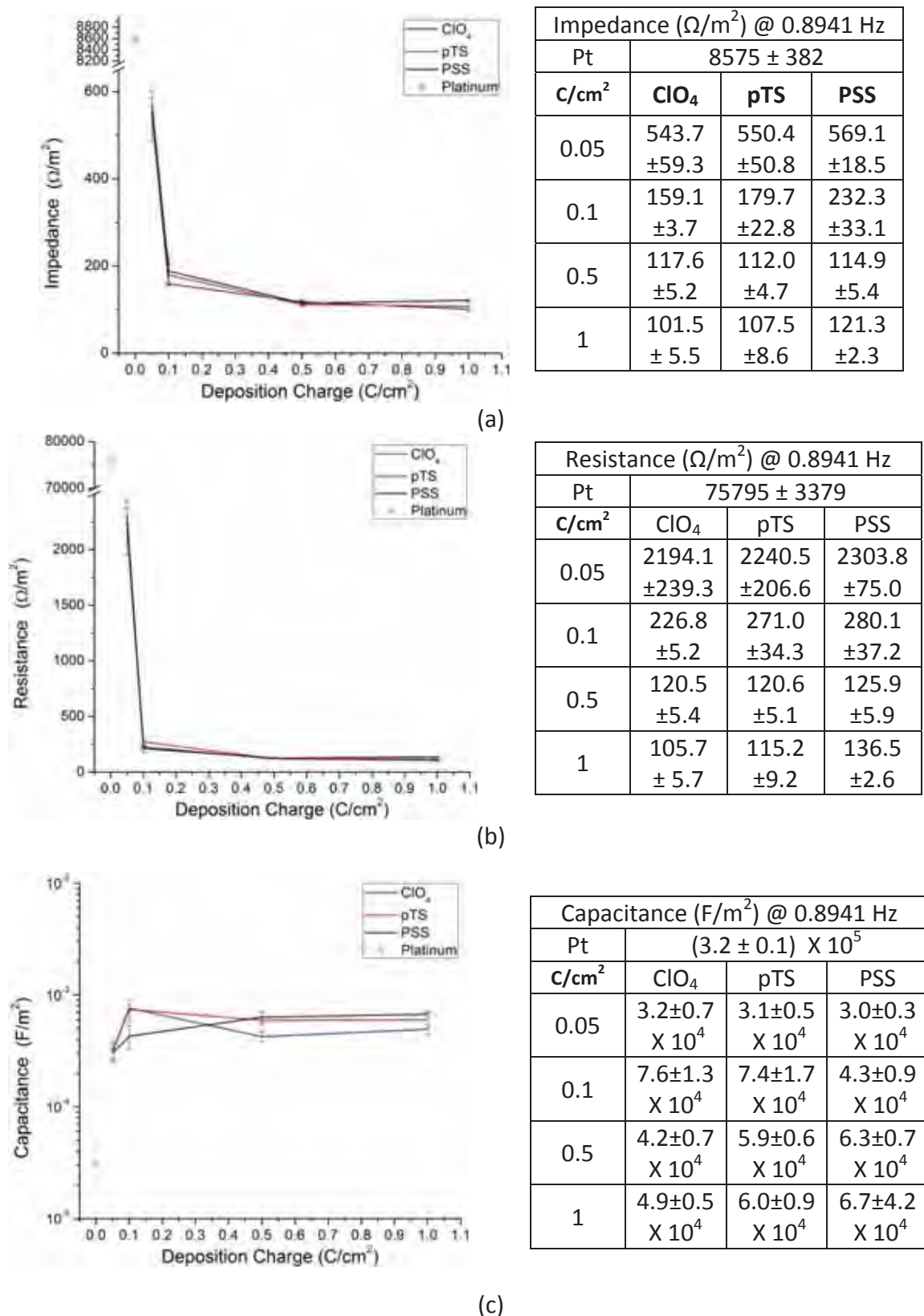


Figure 5.8: Graphs of (a) electrical impedance, (b) resistance, and (c) capacitance versus deposition charge. Data was measured at the lowest frequency, 0.8941 Hz. PEDOT samples were prepared with ClO_4 , pTS, or PSS at the deposition charge of 0.05, 0.1, 0.5 and $1 \text{ C}/\text{cm}^2$. Bare platinum samples were also tested as a reference. Three samples of each type were tested.

Figure 5.8 (a)-(c) shows the change in electrical impedance, resistance, and capacitance associated with changes in deposition charge. From Figure 5.8 (a), the data shows that electrical impedance drops quickly when the charge used to produce PEDOT is increased from 0.05 to 0.1 C/cm². A more gradual drop is observed from 0.1 to 0.5 C/cm². Only a very slight difference in impedance is found between samples deposited with 0.5 and 1 C/cm². From Figure 5.8 (b) and (c), both resistance and capacitance is found to increase rapidly with increasing deposition charge from 0.05 to 0.1 C/cm². This rapid decrease in resistive impedance and conductive reactance produced a relatively small impedance for 0.1 C/cm² films. From 0.1 C/cm² onwards, the resistance gradually decreased in a similar pattern to the impedance graph. The capacitance of PEDOT/CIO₄ and PEDOT/pTS decreased from 0.1 to 0.5 C/cm², but the difference was statistically insignificant. The reduction in the resistive impedance was greater than the gain in the capacitive reactance. Hence, the impedance of 0.5 C/cm² films was lower than that of 0.1 C/cm² films.

5.3.4. PC12 Cell Attachment and Neurite Outgrowth

The effect of the film thickness on neurite outgrowth was investigated by culturing PC12 cells on laminin coated PEDOT films in NGF containing medium for 96 hours. Figure 5.9 shows typical micrographs demonstrating neurite extension on PEDOT samples at the conclusion of the study. For quantitative analysis of neurite outgrowth, 36 images (4 images x 3 samples x 3 repeats) of each PEDOT type and thickness were evaluated in terms of the length and number of neurites as well as the size of PC12 cell bodies.

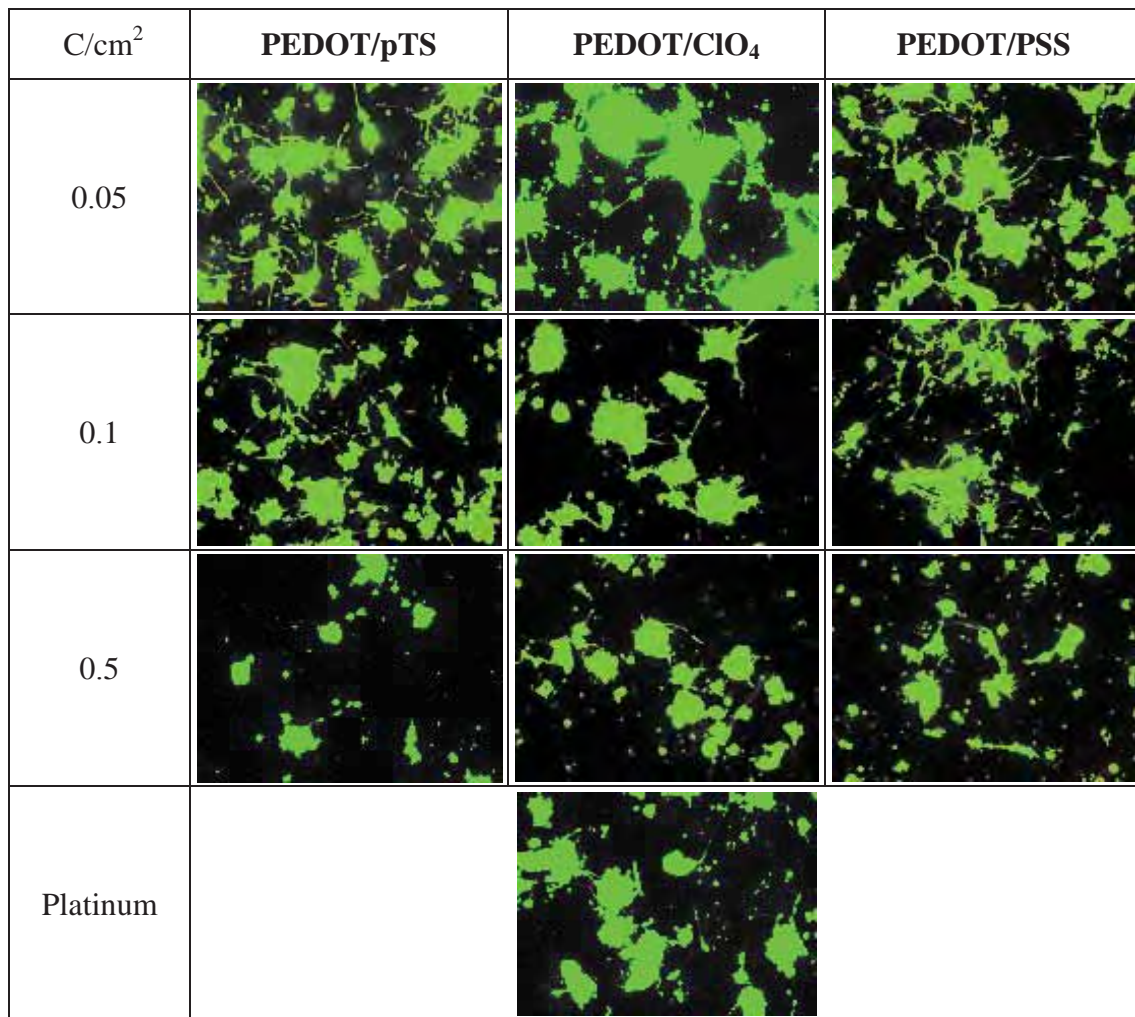
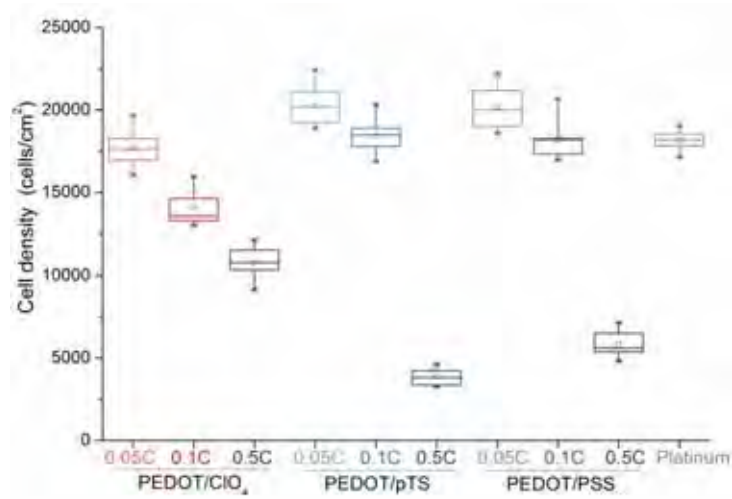
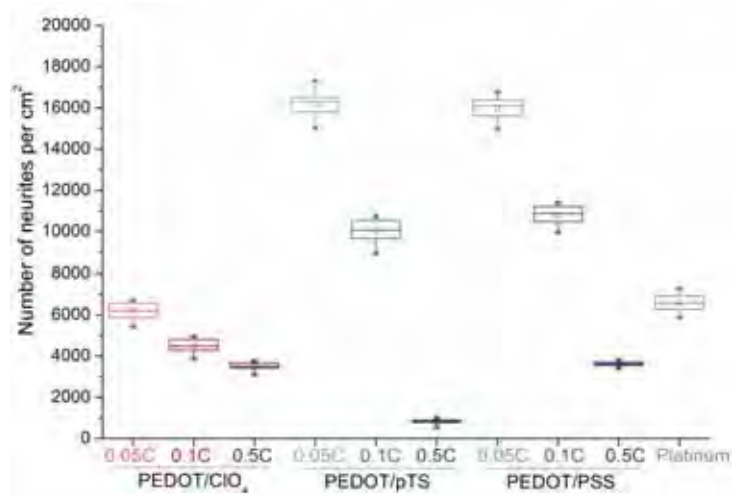


Figure 5.9: Neurite growth in PC12 cells on PEDOT substrates.

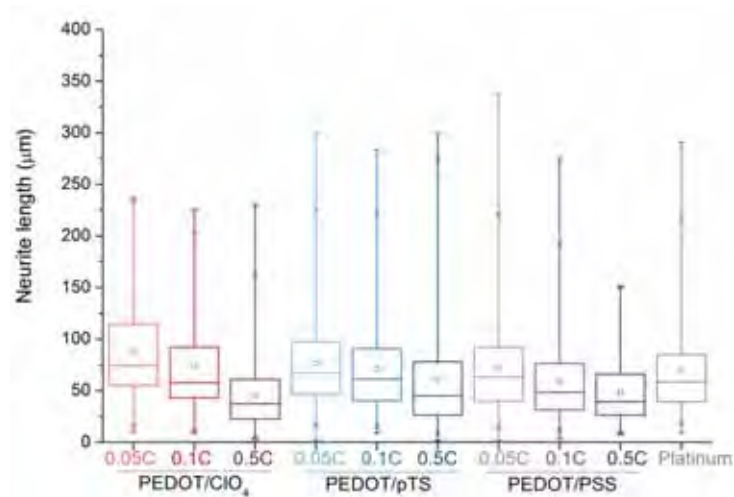
The number and length of neurites and number of PC12 cell bodies are presented in the box and whisker plots shown below in Figure 5.10. Thin pTS and PSS films, deposited with 0.05 or 0.1 C/cm^2 , showed significantly more neurite growth than other films in the test. However, the numbers of neurites on pTS and PSS films diminished rapidly from 0.1 C/cm^2 films to 0.5 C/cm^2 films. At 0.5 C/cm^2 , there were more neurites on ClO_4 films than pTS films. Data for 1 C/cm^2 films can be found in Chapter 4. Thicker films made with charge greater than 0.5 C/cm^2 did not provide biological benefits over conventional platinum electrodes. All thin films made with charge less than 0.1 C/cm^2 , with an exception of 0.1 C/cm^2 ClO_4 , showed greater PC12 cell attachment and number of neurite outgrowth than the platinum control.



(a)



(b)



(c)

Figure 5.10: Results of 96 h pc12 adhesion and neurite outgrowth assay. (a) Number of cells adhered on each sample, (b) Number of neurites found on each sample, and (c) length of neurites outgrown from PC12 cells. Data was collected over three samples of each type in three individual tests ($n = 3 \times 3 = 9$).

To eliminate the bias which arises from the different number of PC12 cells attached on each substrate, neurite outgrowth was further analysed in terms of per attached PC12 cell as shown in Figure 5.11. The length of neurite extending from a cell was shown to decrease with increasing film thickness. However, the number of neurites per cell was not affected by the thickness, but was rather dependent on the choice of a dopant. PEDOT/CIO₄ films have a similar number of neurites per cell for all thicknesses. Conversely, as the PEDOT/pTS film was increased in thickness, the number of neurites decreased. More neurites were shown on 0.05 C/cm² PEDOT/PSS than the thicker films of the same chemical composition.

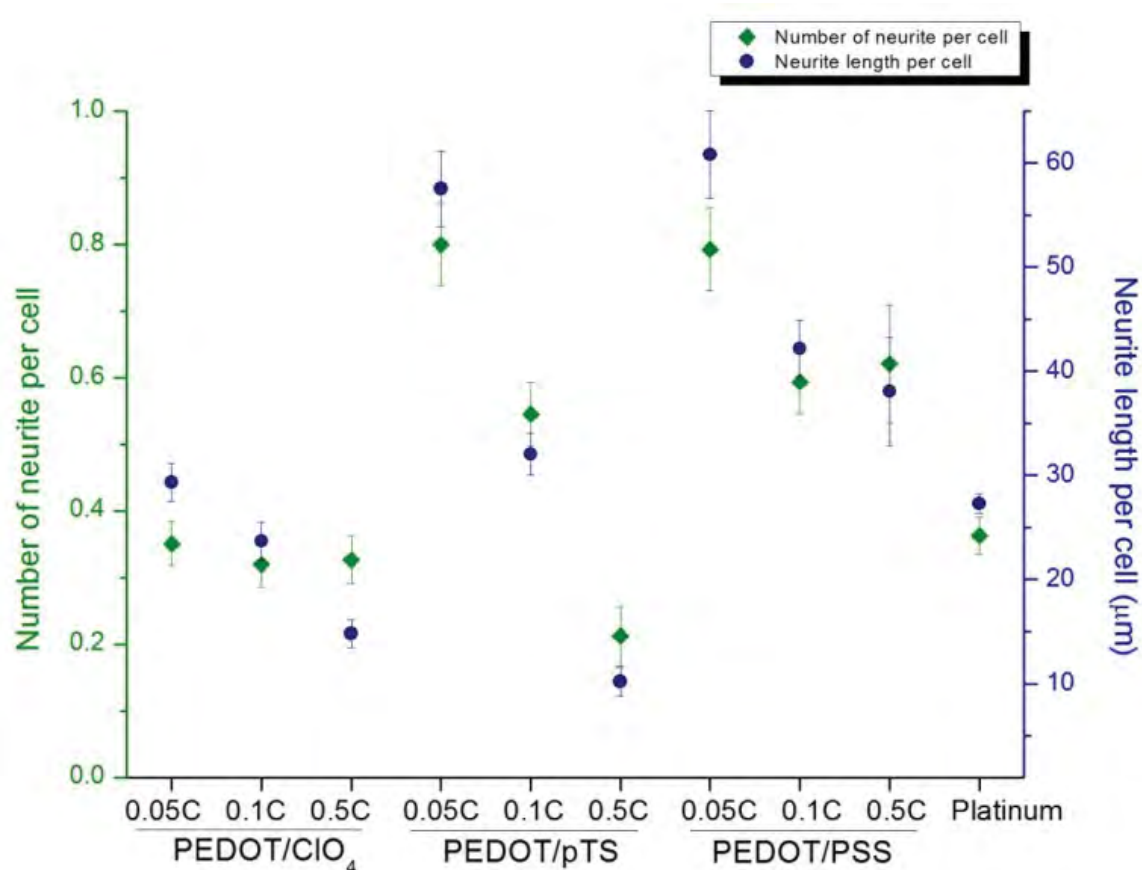


Figure 5.11: Graph of (1) number of neurite per attached PC12 cell (shown in green), (2) neurite length per attached PC12 cell (shown in blue). The number of PC12 cells attached on each sample is shown in Figure 5.10 (a).

5.4. Discussion

It is shown that the physical properties of PEDOT including surface morphology, electrical properties and biological interactions can be directly controlled by the amount of charge used during film deposition. As the charge delivered is increased, both film thickness and nodularity are increased, however the degree of nodularity is strongly dependent on the dopant chemistry. This has direct impact on both the electrical properties and neural cell interactions.

To explore the relationship between film thickness and deposition charge in light of the nodularity of different PEDOT films, it is important to understand the theory. The thickness δ of CPs can be mathematically postulated by the following equation [215]:

$$\delta = \frac{jt}{F} \times EW \times \frac{1}{\rho}, \quad (\text{Equation 5.1}),$$

where j is the current density (A/cm^2), t is the deposition time (s), F is the Faraday constant (96,485.3365 C/mol). EW is the equivalent weight of CP formed per mole of electrons (g/mol), and ρ is the film density (g/cm^3), which is estimated at $1.64 \text{ g}/\text{cm}^3$ for PEDOT, based on a structural model [200]. The EW is calculated by dividing the MW of a single monomer-dopant unit by the number of electrons consumed to form the unit. Two protons per monomer are consumed in the electrochemical polymerisation of the five-membered heterocyclic aromatics [216]. A fraction of electron per monomer is consumed in the doping process (i.e. oxidation) and EQCM studies estimate this at 0.33 of an electron [199, 217]. In an ideal case, EW is given by the following:

$$EW = \frac{(MW \text{ of } EDOT - 2 \times MW \text{ of } H) + 0.33 (MW \text{ of a doping anion})}{2 + 0.33}, \quad (\text{Equation 5.2}).$$

The detailed calculation of EW is shown in Appendix D. Table 5.5 presents the theoretical thickness and a qualitative surface roughness obtained from SEM images shown in Figures 5.2 - 5.4.

There is significant variation between the theoretical and measured thicknesses. At low deposition charge below 0.1 C/cm^2 , it is shown that the films did not grow as fast as theoretically predicted. It is hypothesised that this is because the theoretical film thickness assumes uniform 3D growth and does not account for changes in structure and chain packing which result from the various dopants. In practice, film formation is a two-step process involving formation of a planar 2D layer across the substrate, followed by 3D growth which is strongly influenced by nucleation points and chain packing. The electrocrystallisation theory based on the Stranski-Krastanov model predicts that the initial formation of a 2D film (i.e. films growing along the substrate) is energetically favoured [218]. It is clear that the initial stages of CP growth preferentially form a 2D layer [219], followed by 3D growth from non-uniform nucleation points. As a result the theoretical thickness of PEDOT is initially higher than the measured thickness, but as charge continues to polymerise the CP the theoretical thickness drops below the measured thickness. Hence, it is expected that the thin films, those formed with less than 0.1 C/cm^2 , may be close to 2D layers. This is also in agreement with the qualitative observations of surface roughness, where 0.05 and 0.1 C/cm^2 films were invariably smooth regardless of the dopant choice.

Table 5.5: Changes in theoretical and measured thickness, and qualitative surface roughness with deposition charge. SE is shown in the bracket

Deposition charge (C/cm ²)	Theoretical thickness (μm)			Measured thickness (μm)			Qualitative surface roughness (+)		
	ClO ₄	pTS	PSS	ClO ₄	PTS	PSS	ClO ₄	pTS	PSS
0.05	0.23	0.27	0.27	-	-	-	+	+	+
0.1	0.47	0.53	0.54	0.1 (0.02)	0.12 (0.02)	0.1 (0.02)	+	+	+
0.5	2.35	2.67	2.71	2.11 (0.28)	2.23 (0.39)	2.89 (0.17)	+++	+++	++
1	4.69	5.33	5.41	6.52 (0.62)	6.27 (0.87)	5.9 (0.31)	++++	++++	++

The thickness of 0.5 C/cm² films was close to the theoretically predicted values, correlating with the observed increase in surface roughness. Finally, 1 C/cm² films were thicker than the theoretically calculated values for all PEDOT variants. Stankovic et al. [220] has suggested that decreases in density result in films which are thicker than the theoretical estimations. It is likely that film density is reduced by the non-uniform 3D growth that produces high nodularity. Conversely, doping with PSS, helps to reduce the surface roughness and as a result the theoretical thickness of these films produced with larger amounts of charge is close to the measured values.

The CV and EIS results confirm the electrical advantage of thick CP films. Films deposited with 1 C/cm² provide the highest charge storage capacity and the lowest electrical impedance. This concurs with findings by Yang et al. [35] which suggest that PEDOT/ClO₄ deposited with 0.88 C/cm² provides both the highest surface area (which then remains constant for increased charge) and the lowest impedance. Since the surface area is directly proportion to the capacitance, thicker and hence more nodular films can pass a greater amount of charge. Additionally, CPs are pseudocapacitors that can store charge

through intercalation, electrosorption and Faradaic processes [221]. Bobacka et al. [222] showed that both pseudocapacitance and double layer capacitance of PEDOT films increases linearly with increasing deposition charge. Accordingly, the CSC tabulated in Table 5.4 increased with increasing film thickness. Due to the bulky size of PSS anions, CPs doped with PSS undergo cation (i.e. Na^+) transfer during faradaic reactions [223, 224]. This in combination with the smoother surface of PEDOT/PSS results in the relatively smaller CSC of these films.

CPs present a significant electrochemical advantage over platinum electrodes. In these studies PEDOT films present a 5 to 80 times higher CSC and at least one order of magnitude lower impedance at 1 Hz than platinum. By altering the deposition charge from 0.05 C to 1 C/cm², surface roughness and hence electrochemical properties were greatly increased, but a trade-off in biological properties was apparent. The PC12 assays conducted in this chapter indicate that the number of cells and neurites decrease with increasing film thickness. There are a few factors that may explain poor cell interactions with thick films.

In a standard cell culture, the volume of water, which acts as a percolating agent through a CP film, is constant. Therefore, the leachate concentration at equilibrium is likely to be determined by the amount of dopant, since these hydrotropic ions readily dissolve in water. Having more dopant in the film, thick CP films would impart a greater toxic effect than thin films, although this is obviously dependent on the relative toxicity of these ions. This notion of the toxicity of thicker films was suggested by Fonner et al. [96] who reported lower viable numbers of PC12 and Schwann cells on thick PPy/pTS films (0.65

μm) than on thin films ($0.15\ \mu\text{m}$). However, this result is likely to be influenced by the poor stability of PPy in aqueous conditions [58]. PPy films are easily degraded or reduced in water and could elute out dopants and other degradation products that are toxic to cells.

Unlike PPy, PEDOT films are highly stable in aqueous solutions [58] and are less likely to impart degradation related toxicity. Hence, the influence of the physical cues on cell interaction is expected to be dominant. The main hypothesis of this study was that thin PEDOT films having low surface roughness can improve the adhesion and outgrowth of neural cells. The result of the PC12 assays support this hypothesis with attachment and neurite outgrowth increasing with decreasing film thickness. Thin films made with charge less than $0.1\ \text{C}/\text{cm}^2$ performed better than platinum. In contrast, thicker films made with charge greater than $0.5\ \text{C}/\text{cm}^2$ do not provide biological benefits over platinum.

Among the films tested, $0.05\ \text{C}/\text{cm}^2$ PEDOT/pTS promoted the most significant cell adhesion and neurite outgrowth. In chapter 4, pTS was found to be less toxic than ClO_4 and PSS. However, previously, PEDOT/pTS supported lower densities of cells than PEDOT/ ClO_4 and PEDOT/PSS. This result accentuates the importance of the surface topography on cell adhesion and growth. The islands of surface nodules disappear with decreasing thickness, and as a result the thin pTS films having a flat surface and low intrinsic toxicity outperformed other flat films made with more cytotoxic dopants. Future studies will include quantification of surface roughness and features relative to cell attachment and growth properties.

The adhesion and outgrowth of neural cells on chronic electrode implants are crucial for the long-term function of neuroprostheses. Cell interactions with PEDOT films were shown to improve with decreasing film thickness, but some electrochemical benefits were reduced. Since electrode coatings are aimed at improving metallic interfaces, it is feasible that thin films made with charge lower than 0.1 C/cm^2 can provide both electrochemical and biological benefits over conventional platinum.

5.5. Conclusion

The surface morphology and the thickness of electrodeposited PEDOT films can be controlled by the amount of charge applied during the synthesis. Thicker and rougher films provide electrical benefits when greater amounts of charge are applied. PC12 results indicate that 0.05 C/cm^2 PEDOT/pTS films, having a flat surface and low intrinsic toxicity, promote the most significant cell adhesion and neurite outgrowth. However, electrical properties demonstrate that at this thickness there is a substantial reduction in charge transfer benefits which may be important in neural prosthetic devices. The next chapter seeks to develop a material construct which will address the need for an electrode which will provide both improved charge transfer capacity and optimal biological interactions.

CHAPTER 6. Fabrication of PHEMA nanobrush – CP hybrids

6.1. Introduction

Results in Chapter 4 and 5 have indicated that the physical cues presented to cells are critical to the resulting biological response. In other studies, it has become evident that new generation neural engineering applications will demand soft, deformable substrates that allow preferential attachment and differentiation of neurons while suppressing astroglial scar formation [47, 48]. The demand for soft electroactive biomaterials has spurred the development of composite materials that combine the electrochemical properties of CPs with a softer polymer to mediate the mechanical property. These composite CPs commonly employ a hydrogel component, which is a crosslinked network of hydrophilic polymers [49, 225]. In chapter 5 it was shown that thin CP films present significant electrochemical and biological advantages over platinum. However, the formation of thin composite CPs on metal substrates has been limited by the thickness of the hydrogel component. As a result, a large amount of CP is required to form a composite. The research in this chapter aims to study a new design approach for producing hydrophilic polymer-CP coatings that will allow finer control of physical and mechanical properties.

Coating thickness can only be minimally controlled by the dip processing and gel molding used to form hydrogels in the literature [226, 227]. This results in hybrid coatings of electrodes in the micron range. Kim et al. [226] described the electrodeposition of PPy/PSS through 15 ~ 50 μm thick alginate gel formed on silicon microprobes by dip coating and Green et al. [227] used molding to produce electrode coatings which are around 10 μm thick. In artificial muscle applications, composites have been produced at

around 600 μm [228, 229]. As a result these composites, while softer will significantly deform the tissue in situ. To produce thin hybrids with optimal physico-mechanical properties, it is proposed that a hydrophilic brush structure can be used to impart the mechanical benefits of a hydrogel while allowing a composite to be produced with comparable thickness to thin CPs.

SI-ARTP is a relatively new method that has been explored for nanoscale surface modifications. Yoshikawa et al. [230] has used SI-ATRP in methanol to graft 15 nm thick PHEMA brushes onto a silicon substrate. However, aqueous solvents provide faster reactions and longer brushes but are limited by less control and side reactions such as cross-linking [231]. Huang et al. [232] grafted ~ 700 nm thick PHEMA brushes on gold substrate using a water accelerated SI-ATRP process, which was described previously by Armes et al. [231, 233]. In this chapter, SI-ATRP was utilised as a technique which allows the formation of hydrophilic brushes on electrically conducting substrates while providing nanoscale thickness control.

Most organic films are non-adherent to metal surfaces and delamination is a potential challenge in developing robust CP/hydrogel composites [49, 234, 235]. SI-ATRP is a two-step process consisting of immobilisation of a thiol-initiator followed by ATRP process. The self-assembly of thiol (S-H) compounds on gold substrates, which induces a S-Au bond [236], provides a stable organic platform to immobilise brushes on metal electrodes. Metals, especially gold, have strong binding affinity to sulfur [237]. The strength of the S-Au bond is ~ 44 kcal/mol [238]. This is stronger than the hydrogen bond [239], 1.9 \sim 38.6 kcal/mol, and is roughly one-half that of the C-C covalent bond, 83 \sim 85 kcal/mol [240].

Polymer brushes grown via SI-ATRP are directly bonded to the underlying electrode, and hence are likely to improve the adhesion and mechanical stability of the composites.

ATRP techniques allow polymer brushes to be directly grafted from the immobilised initiator. The persistent radical effect of the ATRP provides good control over the length and polydispersity index (PDI), which indicates the distribution of molecular mass, of the resulting polymers [241]. Polymers end-grafted via SI-ATRP are commonly known as “brushes” because the polymer chains are stretched away from the surface when produced at high density [242]. Yoshikawa et al. [230] and Feng et al. [243] previously showed that the adsorption and diffusion of proteins between polymer brushes were decreased with increasing surface density. It is expected that these same properties can be used to tune the mechanical properties of brushes. Decreased spacing between brushes is likely to increase the stiffness (i.e. mechanical modulus) of the brush.

There are several reports of SI-ATRP of PHEMA on silicon [230, 244] and gold coated silicon [232, 245] wafers. The highest surface density (σ) reported was 0.7 chain/nm², which was measured from the PHEMA brushes grown on silicon [230]. In this chapter, similar ATRP conditions were adopted to maximise the surface density and hence provide substantial mechanical dampening. As a result the surface of these gold substrates was expected to be well-covered with a dense layer of PHEMA brushes. It was hypothesised that this condition presents the toughest environment for the CP to deposit on the underlying substrate. The formation of a hybrid in this extreme condition provides a proof of principle, from which mechanical and electrical properties can be optimised by modulating the density of the brushes.

There are reports in the literature that explore the deposition of CPs on substrates bearing SAMs and polymer brushes. Some of these studies used the monolayer or brush polymer as a template, to block CP deposition in the areas where they were grafted. Gorman et al. [246] used micro-patterned thiol-SAMs and Zhou et al. [247] used PHEMA brushes as a template for the electrodeposition of PPy. While most films were formed on the exposed area of gold, some overgrowth of PPy was also observed. In contrast Willicut and McCarley [248] and Sayre and Collard [249] created surface bound CPs through electrochemical polymerisation of pyrrole-containing alkanethiol monolayers. Upon the application of electrical charge, the pyrrole pedants polymerised without desorption of the thiol moiety from the Au surface [248]. While these studies utilise both components of the hybrid developed in this chapter, this study is the first study examining the electrodeposition of CP on dense PHEMA brushes where both polymers are expected to occupy the same volumetric space.

To combine the electroactivity of CPs and the mechanical softness and stability of hydrophilic brushes, this chapter presents the development of a hybrid material formed via electrodeposition of thin PEDOT/pTS on gold substrates bearing dense PHEMA brushes. The hybrid is fabricated in three steps as illustrated below in Figure 6.1. The first step is the self-assembly of the surface initiator, $(\text{BrC}(\text{CH}_3)_2\text{COO}(\text{CH}_2)_{10}\text{S})_2$, on a gold coated silicon wafer substrate (Figure 6.1, Step 1). The second step is the grafting of PHEMA brushes from the initiator monolayer via atom transfer radical polymerisation (ATRP) (Figure 6.1, Step 2). The final step is the electrodeposition of PEDOT/pTS through the PHEMA brushes (Figure 6.3, Step 3). The successful completion of each step is monitored by contact angle measurement, optical ellipsometry and x-ray photoelectron

spectroscopy (XPS). The main aim of this study is to test the feasibility of forming a hybrid using electrodeposited CPs and polymer brushes grown on gold via SI-ATRP.

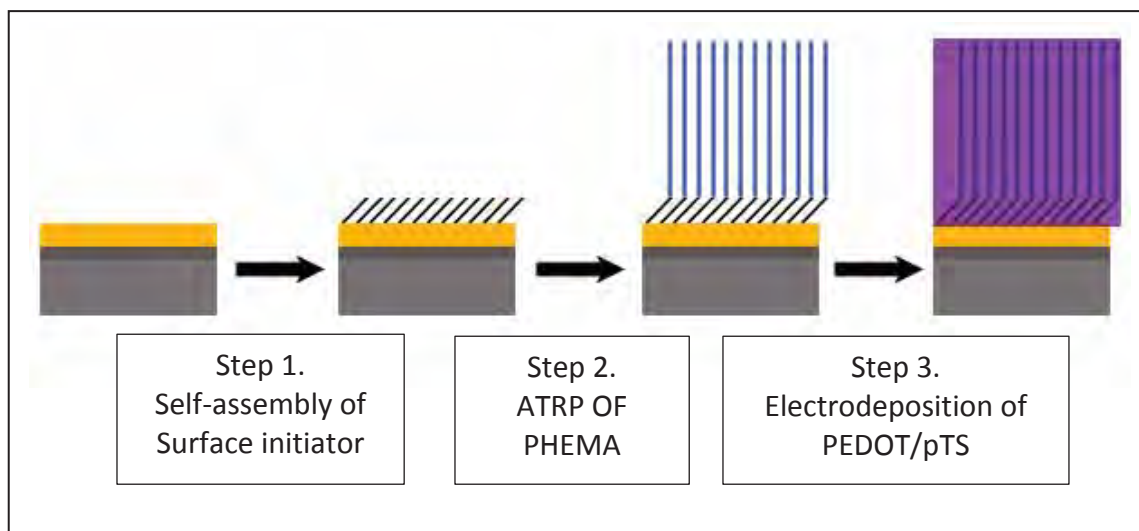


Figure 6.1: Schematic of the fabrication of the CP/brush hybrid. Step 1. Self-assembly of the surface initiator. Step 2. SI-ATRP of PHEMA. Step 3. Electrodeposition of PEDOT/pTS on PHEMA/Au.

6.2. Materials and Methods

6.2.1. Synthesis and self-assembly of initiator - $(\text{BrC}(\text{CH}_3)_2\text{COO}(\text{CH}_2)_{10}\text{S})_2$

Synthesis of the self-assembling initiator

The reactions shown in Figure 6.2 were performed to produce the initiator for the self-assembly process. This was a two-step process which involved synthesis of the disulfide pre-cursor, followed by a second reaction to generate the complete initiator. Specifically, in the first reaction, ethyl acetate (99.5 %, Sigma-Aldrich, cat#:319902) is degassed with nitrogen gas and cooled on ice. The synthesis of the disulfide, bis(11-hydroxyundecyl) disulfide, was carried out in a round bottom flask at low temperature, achieved by cooling on ice, under a nitrogen atmosphere. 11-mercapto-1-undecanol (2.044 g, 10

mmol, 97 %, Sigma-Aldrich, cat#: 447528) and sodium iodide (15 mg, 0.1 mmol, 99.999 %, Sigma-Aldrich, cat#:409286) were dissolved in 20 mL of cold ethyl acetate (99.5 %, Sigma-Aldrich, cat#:319902). While stirring the solution, 30 % hydrogen peroxide (1.021 ml, 10 mmol, Sigma-Aldrich, cat#: 16911), was slowly added to the solution in a drop-wise manner. The mixture was further stirred for 1 h in an ice bath. From the resulting mixture, ethyl acetate was rotary evaporated at 40 °C under 240 mbar. The remaining aqueous phase was then slowly added into a beaker containing 100 mL of cold methanol (Ajax Finechem). After 20 mins stirring, the precipitate was filtered out and washed with 10 ml of cold methanol three times. The filtrand was then dried in an vacuum oven (0.01 mbar, 40 °C) to yield 1.732 g (86 %) of the disulfide. ^1H NMR (300 MHz, CDCl_3): δ = 1.22 (m, 36H, CH_2), 1.59 (q, 4H, CH_2), 2.62 (t, J = 7.5, 4H, SCH_2), 3.61 (t, J = 6.6, 4H, OCH_2).

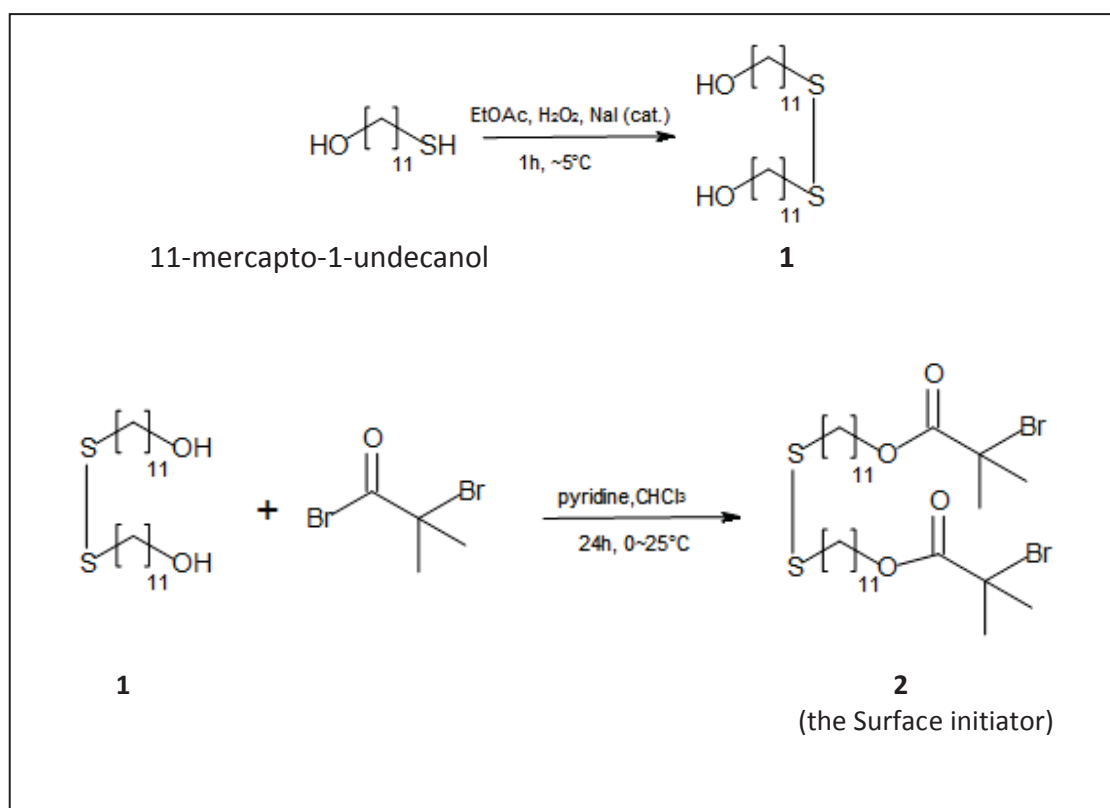


Figure 6.2: Synthesis of the surface initiator.

To complete the synthesis of the surface-initiator, the disulfide (1.634 g, 4.02 mmol) and pyridine (0.78 ml, 9.64 mmol anhydrous, 99.8 %, Sigma-Aldrich, cat#: 270970) were dissolved in 30 ml of dry dichloromethane (anhydrous, 99.8 %, Sigma-Aldrich, cat#: 270997). α -Bromoisobutyryl bromide (1.2 ml, 9.71 mmol, 98 %, Sigma-Aldrich, cat#: 252271) was slowly added drop-wise into the well-stirred solution. The reaction mixture was stirred at 0 °C for 1 h and then at 25 °C for 24 h. The reaction mixture was then diluted with 60 ml of dichloromethane and extracted twice with 150 ml of 1 N HCl solution, then twice with 150 ml of saturated sodium bicarbonate and finally with 150 ml of saturated brine. The aqueous phase was further dried over sodium sulfate. Dichloromethane was rotary evaporated at 40 °C. The crude product was purified by column chromatography on silica gel, eluting with 1:1 by volume hexane/dichloromethane, to produce 2.5 g (88 %) of pale yellow oil. NMR was used to confirm the product was bis[2-(2-bromoisobutyryloxy)undecyl] disulfide. ^1H NMR (300 MHz, CDCl_3): δ = 1.22~1.36 (m, 28H, CH_2), 1.56~1.68 (m, 8H, CH_2), 1.92 (s, 12H, CH_3), 2.66 (t, J = 7.5, 4H, SCH_2), 4.15 (t, J = 6.6, 4H, OCH_2).

Formation of self-assembled monolayers (SAMs) on gold substrate

Silicon wafers (Universitywafer, South Boston, MA, U.S.A., cat#: UW4P111) were sputtered with a 100 Å thick layer of titanium, an adhesive layer, and then with a 1000 Å thick layer of gold using a thermal evaporator (Lesker, Pittsburg, PA). The deposition rate was controlled to 0.2 Å/s. The prepared substrates were cut into 1.5 cm x 1.5 cm squares using a diamond cutter and washed with water, acetone and methanol.

1 mM solution of the self-assembling initiator, bis[2-(2-bromoisobutyryloxy)undecyl] disulfide (MW = 704.7 g/mol, density = 1.177 g/cm³), was prepared by dissolving 14.1 mg or 12 μ l of the initiator in 20 mL of fully degassed ethanol (anhydrous, 99.8 %, Sigma-Aldrich, cat#: 322415). The self-assembly was carried by soaking the gold substrates in the initiator solution at room temperature for 24 h. The resulting substrates were thoroughly rinsed with hexane and methanol, and then dried in nitrogen. Changes in the thickness, surface energy, and surface chemistry were characterised by ellipsometry, sessile drop contact angle measurement, and XPS.

6.2.2. Surface Initiated Atom Transfer Radical Polymerisation (SI-ATRP) of poly(2-hydroxyethyl methacrylate) (pHEMA)

The surface initiated atom transfer radical polymerisation (SI-ATRP) process of HEMA is illustrated in Figure 6.3. Briefly, this involved exposing the substrate to which the surface initiator was bound to a solution containing the hydrophilic monomer (HEMA) in the presence of an activator and ligand, to produce the bound brush structure.

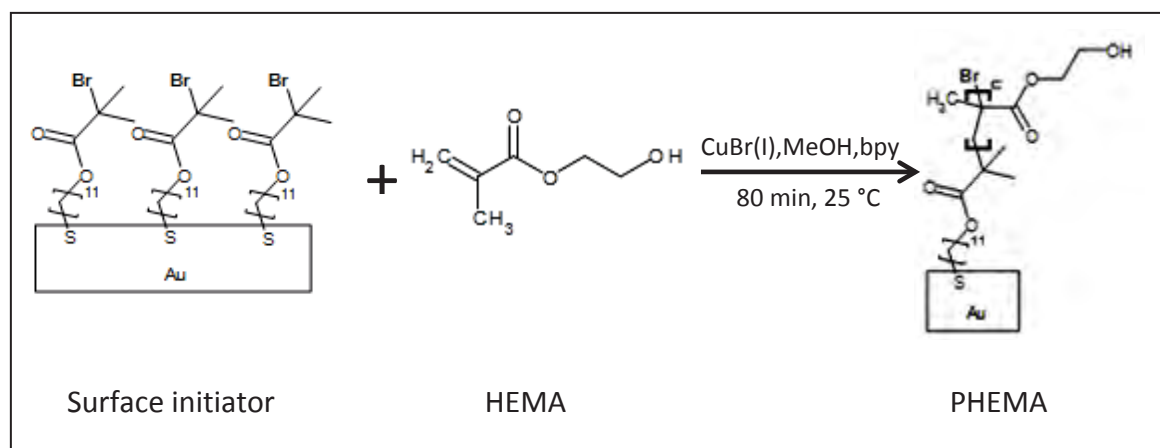


Figure 6.3: SI-ATRP of PHEMA on gold.

Initially, 2-hydroxyethyl methacrylate (HEMA) monomers (97 %, Sigma-Aldrich, cat#: 128635) were purified by column chromatography on silica gel, eluting with 30/70 volume% benzene/ethyl acetate, followed by distillation under reduced pressure. The reaction solution for SI-ATRP was prepared in a glove box. Before placing chemicals in the glove box, solids were vacuumed for 20 minutes and liquids were degassed through three consecutive freeze-pump-thaw cycles on a Schlenk line.

In the glove box, the activator, CuBr (16 mg, 0.11 mmol, 99.999 %, Sigma-Aldrich, cat#: 254185), and the ligand, 2,2'-bipyridyl (bpy) (35 mg, 0.22 mmol, 99 %, Sigma-Aldrich, cat#: 14454), were dissolved in 2 ml of degassed methanol and stirred vigorously for 1 h. The resulting mixture was dark brown in colour. The monomer, purified HEMA (3.72 ml, 30.67 mmol), and the free initiator, ethyl 2-bromoisobutyrate (15 μ l, 0.10 mmol, 98 %, Sigma-Aldrich, cat#: E14403), were mixed with 1.5 ml of methanol in a Schlenk tube. The resulting solution was degassed on a Schlenk line before placing in the glove box.

In the glove box, SI-ATRP was started by adding the monomer solution to the well-stirred activator/ligand mixture. Aliquots of the resulting solution were transferred into reaction tubes containing two gold substrates, which were placed back to back with the SAMs facing the outside. The tubes were then capped with rubber septa and removed immediately from the glove box. Polymerisation was carried out at 25 °C in an incubator shaker. The thickness of the brush layer was controlled by the polymerisation time. Preliminary studies (data not shown) indicated that the control over the molecular weight (MW) was lost after 90 mins of polymerisation. A linear relationship between

molecular weight and polymerisation time was maintained for the first 80 mins of polymerisation. Accordingly, PHEMA brushes in study are polymerised for 80 mins.

At the end of the polymerisation, a small portion of the reaction solution was collected. This solution contains loose PHEMA chains, which are polymerised from the free initiator. The molecular weight (MW) and the polydispersity index (PDI) were measured by gel permeation chromatography (GPC). The gold substrates bearing brushes were removed from the reaction solution and rinsed thoroughly with tetrahydrofuran (THF), ethanol, methanol, and water to eliminate untethered polymers. The brushes were dried under nitrogen atmosphere and characterised by ellipsometry, contact angle, and XPS.

6.2.3. Electrodeposition of the CP

PEDOT/pTS films were electrodeposited on a selective area of the PHEMA brushes bound to the Au substrate using the silicone well system previously described in Section 4.2.1. A single well of FlexiPERM[®] micro12A, a self-adherent silicone gasket with a diameter of 6.5 mm, was placed on the brush substrate having geometry of a 1.5 x 1.5 cm square. Brushes on one corner of the substrate were scraped off using a razor blade. A long platinum strip, which was placed between the gasket and the scraped corner of the substrate, provided an electrical contact to the brush substrate. The assembled structure was sandwiched between two computer-numerical-control (CNC) machined polycarbonate sheets and clamped together as shown previously in Figure 4.1. In a well, having the surface area of 0.3318 cm², 150 µL of monomer solution was placed. The amount of chemicals used to make 2ml of monomer solution is shown in Table 6.1. A

platinum wire loop, which serves as a counter electrode, was placed in the well gasket. The electropolymerisation was carried out at 0.166 mA or 0.5 mA/cm² for 60 and 100 sec. The total charge applied was 0.03 and 0.05 C/cm², respectively. The formed hybrid was characterised by XPS.

Table 6.1: Amount of chemicals used to make 2 ml of a monomer solution

Solutions	ACN (mL)	H ₂ O (mL)	EDOT (μL)	NapTS (mg)
EDOT/pTS	0.806	0.806	21.4	19.418

6.2.4. Characterisation

Ellipsometry

Ellipsometry was performed using a Gaertner L116A ellipsometer (Gaertner Scientific Corp, Skokie, IL, U.S.A.) equipped with a He-Ne laser (632.8 nm). The angle of incidence was set at 70 °C. Five measurements were made on each sample. The ellipsometric thickness was determined by using a Cauchy layer model. The reflective index (n) and the extinction coefficient of the surface initiator and pHEMA brushes were set to (1.45, 0.01) and (1.46, 0.01), respectively. The grafting density (σ) of the brushes was determined from the ellipsometric thickness (L) by the following equation [230]:

$$\sigma = \frac{L \times \rho \times N_A}{M_n}, \quad (\text{Equation 6.1}),$$

where h is the ellipsometric thickness (nm), ρ is the bulk density of PHEMA (1.15 g/cm³), N_A is the Avogadro constant ($6.022 \times 10^{23} \text{ mol}^{-1}$), and M_n is the number average molecular weight of the brush, which was obtained from GPC.

Contact angle measurement

The static contact angle of substrates was measured by the sessile drop method using a KSV CAM200 Contact Angle system (KSV Instruments Ltd., Finland). Deionised water was used as probe liquid. A drop of water was placed on the substrate and images were captured at a frequency of 1 Hz. The static contact angle was analysed using the image analysis software (fitting method: Young-Laplace, CAM 200 Software, KSV). Data is presented as an average \pm standard deviation of three samples. All measurements were made in standard laboratory conditions.

Gel Permeation Chromatography (GPC)

Degree of polymerisation (DP) and molecular weight (MW) distributions were estimated by GPC (Shimadzu Co., Japan) eluting with dimethylacetamide (DMAc) containing 0.05 %w/v LiBr and 0.05 % butylated hydroxytoluene at 40 °C. The GPC system was comprised of an auto-injector (SIL-10AD), a solvent degasser (DGU-12A), a pump (LC-10AT), a column oven (CTO-10A), a refractive index detector (RID-10A) and column series, a 5.0 μ m mixed column (50 \times 7.8 mm, Polymer LaboratoriesTM, cat#: 1110-1520) followed by four linear columns (300 \times 7.8 mm, Polymer LaboratoriesTM) with pore sizes of 10⁵, 10⁴, 10³ and 500 Å. The flow rate was 1 ml/min. The column was calibrated against polystyrene standards with molecular weights ranging from 500 to 10⁶ g/mol. The theoretical molecular weight of the PHEMA was calculated by the following equation [230]:

$$M_{n,theo} = \frac{[HEMA]_0}{[EBIB]_0} \times 130.14 \times \frac{\%Conversion}{100}, \quad \text{(Equation 6.2),}$$

where $[\text{HEMA}]_0$ and $[\text{EBIB}]_0$ is the concentration of the monomer and the free initiator and the %Conversion is the monomer conversion in percent.

X-ray Photoelectron Spectroscopy (XPS)

The chemical composition of material surfaces was measured on an ESCALAB220i-XL x-ray photoelectron spectrometer using an aluminium $K\alpha$ radiation (photon energy = 1486.6 eV). The take-off angle was 90°. Survey scans were obtained using a pass energy of 100 eV and high resolution scans were obtained using a pass energy of 20 eV and energy resolution of 0.1 eV. High resolution C1s and O1s scans were made on gold substrate bearing brushes, 0.05 C/cm² PEDOT/pTS and the hybrids formed with 0.05 C/cm² and 0.03 C/cm². The energy range for C1s and O1s scan was from 280.08 to 296.08 eV and from 525.08 to 541.08 eV, respectively. The grafting of PHEMA brushes on gold substrate was verified from the C1s scan of brushes laden substrates. Spectra were deconvoluted using the peak fitting software, Eclipse 2.0. Three different spots on each of three samples from different batch were analysed.

6.3. Results

6.3.1. Synthesis and characterisation of the surface initiator monolayer

The two-step synthesis of the surface initiator, bis[2-(2-bromoisobutyryloxy)undecyl] disulfide, was successful with both products being obtained with high yield. The disulfide

(compound **1**, in Figure 6.2) and the initiator (compound **2**, in Figure 6.2) were produced with 86 % and 88 % yield, respectively. Compound **1** was a white solid and the final product, Compound **2**, was a pale yellow oil.

Sessile drop analysis of the resulting substrate determined that the static contact angle between DI water and the monolayer was $76.6 \pm 1.9^\circ$. Ellipsometry determined that the thickness of the initiator monolayer was 1.7 ± 0.1 nm. Similar results were reported by Shah et al. [250] and Rakhmatullina et al. [251]. The atomic composition was analysed using XPS. Table 1 compares the theoretical and empirical atomic composition of the monolayer. It can be seen that the empirical results generally correlated with theoretical values.

Table 6.2: Theoretical and empirical atomic composition of the surface initiator monolayer

	Theoretical composition (%)	Empirical Composition (%)
C	77.78	77.28 ± 2.52
O	11.11	17.64 ± 3.15
S	5.56	3.04 ± 0.47
Br	5.56	2.04 ± 0.18

6.3.2. Fabrication and characterisation of PHEMA brushes via ATRP

The SI-ATRP process of HEMA was successful, with GPC results, plotted in Figure 6.4, indicating that after 80 mins of polymerisation, 87 % of the monomers were converted to polymers. The average molecular weight M_n measured from GPC was 31009 ± 875 Da.

The theoretical molecular weight for PHEMA at 87 % conversion is 34162 Da [252]. The low PDI (<1.2) combined with a molecular weight close to that of the theoretical line confirm the persistent radical effect of ATRP providing controlled growth of polymer chains.

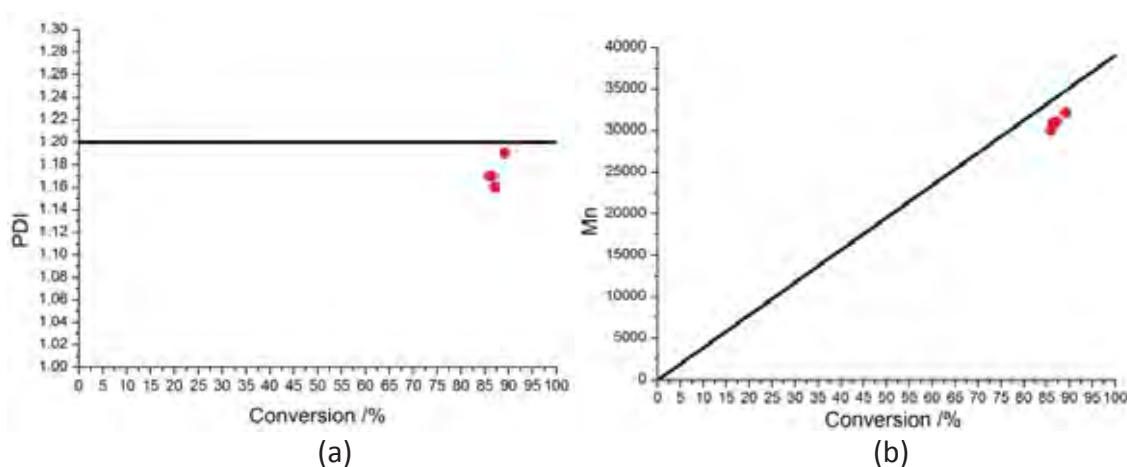


Figure 6.4: The GPC results of SI-ATRP of PHEMA. Data obtained from four samples from different batches. (a) low polydispersity index (PDI <1.2) and (b) the molecular weight close to the theoretical line (shown in black straight lines) indicate controlled radical polymerisation via ATRP mechanism.

The length L of the dry PHEMA brushes was measured by ellipsometry as shown in Table 6.3. While most data points are in good agreement across multiple samples, there are a couple of data points (shown in red letters in table 6.3) that deviate from the average. This was likely due to the defects in the SAM layer, which are described in the discussion. The average length of the brushes was calculated from all data points and found to be 15.3 ± 0.5 nm. The grafting density can be presented as the gradient of the L vs. M_n graph as shown in Figure 6.5. For all samples, the grafting density is close to 0.35 chains/nm².

Table 6.3: The elliptical length of dry PHEMA brushes
(Four samples from different batches are tested and 8 data points are measured on each sample)

Sample	Elliptical length (nm)							
1	15.5	15.6	15.4	15.5	15.4	9.8	15.4	15.4
2	15.3	15.5	15.5	15.6	15.3	15.3	15.4	15.5
3	16	15.6	15.8	10.2	15.9	15.8	16	15.9
4	15.8	15.9	16	15.8	16.1	16.1	15.8	15.7

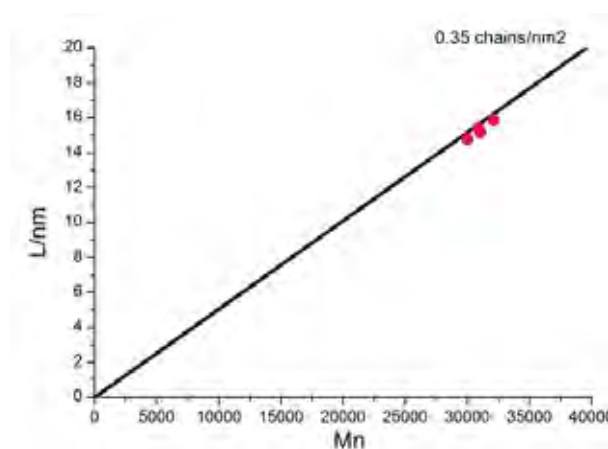


Figure 6.5: The graph of elliptical length versus molecular weight. The grafting density (σ) is estimated at 0.35 chains/nm^2 , calculated from the gradient of the black line. Red dots represent each sample.

Upon the grafting of PHEMA brushes, the water contact angle of the substrate was decreased by 37° as shown in Table 6.4. XPS further confirmed the successful grafting of PHEMA brushes. The carbon to oxygen ratio of the brush substrate was determined by XPS as shown in Table 6.5. The XPS result was very close to the theoretical value of PHEMA.

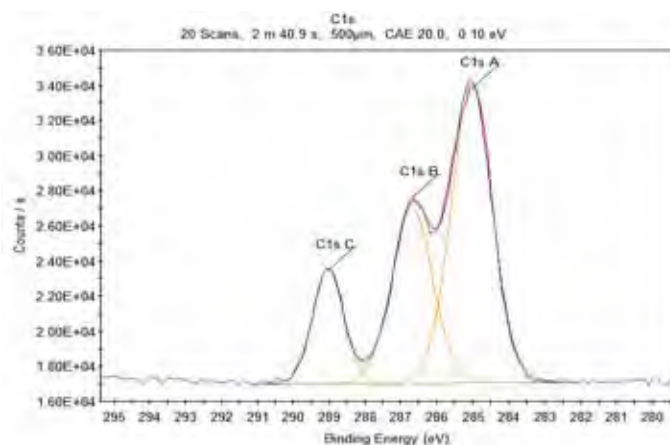
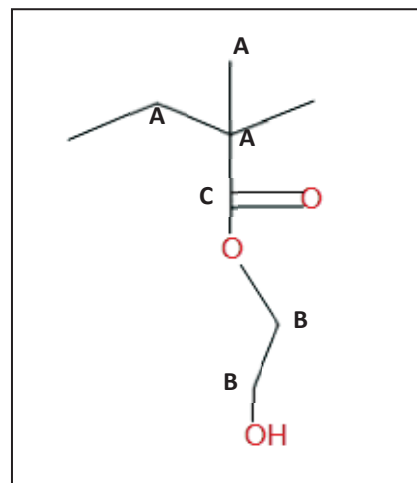
Table 6.4: The change in static contact angle upon the grafting of PHEMA brushes

	Contact angle ($^\circ$)
Before the grafting (surface initiator monolayer)	76.6 ± 1.9
After the grafting (PHEMA brushes)	39.9 ± 1.8

Table 6.5: Theoretical and empirical atomic composition of the PHEMA brushes

	Empirical Composition (%)	Theoretical composition (%)
C	69.87 ± 2.00	66.67
O	30.13 ± 2.02	33.33

The high resolution XPS scan of C1s region, shown in Figure 6.6, demonstrated three peaks at 285.03, 286.69 and 289.03 eV, which correspond to the C-C, C-O and O-C=O bonds, respectively. The ratio between these three peaks was 3.4:2:1 as summarised in Table 6.6. This ratio is well aligned with the theoretical ratio, 3:2:1, for PHEMA. The chemical composition obtained from XPS in combination with physical characteristics such as uniform elliptical thickness and low surface contact angle indicate that the dense PHEMA brushes were successfully grafted on to the gold substrate.

**Figure 6.6:** XPS analysis of C 1s on PHEMA brushes.**Table 6.6:** The theoretical and experimental C 1S peak ratio of PHEMA

C 1s PEAK	Binding energy [eV]	Corresponding Carbon	Theoretical ratio	Measured ratio
A	285.03	C-C	3	32.81 (3.42842)
B	286.69	C-O	2	19.28 (2.015)
C	289.03	O-C=O	1	9.57 (1)

6.3.3. Electrodeposition of PEDOT/pTS through PHEMA brush modified gold substrate

Following electrodeposition a transparent dark blue film was formed on the substrate as shown in Figure 6.7. The SEM micrograph, shown in appendix F, of PEDOT formed on the brushes was similar to that of homogeneous PEDOT formed on bare gold. Figure 6.8 shows the XPS spectra of the hybrid formed with the deposition charge of 0.03C. Chemical characteristics of both PEDOT and PHEMA are reflected on the spectra. This indicated the successful integration of PEDOT with PHEMA brushes. XPS of the hybrid formed with the deposition charge of 0.05 C/cm² revealed that brush layer was completely covered by the thicker conducting polymer layer.



Figure 6.7: A picture of the 0,05C PEDOT/pTS film deposited on the gold substrate bearing PHEMA brushes.

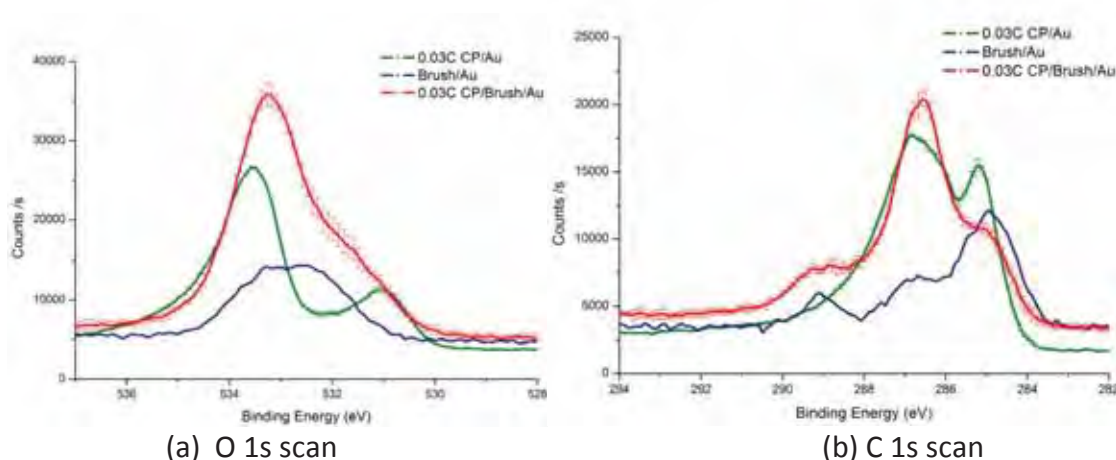


Figure 6.8: High resolution XPS spectrum of 0.03C PEDOT formed on the PHEMA brushed modified gold at (a) O 1s range (b) C 1s range.

6.4. Discussion

A hybrid CP-brush structure was developed with each step of the fabrication process characterised to define the resulting material composition. This process determined that all reagents were synthesised with high yield. The initiator monolayer was successfully bound to the metallic substrate and PHEMA brushes were grown from this graft surface. Finally PEDOT/pTS was electrodeposited through the brush structure with elements of each polymer detected at the surface when a small amount of charge was delivered during polymerisation.

Physical changes associated with grafting of the surface initiator and the PHEMA brushes are well depicted by the changes in hydrophilicity of the resulting surfaces. The water contact angle was changed from $76.6 \pm 1.9^\circ$ to $39.9 \pm 1.8^\circ$ upon grafting of hydrophilic PHEMA brushes. The contact angle of PHEMA brushes were reported to be in the range of 29 to 61° , depending on the brush length and substrate [230, 244, 251, 253, 254]. A similar decrease in contact angle was reported by Yang et al. [253] who presented 25° decrease in contact angle upon the grafting of ~ 10 nm thick PHEMA brushes on barnacle cement modified stainless steel substrate.

XPS spectra of PHEMA brushes show that the atomic compositions of the synthesised compounds are also in agreement with the theoretical estimates. The shape and distribution of the spectra is also identical to those measured reported by Castner et al. [255] using anionic polymerised PHEMA films cast onto glass coverslips. The high grafting density of 0.35 chains/nm² indicates that the fabricated PHEMA would have 'brush-like'

structure. "High density" PHEMA brushes with the density of 0.3 chains/nm² were reported by Yoshikawa et al [256].

The fabrication of PHEMA brushes on gold substrates via SI-ATRP is a well established technique that has been described extensively in the literature. However, the electrodeposition of CP through the brushes to produce a hybrid biomaterial has not been reported. This concept may seem counter-intuitive as both PHEMA brushes and underlying SAM layers have been used for template patterning of electropolymerised CPs. Zhou et al. [247] grafted poly(methyl methacrylate) (PMMA) brushes on gold substrate via SI-ATRP and reported that the electrodeposition of PPy was confined to the area defined by the brush template. This study and others in literature [246, 247], however, demonstrated that the CP can be electrodeposited through the underlying SAM, which is an important initial step to producing a CP integrated with the brush structure. Both Zhou et al. [247] and Gorman et al. [246] reported electrodeposition of CPs on alkylthiol SAMs patterned on gold electrodes, an effect which was considered undesirable. It is hypothesised that as nucleophilic growth of CPs relies on an initial interaction with the underlying substrate, the susceptibility of SAMs to CP interaction can be utilised to guide CP ingrowth to the grafted PHEMA brush.

Sayre and Collard studied the cyclic voltammetric electrodeposition of PPy and PANI on unpatterned SAM/Au substrates [249]. As the number of cycles was increased, PPy films were gradually formed on all substrates which were modified with five different SAMs. By the 72nd cycle, the CSC of the PPy formed on SAM/Au was roughly two times higher than that of the PPy on bare Au. It was suggested that the CP penetration of the SAM

later was a result of either defects developed during the fabrication or polymerisation of the monomer that partitions the SAM. SAMs on gold substrates always carry surface defects such as pinholes and domain boundaries that can be preferred sites for CP nucleation and growth. Figure 6.9 shows the typical “pinhole” defects found on thiol SAMs formed on Au. The blue dot drawn next to the picture indicates the gyration size of a single PHEMA brush. It can be seen that the defects reported on SAMs are similar or slightly larger than the size of single brushes. Previous studies indicated that about 1 % of the current applied is transferred through these pinhole defects, and the other 99 % of current is passivated by the SAM [257]. Sabatani et al. [258, 259] has suggested that pinhole defects can serve as an array of ultra-microelectrodes with an average diameter of 5 – 10 nm.

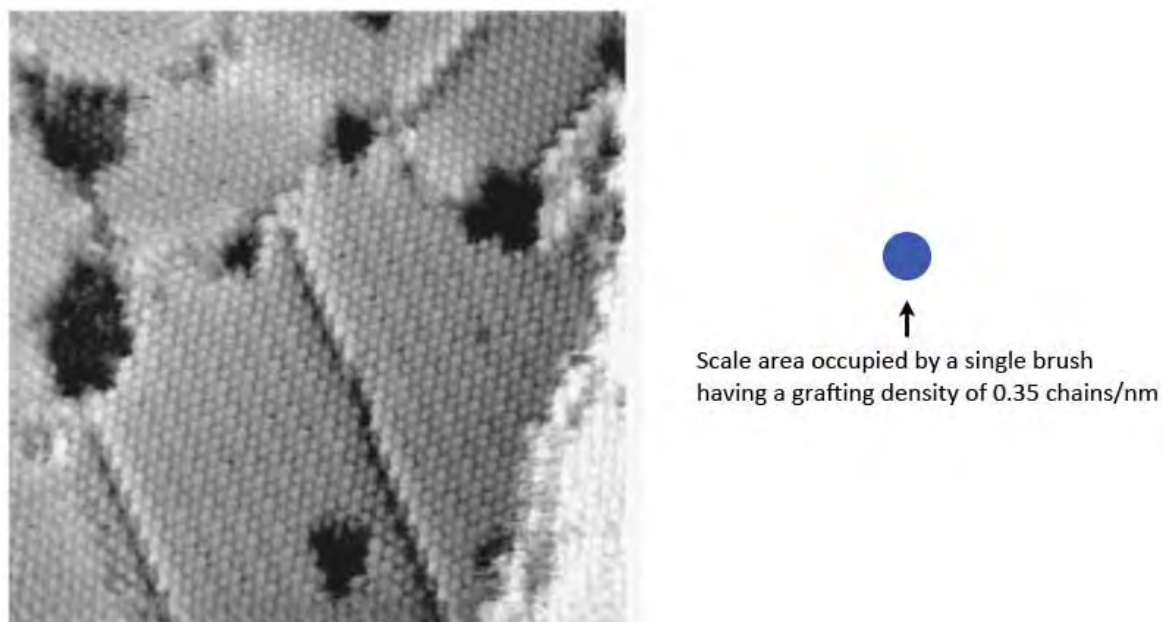


Figure 6.9: The typical “pinhole” defects found on thiol SAMs formed on Au. Reprinted from [260].

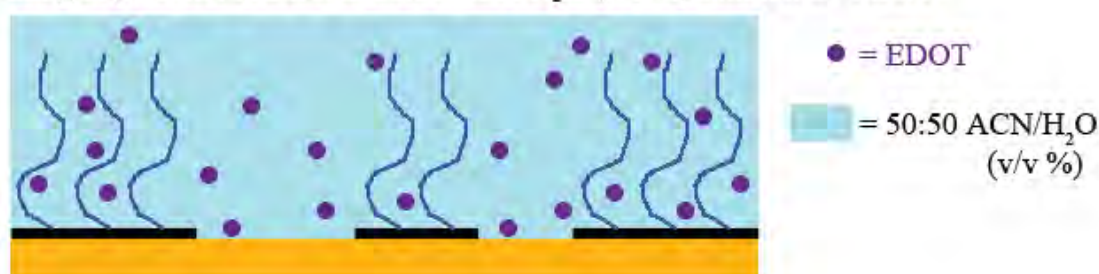
Accordingly, it was theorised in this study that the electrodeposition through the PHEMA brush also occurred through these pinhole defects as illustrated in Figure 6.10. The

spacing between PHEMA brushes is likely to increase during the electrodeposition of a CP. Swelling of the brushes in the aqueous monomer solution will thermodynamically stretch out chains. The application of electrical current will elongate the brush further with electrostatic interaction. While the resulting penetration of the CP through the PHEMA brush remains undetermined, the XPS results indicated the co-existence of the brush and the CP at the material surface.

1. Dry pHEMA brushes on Au



2. Swelling of pHEMA brushes in 50:50 ACN/H₂O (v/v %) solution of EDOT



3. Initial nucleation of PEDOT through the defect sites in the SAM

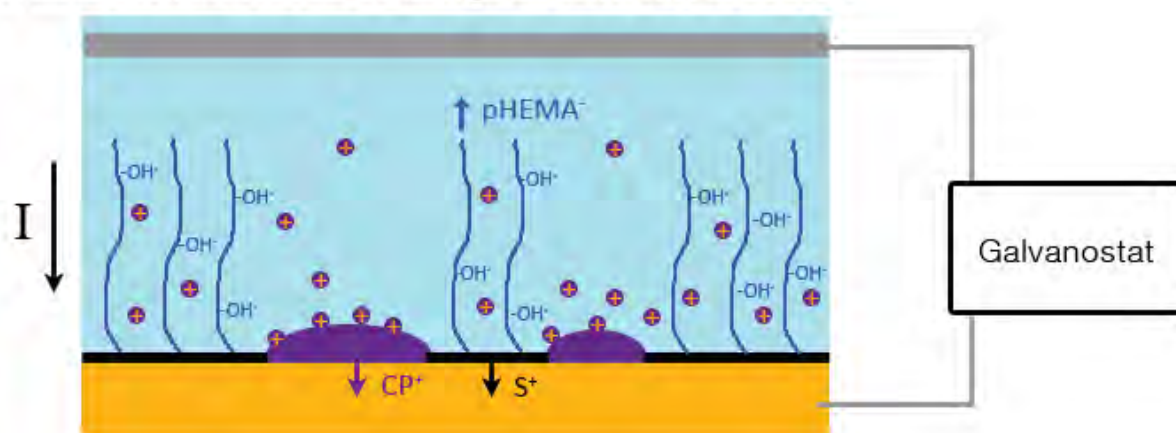


Figure 6.10: Schematic illustration of the electrodeposition of CP through brushes.

From the XPS result, it is clear that PEDOT deposited with the charge of 0.05 C/cm^2 formed a significant overlying layer that masked the atomic signals of underlying brush structure. Since no PHEMA signals were found, this result also indicates that the brushes were not cleaved off during the electrodeposition, as cleaved brushes are likely to be randomly entrapped in CP layer and be detected in the XPS signal. At the deposition charge of 0.03 C , the CP was less likely to have encapsulated the brush structure. The atomic composition of this surface was a combination of both PHEMA and PEDOT. Although the SEM images did not have discernable brush features, the maximum profiling depth of XPS is less than 10 nm , which suggests minimal coverage of the upper surface of the brush structure.

The exact structure of the resulting hybrid is yet to be determined, but several possible configurations have been considered. These are illustrated in Figure 6.11. If the size of the CP nucleate is bigger than that of the pinhole defect, the CP is likely to nucleate on the brushes and form an overlying film as shown in Figure 6.11 (a). Depending on the size of the surface defect, the distance between brushes, the size and percolation of CP nuclei, the alternate structures shown in 6.11 (b), (c) and (d) can be achieved. These structures represent the various penetration options for the CP, assuming defects in the SAMs. In Figure 6.11 (b) it is considered that only defect nucleation occurs and the CP grows above the brush. In Figure 6.11 (c) both the defects and spacing between brushes enable CP nucleation and finally in Figure 6.11 (d) the CP forms in intimate integration with the brush structure, having minimal reliance on defects to polymerise. The scenario depicted in (c) is thought to be the most promising for neural interfaces. This structure will enable both mechanical softening and the passage of electrical charge. As a result, future work

will involve the manipulation and quantification of the interface between the CP and brush structure.

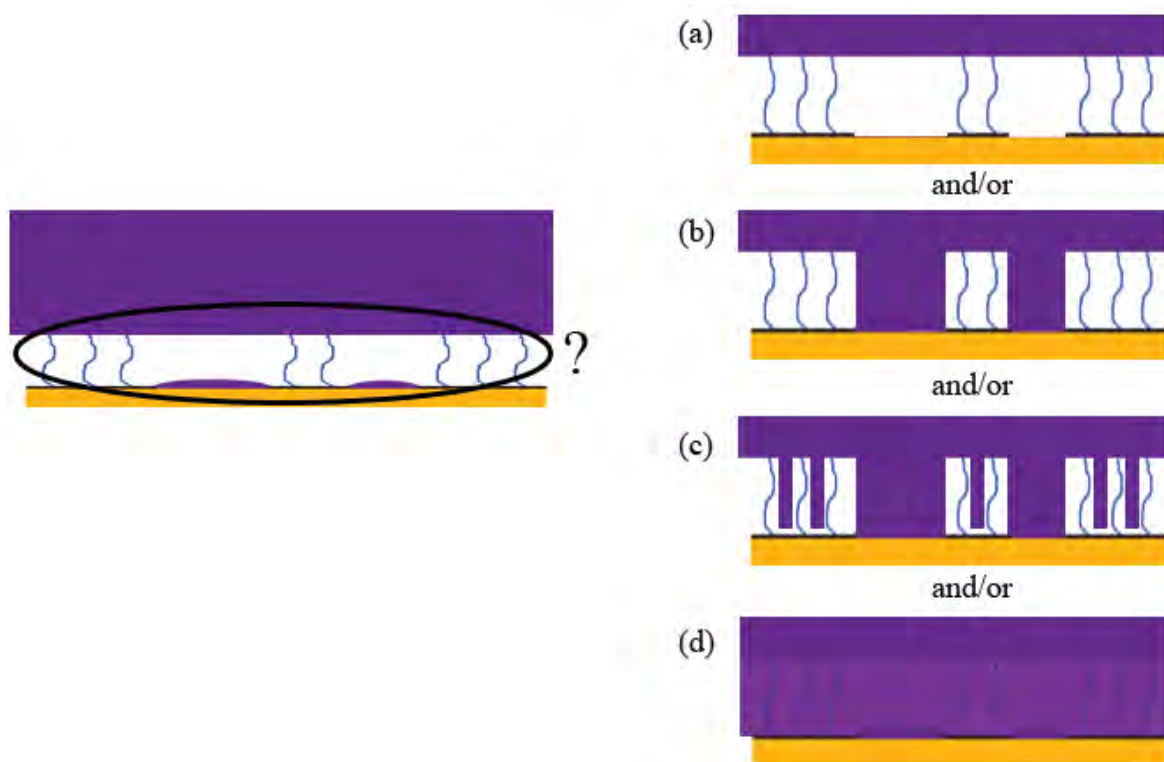


Figure 6.11: Schematic illustration of the interface between the brush and CP.

6.5. Conclusion

The fabrication of a novel hybrid combining the hydrophilic PHEMA brushes and electrodeposited PEDOT films was reported herein. A dense layer of hydrophilic PHEMA brushes were successfully grafted on SAM carrying gold substrate via a SI-ATRP technique. The electrodeposition of PEDOT/pTS was galvanostatically carried out on this brush structure. While the detailed configuration of the hybrid was beyond the current scope of the study, the hybrid formed with the charge of 0.05 C/cm^2 is estimated to have a bilayer structure. The bottom layer is a composite of the PHEMA brushes and the CP and the

upper layer is purely overlying CP. However, it is considered that the hybrid layer may potentially act as a soft cushion for cell interaction while maintaining the desired electrical properties. The next chapter will seek to characterise this material for application in stimulating neuroprostheses.

CHAPTER 7. PHEMA nanobrush – CP hybrids as neural interfaces

7.1. Introduction

Hybrid materials composed of nanostructured building blocks often provide synergistic properties of the two constituents or new properties that are unforeseen in ordinary macroscopic composites. Anticipating the synergistic effect of electroactive PEDOT and biocompatible PHEMA brushes, a novel PEDOT/PHEMA hybrid was devised as described in Chapter 6. The hybrid has broad potential applications including neural interfaces [105, 112, 226, 261], controlled drug delivery systems [112, 262-264], biosensors [264-266], and artificial muscles [267], where conventional CP/hydrogel composites have shown potential benefits. One specific application of interest is the use of the hybrid as a bioelectrode material for recording and stimulation of neural activity.

At neuron-electrode interfaces, the quality of device to tissue communication is determined by the charge transfer characteristics of the material as well as the attachment and survival of neurons at the electrode surface. Therefore, the electrical parameters such as charge storage capacity (CSC), electrical impedance, and biphasic charge injection, as well as the neuronal interactions, which can be driven by physico-mechanical cues, are all important performance indicators. As an electroactive biomaterial for neural interfacing, the hybrid system could provide electrical, mechanical and biological benefits over conventional CP systems.

The electrical properties of CPs are key to their performance as bioelectrodes. The creation of a hybrid structure where one component is non-conductive raises concerns regarding the charge transfer properties of these materials. Hydrophilic polymers in the

literature including hydrogels which have been used to form composite CPs, demonstrate that electroactivity can be preserved [261, 264, 266]. It is thought that this is due to preservation of the volumetric transfer of charge, as the doping ions maintain their mobility within the wider matrix of the hydrogel polymer. Additionally, it is proposed that the hydrophilic PHEMA nanobrushes used in this design can provide an increase in surface area, to also increase charge transfer through double layer charging. This capacitive mechanism which is the dominant mode of charge transduction in metals is directly proportional to the electrode surface area. Kim, Abidian and Martin [226, 261] reported that PPy electrodeposited through an alginate gel layer provided a higher surface area than that formed homogeneously on a metal substrate, but this is expected to be the result of an increased volume of materials on the electrode array. Nanomaterials are proposed to impart a greater increase in surface area compared to macroscopic gels. This was demonstrated by Abidian and Martin [112] who reported that the electrical impedance of PEDOT-PLGA nanotubes was $10.7 \pm 2 \text{ k}\Omega$ at 1Hz compared to macroscopic alginate gels with an impedance of $33.1 \pm 4 \text{ k}\Omega$ at 1 Hz. The electrical properties of the nanobrush hybrid developed in Chapter 6 have been investigated to demonstrate that this new structure can improve the electrical performance of the CP film without requiring an increase in CP thickness.

The hybrid containing soft hydrophilic brushes was developed as a system which has the potential to improve the strain mismatch at the neural interface. The long term function of the electrode-tissue interface is severely limited by gliosis, a scar tissue formation that encapsulates the implant [1]. This inflammatory reaction is known to be exacerbated by mechanical consequences such as interfacial micromotion causing traumatic injuries and

strain shielding [22, 268]. The main cause of the micromotion was suggested to be severe strain mismatch between metallic electrodes and the tissue [269]. The issues of the strain match have commonly been addressed by the use of thick (micrometer scale) CP/hydrogel composites [226, 227, 261]. In order to reduce the overall thickness of the coating it was hypothesised that hydrophilic brushes could be used to impart a similar reduction in stiffness. The concept of using hydrophilic polymer brushes as a soft cushioning layer was previously explored by Tanaka and Sackmann [270, 271]. In their design of synthetic surface membranes, hydrophilic polymer brushes were used as a “cushioning” layer for the lipid bilayer formed on top. The hydrophilic brushes in this design are expected to provide similar mechanical buffering effects.

A major biological advantage of hydrophilic polymers is their strong antifouling properties. In an implant application, successful implementation of these properties has the potential to reduce post-implantation complications involving biofouling, severe thrombosis and gliosis. Previously, PHEMA brushes have demonstrated a strong resistance to adsorption of various proteins [230] including aprotinin, myoglobin, BSA, IgG, thyroglobulin, fibrinogen, and bacteria [253] such as salmonella as well as human blood serum/plasma [253]. However, it is also important that these materials support the survival and growth of neural cells. Often materials with strong antifouling properties also prevent the interaction of ECM proteins required to support target cell attachment. This chapter will explore whether antifouling properties can be preserved and selectively presented in the hybrid structure following CP deposition. Furthermore, the neural cell survival and growth of neural processes will be assessed in comparison to conventional CPs and metallic substrates.

The aim of this chapter is to validate the hybrid CP-brush system as an electrode coating across a range of implant specific performance metrics. In this chapter the PEDOT/PHEMA hybrids are assessed in comparison to conventional gold electrodes. Application-related electrical properties such as electrical impedance, charge storage capacity, and stability under stimulation were analysed by electrochemical impedance spectroscopy (EIS), cyclic voltammetry (CV), and accelerated biphasic stimulation, respectively. The adhesion and neurite outgrowth of neural model cells, PC12s, were observed to deduce the biological performance of the CP-brush structure. This study will serve as a starting point for future studies of CP/brush hybrids as electroactive biomaterials for biomedical applications including biosensors, drug-delivery systems, and bionic electrodes.

7.2. Materials and Methods

7.2.1. Sample preparation

The four samples used throughout these studies were bare gold (Au), brush structured Au (Brush), PEDOT/pTS coated Au (PEDOT/pTS) and the hybrid PEDOT/PHEMA coated on Au (Hybrid). The detailed fabrication procedure of each sample can be found in Chapter 6. The bare Au samples were prepared by sputtering and were cut into 1cm x 1cm squares using a diamond tipped cutter. Brush samples were prepared by grafting PHEMA brushes on gold squares via SI-ATRP. The grafting density and the length of the brushes were 0.35

chains/nm² and $17.0 \pm 0.5 \text{ nm}^\dagger$, respectively. Hybrid and PEDOT/pTS samples were produced by the electrodeposition of PEDOT/pTS on Brush and Au substrates, respectively. The electrodeposition process was carried out using the silicone gasket masking method described in Chapter 6. The area of the electrodeposited site was 0.332 cm². The total charge used to polymerise the PEDOT/pTS was 0.05 C/cm². CP films were cleaned with DI water to remove excess electrolyte and dried at room temperature.

7.2.2. Indentation modulus - AFM

The indentation moduli of the hybrid and PEDOT were obtained by peak-force nanomechanical mapping (PF-QNM) using a Nanoscope Multimode Atomic Force Microscope (Veeco Instruments Inc. NY). Samples were placed in a fluid cell and DI water was used to flood the chamber. The system was allowed 30 min to thermally equilibrate prior to scanning. Three 2.5 μm^2 scans were taken of each sample at 0.3 Hz with a maximum force of 1 nN to produce a penetration depth of 5 – 15 nm depending on material type. 512 data points per line were recorded and presented with standard deviation. The DMT contact model was used to evaluate the elastic properties of samples. The details of the model are described in Chapter 3. Samples were prepared, air dried and stored under vacuum prior to analysis. Gwiddion software (Freeware, Australia) was used to remove artefact and analyse data to produce mean stiffness values for each material type under hydration.

[†] The brush length shown here is the combined length of the initiator layer ($1.7 \pm 0.1 \text{ nm}$) and the PHEMA layer ($15.3 \pm 0.5 \text{ nm}$)

7.2.3. Electrochemical stability - Cyclic voltammetry

The electrochemical stability of the untreated Au, Brush, PEDOT/pTS, and Hybrid were compared via CV. The detailed experimental procedures can be found in Section 4.2.4. The initial CSC was determined from the first stable voltammogram. The loss in CSC over 800 cycles was recorded to determine the comparative electrochemical stability of the samples. The results were presented as the average and standard deviation of three individually prepared samples.

7.2.4. Electrical Impedance spectroscopy (EIS)

Electrical impedance was measured in a frequency range from 1 Hz to 10 kHz. Experimental details can be found in Section 4.2.5. Three samples of each type were tested. The graphs of impedance magnitude, phase, conductance and capacitance represent the average \pm standard deviation of the three samples tested.

7.2.5. Biphasic stimulation

The charge injection behaviour of Au, PEDOT/pTS, and Hybrid samples were examined under constant biphasic stimulation in 0.9 % saline solution at 37 °C for 20 days using an in-house built biphasic stimulator. Current was applied between the samples and large low-impedance platinum counter electrodes. The current amplitude was ± 0.1 A with 0.4 ms phase duration repeated at 250 Hz ($3013.6 \mu\text{A}/\text{mm}^2$, $1205.4 \text{ nC}/\text{mm}^2/\text{phase}$ or $40 \mu\text{C}/\text{phase}$). Data of the voltage waveform was recorded from an isolated oscilloscope (CRO) daily to determine any changes in performance over the test period.

7.2.6. PC12 cell attachment and neurite outgrowth

This study was carried out under similar passive conditions to those presented in Chapter 4 and 5, except that the gasket system used in previous studies was not used. To investigate the preferential behaviour of neural cell attachment and antifouling properties of the brushes, this assay was performed in conventional tissue culture plates. Square samples (1x1 cm²) were disinfected by soaking in 70 % ethanol for 30 min. All disinfected substrates were placed in the laminar flow hood and rinsed three times with deionised water and left to dry for 30 mins. Samples were placed in a 24 well plate (CELLSTAR®, Greiner Bio-One GmbH, Cat#: 662 1160). To mediate initial cell attachment, sample surfaces were coated with 5 µg/ml laminin (derived from Engelbreth-Holm-Swarm (EHS) sarcoma, Sigma Aldrich, cat#: L2020) in phosphate buffered saline (PBS) (Sigma-Aldrich, cat#: D5652). After the incubation at 37°C for 12 hr, the samples were washed three times with PBS then placed in a new 24 well plate for PC12 assay. The formation of a coating was observed under microscopy.

Fluorescent PC12 cell seeding was performed according to methods described in Section 4.2.6. 0.5 ml of cell suspension was plated in each well (surface area = 1.9 cm²) to provide a seeding density of 2.5x10⁴ cells/cm². The neurite outgrowth was assessed using fluorescence microscopy after 96 hr of incubation at 37 °C with 5 % CO₂. During the culture, two thirds of culture medium was replaced every 48 hr with low serum medium containing 100 ng/ml NGF.

For each sample type, 4 images were taken on each of 3 samples in each experiment which repeated 3 times. From 27 images (4 images x 3 samples x 3 repeats) collected, the

number of attached PC12 cells and neurites and the neurite lengths were analysed as illustrated by the box-whisker plots.

7.3. Results

7.3.1. Mechanical modulus - AFM

The AFM modulus map of the CP samples with and without brushes is shown in Figure 7.1 (a)-(b), respectively. The average indentation modulus of the Hybrid and PEDOT/pTS evaluated from 3 image sets was 176 ± 40 MPa and 185 ± 67 MPa, respectively. The standalone Au was not able to be accurately characterised as a substantially harder tip was not available, but the literature value of 69 GPa was used for comparative purposes [272]. The average indentation modulus of the Brush alone was 143 ± 40 MPa.

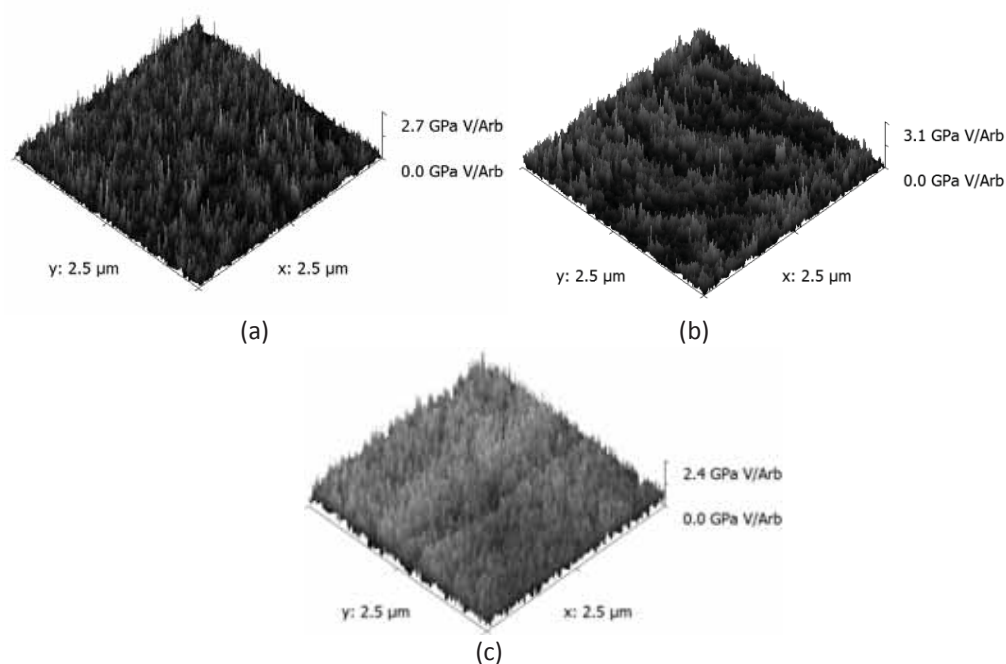


Figure 7.1: The AFM stiffness map of (a) the Hybrid, (b) PEDOT and (c) the Brush.

7.3.2. Electrochemical stability - CV

Figure 7.2 (a) shows cyclic voltammograms of the four samples at cycle 1. The initial CSC of the gold substrate, was $0.86 \pm 0.18 \text{ mC/cm}^2$. Grafting of PHEMA brushes onto the gold substrate reduced the CSC by 62.5 % to $0.27 \pm 0.01 \text{ mC/cm}^2$. The CSC of the Hybrid, $11.08 \pm 0.27 \text{ mC/cm}^2$, was however, higher than that of the PEDOT/pTS, $9.39 \pm 0.64 \text{ mC/cm}^2$. This value is similar to that observed in Chapter 5 for the identical film formed on platinum ($\text{CSC}_{\text{PEDOT/pTS on Pt}} = 10.43 \pm 0.76 \text{ mC/cm}^2$).

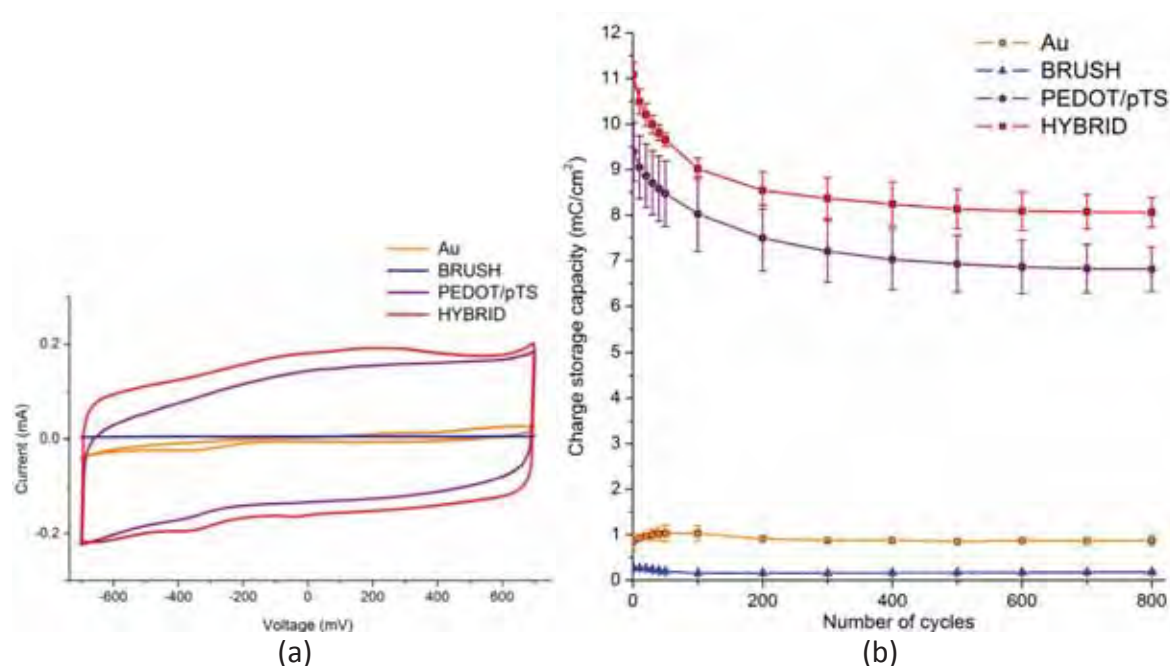


Figure 7.2: (a) The Cyclic voltammogram at cycle 1 and (b) the change in CSC during 800 cycles of Au, PEDOT/pTS, BRUSH and HYBRID in 0.9 % saline ($n=3$, error bar = standard deviation, scan rate = 120 mv/s).

The electrochemical stability of the various materials was examined by the change in CSC during 800 cycles of CV as illustrated in Figure 7.1 (b). The Hybrid exhibited similar electrochemical stability to the conventional CP sample. Both samples followed a similar exponential decay pattern and lost approximately 27 % of the initial CSC after 800 cycles.

The CSC of the hybrid was greater than that of the conventional PEDOT throughout the 800 cycles. When compared to the Au sample, the hybrid provided 9 times higher CSC than the Au sample at cycle 800.

7.3.3. Electrochemical Impedance spectroscopy (EIS)

The impedance spectra of the interface between the sample and 0.9 % saline were measured in the frequency range from 1 Hz to 1 MHz as shown in Figure 7.3 (a). Impedance spectra for the gold and CP samples were similar to those observed for comparable platinum samples shown in chapter 5.

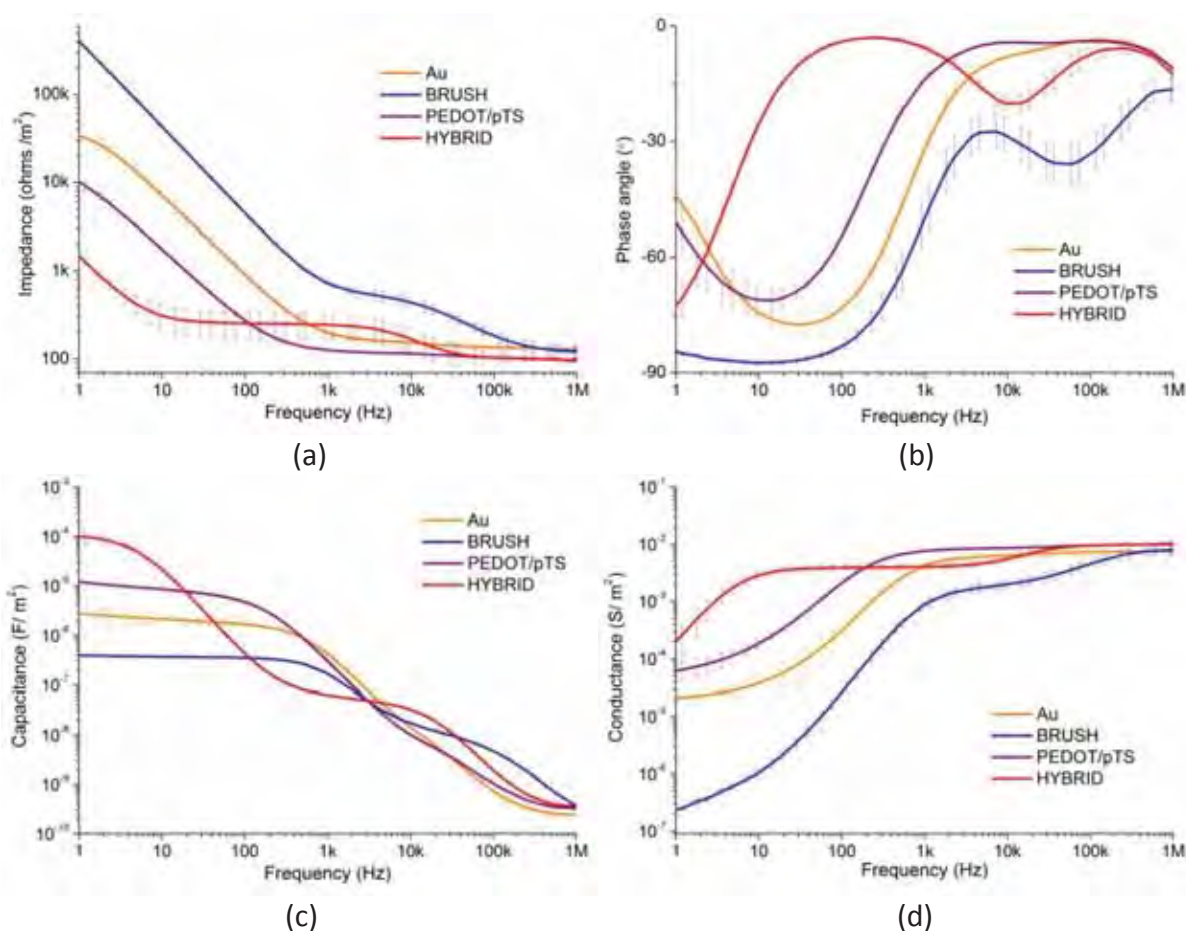


Figure 7.3: (a) the electrical impedance, (b) phase angle, (c) capacitance and (d) conductance of the samples. ($n=3$, error bar = SE).

The Hybrid provides significantly low impedance at frequencies below 100 Hz. At 1 Hz, the impedance of the Hybrid was almost one order of magnitude lower than that of conventional PEDOT/pTS. The low impedance of the hybrid was a result of both high capacitance and conductance as shown in Figure 7.3 (c) and (d), respectively.

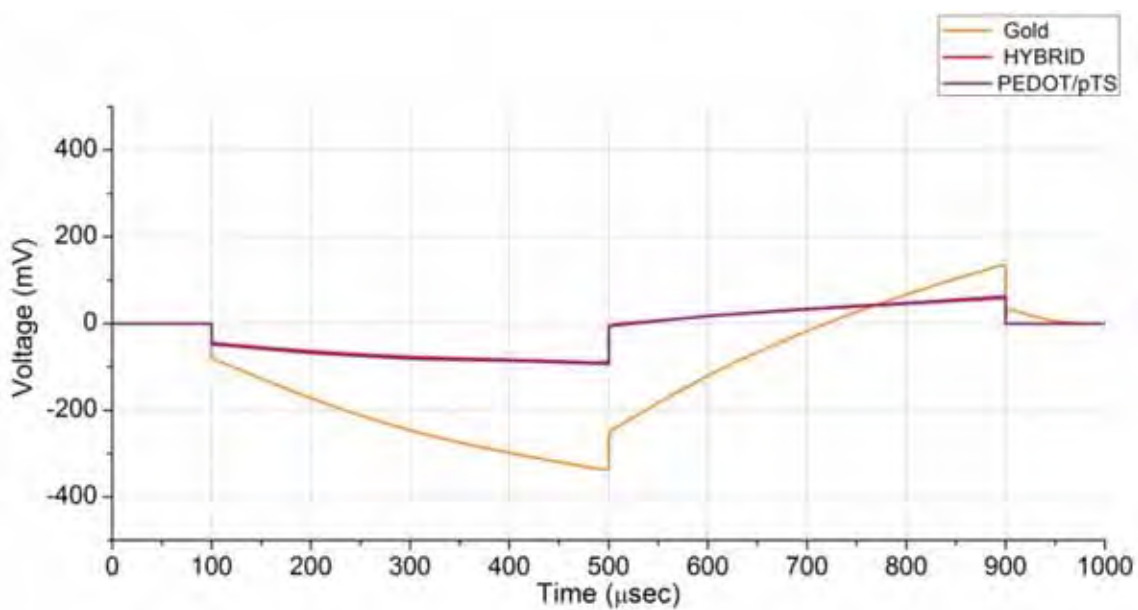
At high frequencies, the electrical behaviour of the Hybrid seems to be strongly influenced by the Brush component. The spectroscopic features of the Brush sample such as the convex on the impedance spectrum (Fig 7-3 (a)), the concave in phase angle spectrum (Fig 7-3 (b)) and the transitions on capacitance and conductance spectra (Fig 7-3 (c) & (d)) are also depicted in the corresponding spectra of the Hybrid.

7.3.4. Biphasic stimulation

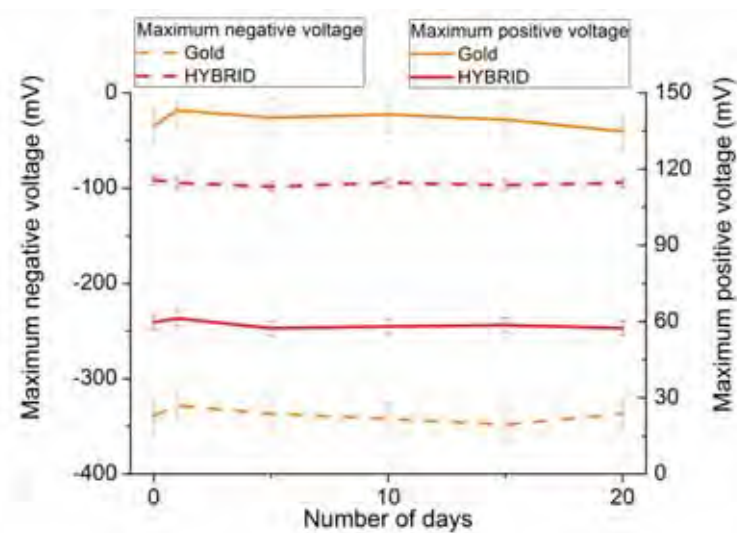
Figure 7.4 (a) shows the voltage responses of the gold, PEDOT/pTS, and Hybrid samples in 0.9 % saline after 3 hr under biphasic current injection. The voltage responses of the Hybrid samples and PEDOT/pTS were almost identical. As a result, their voltage excursions, shown in Figure 7.4 (a), are overlapped. Table 7.1 presents the maximum negative and positive voltages recorded from each sample. Voltages on gold samples were three times higher than those of the Hybrid and CP samples. Figure 7.4 (b) shows the change in the maximum peak voltages of the Hybrid and bare Au samples during biphasic stimulation for 20 consecutive days. Both the samples maintain the initial peak voltages over the testing period.

Table 7.1: The maximum positive and negative voltages recorded after 3h of stimulation

	Gold	HYBRID	PEDOT/pTS
Maximum positive voltage (mV)	137.0	59.8	61.6
Maximum negative voltage (mV)	-339.2	-91.4	-92.3



(a)



(b)

Figure 7.4: (a) Oscilloscopic diagrams of the voltage responses of the gold, PEDOT/pTS, and hybrid samples to the galvanostatic biphasic stimulation with the current amplitude and phase of 0.1 A and 0.4 ms ($3013.6 \mu\text{A}/\text{mm}^2$, $1205.4 \text{ nC}/\text{mm}^2/\text{phase}$). (b) the change in the maximum negative and positive potentials of the gold and HYBRID samples over the stimulation period of 20 days.

7.3.5. PC 12 adhesion and neurite Outgrowth

The fluorescence micrographs of PC12 cells cultured on the Au, Brush, PEDOT/pTS and Hybrid samples are shown in Figure 7.4 (a)-(d), respectively. Figure 7.5 (a) shows the average number of PC12 cells attached on the samples. The PC12 density on the Hybrid, CP and Au samples were close to the seeding density, 25,000 cells/cm². The figure 7.5 (b) clearly indicates that more neurites were differentiated out from the hybrid and CP than from the Au. The average number neurites found on the Hybrid was roughly 14,000 neurites/cm², which is 56 % more than that on the Au, 9,000 neurites/cm². No significant difference in neurite length was observed on different substrates as illustrated in Figure 7.5 (c).

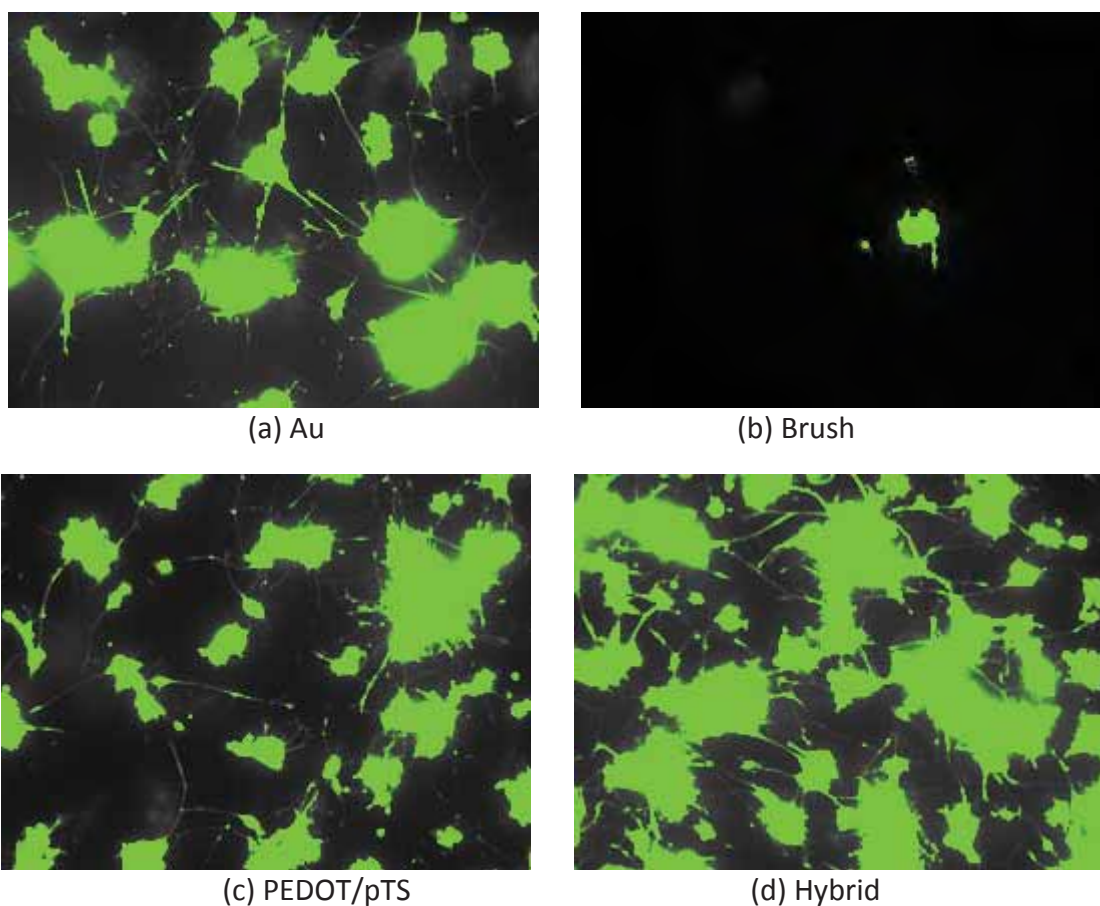


Figure 7.5: Fluorescence micrographs of (a) Au, (b) BRUSH, (c) PEDOT/pTS and (d) Hybrid.

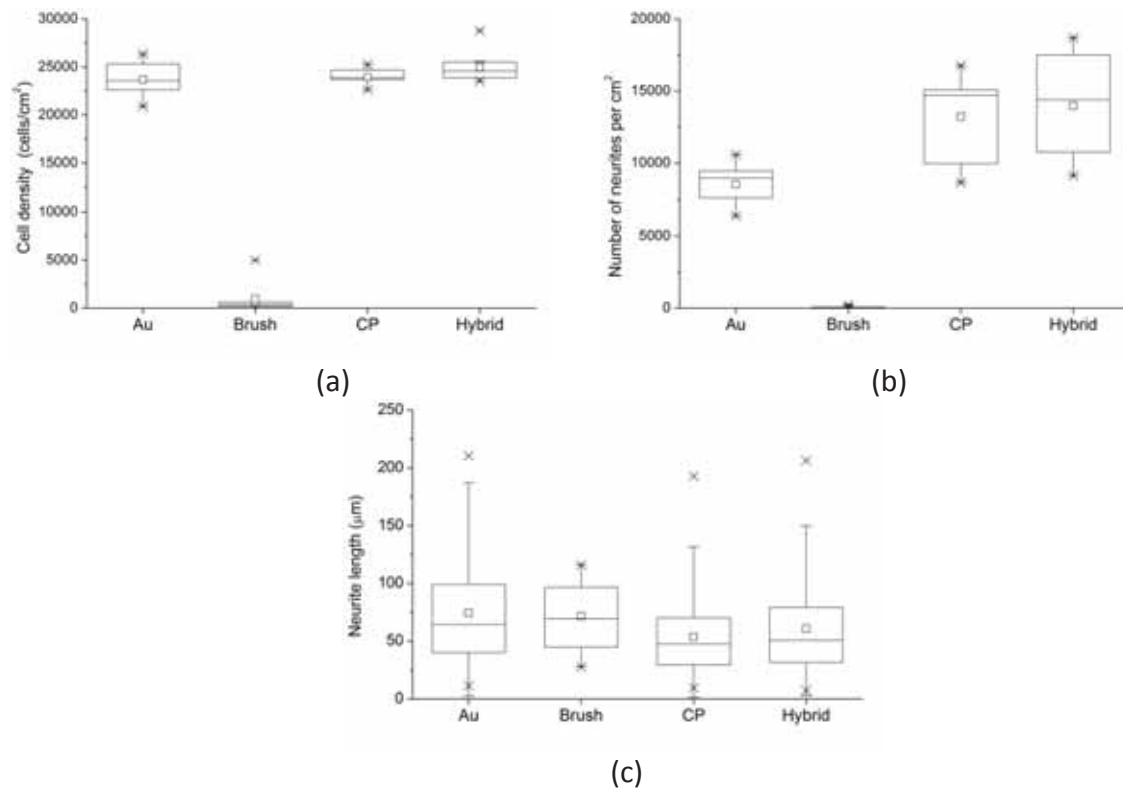


Figure 7.6: The box plots of (a) the PC12 cell density (b) the number of neurites and (c) the neurite length (N=4).

It was clear in Figure 7.4 (b) that surface grafted PHEMA brushes prevented the PC12 cell adhesion. An interesting result was observed at the border region between the Hybrid and the outlying Brush. In Figure 7.6, PC 12 cells were seen to be selectively adhered to the CP coated region in preference to the adjacent brush only region.

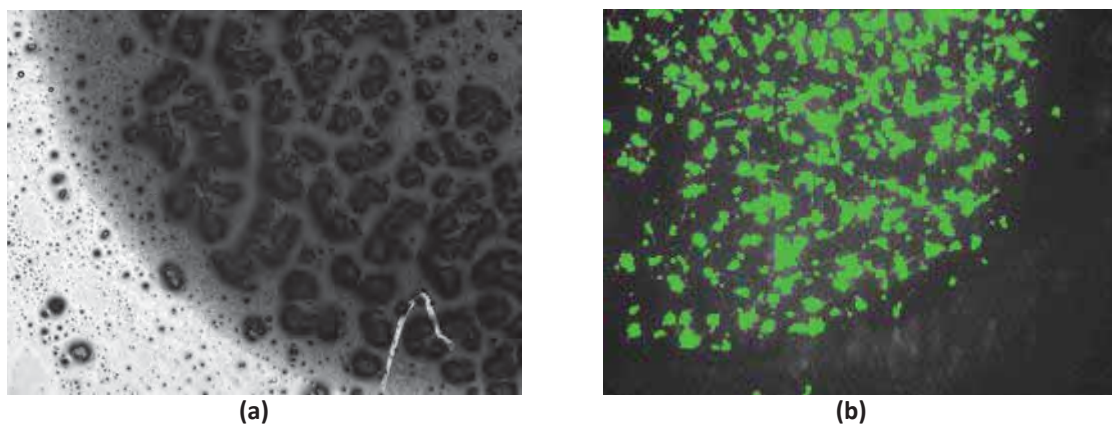


Figure 7.7: (a) The optical and (b) the fluorescence micrograms of the border between the hybrid and the brush/Au. It can be seen that the brush prevents adhesion of PC12 cells.

7.4. Discussion

The hybrid material developed in Chapter 6 has been characterised with respect to neural electrode applications and exhibits properties which suggest it is a feasible material for these biological interfaces. It is significantly softer than conventional metallic electrodes and exhibits superior electrical properties than both Au and PEDOT/pTS, which is sustained under biphasic stimulation regimes.

Although the structure of the hybrid is still largely unknown, impedance spectra shown in Fig 7.4 provides evidence of the brush structure influencing charge transfer through the hybrid. The hybrid and brush samples exhibited distinct impedance characteristics that were not observed on other samples. The mechanical influence of the brush structure was, however, less significant. The AFM study revealed that the stiffness of the hybrid, (176 MPa), was only slightly less than the PEDOT/pTS alone (185 MPa). The limited cushioning effect is likely due to low thickness as well as relatively high mechanical stiffness of the PHEMA brushes (143 MPa). The thickness of dry PHEMA brushes was measured to 17.0 ± 0.5 nm by ellipsometry in Chapter 6. Cross-sectional SEM of the 0.05 C/cm^2 PEDOT/pTS films in Chapter 5 suggest that the CP component is produced at a thickness of $0.1 \text{ }\mu\text{m}$. It is likely that in even in the hydrated state, brushes produced at this length would not extend throughout the material in such a way to mediate the mechanics significantly.

Additionally, the AFM of the brush only structure indicated, that this polymer has an indentation modulus of 143 MPa. The PHEMA brushes were considerably stiffer than

crosslinked PHEMA hydrogels. The indentation modulus of crosslinked PHEMA gels is reported to be $0.82 \pm 0.01 \text{ MPa} \sim 1.57 \pm 0.40 \text{ MPa}$ [273]. It is thought that despite the identical chemistries of these two polymer constructs, the discrepancy in mechanical stiffness is a result of the structural arrangement of the polymer chains. Yamamoto et al. [274] suggests that dense polymer brushes are highly resistant to compression and that the compressibility decreases with increasing brush length. Urayama et al. [275] reports similar findings which suggest that the low compressibility is attributed to the strain-hardening effect and entanglement of brushes. Since thicker brushes are required to offset the thickness of overlying CPs, it is concluded that the brush component of this system would provide greater mechanical benefit if it was fabricated with a polymer which was substantially softer than PHEMA. SI-ATRP of macromonomers containing PEG segments could be one possibility. Neugebauer et al. [276] previously synthesised elastomers with soft rubber like mechanical properties ($G' \sim 10^4 \text{ Pa}$) by ATRP and consequent cross-linking of macromonomers containing PEG segments. Such soft, deformable brushes would provide a conducive environment for the growth and differentiation of neurons.

The hybrid PHEMA/PEDOT structure was shown to function effectively as a neural electrode, with comparable electrical properties to homogenous PEDOT and improved capacitive charge transfer than conventional metallic electrodes. The charge storage capacity (CSC) of the hybrid is 15 times higher than that of Au, and 40 times higher than the Brush prior to CP deposition. Additionally, the hybrid has a CSC 14 % higher than that of the homogenous PEDOT. Impedance results showed similar electrochemical advantages of the Hybrid at low frequency range. At 1 Hz, both the capacitance and

conductance of the hybrid was clearly higher than that of comparable PEDOT/pTS. It is clear that the nanostructure of PHEMA brushes improved the electrochemical properties of the hybrid construct. One possibility is that thicker coatings may have formed due to the limited nucleation sites. Since brushes are occupying the surface of the hybrid, thicker films could form from the same mass of CP. It was previously suggested that the mass of CP formed is largely controlled by the deposition charge [215, 220]. Hence, the Hybrid deposited with 0.05 C/cm^2 is likely to be thicker than the comparable CP film. Physical characterisations at the interface between the brushes and the CP remain as an important future study to understand the full potential of the Hybrid.

Unlike Faradaic electrodes such as iridium oxide, which have previously suffered the brittle fracture and delamination upon the continuous biphasic stimulation [277], the hybrid was both electrochemically and physically stable under continuous biphasic stimulation at 37°C for 20 days. While a direct comparison between biphasic studies is difficult due to various stimulation schemes, the charge injection density, $121 \mu\text{C/cm}^2$, used in this study is comparable to the threshold density required to excite neural tissue in the literature. Branner et al. reported the threshold charge density of $96 \mu\text{C/cm}^2$ for stimulation of cat sciatic nerve [278]. The threshold charge density for stimulating human cortex was reported to $11 \mu\text{C/cm}^2$ by Hambrecht [279].

The biological stability was also supported by the neural cell adherence and outgrowth study. The hybrid promoted both PC12 adhesion and outgrowth, demonstrating that the PEDOT surface was accessible to cells and dominant over the antifouling brush structure. The protein and cell repelling properties of PHEMA brushes have been reported widely

and the consequent use of the brush layer as an antifouling surface has been studied by Yoshikawa et al. [230]. This result further confirms that when the hybrid is produced with these fabrication parameters, the PEDOT is thicker than the brush structure and hence dominant in determining material properties.

However, it is also shown that the selective electrodeposition of CP on the brush layer can provide a facile method of creating an electric contact with selective cell binding. The design of cell specific binding electrodes has been pursued by Tourovskaia et al. [280], but the processes are often complicated, involving multiple masking and etching steps. Hence, it is proposed that with minor manipulation, this hybrid material could provide a relatively simple process for cell selective electrodes. Additionally, Palanker et al. [281] suggested that the fabrication of microelectrodes with specific cell binding would increase the spatial resolution of neural stimulation. As a result, future studies will also look to adapt the processes detailed in Chapter 6 and 7 for application to microelectrode arrays.

The hybrid characterised in this chapter shows a promising combination of properties. However, there remains significant potential to optimise the structure of hybrid. Since the capacitance is directly related to the thickness of dielectric layer, the density and length of brushes influence the overall electrical properties of the hybrid. It is clear that an important next step is to investigate the optimal thickness for the CP component to allow a more significant contribution from the brush component to the overall material properties. Future studies will also encompass the cell culture under stimulation condition to elaborate the benefits of the hybrids in neural stimulation applications.

7.5. Conclusion

The PHEMA nanobrushes fabricated via SI-ATRP techniques provide a unique building block to form a new type of CP hybrid. The synergistic incorporation of PEDOT and PHEMA brushes resulted in desirable electrical properties such as high CSC and highly capacitive charge transfer for neural applications. Using the contradictory cell/protein adhesion properties of the brush and the hybrid can be used as an electric contact providing selective cell binding. Future work will optimise the density, length and type of brush combined with definition of the ideal thickness for CPs to produce an integrated functional electrode coating.

CHAPTER 8.

Final Conclusion and Recommendations

8.1. Conclusion

The main aim of this thesis was to understand and improve the physical cues of electrodeposited PEDOT films for enhancing neural electrode interfaces. PEDOT coatings doped with non-nucleophilic dopants have tremendous potential in neural applications. The realisation of this potential has been brought closer by the designs explored in this thesis. Physical characteristics such as surface morphology and roughness, softness and elasticity can be controlled by the choice of a dopant and the amount of charge applied to make a film. Non-nucleophilic dopants are essential for producing coatings with high stability and electroactivity.

PEDOT coatings doped with five non-nucleophilic anions were analysed in terms of physical, electrochemical and biological properties. Nanoindentation results indicated that the elastic modulus increased with the size of the dopant. Attachment of a benzene ring as well as an aliphatic chain on the dopant anion resulted in stiffer films. The size of surface features decreased with increasing dopant size. Long aliphatic chains increased not only the dopant size but also the chain packing order as well as steric hindrance. As a result, films doped with smaller non-aliphatic dopants such as ClO_4 , BS and pTS exhibited nodular morphology and provided higher charge storage capacity and electrochemical conductivity than those doped with larger aliphatic dopants, DBS and PSS. The intrinsic toxicity of the dopant increased with the hydrophobicity of the dopant. The adhesion and neurite outgrowth of PC12 cells on PEDOT films was influenced by both the surface topography and toxicity of the dopant. Highly nodular films formed with low toxicity dopants such as pTS and BS inhibited PC12 adhesion. ClO_4 and PSS were more toxic than

BS or pTS but the resulting films showed good PC12 compatibility. It was concluded that the ideal biological interactions which can be achieved with CPs requires balance between the desired physical cues and required dopant chemistry.

To improve the biocompatibility, it was proposed that surface nodularity and film thickness could be modified by controlling the amount of charge applied to make a film and that resultant films would support improved cell interactions. In Chapter 5, it was found that the size and roughness of surface nodules as well as the electrical properties such as charge storage capacity and electrochemical conductance decreased with decreasing deposition charge. Nonetheless, even the thinnest films deposited with 0.05 C/cm² provided 15 times lower impedance at 1 Hz and 5 times higher charge storage capacity than conventional platinum electrodes. PC12 cell adhesion and neurite outgrowth were greatly improved with decreasing film thickness. Thin PEDOT/pTS films formed with the charge of 0.05 C/cm² showed optimal PC12 performance among the samples tested, including pristine platinum. Since the distance between neurons and electrodes is one of the factors determining the stimulation performance as well as the chronic function of neural implants [19, 282], thin PEDOT/pTS presents a suitable candidate for neural electrode applications with improved electrical performance and biological interactions.

To further improve the physical cues of CPs, the next stage of the research developed a hybrid coating consisting of hydrophilic PHEMA nanobrushes integrated with electrodeposited thin film CP. PHEMA nanobrushes were grafted from a SAM initiator on a gold surface using surface-initiated atom transfer radical polymerisation (SI-ATRP). Thin

PEDOT/pTS films were successfully electrodeposited through the PHEMA brushes to form a novel hybrid structure. Chemical characterisation indicated that the PEDOT/pTS was formed and that both material components were present in the hybrid. It was concluded that defects in the underlying initiator monolayer can be successfully utilised as nucleation sites for PEDOT polymerisation, enabling both the CP and hydrophilic brush to occupy the same coating volume.

The resulting hybrid was characterised in terms of physical, electrochemical and biological properties. AFM peak-force nanomechanical mapping showed a small reduction of elastic modulus when the brushes were incorporated into the CP layer. The brush structures in the hybrid have the capacity to modify coating mechanics, however further optimisation of the brush length and density is required to further improve the mechanical properties. The charge storage capacity of the hybrid was 18% higher than that of a conventional CP coating and the electrical impedance at 1 Hz of the hybrid was approximately one order of magnitude lower than that of PEDOT/pTS. Electrical performance is likely to be influenced by the nucleation and growth of PEDOT films in presence of the brushes. The hybrid supported PC12 cell adhesion and promoted significantly higher levels of neurite outgrowth than gold substrate alone. In contrast, the cell adhesion was prevented in the region surrounding the hybrid where PHEMA alone was present. This material system also has potential to provide significant advantage in biomedical applications where patterning of brush and hybrid areas within the same coating application will promote selective cell binding.

In conclusion, it was found that topographical and biochemical cues can be used to develop optimal materials for neural interfaces with beneficial electrical, mechanical and biological properties. These CP based materials require trade-offs between each of the desired properties, but can still provide significant benefit in all performance metrics when produced on the nanoscale. A new material concept consisting of a nanobrush-CP hybrid has been developed for neural stimulating applications, with a flexible design, such that it can be tailored to a wider range of medical applications. Future studies will enable a greater understanding of the hybrid structure and function to support further optimisation and realisation of the full potential of the hybrid.

8.2. Future Work and Recommendations

Figure 8.1 shows a concept (C) – knowledge (K) diagram outlining the design logic and flow of this thesis. In C-K theory, each concept provides new knowledge and the knowledge gained is used to generate new concepts. Based on the previous knowledge, shown in the red box in the upper right of Figure 8.1, it was proposed that the neural interactions with PEDOT films could be improved by controlling the physical properties such as surface topography and elastic modulus. This became the key concept of this thesis, shown in the black box in the upper-left of Figure 8.1.

New knowledge gained throughout the research presented in this thesis is shown in the blue box in the lower-right of Figure 8.1. The gained knowledge suggested that the formation of flat PEDOT films on hydrophilic brush layers is a promising concept to modulate neural interactions as well as electrochemical properties. The hybrid is

composed of CP and substrate-bound polymer brushes. The versatility of the hybrid design comes from the modification, incorporation, and optimisation of each component. Nonetheless, the research conducted in this thesis developed the concept and verified proof of concept using one variation of the hybrid based on maximum density and length of PHEMA brushes. There are a number of unknowns that should be addressed in order to further understand the brush-CP interactions and to realise the full potential of the hybrid. Future studies and concepts, shown in the lower-left of Figure 8.1, are suggested to address questions related to these unknowns as well as to further improve the function of the hybrid for biomedical applications.

Recommendations

The details of the recommendations for future work proposed are outlined in the following sections.

- 1. Optimisation of brush geometry and species.

While the research in this thesis provided proof of concept of the brush-CP approach, there are several variables relating to brush density, length and chemistry that should be further investigated. Variation of polymer brush density could be achieved by co-immobilisation of alkane thiols with surface-initiating thiols. Given that the CP tends to deposit rapidly and results in considerably thicker films than the brush length, grafting of longer polymer chains on the surface may allow greater control of the mechanics. This

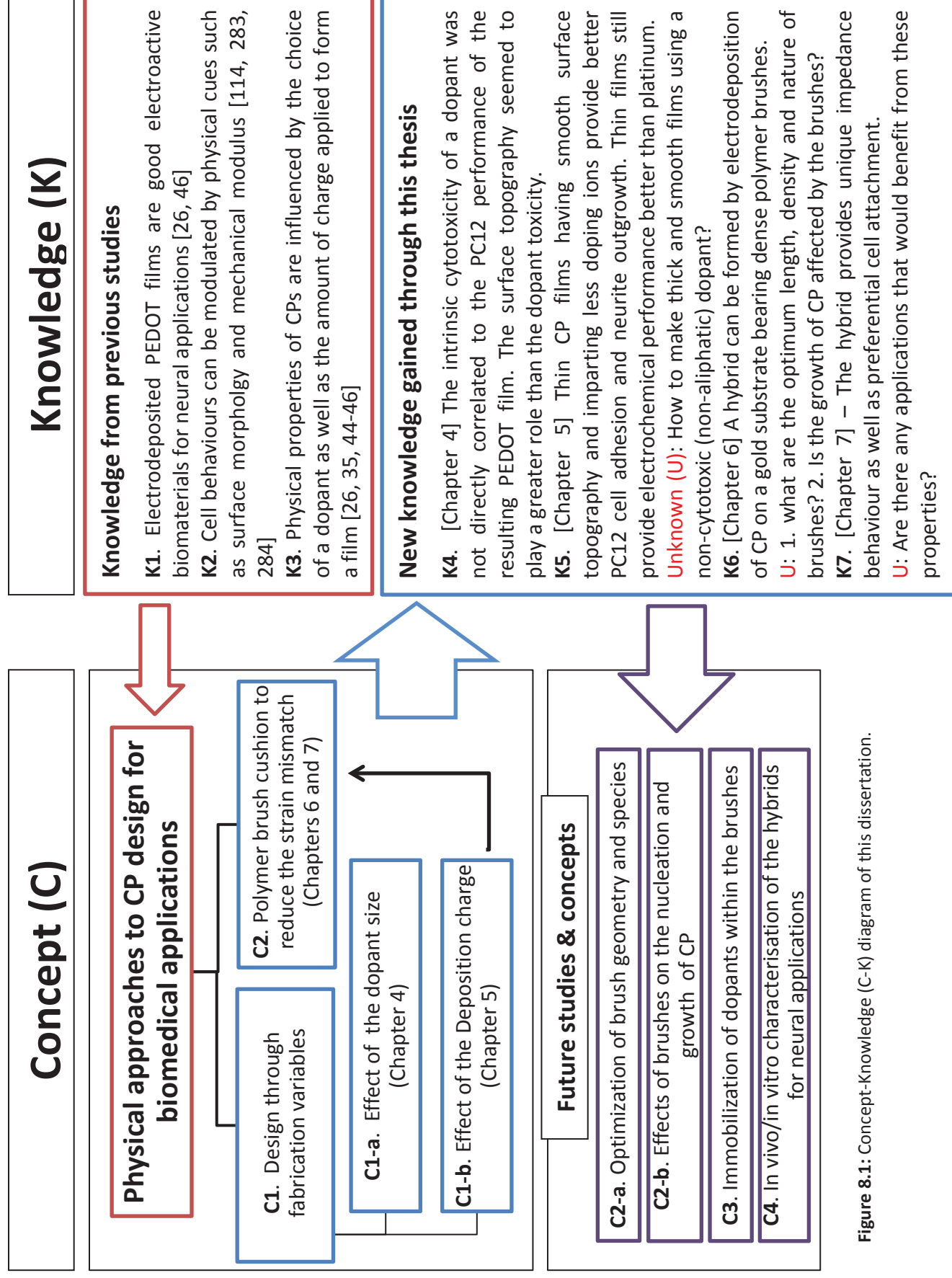


Figure 8.1: Concept-Knowledge (C-K) diagram of this dissertation.

could be achieved by water accelerated ATRP reactions. Modifying the chemistry of the brushes may also have significant impact on the interactions with this CP. For example, more hydrophilic polymers will absorb more water and are therefore likely to provide softer brushes. In summary, studying a range of chemical species and geometries has significant potential to improve the integration of CP with brush and the mechanical cushioning effect and hence neural compatibility of the resulting hybrid.

- 2. Effects of brushes on the nucleation and growth of CP

The nucleation and growth of CP is likely to be affected by the presence of the brushes on the substrate. Electrochemical polymerisation is a combination of instantaneous two dimensional (2-D) and three dimensional (3-D) and 3-D nucleation mechanisms [218]. That is, for 2-D, growth is limited to parallel to the substrate and for 3-D, growth is in both parallel and perpendicular directions. At the initial stage of nucleation, 2-D growth is likely to be affected by the physical hindrance of brushes. By controlling the passage of charge, different stages of the electropolymerisation process can be monitored. Chronoamperometry can be performed to monitor the nucleation mechanism. Observation of CP growth on the brushes will provide an insight into the physical and electrochemical structures of the hybrid. The knowledge of the growth mechanism and structure will help in developing the design strategies as well as the fundamental understanding of the hybrid as an electroactive biomaterial.

- 3. Immobilisation of dopants within the brushes

Brushes could be used to immobilise dopant anions on the substrate which could improve the adhesion of the CP to the substrate as well as enhancing electrical properties. The cytotoxicity associated with the release of the dopant could also be reduced. SI-ATRP of PSS has been reported previously [285] Brushes made of PSS could act as surface-bound dopants. Figure 8.2 outlines a strategy to immobilise dopant anions between brushes. Distance between brushes could be controlled by stamping of non-initiating thiols on gold substrate. Subsequently, ATRP initiating thiols could be self-assembled on the substrate and using the ATRP process, brushes could be formed. Dopants or other functional chemicals attached onto brushes either as crosslinkers or pendants theoretically could enhance the CP integration and thus impact on film properties. Myriads of configurations are possible using different brush and dopant species.

Figure 8.2 presents a method to deposit hybrids in a specific pattern. A particular design shown in the figure utilises hydrophilic brushes with hydrophobic chemicals. EDOT is a hydrophobic liquid at room temperature. Selective adsorption of EDOT in the hydrophobic region would lead to a formation of CP islands surrounded by the sea of hydrophilic brushes.

Nanobrush CP hybrids present the potential for developing a new type of soft electroactive biomaterial that can benefit from the mechanical properties of the brushes and the electrochemical properties of CPs. This research presented only the beginning of what can be done with nanostructured brushes and CPs. Understanding the CP growth

through or onto the brushes will be the key to realising the potential of this material system. Optimisation of brush geometries and chemistry will be an important next step to enabling the ideal function of brushes as a cushion for CPs.

- 4. In-vitro/in-vivo characterisation of the hybrids for neural stimulation/recording applications

Finally, it is hypothesised that the contrasting electrical and biological properties of hybrids and brushes could be used to improve the function of neural interface. In-vitro and in-vivo characterisation of the hybrids under passive and stimulation conditions will be explored to elaborate the benefits of the hybrids in neural applications. The brush coated gold substrates were shown to provide low electrochemical activity and low cell adhesion whereas the hybrid provided high electrochemical activity and high cell adhesion. Such clear contrasts in electrochemical and biological properties would improve the signal to noise ratio and direct the cell growth in confined regions of electrodes. Hence, this could help to increase the spatial selectivity of the neural signals.

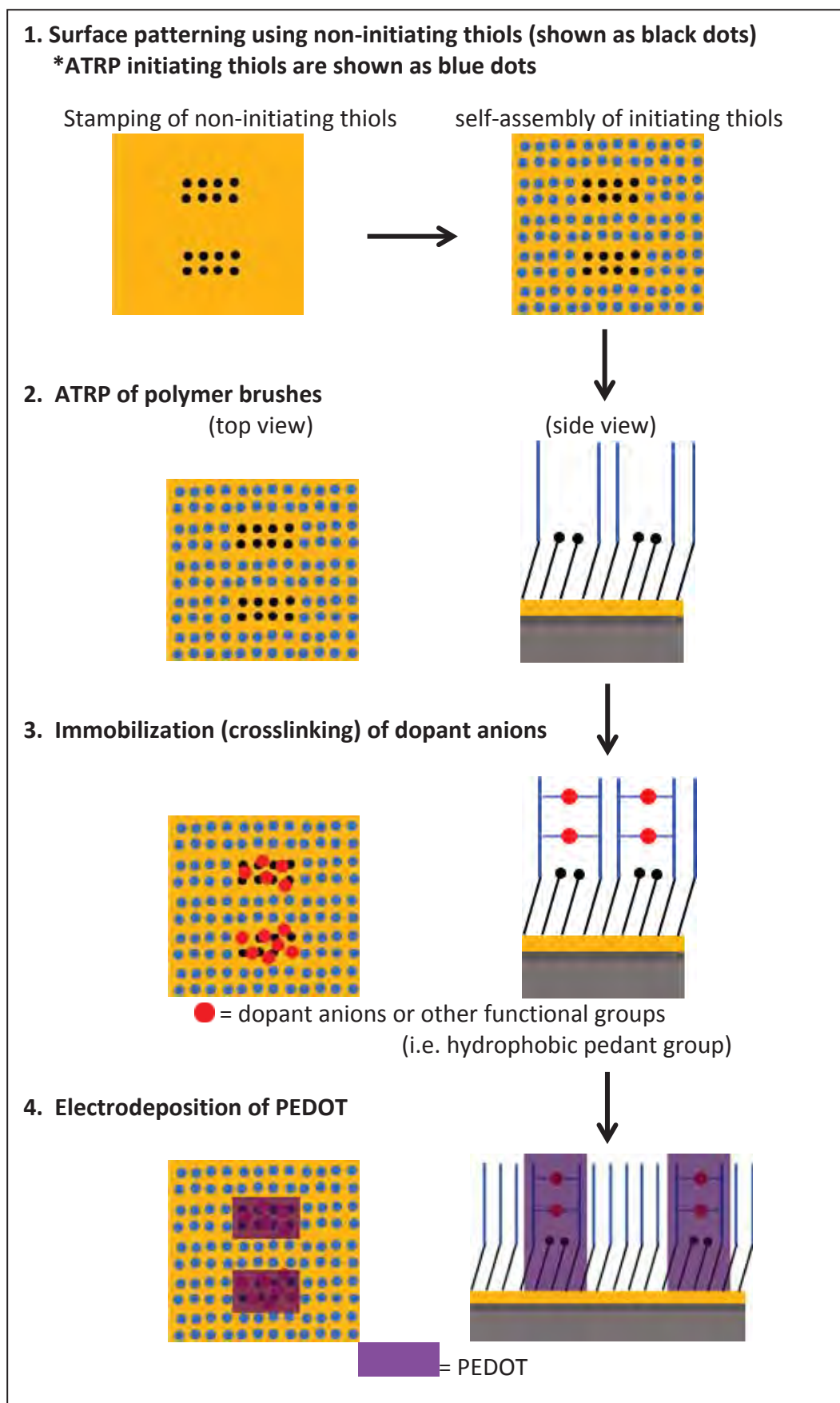


Figure 8.2: Schematics of the formation of the hybrid with dopant anions (or other functional chemicals) immobilised between the brushes.

Appendices

APPENDIX A. Mechanical and Electrical properties of PEDOT and PPy

Table A.1: Mechanical properties of PEDOT and PPy

monomer/ dopant (ratio)	Solvent	Substrate	Deposition method	Testing method	Result	Reference
PEDOT/CIO ₄ (0.01M/0.01M)	H ₂ O	Au	0.5 mA/cm ²	Nanoindentation (Berkovich indenter)	Qualitative Measurement	[35]
PEDOT/CIO ₄ (0.1M/0.1M)	ACN or PC	Au	1.20~1.25 V	Acoustic impedance	Unit: pa G' (ACN)= 10 ^{5.4~5.7} G''(ACN)= 10 ^{5.7~6.6} G' (PC) = 10 ^{5.8~6.4} G''(PC) = 10 ^{6.0~7.1}	[288]
PEDOT/PSS [Baytron P] 1 : 20 (by wt)	Solvent-casting in a polystyrene petri dish			Micro-tensile	1 < E < 2.7GPa 25 < σ < 55MPa	[77]
PEDOT/PSS [Baytron P] VPA14083	Spin-coating on PDMS substrate			Buckling	2.26 ± 0.05 GPa	[289]
PPy/pTS (0.2M/0.05M)	Not available		3 mA/cm ²	In situ Micro-tensile in 1M NaCl	E = 3.6 GPa	[290]
PPy/TEAPF ₆ (0.05 M/0.05 M)	H ₂ O +1vol% PC	Glassy Carbon	0.5 mA/cm ² for 18h	DMA	100< E < 350 MPa	[291]
PPy/CIO ₄ (0.2 M/0.1 M)	ACN + 2% H ₂ O	AISI 304 SS	Square wave -372 mV for 2s 872 mV for 8s Polarized at 720 mV Total Q = 27 C	Micro-tensile	310 MPa (Dry) 180 MPa (wet)	[292]
PPy/CIO ₄ (0.5 M/0.1 M)	H ₂ O	SS	2 C/cm ²	Hardness testing (Vickers indenter)	Average hardness 280 mN/m ²	[293]
PPy/CIO ₄ PPy/pTS (0.05 M/0.1 M)	H ₂ O	Au	0.2 ~ 0.7 V vs.SCE	Acoustic impedance	G' = 6 x 10 ⁶ (CIO ₄) 2.5 x 10 ⁸ (pTS) G' = 2 x 10 ⁶ (CIO ₄) 1.1x 10 ⁸ (pTS)	[294]

- Note: if a CP system does not contain sulfur (e.g. PPy doped with ClO₄ or TEAPF₆), the adhesion between the electrodeposited CP and a metal substrate is weak. Hence, these films were peeled off from the substrate and tested using techniques requiring free standing samples.

Table A.2: Electrical properties of PEDOT and PPY

monomer/ dopant (ratio)	Solvent	Substrate	Deposition method	Testing method	Result	Reference
Electrochemical stability						
PPY/PSS (0.1M/0.05M)	H ₂ O	Pt	1.5 mA/cm ² (0.9 C/cm ²)	CV (-700-600 mV) at 120 mV/s for 400 cycles in 0.9% saline	38% charge capacity retained	[295]
PEDOT/pTS (0.1M/0.05M)	50% H ₂ O/ ACN				90% charge capacity retained	
PEDOT/PSS (0.01M/0.1M)	H ₂ O	Au	no specific setting (either 0.5 ~ 2 mA/cm ² or 1.1V)	Cyclic voltammetry (-900-500 mV) at 100 mV/s for 400 cycles in DI water	PEDOT/PSS retained more charge than PPy/PSS	[296]
PPY/PSS (unknown)	Unknown					
Electrical conductivity						
PPY/PSS (0.1M/0.05M)	H ₂ O	Pt	1.5 mA/cm ² (0.9 C/cm ²)	Four point probe test	18.24 S/cm	[295]
PEDOT/pTS (0.1M/0.05M)	50% H ₂ O/ACN				88.84 S/cm	
PPY/BS (0.2M/0.3M)	H ₂ O	ITO	0.3mA/cm ² (1.2C/cm ²) @ 0°C		110 S/cm	[297]
PPY/pTS (0.2M/0.3M)					160 S/cm	
PPY/DBS (0.2M/0.3M)					14 S/cm	
PPY/BS (0.1M/0.1M)	2% H ₂ O/ACN	ITO	2mA/cm ² (27.7C/cm ²)		81S/cm	[44]
PPY/pTS (0.1M/0.1M)	H ₂ O	Au			121 S/cm	
PPY/DBS (0.1M/0.1M)					29 S/cm	
PPY/PSS (0.1M/0.1M)					9 S/cm	
PPY/Cl (0.1M/0.1M)	H ₂ O	ITO or Au	96mV/cm ² (0.084C/cm ²)		~3 S/cm	[96]
PPY/ pTS (0.1M/0.1M)					~ 53 S/cm	
PPy/PSS (0.1M/0.1M)					~6 S/cm	

APPENDIX B. Determination of the water window for CV

The standard potential (E^0) of the Ag/AgCl/3 M KCl reference electrode was considered to be $E^0 = + 0.209$ V versus standard hydrogen electrode (SHE) at 25 °C [298]. The potential sweep range was adopted from the water electrolysis window. The reduction (E_{red}) and oxidation (E_{ox}) potentials of water at pH level are illustrated in the Pourbaix diagram shown in Figure A.1 [299] and are thermodynamically defined by the following equations based on the Nernst equation:

$$2\text{H}_2\text{O} = \text{O}_2(\text{g}) + 4\text{H}^+ + 4\text{e}^- E_{ox} = 1.228 - 0.0591 \text{ pH (vs. SHE)} \quad (\text{Equation A.1})$$

$$2\text{H}_2\text{O} + 2\text{e}^- = \text{H}_2(\text{g}) + 2\text{OH}^- E_{red} = 0.000 - 0.0591 \text{ pH (vs. SHE)} \quad (\text{Equation A.2})$$

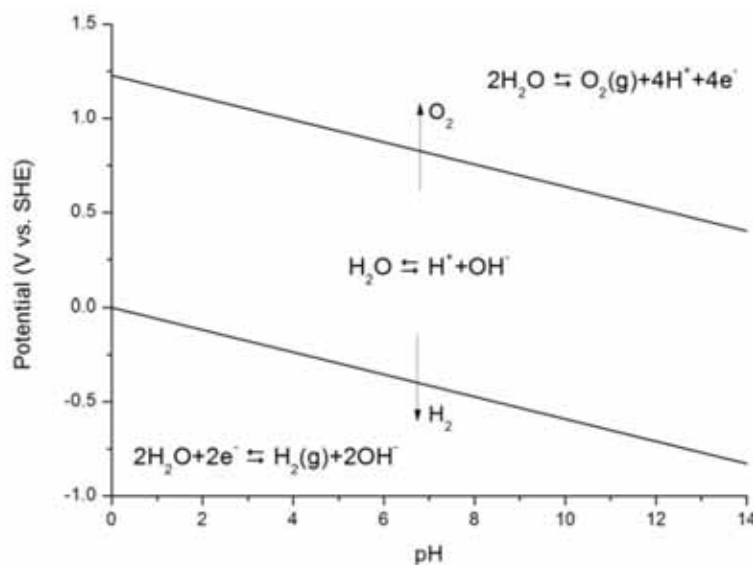


Figure A.1: Pourbaix diagram of water at 25 °C, 1 atm.

From the Equations A.1 and A.2, the water electrolysis window at pH 5.5 is determined to be $-0.325 \text{ V} \sim +0.903 \text{ V}$ versus SHE. This range is equivalent to $-0.534 \text{ V} \sim +0.694 \text{ V}$ versus Ag/AgCl/3M KCl. However, it is well known that the overpotential losses in electrochemical reactions broaden the water window. Cogan [19] defined the water

window for platinum electrode as -0.6 V to 0.8 V versus Ag/AgCl in phosphate buffered saline (PBS, pH = 7.2). Martin et al. [34, 35, 80, 226, 300] used the window of -0.9 V to 0.5 V versus saturated calomel electrode ($E^0 = +0.241$ vs. SHE, or $E^0 = +0.032$ vs. 3 M Ag/AgCl [298]) for PEDOT films in PBS (pH = 7). The common window size in these studies was 1.4 V.

Figure A.2 shows the cyclic voltammograms of PEDOT/DBS measured at three different scan ranges, ± 0.6 , ± 0.7 , and ± 0.8 V. A reduction tail, where water was reduced to hydrogen gas, was observed at -0.8 V. To avoid this irreversible reduction, while keeping the common window size of 1.4 V in the literature, the scan range was set to ± 0.7 V. However, it is apparent in the figure that water was not oxidized even at 0.8 V. This indicates that a broader scanning range is also possible.

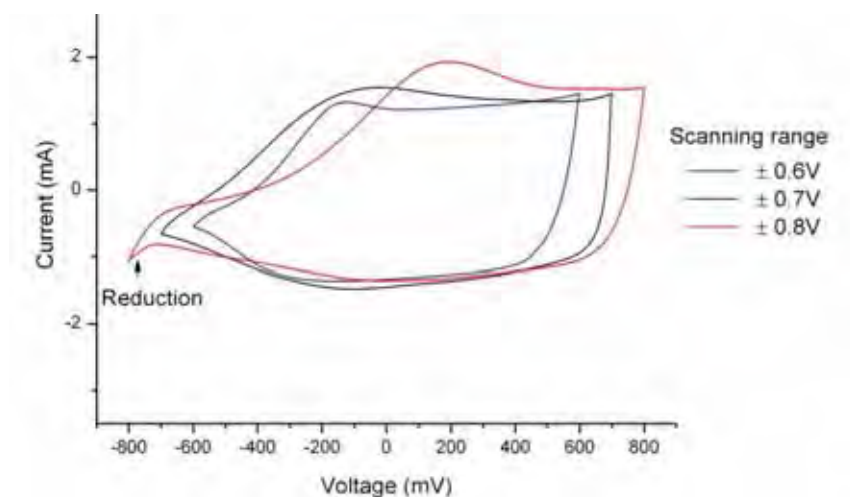


Figure A.2: Cyclic voltammograms of PEDOT/DBS with scan ranges of ± 0.6 , ± 0.7 , and ± 0.8 V. The graphs represent the 200th cycle measured versus 3M AgCl. Scan rate was 120 mV/s and Pt counter was used.

APPENDIX C. Statistical analysis of Indentation data

Shapiro-Wilk normality test was performed using OriginPro 8.0 (OriginLab Coporation). The result shown in Table A.3 indicated that the data was not significantly drawn from a normally distributed population with 95% confidence. The distribution of the indentation data is illustrated by histograms shown in Figure A.3

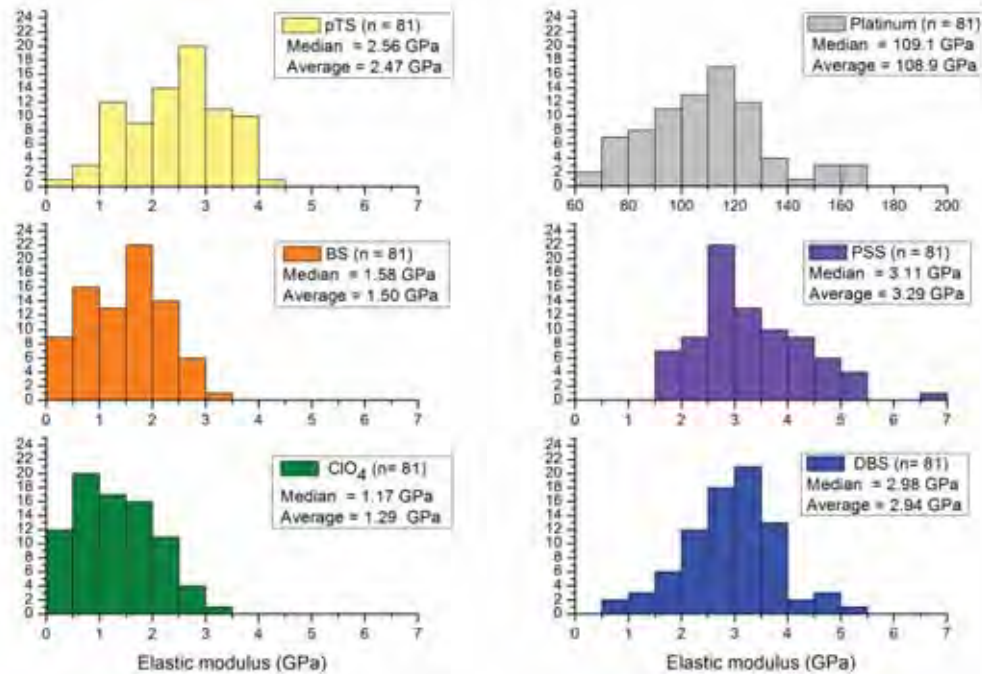


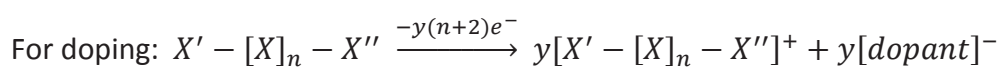
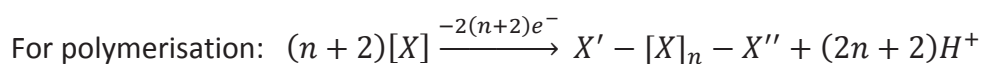
Figure A.3: Histogram of indentation data.

Table A.3: The result of Shapiro-Wilk normality test

Indentation sample	DF	Statistic	Prob<W
ClO ₄	81	0.95833	0.01
BS	81	0.96543	0.02761
pTS	81	0.97989	0.23289
DBS	81	0.98864	0.69947
PSS	81	0.95484	0.00616
Pt	81	0.96708	0.03514

APPENDIX D. Stoichiometric calculation of the amount and thickness of CP formed

The stoichiometry of electrochemical polymerisation of CPs [216] can be represented by following equations:

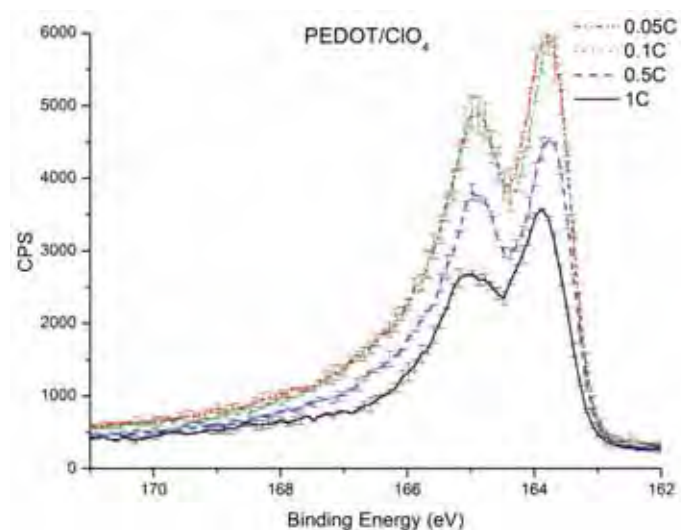


where X is monomer and y is the doping ratio, a ratio of number of dopant per monomer, which can be determined by XPS as shown by Zotti et al. [199]. Figure A.4 shows the S(2p) XPS peaks of PEDOT coatings doped with pTS, ClO_4 and PSS prepared with the deposition of 0.05, 0.1, 0.5 and 1 C/cm². XPS was performed according to methods described in Section 6.2. The doping ratio was calculated by comparing the enclosed area of the PEDOT peaks, 163.84 and 164.74 eV, and the dopant peak, >165 eV. The doping ratio is summarised in Table A.4.

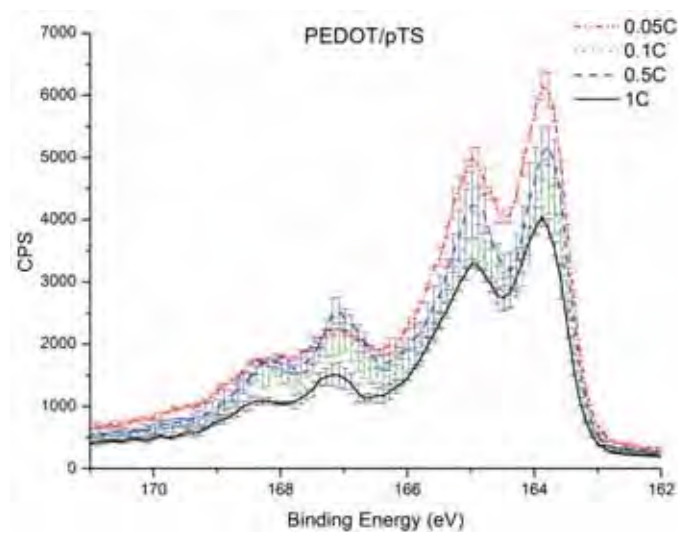
The amount W_{cp} and the thickness δ of the electrochemically prepared CP can be estimated from the stoichiometry shown above and can be presented by the following equations assuming the charge transfer efficiency of 100 %:

$$W_{CP} = \frac{q}{F} \times EW, \quad (\text{Equation A.3}),$$

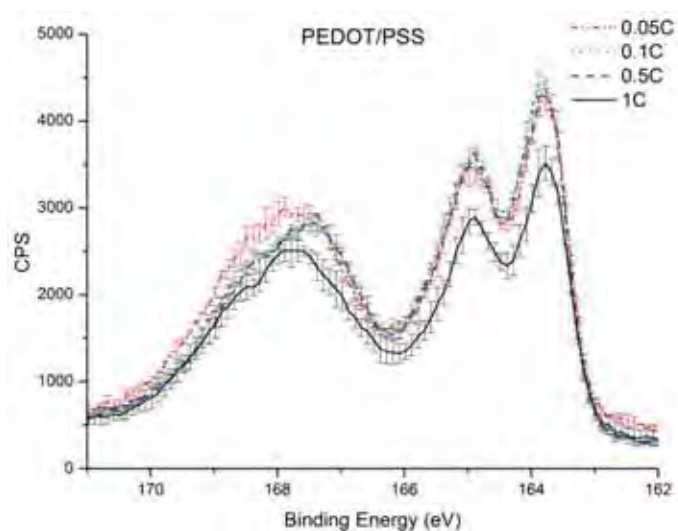
$$\delta = \frac{jt}{F} \times EW \times \frac{1}{\rho}, \quad (\text{Equation A.4}),$$



(a)



(b)



(c)

Figure A.4: S(2p) XPS signals from (a) PEDOT/CIO₄, (b) PEDOT/pTS and (c) PEDOT/PSS formed with the deposition charge of 0.05, 0.1, 0.5 and 1 C/cm².

where q is the total charge applied across the surface area ($j \times t \times$ planar surface area of the electrode), j is the current density (A/cm^2), t is the deposition time (s), F is the Faraday constant ($96,485.3365 \text{ C}/\text{mol}$). EW is the equivalent weight of CP formed per mole of electrons (g/mol), and ρ is the film density (g/cm^3), which is estimated at $1.64 \text{ g}/\text{cm}^3$ for PEDOT, based on a structural model [200].

The EW is calculated by dividing the MW of a single monomer-dopant unit by the number of electrons consumed to form the unit and is given by the following equation:

$$EW = \frac{(MW \text{ of } EDOT - 2 \times MW \text{ of } H) + y (MW \text{ of a doping anion})}{2+y}, \text{ (Equation A.5).}$$

Table A.4 summarises the doping ratio, EW , W_{cp} and δ of PEDOT/ ClO_4 , pTS and PSS prepared with charge of 0.05, 0.1, 0.5 and $1 \text{ C}/\text{cm}^2$. The amount of dopant W_{dopant} is given by multiplying the total amount W_{cp} with the doping ratio.

Table A.4: The doping ratio, equivalent molecular weight EW , theoretical total amount W_{cp} , and theoretical thickness of PEDOT/ ClO_4 , pTS and PSS prepared with the deposition charge of 0.05, 0.1, 0.5 and $1 \text{ C}/\text{cm}^2$. The theoretical amount of dopant in the film W_{dopant} is also calculated

	Deposition charge (C/cm^2)	Avg. Doping ratio y (No. dopant per monomer)	EW (g/mol)	W_{cp} (mg)	δ (μm)	W_{dopant} (mg)
ClO_4	0.05	0.27	73.58	0.01	0.23	0.003
	0.1	0.39	74.87	0.03	0.47	0.010
	0.5	0.38	74.77	0.13	2.36	0.049
	1	0.32	74.13	0.25	4.68	0.082
pTS	0.05	0.29	82.89	0.01	0.26	0.004
	0.1	0.36	85.51	0.03	0.54	0.011
	0.5	0.36	85.51	0.15	2.70	0.053
	1	0.35	85.14	0.29	5.38	0.102
PSS	0.05	0.70	98.63	0.02	0.31	0.012
	0.1	0.62	96.14	0.03	0.61	0.020
	0.5	0.63	96.46	0.17	3.05	0.104
	1	0.69	98.33	0.34	6.21	0.233

References

1. Normann, R.A., et al., *A neural interface for a cortical vision prosthesis*. Vision Research, 1999. **39**(15): p. 2577-2587.
2. Zrenner, E., *Will retinal implants restore vision?* Science, 2002. **295**(5557): p. 1022-1025.
3. Humayun, M.S., et al., *Visual perception in a blind subject with a chronic microelectronic retinal prosthesis*. Vision Research, 2003. **43**(24): p. 2573-2581.
4. Wilson, B.S., et al., *Better speech recognition with cochlear implants*. Nature, 1991. **352**(6332): p. 236-238.
5. Von Ilberg, C., et al., *Electric-acoustic stimulation of the auditory system. New technology for severe hearing loss*. ORL, 1999. **61**(6): p. 334-340.
6. Shannon, R.V., *Multichannel electrical stimulation of the auditory nerve in man. I. Basic psychophysics*. Hearing Research, 1983. **11**(2): p. 157-189.
7. Groves, D.A. and V.J. Brown, *Vagal nerve stimulation: a review of its applications and potential mechanisms that mediate its clinical effects*. Neuroscience & Biobehavioral Reviews, 2005. **29**(3): p. 493-500.
8. Nicolelis, M.A.L., *Actions from thoughts*. Nature, 2001. **409**(6818): p. 403-407.
9. Handforth, A., et al., *Vagus nerve stimulation therapy for partial-onset seizures: A randomized active-control trial*. Neurology, 1998. **51**(1): p. 48-55.
10. Alesch, F., et al., *Stimulation of the ventral intermediate thalamic nucleus in tremor dominated Parkinson's disease and essential tremor*. Acta Neurochirurgica, 1995. **136**(1-2): p. 75-81.
11. Caparros-Lefebvre, D., et al., *Chronic thalamic stimulation improves tremor and levodopa induced dyskinesias in Parkinson's disease*. Journal of Neurology Neurosurgery and Psychiatry, 1993. **56**(3): p. 268-273.
12. Hochberg, L.R., et al., *Neuronal ensemble control of prosthetic devices by a human with tetraplegia*. Nature, 2006. **442**(7099): p. 164-171.
13. Lebedev, M.A. and M.A.L. Nicolelis, *Brain-machine interfaces: past, present and future*. Trends in Neurosciences, 2006. **29**(9): p. 536-546.
14. Navarro, X., et al., *A critical review of interfaces with the peripheral nervous system for the control of neuroprostheses and hybrid bionic systems*. Journal of the Peripheral Nervous System, 2005. **10**(3): p. 229-258.
15. North, R.B., et al., *Spinal cord stimulation for chronic, intractable pain: Experience over two decades*. Neurosurgery, 1993. **32**(3): p. 384-395.
16. Siegel, S.W., et al., *Long-term results of a multicenter study on sacral nerve stimulation for treatment of urinary urge incontinence, urgency-frequency, and retention*. Urology, 2000. **56**(6 SUPPL. 1): p. 87-91.
17. Turner, J.A., et al., *Spinal cord stimulation for chronic low back pain: A systematic literature synthesis*. Neurosurgery, 1995. **37**(6): p. 1088-1096.
18. Wolpaw, J.R., et al., *Brain-computer interfaces for communication and control*. Clinical Neurophysiology, 2002. **113**(6): p. 767-791.
19. Cogan, S.F., *Neural Stimulation and Recording Electrodes*. Annual Review of Biomedical Engineering, 2008. **10**(1): p. 275.
20. Dillow, A.K. and A.M. Lowman, *Biomimetic materials and design : biointerfacial strategies, tissue engineering, and targeted drug delivery*, ed. A.K. Dillow and A.M. Lowman. 2002, New York: New York : Marcel Dekker.

21. Szarowski, D.H., et al., *Brain responses to micro-machined silicon devices*. Brain Res, 2003. **983**(1-2): p. 23-35.
22. Polikov, V.S., P.A. Tresco, and W.M. Reichert, *Response of brain tissue to chronically implanted neural electrodes*. Journal of Neuroscience Methods, 2005. **148**(1): p. 1-18.
23. Schmidt, C.E., et al., *Stimulation of neurite outgrowth using an electrically conducting polymer*. Proc Natl Acad Sci U S A, 1997. **94**(17): p. 8948-53.
24. Kotwal, A. and C.E. Schmidt, *Electrical stimulation alters protein adsorption and nerve cell interactions with electrically conducting biomaterials*. Biomaterials, 2001. **22**(10): p. 1055-64.
25. Cui, X., et al., *Electrochemical deposition and characterization of conducting polymer polypyrrole/PSS on multichannel neural probes*. Sensors and Actuators, A: Physical, 2001. **93**(1): p. 8-18.
26. Cui, X. and D.C. Martin, *Electrochemical deposition and characterization of poly(3,4-ethylenedioxythiophene) on neural microelectrode arrays*. Sensors and Actuators, B: Chemical, 2003. **89**(1-2): p. 92-102.
27. Cui, X.T. and D.D. Zhou, *Poly (3,4-ethylenedioxythiophene) for chronic neural stimulation*. Ieee Transactions on Neural Systems and Rehabilitation Engineering, 2007. **15**(4): p. 502-508.
28. Richardson-Burns, S.M., et al., *Polymerization of the conducting polymer poly(3,4-ethylenedioxythiophene) (PEDOT) around living neural cells*. Biomaterials, 2007. **28**(8): p. 1539-1552.
29. Xiao, Y., et al., *Synthesis and characterization of p-toluenesulfonate incorporated poly(3,4-ethylenedioxythiophene)*. Talanta, 2007. **72**(2): p. 532-538.
30. Asplund, M., et al., *Toxicity evaluation of PEDOT/biomolecular composites intended for neural communication electrodes*. Biomedical Materials, 2009. **4**(4): p. 045009.
31. Green, R.A., N.H. Lovell, and L.A. Poole-Warren, *Cell attachment functionality of bioactive conducting polymers for neural interfaces*. Biomaterials, 2009. **30**(22): p. 3637-3644.
32. Venkatraman, S., et al. *PEDOT coated Microelectrode Arrays for Chronic Neural Recording and Stimulation*. in *Proceedings of the 4th International IEEE EMBS Conference on Neural Engineering*. 2009. Antalya, Turkey.
33. Wilks, S.J., et al., *Poly(3,4-ethylene dioxythiophene) (PEDOT) as a micro-neural interface material for electrostimulation*. Frontiers in Neuroengineering, 2009. **2**(7).
34. Yang, J.Y., et al., *Ordered surfactant-templated poly(3,4-ethylenedioxythiophene) (PEDOT) conducting polymer on microfabricated neural probes*. Acta Biomaterialia, 2005. **1**(1): p. 125-136.
35. Yang, J. and D.C. Martin, *Impedance spectroscopy and nanoindentation of conducting poly(3,4-ethylenedioxythiophene) coatings on microfabricated neural prosthetic devices*. Journal of Materials Research, 2006. **21**(5): p. 1124-1132.
36. Ludwig, K.A., et al., *Chronic neural recordings using silicon microelectrode arrays electrochemically deposited with a poly(3,4-ethylenedioxythiophene) (PEDOT) film*. Journal of Neural Engineering, 2006. **3**(1): p. 59-70.
37. Abidian, M.R., et al. *In-vivo Evaluation of Chronically Implanted Neural Microelectrode Arrays Modified with Poly (3,4-ethylenedioxythiophene) Nanotubes*. in *Neural Engineering, 2007. CNE '07. 3rd International IEEE/EMBS Conference on*. 2007.
38. Dowell-Mesfin, N.M., et al., *Topographically modified surfaces affect orientation and growth of hippocampal neurons*. J Neural Eng, 2004. **1**(2): p. 78-90.
39. Chen, C.S., et al., *Geometric control of cell life and death*. Science, 1997. **276**(5317): p. 1425-1428.
40. Khan, S.P., G.G. Auner, and G.M. Newaz, *Influence of nanoscale surface roughness on neural cell attachment on silicon*. Nanomedicine: Nanotechnology, Biology and Medicine, 2005. **1**(2): p. 125-129.

41. Gunn, J.W., S.D. Turner, and B.K. Mann, *Adhesive and mechanical properties of hydrogels influence neurite extension*. Journal of Biomedical Materials Research Part A, 2005. **72A**(1): p. 91-97.
42. Cheng, M., et al., *Study on physical properties and nerve cell affinity of composite films from chitosan and gelatin solutions*. Biomaterials, 2003. **24**(17): p. 2871-2880.
43. Levental, I., P.C. Georges, and P.A. Janmey, *Soft biological materials and their impact on cell function*. Soft Matter, 2007. **3**(3): p. 299-306.
44. Warren, L.F., et al., *A study of conducting polymer morphology - The effect of dopant anions upon order*. Journal of the Electrochemical Society, 1989. **136**(8): p. 2286-2295.
45. Barisci, J.N., et al., *Characterisation of the topography and surface potential of electrodeposited conducting polymer films using atomic force and electric force microscopies*. Electrochimica Acta, 2000. **46**(4): p. 519-531.
46. Green, R.A., et al., *Conducting polymers for neural interfaces: Challenges in developing an effective long-term implant*. Biomaterials, 2008. **29**(24-25): p. 3393-3399.
47. Flanagan, L.A., et al., *Neurite branching on deformable substrates*. NeuroReport, 2002. **13**(18): p. 2411-2415.
48. Georges, P.C., et al., *Matrices with compliance comparable to that of brain tissue select neuronal over glial growth in mixed cortical cultures*. Biophysical Journal, 2006. **90**(8): p. 3012-3018.
49. Green, R.A., et al., *Conducting polymer-hydrogels for medical electrode applications*. Science and Technology of Advanced Materials, 2010. **11**(1): p. 014107.
50. Heeger, A.J., *Semiconducting and Metallic Polymers: The Fourth Generation of Polymeric Materials (Nobel Lecture)*. Angewandte Chemie International Edition, 2001. **40**(14): p. 2591-2611.
51. Permentier, H.P., et al., *Electrochemical oxidation and cleavage of peptides analyzed with on-line mass spectrometric detection*. Rapid Commun Mass Spectrom, 2003. **17**(14): p. 1585-92.
52. Yen, S.P.S., et al., *Stability of polyacetylene films*. Solid State Communications, 1980. **36**(4): p. 339-343.
53. Kanazawa, K., et al., *Polypyrrole: An electrochemically synthesized conducting organic polymer*. Synthetic Metals, 1980. **1**(3): p. 329-336.
54. Otero, T.F. and E. Angulo, *Oxidation-reduction of polypyrrole films. Kinetics, structural model and applications*. Solid State Ionics, 1993. **63-65**: p. 803-809.
55. Bartlett, P.N. and P.R. Birkin, *The application of conducting polymers in biosensors*. Synthetic Metals, 1993. **61**(1-2): p. 15-21.
56. Wong, J.Y., R. Langer, and D.E. Ingber, *Electrically conducting polymers can noninvasively control the shape and growth of mammalian cells*. Proceedings of the National Academy of Sciences, 1994. **91**(8): p. 3201-3204.
57. Williams, R.L. and P.J. Doherty, *A preliminary assessment of poly(pyrrole) in nerve guide studies*. Journal of Materials Science: Materials in Medicine, 1994. **5**(6): p. 429-433.
58. Yamato, H., M. Ohwa, and W. Wernet, *Stability of polypyrrole and poly(3,4-ethylenedioxythiophene) for biosensor application*. Journal of Electroanalytical Chemistry, 1995. **397**(1-2): p. 163-170.
59. Diaz, A.F., K.K. Kanazawa, and G.P. Gardini, *Electrochemical polymerization of pyrrole*. Journal of the Chemical Society, Chemical Communications, 1979(14): p. 635-636.
60. Bakhshi, A.K., J. Ladik, and M. Seel, *Comparative study of the electronic structure and conduction properties of polypyrrole, polythiophene, and polyfuran and their copolymers*. Physical Review B, 1987. **35**(2): p. 704-712.
61. Diaz, A.F., et al., *Electrochemistry of some substituted pyrroles*. Journal of Electroanalytical Chemistry, 1981. **130**: p. 181-187.

62. Tourillon, G. and F. Garnier, *STABILITY OF CONDUCTING POLYTHIOPHENE AND DERIVATIVES*. Journal of the Electrochemical Society, 1983. **130**(10): p. 2042-2044.
63. Groenendaal, L., et al., *Poly(3,4-ethylenedioxythiophene) and Its Derivatives: Past, Present, and Future*. Advanced Materials, 2000. **12**(7): p. 481-494.
64. Groenendaal, L., et al., *Electrochemistry of Poly(3,4-alkylenedioxythiophene) Derivatives*. Advanced Materials, 2003. **15**(11): p. 855-879.
65. Heywang, G. and F. Jonas, *Poly(alkylenedioxythiophene)s—new, very stable conducting polymers*. Advanced Materials, 1992. **4**(2): p. 116-118.
66. Abidian, M.R., D.H. Kim, and D.C. Martin, *Conducting-polymer nanotubes for controlled drug release*. Advanced Materials, 2006. **18**(4): p. 405-+.
67. Nyberg, T., A. Shimada, and K. Torimitsu, *Ion conducting polymer microelectrodes for interfacing with neural networks*. Journal of Neuroscience Methods, 2007. **160**(1): p. 16-25.
68. Lau, S.S., et al., *Sequential oxidation and glutathione addition to 1,4-benzoquinone: correlation of toxicity with increased glutathione substitution*. Molecular Pharmacology, 1988. **34**(6): p. 829-836.
69. Arsov, L.D., W. Plieth, and G. Koßmehl, *Electrochemical and Raman spectroscopic study of polyaniline; influence of the potential on the degradation of polyaniline*. Journal of Solid State Electrochemistry, 1998. **2**(5): p. 355-361.
70. Planes, G.A., et al., *Spectroscopic evidence for intermediate species formed during aniline polymerization and polyaniline degradation*. Physical Chemistry Chemical Physics, 2010. **12**(35): p. 10584-10593.
71. Bidez, P.R., et al., *Polyaniline, an electroactive polymer, supports adhesion and proliferation of cardiac myoblasts*. Journal of Biomaterials Science, Polymer Edition, 2006. **17**(1-2): p. 199-212.
72. Li, M., et al., *Electrospinning polyaniline-contained gelatin nanofibers for tissue engineering applications*. Biomaterials, 2006. **27**(13): p. 2705-2715.
73. Kirchmeyer, S. and K. Reuter, *Scientific importance, properties and growing applications of poly(3,4-ethylenedioxythiophene)*. Journal of Materials Chemistry, 2005. **15**(21): p. 2077-2088.
74. Kim, W.H., et al., *Molecular organic light-emitting diodes using highly conducting polymers as anodes*. Vol. 80. 2002: AIP. 3844-3846.
75. Zhang, F., et al., *Polymer Photovoltaic Cells with Conducting Polymer Anodes*. Advanced Materials, 2002. **14**(9): p. 662-665.
76. Lang, U. and J. Dual, *Mechanical properties of BAYTRON P*. in *Polymers and Adhesives in Microelectronics and Photonics, 2004. POLYTRONIC 2004. 4th IEEE International Conference on*. 2004.
77. Lang, U., N. Naujoks, and J. Dual, *Mechanical characterization of PEDOT:PSS thin films*. Synthetic Metals, 2009. **159**(5-6): p. 473-479.
78. Lang, U. and J. Dual, *Mechanical properties of the intrinsically conductive polymer poly(3,4-ethylenedioxythiophene) poly(styrenesulfonate) (PEDOT/PSS)*. Mechanical Behavior of Materials X, Pts 1 and 2, 2007. **345-346**: p. 1189-1192.
79. Joo, J., et al., *Physical Characterization of Electrochemically and Chemically Synthesized Polypyrroles*. Macromolecules, 2000. **33**(14): p. 5131-5136.
80. Xiao, Y.H., X.Y. Cui, and D.C. Martin, *Electrochemical polymerization and properties of PEDOT/S-EDOT on neural microelectrode arrays*. Journal of Electroanalytical Chemistry, 2004. **573**(1): p. 43-48.
81. Xiao, Y.H., et al., *Electrochemical polymerization of poly(hydroxymethylated-3,4-ethylenedioxythiophene) (PEDOT-MeOH) on multichannel neural probes*. Sensors and Actuators B-Chemical, 2004. **99**(2-3): p. 437-443.

82. Xiao, Y., et al., *Surface modification of neural probes with conducting polymer poly(hydroxymethylated-3,4-ethylenedioxythiophene) and its biocompatibility*. Applied Biochemistry and Biotechnology, 2006. **128**(2): p. 117-129.
83. Holly, F.J. and M.F. Refojo, *Wettability of hydrogels. I. Poly (2-hydroxyethyl methacrylate)*. J Biomed Mater Res, 1975. **9**(3): p. 315-26.
84. Buckley, L.J., D.K. Roylance, and G.E. Wnek, *Influence of dopant ion and synthesis variables on mechanical properties of polypyrrole films*. Journal of Polymer Science Part B: Polymer Physics, 1987. **25**(10): p. 2179-2188.
85. Kuwabata, S., J. Nakamura, and H. Yoneyama, *The effect of basicity of dopant anions on the conductivity of polypyrrole films*. Journal of the Chemical Society-Chemical Communications, 1988(12): p. 779-780.
86. Diaz, A.F. and J. Bargon, *Electrochemical synthesis of conducting polymers*, in *Handbook of Conducting Polymers*, T.A. Skotheim, Editor. 1986, Marcel Dekker. p. 81-115.
87. Tanaka, K., T. Shichiri, and T. Yamabe, *Influence of polymerization temperature on the characteristics of polythiophene films*. Synthetic Metals, 1986. **16**(2): p. 207-214.
88. Liang, W., J. Lei, and C.R. Martin, *Effect of synthesis temperature on the structure, doping level and charge-transport properties of polypyrrole*. Synthetic Metals, 1992. **52**(2): p. 227-239.
89. Avlyanov, J.K., et al., *Polyaniline: conformational changes induced in solution by variation of solvent and doping level*. Synthetic Metals, 1995. **72**(1): p. 65-71.
90. Green, R.A., et al., *Nanostructured Conductive Polymers as Biomaterials*, in *Nanostructured Conductive Polymers*. 2010, John Wiley & Sons, Ltd. p. 707-736.
91. Sotzing, G.A., J.R. Reynolds, and P.J. Steel, *Poly(3,4-ethylenedioxythiophene) (PEDOT) prepared via electrochemical polymerization of EDOT, 2,2'-bis(3,4-ethylenedioxythiophene) (BiEDOT), and their TMS derivatives*. Advanced Materials, 1997. **9**(10): p. 795-&.
92. Diaz, A.F., et al., *Electrochemistry of conducting polypyrrole films*. Journal of Electroanalytical Chemistry, 1981. **129**(1-2): p. 115-132.
93. Roncali, J., *Conjugated poly(thiophenes): synthesis, functionalization, and applications*. Chemical Reviews, 1992. **92**(4): p. 711-738.
94. Roncali, J., et al., *REDUCTION OF THE STERIC HINDRANCE TO CONJUGATION IN 3,4-DISUBSTITUTED POLY(THIOPHENES) - CYCLOPENTA[C]THIOPHENE AND THIENO[C]THIOPHENE AS PRECURSORS OF ELECTROGENERATED CONDUCTING POLYMERS*. Journal of the Chemical Society-Chemical Communications, 1987(19): p. 1500-1502.
95. Yassar, A., J. Roncali, and F. Garnier, *Conductivity and conjugation length in poly(3-thiophene) thin-films*. Macromolecules, 1989. **22**(2): p. 804-809.
96. Fonner, J.M., et al., *Biocompatibility implications of polypyrrole synthesis techniques*. Biomedical Materials, 2008. **3**(3).
97. Asavapiriyant, S., et al., *The electrodeposition of polypyrrole films from aqueous solutions*. Journal of Electroanalytical Chemistry and Interfacial Electrochemistry, 1984. **177**(1-2): p. 229-244.
98. Qian, R., J. Qiu, and D. Shen, *Conducting polypyrrole electrochemically prepared from aqueous solutions*. Synthetic Metals, 1987. **18**(1-3): p. 13-18.
99. Aeiya, S., J.E. Dubois, and P.C. Lacaze, *Medium effect on the anodic fabrication of poly-(p-phenylene) films on platinum electrodes*. Journal of the Chemical Society, Chemical Communications, 1986(22): p. 1668-1669.
100. Waltman, R.J., A.F. Diaz, and J. Bargon, *Substituent effects in the electropolymerization of aromatic heterocyclic compounds*. The Journal of Physical Chemistry, 1984. **88**(19): p. 4343-4346.
101. Dong, S. and J. Ding, *Study on polypyrrole film by electrochemical polymerization in aqueous solution*. Synthetic Metals, 1987. **20**(1): p. 119-124.

102. Rose, T.L. and L.S. Robblee, *Electrical Stimulation with Pt Electrodes; VIII. Electrochemically Safe Charge Injection Limits with 0.2 ms Pulses*. IEEE Trans Biomed Eng, 1990. **37**(11).
103. Green, R.A., et al., *Substrate dependent stability of conducting polymer coatings on medical electrodes*. Biomaterials, 2012. **33**(25): p. 5875-5886.
104. Cui, X., et al., *In vivo studies of polypyrrole/peptide coated neural probes*. Biomaterials, 2003. **24**(5): p. 777-787.
105. Kim, D.H., et al., *Soft, Fuzzy, and Bioactive Conducting Polymers for Improving the Chronic Performance of Neural Prosthetic Devices*, in *Indwelling Neural Implants: Strategies for Contending with the In Vivo Environment*, W.M. Reichert, Editor. 2008, Taylor & Francis Group, LLC: Boca Raton FL.
106. Gus, et al., *Silk-inspired 'molecular chimeras': atomistic simulation of nanoarchitectures based on thiophene-peptide copolymers*. Chemical Physics Letters, 2008. **461**(1-3): p. 64-70.
107. Thompson, B.C., et al., *Optimising the incorporation and release of a neurotrophic factor using conducting polypyrrole*. Journal of Controlled Release, 2006. **116**(3): p. 285-294.
108. Richardson, R.T., et al., *The effect of polypyrrole with incorporated neurotrophin-3 on the promotion of neurite outgrowth from auditory neurons*. Biomaterials, 2007. **28**(3): p. 513-523.
109. Evans, A.J., et al., *Promoting neurite outgrowth from spiral ganglion neuron explants using polypyrrole/BDNF-coated electrodes*. Journal of Biomedical Materials Research Part A, 2009. **91A**(1): p. 241-250.
110. Green, R.A., N.H. Lovell, and L.A. Poole-Warren, *Impact of co-incorporating laminin peptide dopants and neurotrophic growth factors on conducting polymer properties*. Acta Biomaterialia, 2010. **6**: p. 63-71.
111. Wadhwa, R., C.F. Lagenaur, and X.T. Cui, *Electrochemically controlled release of dexamethasone from conducting polymer polypyrrole coated electrode*. Journal of Controlled Release, 2006. **110**(3): p. 531-541.
112. Abidian, M.R. and D.C. Martin, *Multifunctional Nanobiomaterials for Neural Interfaces*. Advanced Functional Materials, 2009. **19**(4): p. 573-585.
113. Collier, J.H., et al., *Synthesis and characterization of polypyrrole-hyaluronic acid composite biomaterials for tissue engineering applications*. Journal of Biomedical Materials Research, 2000. **50**(4): p. 574-584.
114. Li, G.N. and D. Hoffman-Kim, *Tissue-Engineered Platforms of Axon Guidance*. Tissue Engineering Part B: Reviews, 2008. **14**(1): p. 33-51.
115. Janmey, P.A., et al., *The hard life of soft cells*. Cell Motility and the Cytoskeleton, 2009. **66**(8): p. 597-605.
116. Silk, T., et al., *AFM studies of polypyrrole film surface morphology II. Roughness characterization by the fractal dimension analysis*. Synthetic Metals, 1998. **93**(1): p. 65-71.
117. Silk, T., et al., *AFM studies of polypyrrole film surface morphology I. The influence of film thickness and dopant nature*. Synthetic Metals, 1998. **93**(1): p. 59-64.
118. Che, J.F., et al., *Electro-synthesized PEDOT/glutamate chemically modified electrode: a combination of electrical and biocompatible features*. Polymer International, 2008. **57**(5): p. 750-755.
119. Diaz, A.F. and B. Hall, *Mechanical Properties of Electrochemically Prepared Polypyrrole Films*. IBM Journal of Research and Development, 1983 **27**(4): p. 342-347.
120. Satoh, M., K. Kaneto, and K. Yoshino, *Dependences of electrical and mechanical properties of conducting polypyrrole films on conditions of electrochemical polymerization in an aqueous medium*. Synthetic Metals, 1986. **14**(4): p. 289-296.
121. Sun, B., et al., *Stability and mechanical properties of electrochemically prepared conducting polypyrrole films*. Journal of Materials Science, 1989. **24**(11): p. 4024-4029.
122. Gandhi, M., et al., *Film substructure and mechanical properties of electrochemically prepared polypyrrole*. Polymer, 1995. **36**(25): p. 4761-4765.

123. Jansen, K.M.B., et al., *State-of-the-Art of Thermo-Mechanical Characterization of Thin Polymer Films*. Journal of Electronic Packaging, 2005. **127**(4): p. 530-536.
124. Stafford, C.M., et al., *A buckling-based metrology for measuring the elastic moduli of polymeric thin films*. Nat Mater, 2004. **3**(8): p. 545-550.
125. Palevski, A., et al., *Stress relaxation of porcine gluteus muscle subjected to sudden transverse deformation as related to pressure sore modeling*. Journal of Biomechanical Engineering, 2006. **128**(5): p. 782-787.
126. Pailler-Mattei, C., S. Bec, and H. Zahouani, *In vivo measurements of the elastic mechanical properties of human skin by indentation tests*. Medical Engineering and Physics, 2008. **30**(5): p. 599-606.
127. Stolz, M., et al., *Dynamic Elastic Modulus of Porcine Articular Cartilage Determined at Two Different Levels of Tissue Organization by Indentation-Type Atomic Force Microscopy*. Biophysical Journal, 2004. **86**(5): p. 3269-3283.
128. Carter, F.J., et al., *Measurements and modelling of the compliance of human and porcine organs*. Medical Image Analysis, 2001. **5**(4): p. 231-236.
129. Mathur, A.B., et al., *Endothelial, cardiac muscle and skeletal muscle exhibit different viscous and elastic properties as determined by atomic force microscopy*. Journal of Biomechanics, 2001. **34**(12): p. 1545-1553.
130. Rosenbluth, M.J., W.A. Lam, and D.A. Fletcher, *Force microscopy of nonadherent cells: A comparison of leukemia cell deformability*. Biophysical Journal, 2006. **90**(8): p. 2994-3003.
131. Sato, M., et al., *Local mechanical properties measured by atomic force microscopy for cultured bovine endothelial cells exposed to shear stress*. Journal of Biomechanics, 2000. **33**(1): p. 127-135.
132. Touhami, A., B. Nysten, and Y.F. Dufr ne, *Nanoscale mapping of the elasticity of microbial cells by atomic force microscopy*. Langmuir, 2003. **19**(11): p. 4539-4543.
133. Alcaraz, J., et al., *Microrheology of human lung epithelial cells measured by atomic force microscopy*. Biophysical Journal, 2003. **84**(3): p. 2071-2079.
134. Solon, J., et al., *Fibroblast adaptation and stiffness matching to soft elastic substrates*. Biophysical Journal, 2007. **93**(12): p. 4453-4461.
135. Jacot, J.G., et al., *A simple microindentation technique for mapping the microscale compliance of soft hydrated materials and tissues*. Journal of Biomedical Materials Research - Part A, 2006. **79**(3): p. 485-494.
136. Ebenstein, D.M. and L.A. Pruitt, *Nanoindentation of soft hydrated materials for application to vascular tissues*. Journal of Biomedical Materials Research Part A, 2004. **69A**(2): p. 222-232.
137. Matzelle, T.R., et al., *Micromechanical properties of "smart" gels: Studies by scanning force and scanning electron microscopy of PNIPAAm*. Journal of Physical Chemistry B, 2002. **106**(11): p. 2861-2866.
138. Uricanu, V.I., et al., *Local structure and elasticity of soft gelatin gels studied with atomic force microscopy*. Langmuir, 2003. **19**(20): p. 8182-8194.
139. Gilchrist, A. and N.J. Mills, *Impact deformation of rigid polymeric foams: Experiments and FEA modelling*. International Journal of Impact Engineering, 2001. **25**(8): p. 767-786.
140. Liu, Z., C.S.L. Chuah, and M.G. Scanlon, *Compressive elastic modulus and its relationship to the structure of a hydrated starch foam*. Acta Materialia, 2003. **51**(2): p. 365-371.
141. Yu, W., et al., *Softness measurements for open-cell foam materials and human soft tissue*. Measurement Science and Technology, 2006. **17**(7): p. 1785-1791.
142. Hobbs, J.K., et al., *Nanoindentation of polymers: An overview*. Macromolecular Symposia, 2001. **167**: p. 15-43.
143. Klapperich, C., K. Komvopoulos, and L. Pruitt, *Nanomechanical properties of polymers determined from nanoindentation experiments*. Journal of Tribology, 2001. **123**(3): p. 624-631.

144. Lu, H., et al., *Measurement of creep compliance of solid polymers by nanoindentation*. Mechanics Time-Dependent Materials, 2003. **7**(3-4): p. 189-207.
145. Raghavan, D., et al., *Mapping polymer heterogeneity using atomic force microscopy phase imaging and nanoscale indentation*. Macromolecules, 2000. **33**(7): p. 2573-2583.
146. Raghavan, D., et al., *Characterization of heterogeneous regions in polymer systems using tapping mode and force mode atomic force microscopy*. Langmuir, 2000. **16**(24): p. 9448-9459.
147. Domke, J. and M. Radmacher, *Measuring the elastic properties of thin polymer films with the atomic force microscope*. Langmuir, 1998. **14**(12): p. 3320-3325.
148. Nix, W.D., *Mechanical properties of thin films*. Metallurgical Transactions A, 1989. **20**(11): p. 2217-2245.
149. Nix, W.D., *Elastic and plastic properties of thin films on substrates: Nanoindentation techniques*. Materials Science and Engineering A, 1997. **234-236**: p. 37-44.
150. Saha, R. and W.D. Nix, *Effects of the substrate on the determination of thin film mechanical properties by nanoindentation*. Acta Materialia, 2002. **50**(1): p. 23-38.
151. Tsui, T.Y. and G.M. Pharr, *Substrate effects on nanoindentation mechanical property measurement of soft films on hard substrates*. Journal of Materials Research, 1999. **14**(1): p. 292-301.
152. Goertz, M.P. and N.W. Moore, *Mechanics of soft interfaces studied with displacement-controlled scanning force microscopy*. Progress in Surface Science. **85**(9-12): p. 347-397.
153. Doerner, M.F. and W.D. Nix, *A method for interpreting the data from depth-sensing indentation instruments*. Journal of Materials Research, 1986. **1**(4): p. 601-9.
154. Hysitron_Inc., *Hysitron TI-900 Triboindenter User Manual*. , Hysitron, Inc, MN, U.S.A.
155. Oliver, W.C. and G.M. Pharr, *Improved technique for determining hardness and elastic modulus using load and displacement sensing indentation experiments*. Journal of Materials Research, 1992. **7**(6): p. 1564-1580.
156. Fischer-Cripps, A.C., *Nanoindentation*, ed. 2. 2004, New York: Springer.
157. ISO, *Metallic Materials-Instrumented Indentation Test for Hardness and Materials Parameters* G. International Organization for Standardization, Switzerland, Editor 2002.
158. Kumar, R.V. and et al., *Young's modulus measurements of silicon nanostructures using a scanning probe system: a non-destructive evaluation approach*. Smart Materials and Structures, 2003. **12**(6): p. 1028.
159. Butt, H.-J.r., B. Cappella, and M. Kappl, *Force measurements with the atomic force microscope: Technique, interpretation and applications*. Surface Science Reports, 2005. **59**(1-6): p. 1-152.
160. Wood, L., *Compressibility of Natural Rubber at Pressures Below 500 KG/CM²*. Rubber Chem. Technol., 1964. **37**(4): p. 850.
161. Holownia, B., *Effect of Carbon Black on Poisson's Ratio of Elastomers*. Rubber Chem. Technol., 1975. **48**(2): p. 246.
162. Urayama, K., T. Takigawa, and T. Masuda, *Poisson's ratio of poly(vinyl alcohol) gels*. Macromolecules, 1993. **26**(12): p. 3092-3096.
163. Popelar, C.F., C.H. Popelar, and V.H. Kenner, *Viscoelastic material characterization and modeling for polyethylene*. Polymer Engineering & Science, 1990. **30**(10): p. 577-586.
164. Warfield, R.W., J.E. Cuevas, and F.R. Barnet, *Single specimen determination of Young's and bulk moduli*. Journal of Applied Polymer Science, 1968. **12**(5): p. 1147-1149.
165. Hughes, D., *Variation of Elastic Moduli and Wave Velocity with Pressure and Temperature in Plastics*. J. Appl. Phys., 1950. **21**(4): p. 294.
166. Han, D.-H., H.J. Lee, and S.-M. Park, *Electrochemistry of conductive polymers XXXV: Electrical and morphological characteristics of polypyrrole films prepared in aqueous media studied by current sensing atomic force microscopy*. Electrochimica Acta, 2005. **50**(15): p. 3085-3092.

167. Wu, Y., et al., *Soft Mechanical Sensors Through Reverse Actuation in Polypyrrole*. Advanced Functional Materials, 2007. **17**(16): p. 3216-3222.
168. Tsai, H., *15 - Elastic properties, damping capacity and shape memory alloys*, in *Smithells Metals Reference Book (Eighth Edition)*, W.F. Gale, PhD, and P. T.C. Totemeier, Editors. 2004, Butterworth-Heinemann: Oxford. p. 1-45.
169. Hertz, H., *J. Reine Angew. Math*, 1882(92): p. 156.
170. Sneddon, I.N., *The relation between load and penetration in the axisymmetric boussinesq problem for a punch of arbitrary profile*. International Journal of Engineering Science, 1965. **3**(1): p. 47-57.
171. Fischer-Cripps, A.C., *Critical review of analysis and interpretation of nanoindentation test data*. Surface and Coatings Technology, 2006. **200**(14-15): p. 4153-4165.
172. Oliver, W.C. and G.M. Pharr, *Measurement of hardness and elastic modulus by instrumented indentation: Advances in understanding and refinements to methodology*. Journal of Materials Research, 2004. **19**(1): p. 3-20.
173. King, R.B., *Elastic analysis of some punch problems for a layered medium*. International Journal of Solids and Structures, 1987. **23**(12): p. 1657-1664.
174. Martin, M. and M. Troyon, *Fundamental relations used in nanoindentation: Critical examination based on experimental measurements*. Journal of Materials Research, 2002. **17**(9): p. 2227-2234.
175. Dao, M., et al., *Computational modeling of the forward and reverse problems in instrumented sharp indentation*. Acta Materialia, 2001. **49**(19): p. 3899-3918.
176. Cheng, Y.-T. and C.-M. Cheng, *Scaling approach to conical indentation in elastic-plastic solids with work hardening*. Journal of Applied Physics, 1998. **84**(3): p. 1284-1291.
177. Hay, J.C., A. Bolshakov, and G.M. Pharr, *Critical examination of the fundamental relations used in the analysis of nanoindentation data*. Journal of Materials Research, 1999. **14**(6): p. 2296-2305.
178. Borodich, F.M. and L.M. Keer, *Evaluation of elastic modulus of materials by adhesive (no-slip) nano-indentation*. Proceedings of the Royal Society of London. Series A: Mathematical, Physical and Engineering Sciences, 2004. **460**(2042): p. 507-514.
179. A.C. F.-C., *A review of analysis methods for sub-micron indentation testing*. Vacuum, 2000. **58**(4): p. 569-585.
180. Pelletier, C.G.N., et al., *The influence of indenter-surface misalignment on the results of instrumented indentation tests*. Polymer Testing, 2007. **26**(7): p. 949-959.
181. R. Kiebooms, R.M., K. Lee in *Handbook of Advanced Electronic and Photonic Materials and Devices*, H.S. Halwa, Editor. 2001.
182. Ji, G., et al., *Concentration dependence of crystallinity of polycarbonate by shock-cooling and subsequent freeze-drying of its various solutions*. Polymer, 1996. **37**(15): p. 3255-3258.
183. Cheng, Y.-T. and C.-M. Cheng, *Scaling, dimensional analysis, and indentation measurements*. Materials Science and Engineering: R: Reports, 2004. **44**(4-5): p. 91-149.
184. Johnson, K.L., K. Kendall, and A.D. Roberts, *Surface Energy and the Contact of Elastic Solids*. Proceedings of the Royal Society of London. Series A, Mathematical and Physical Sciences, 1971. **324**(1558): p. 301-313.
185. Derjaguin, B.V., V.M. Muller, and Y.P. Toporov, *Effect of contact deformations on the adhesion of particles*. Journal of Colloid and Interface Science, 1975. **53**(2): p. 314-326.
186. Muller, V.M., V.S. Yushchenko, and B.V. Derjaguin, *On the influence of molecular forces on the deformation of an elastic sphere and its sticking to a rigid plane*. Journal of Colloid and Interface Science, 1980. **77**(1): p. 91-101.
187. Muller, V.M., B.V. Derjaguin, and Y.P. Toporov, *On two methods of calculation of the force of sticking of an elastic sphere to a rigid plane*. Colloids and Surfaces, 1983. **7**(3): p. 251-259.
188. SIGMA-ALDRICH, *Material Safety Data Sheet (MSDS) version 4.2 - Sodium perchlorate, product number 410241*, 10.09.2011.

189. SIGMA-ALDRICH, *Material Safety Data Sheet (MSDS) version 4.0 - Lithium perchlorate trihydrate, product number 205303*, 13.03.2010.
190. SIGMA-ALDRICH, *Material Safety Data Sheet (MSDS) version 4.0 - Sodium p-toluenesulfonate, product number 152536*, 27.02.2010.
191. SIGMA-ALDRICH, *Material Safety Data Sheet (MSDS) version 3.3 - Sodium dodecylbenzenesulfonate, product number 289957*, 28.07.1012.
192. SIGMA-ALDRICH, *Material Safety Data Sheet (MSDS) version 3.1 - Poly(sodium 4-styrenesulfonate), product number 243051*, 25.01.2010.
193. Hodge, H.C. and J.H. Sterner, *Tabulation of Toxicity Classes*. American Industrial Hygiene Association Quarterly, 1949. **10**(4): p. 93-96.
194. Rylie, A.G., *Conducting polymers for neural interfaces: Impact of physico-chemical properties on biological performance*, in *GSBME2009*, UNSW.
195. BAXTER, *Material safety data sheet (MSDS) - 0.9% Sodium Chloride Irrigation solution (Product id: 1214283)*, 2009.
196. eDAQ, *INPHAZE HiRes-EIS Three Terminal Sample Chamber (SC3T) Document Number: M-INPSC3-0210*, 2010.
197. Marinpharm-GmbH. 2012 [cited 2012 Mar/08]; Available from: http://marinpharm.com/index.php?option=com_content&task=view&id=26&Itemid=30.
198. Sanghvi, A.B., et al., *Biomaterials functionalization using a novel peptide that selectively binds to a conducting polymer*. *Nat Mater*, 2005. **4**(6): p. 496-502.
199. Zotti, G., et al., *Electrochemical and XPS Studies toward the Role of Monomeric and Polymeric Sulfonate Counterions in the Synthesis, Composition, and Properties of Poly(3,4-ethylenedioxythiophene)*. *Macromolecules*, 2003. **36**(9): p. 3337-3344.
200. Aasmundtveit, K.E., et al., *Structure of thin films of poly(3,4-ethylenedioxythiophene)*. *Synthetic Metals*, 1999. **101**(1-3): p. 561-564.
201. Voigt, W., *Ann. Phys. (Berlin)*, 1889: p. 573-587.
202. Reuss, A., *Berechnung der Fliebgrenze von Mischkristallen Auf Grund der Plastizitätsbedingung für Einkristalle*, ZAMM, 1929. **9**: p. 49.
203. Shafieian, M., K.K. Darvish, and J.R. Stone, *Changes to the viscoelastic properties of brain tissue after traumatic axonal injury*. *Journal of Biomechanics*, 2009. **42**(13): p. 2136-2142.
204. Flanagan, L.A., et al., *Neurite branching on deformable substrates*. *NeuroReport*, 2002. **13**(18): p. 2411-2415.
205. Jennie, B.L., et al., *Neurite outgrowth and branching of PC12 cells on very soft substrates sharply decreases below a threshold of substrate rigidity*. *Journal of Neural Engineering*, 2007. **4**(2): p. 26.
206. Tanguy, J., N. Mermilliod, and M. Hoclet, *Capacitive Charge and Noncapacitive Charge in Conducting Polymer Electrodes*. *Journal of the Electrochemical Society*, 1987. **134**(4): p. 795-802.
207. Ren, X. and P.G. Pickup, *Ion transport in polypyrrole and a polypyrrole/polyanion composite*. *The Journal of Physical Chemistry*, 1993. **97**(20): p. 5356-5362.
208. Park, D.S., Y.B. Shim, and S.M. Park, *Degradation of Electrochemically Prepared Polypyrrole in Aqueous Sulfuric Acid*. *Journal of the Electrochemical Society*, 1993. **140**(3): p. 609-614.
209. Ghosh, S., et al., *Infrared and Raman spectroscopic studies of the electrochemical oxidative degradation of polypyrrole*. *Synthetic Metals*, 1998. **95**(1): p. 63-67.
210. Neoh, K.G., et al., *Structural and mechanical degradation of polypyrrole films due to aqueous media and heat treatment and the subsequent redoping characteristics*. *Journal of Applied Polymer Science*, 1997. **64**(3): p. 519-526.
211. Kros, A., N.A.J.M. Sommerdijk, and R.J.M. Nolte, *Poly(pyrrole) versus poly(3,4-ethylenedioxythiophene): implications for biosensor applications*. *Sensors and Actuators B: Chemical*, 2005. **106**(1): p. 289-295.

212. Schlenoff, J.B. and H. Xu, *Evolution of Physical and Electrochemical Properties of Polypyrrole during Extended Oxidation*. Journal of the Electrochemical Society, 1992. **139**(9): p. 2397-2401.
213. Pfluger, P. and G.B. Street, *Chemical, electronic, and structural properties of conducting heterocyclic polymers: A view by XPS*. The Journal of Chemical Physics, 1984. **80**(1): p. 544-553.
214. Chen, C.S., et al., *Cell shape provides global control of focal adhesion assembly*. Biochemical and Biophysical Research Communications, 2003. **307**(2): p. 355-361.
215. Tallman, D.E., et al., *Direct Electrodeposition of Polypyrrole on Aluminum and Aluminum Alloy by Electron Transfer Mediation*. Journal of the Electrochemical Society, 2002. **149**(3): p. C173-C179.
216. Waltman, R.J., J. Bargon, and A.F. Diaz, *Electrochemical studies of some conducting polythiophene films*. The Journal of Physical Chemistry, 1983. **87**(8): p. 1459-1463.
217. Zotti, G., et al., *Conductive and magnetic properties of 3,4-dimethoxy- and 3,4-ethylenedioxy-capped polypyrrole and polythiophene*. Chemistry of Materials, 2000. **12**(10): p. 2996-3005.
218. Randriamahazaka, H., V. Noël, and C. Chevrot, *Nucleation and growth of poly(3,4-ethylenedioxythiophene) in acetonitrile on platinum under potentiostatic conditions*. Journal of Electroanalytical Chemistry, 1999. **472**(2): p. 103-111.
219. Venables, J.A., G.D.T. Spiller, and M. Hanbucken, *Nucleation and growth of thin films*. Reports on Progress in Physics, 1984. **47**(4): p. 399-459.
220. Stanković, R., et al., *The effects of preparation conditions on the properties of electrochemically synthesized thick films of polypyrrole*. European Polymer Journal, 1994. **30**(3): p. 385-393.
221. Conway, B.E., V. Birss, and J. Wojtowicz, *The role and utilization of pseudocapacitance for energy storage by supercapacitors*. Journal of Power Sources, 1997. **66**(1-2): p. 1-14.
222. Bobacka, J., A. Lewenstam, and A. Ivaska, *Electrochemical impedance spectroscopy of oxidized poly(3,4-ethylenedioxythiophene) film electrodes in aqueous solutions*. Journal of Electroanalytical Chemistry, 2000. **489**(1): p. 17-27.
223. Morita, M., et al., *Electrochemical Behavior of Polyaniline-Poly(styrene sulfonate) Composite Films in Organic Electrolyte Solutions*. Journal of the Electrochemical Society, 1994. **141**(6): p. 1409-1413.
224. Bobacka, J., *Potential Stability of All-Solid-State Ion-Selective Electrodes Using Conducting Polymers as Ion-to-Electron Transducers*. Analytical Chemistry, 1999. **71**(21): p. 4932-4937.
225. Hoffman, A.S., *Hydrogels for biomedical applications*. Advanced Drug Delivery Reviews, 2002. **54**(1): p. 3-12.
226. Kim, D.R., M. Abidian, and D.C. Martin, *Synthesis and characterization of conducting polymers grown in hydrogels for neural applications*. Architecture and Application of Biomaterials and Biomolecular Materials, 2004. **1**: p. 55-60.
227. Green, R.A., et al., *Conductive Hydrogels: Mechanically Robust Hybrids for Use as Biomaterials*. Macromolecular Bioscience, 2012. **12**(4): p. 494-501.
228. Small, C.J., C.O. Too, and G.G. Wallace, *Responsive conducting polymer-hydrogel composites*. Polymer Gels and Networks, 1997. **5**(3): p. 251-265.
229. Kim, B.C., et al., *Preparation and characterisation of processable conducting polymer-hydrogel composites*. Reactive and Functional Polymers, 2000. **44**(1): p. 31-40.
230. Yoshikawa, C., et al., *Protein Repellency of Well-Defined, Concentrated Poly(2-hydroxyethyl methacrylate) Brushes by the Size-Exclusion Effect*. Macromolecules, 2006. **39**(6): p. 2284-2290.
231. Robinson, K.L., et al., *Controlled Polymerization of 2-Hydroxyethyl Methacrylate by ATRP at Ambient Temperature*. Macromolecules, 2001. **34**(10): p. 3155-3158.

232. Huang, W., et al., *Functionalization of Surfaces by Water-Accelerated Atom-Transfer Radical Polymerization of Hydroxyethyl Methacrylate and Subsequent Derivatization*. *Macromolecules*, 2002. **35**(4): p. 1175-1179.
233. Wang, X.S., et al., *Facile synthesis of well-defined water-soluble polymers via atom transfer radical polymerization in aqueous media at ambient temperature*. *Chemical Communications*, 1999(18): p. 1817-1818.
234. Leidheiser Jr, H., W. Wang, and L. Igetoft, *The mechanism for the cathodic delamination of organic coatings from a metal surface*. *Progress in Organic Coatings*, 1983. **11**(1): p. 19-40.
235. Fürbeth, W. and M. Stratmann, *The delamination of polymeric coatings from electrogalvanised steel – a mechanistic approach.: Part 1: delamination from a defect with intact zinc layer*. *Corrosion Science*, 2001. **43**(2): p. 207-227.
236. Bain, C.D. and G.M. Whitesides, *Molecular-Level Control over Surface Order in Self-Assembled Monolayer Films of Thiols on Gold*. *Science*, 1988. **240**(4848): p. 62-3.
237. Bain, C.D., J. Evall, and G.M. Whitesides, *Formation of monolayers by the coadsorption of thiols on gold: Variation in the head group, tail group, and solvent*. *Journal of the American Chemical Society*, 1989. **111**(18): p. 7155-7164.
238. Dubois, L.H. and R.G. Nuzzo, *Synthesis, Structure, and Properties of Model Organic Surfaces*. *Annual Review of Physical Chemistry*, 1992. **43**(1): p. 437-463.
239. Emsley, J., *Very strong hydrogen bonding*. *Chemical Society Reviews*, 1980. **9**(1): p. 91-124.
240. Blanksby, S.J. and G.B. Ellison, *Bond Dissociation Energies of Organic Molecules*. *Accounts of Chemical Research*, 2003. **36**(4): p. 255-263.
241. Fischer, H., *The persistent radical effect in controlled radical polymerizations*. *Journal of Polymer Science Part A: Polymer Chemistry*, 1999. **37**(13): p. 1885-1901.
242. Yamamoto, S., et al., *Surface Interaction Forces of Well-Defined, High-Density Polymer Brushes Studied by Atomic Force Microscopy. 2. Effect of Graft Density*. *Macromolecules*, 2000. **33**(15): p. 5608-5612.
243. Feng, W., J.L. Brash, and S. Zhu, *Non-biofouling materials prepared by atom transfer radical polymerization grafting of 2-methacryloxyethyl phosphorylcholine: Separate effects of graft density and chain length on protein repulsion*. *Biomaterials*, 2006. **27**(6): p. 847-855.
244. Mei, Y., et al., *Tuning cell adhesion on gradient poly(2-hydroxyethyl methacrylate)-grafted surfaces*. *Langmuir*, 2005. **21**(26): p. 12309-12314.
245. Brantley, E.L. and G.K. Jennings, *Fluorinated Polymer Films from Acylation of ATRP Surface-Initiated Poly(hydroxyethyl methacrylate)*. *Macromolecules*, 2004. **37**(4): p. 1476-1483.
246. Gorman, C.B., H.A. Biebuyck, and G.M. Whitesides, *Fabrication of Patterned, Electrically Conducting Polypyrrole Using a Self-Assembled Monolayer: A Route to All-Organic Circuits*. *Chemistry of Materials*, 1995. **7**(3): p. 526-529.
247. Zhou, F., et al., *Fabrication of Conducting Polymer and Complementary Gold Microstructures Using Polymer Brushes as Templates*. *Advanced Functional Materials*, 2003. **13**(12): p. 938-942.
248. Willicut, R.J. and R.L. McCarley, *Electrochemical Polymerization of Pyrrole-Containing Self-Assembled Alkanethiol Monolayers on Au*. *Journal of the American Chemical Society*, 1994. **116**(23): p. 10823-10824.
249. Sayre, C.N. and D.M. Collard, *Self-Assembled Monolayers of Pyrrole-Containing Alkanethiols on Gold*. *Langmuir*, 1995. **11**(1): p. 302-306.
250. Shah, R.R., et al., *Using Atom Transfer Radical Polymerization To Amplify Monolayers of Initiators Patterned by Microcontact Printing into Polymer Brushes for Pattern Transfer*. *Macromolecules*, 2000. **33**(2): p. 597-605.
251. Rakhmatullina, E., et al., *Solid-supported amphiphilic triblock copolymer membranes grafted from gold surface*. *Journal of Polymer Science Part A: Polymer Chemistry*, 2009. **47**(1): p. 1-13.

252. *The MW OF PHEMA and free initiator is 130.14 and 195.05 g/mol, r.A.c., $MW_{theo,87\%} = 195.05 + 300 \cdot 0.87 \cdot 130.14 = 34161.59$ Da.
253. Yang, W.J., et al., *Biomimetic anchors for antifouling and antibacterial polymer brushes on stainless steel*. Langmuir, 2011. **27**(11): p. 7065-76.
254. Mrabet, B., et al., *Anti-fouling poly(2-hydroxyethyl methacrylate) surface coatings with specific bacteria recognition capabilities*. Surface Science, 2009. **603**(16): p. 2422-2429.
255. Castner, D.G., et al., *Characterization of Poly(2-Hydroxyethyl Methacrylate) (PHEMA) by XPS*. Surface Science Spectra, 1996. **4**(1): p. 14-20.
256. Yoshikawa, C., et al., *Fabrication of High-Density Polymer Brush on Polymer Substrate by Surface-Initiated Living Radical Polymerization*. Macromolecules, 2005. **38**(11): p. 4604-4610.
257. Porter, M.D., et al., *Spontaneously organized molecular assemblies. 4. Structural characterization of n-alkyl thiol monolayers on gold by optical ellipsometry, infrared spectroscopy, and electrochemistry*. Journal of the American Chemical Society, 1987. **109**(12): p. 3559-3568.
258. Sabatani, E., et al., *Organized self-assembling monolayers on electrodes: Part I. Octadecyl derivatives on gold*. Journal of Electroanalytical Chemistry and Interfacial Electrochemistry, 1987. **219**(1-2): p. 365-371.
259. Sabatani, E. and I. Rubinstein, *Organized self-assembling monolayers on electrodes. 2. Monolayer-based ultramicroelectrodes for the study of very rapid electrode kinetics*. The Journal of Physical Chemistry, 1987. **91**(27): p. 6663-6669.
260. Smith, R.K., P.A. Lewis, and P.S. Weiss, *Patterning self-assembled monolayers*. Progress in Surface Science, 2004. **75**(1-2): p. 1-68.
261. Kim, D.H., M. Abidian, and D.C. Martin, *Conducting polymers grown in hydrogel scaffolds coated on neural prosthetic devices*. J Biomed Mater Res A, 2004. **71**(4): p. 577-85.
262. Low, L.-M., et al., *Microactuators toward microvalves for responsive controlled drug delivery*. Sensors and Actuators B: Chemical, 2000. **67**(1-2): p. 149-160.
263. Lira, L.M. and S.I. Córdoba de Torresi, *Conducting polymer-hydrogel composites for electrochemical release devices: Synthesis and characterization of semi-interpenetrating polyaniline-polyacrylamide networks*. Electrochemistry Communications, 2005. **7**(7): p. 717-723.
264. Brahim, S., D. Narinesingh, and A. Guiseppi-Elie, *Bio-smart hydrogels: co-joined molecular recognition and signal transduction in biosensor fabrication and drug delivery*. Biosensors and Bioelectronics, 2002. **17**(11-12): p. 973-981.
265. Åsberg, P. and O. Inganäs, *Hydrogels of a conducting conjugated polymer as 3-D enzyme electrode*. Biosensors and Bioelectronics, 2003. **19**(3): p. 199-207.
266. Brahim, S., D. Narinesingh, and A. Guiseppi-Elie, *Polypyrrole-hydrogel composites for the construction of clinically important biosensors*. Biosens Bioelectron, 2002. **17**(1-2): p. 53-9.
267. Baughman, R.H., *Conducting polymer artificial muscles*. Synthetic Metals, 1996. **78**(3): p. 339-353.
268. Gilletti, A. and J. Muthuswamy, *Brain micromotion around implants in the rodent somatosensory cortex*. J Neural Eng, 2006. **3**(3): p. 189-95.
269. Griffith, R.W. and D.R. Humphrey, *Long-term gliosis around chronically implanted platinum electrodes in the Rhesus macaque motor cortex*. Neurosci Lett, 2006. **406**(1-2): p. 81-6.
270. Tanaka, M. and E. Sackmann, *Polymer-supported membranes as models of the cell surface*. Nature, 2005. **437**(7059): p. 656-663.
271. Sackmann, E. and M. Tanaka, *Supported membranes on soft polymer cushions: fabrication, characterization and applications*. Trends in Biotechnology, 2000. **18**(2): p. 58-64.
272. Salvadori, M.C., et al., *Measurement of the elastic modulus of nanostructured gold and platinum thin films*. Physical Review B, 2003. **67**(15): p. 153404.

273. Kaufman, J.D., et al., *Time-dependent mechanical characterization of poly(2-hydroxyethyl methacrylate) hydrogels using nanoindentation and unconfined compression*. J Mater Res, 2008. **23**(5): p. 1472-1481.
274. Yamamoto, S., et al., *Surface Interaction Forces of Well-Defined, High-Density Polymer Brushes Studied by Atomic Force Microscopy. 1. Effect of Chain Length*. Macromolecules, 2000. **33**(15): p. 5602-5607.
275. Urayama, K., et al., *Elastic Properties of Well-Defined, High-Density Poly(methyl methacrylate) Brushes Studied by Electromechanical Interferometry*. Macromolecules, 2002. **35**(25): p. 9459-9465.
276. Neugebauer, D., et al., *Densely-Grafted and Double-Grafted PEO Brushes via ATRP. A Route to Soft Elastomers*. Macromolecules, 2003. **36**(18): p. 6746-6755.
277. Hecker, S.S., D.L. Rohr, and D.F. Stein, *Brittle fracture in iridium*. Journal Name: Metall. Trans., A; (United States); Journal Volume: 9A; Journal Issue: 4, 1978: p. Medium: X; Size: Pages: 481-488.
278. Branner, A., R.B. Stein, and R.A. Normann, *Selective Stimulation of Cat Sciatic Nerve Using an Array of Varying-Length Microelectrodes*. Journal of Neurophysiology, 2001. **85**(4): p. 1585-1594.
279. Hambrecht, F.T., *Visual prostheses based on direct interfaces with the visual system*. Baillieres Clin Neurol, 1995. **4**(1): p. 147-65.
280. Tourovskaia, A., et al., *Micropatterns of Chemisorbed Cell Adhesion-Repellent Films Using Oxygen Plasma Etching and Elastomeric Masks*. Langmuir, 2003. **19**(11): p. 4754-4764.
281. Daniel, P., et al., *Design of a high-resolution optoelectronic retinal prosthesis*. Journal of Neural Engineering, 2005. **2**(1): p. S105.
282. Grill, W.M., *Signal Considerations for Chronically Implanted Electrodes for Brain Interfacing*, in *Indwelling Neural Implants: Strategies for Contending with the In Vivo Environment*, W.M. Reichert, Editor. 2008, Taylor & Francis Group, LLC: Boca Raton FL.
283. Bettinger, C.J., R. Langer, and J.T. Borenstein, *Engineering Substrate Topography at the Micro- and Nanoscale to Control Cell Function*. Angewandte Chemie International Edition, 2009. **48**(30): p. 5406-5415.
284. Saha, K., et al., *Substrate modulus directs neural stem cell behavior*. Biophysical Journal, 2008. **95**(9): p. 4426-4438.
285. Chen, X., et al., *Synthesis and aqueous solution properties of polyelectrolyte-grafted silica particles prepared by surface-initiated atom transfer radical polymerization*. J Colloid Interface Sci, 2003. **257**(1): p. 56-64.
286. Farina, D., et al., *Surface EMG crosstalk evaluated from experimental recordings and simulated signals. Reflections on crosstalk interpretation, quantification and reduction*. Methods Inf Med, 2004. **43**(1): p. 30-5.
287. Winter, D.A., A.J. Fuglevand, and S.E. Archer, *Crosstalk in surface electromyography: Theoretical and practical estimates*. Journal of Electromyography and Kinesiology, 1994. **4**(1): p. 15-26.
288. Bund, A. and M. Schneider *Characterization of the Viscoelasticity and the Surface Roughness of Electrochemically Prepared Conducting Polymer Films by Impedance Measurements at Quartz Crystals*. Journal of the Electrochemical Society, 2002. **149**(9): p. E331-E339.
289. Tahk, D., H.H. Lee, and D.-Y. Khang, *Elastic Moduli of Organic Electronic Materials by the Buckling Method*. Macromolecules, 2009. **42**(18): p. 7079-7083.
290. Murray, P., et al., *In-situ mechanical properties of tosylate doped (pTS) polypyrrole*. Synthetic Metals, 1997. **84**(1-3): p. 847-848.
291. Pytel, R.Z., E.L. Thomas, and I.W. Hunter, *In situ observation of dynamic elastic modulus in polypyrrole actuators*. Polymer, 2008. **49**(8): p. 2008-2013.
292. Otero, T.F., J.J. López Cascales, and G. Vázquez Arenas, *Mechanical characterization of free-standing polypyrrole film*. Materials Science and Engineering: C, 2007. **27**(1): p. 18-22.

- 293. Herrasti, P., et al., *Electrochemical and mechanical properties of polypyrrole coatings on steel*. *Electrochimica Acta*, 2004. **49**(22–23): p. 3693-3699.
- 294. Koehler, S., A. Bund, and I. Efimov, *Shear moduli of anion and cation exchanging polypyrrole films*. *Journal of Electroanalytical Chemistry*, 2006. **589**(1): p. 82-86.
- 295. Green, R.A., et al. *Novel neural interface for vision prosthesis electrodes: Improving electrical and mechanical properties through layering*. 2007. Kohala Coast, HI: IEEE.
- 296. Cui, X.Y. and D.C. Martin, *Electrochemical deposition and characterization of poly(3,4-ethylenedioxythiophene) on neural microelectrode arrays*. *Sensors and Actuators B-Chemical*, 2003. **89**(1-2): p. 92-102.
- 297. Masuda, H. and D.K. Asano, *Preparation and properties of polypyrrole*. *Synthetic Metals*, 2003. **135**(1-3): p. 43-44.
- 298. Smith, T.J. and K.J. Stevenson, *4 - Reference Electrodes*, in *Handbook of Electrochemistry*, G.Z. Cynthia, Editor. 2007, Elsevier: Amsterdam. p. 73-110.
- 299. Pourbaix, M., *Atlas of electrochemical equilibria in aqueous solutions*. 1st English ed. ed. 1966: Oxford, New York, Pergamon Press.
- 300. Cui, X.Y., et al., *Surface modification of neural recording electrodes with conducting polymer/biomolecule blends*. *Journal of Biomedical Materials Research*, 2001. **56**(2): p. 261-272.